Examination of the stir-casting method to produce Al-SiC composites

by

Sumsun Naher

B.Sc.Eng, M.Sc.Eng

A thesis submitted for the degree of
Doctor of Philosophy

School of Mechanical and Manufacturing Engineering
Faculty of Engineering and Computing
Dublin City University

February 2004

Supervisors
Dr. Dermot Brabazon
Dr. Lisa Looney

Declaration

I hereby certify that this material, which I now submit for assessment on the programme of study leading to the award of Doctor of Philosophy is entirely my own work and has not been taken from the work of others and to the extent that such work has been cited and acknowledged within the text of my work.

S. Naher 06/05/04

SUMSUN NAHER
ID No: 99145650
February 2004

This work has been disseminated through the following publications.

Journal Papers:

• S. Naher, D. Brabazon, and L. Looney, Simulation of the stir casting process *Journal of Materials Processing Technology*, pages 567-571, 143-144, 2003.

Conference papers:

• S. Naher, D. Brabazon, and L. Looney, A computational two phase model for liquid and semi solid MMC's processing, *Proceedings of the Seventh International Conference on the Semi-Solid Processing of Alloys and Composites*, pages 443-448, Tsukuba, Japan, 25th–27th September 2002.

• S. Naher, D. Brabazon, and L. Looney, A computational model for MMC's processing, *Proceedings of Int. Conf. on Advances in Materials and Processing Technologies*, pages 535-538, Dublin, Ireland, 8th–11th July 2003.

Dedication

This thesis is dedicated to my father Shamsul Hoque Bhuiyan and my brother Zahirul Hoque Bhuiyan whose inspiration and constant support allowed me to come up to this point and to me who are the symbol of love, trust and greatest personality.

Acknowledgements

The author wishes to express her heartiest gratitude and profound indebtness to her thesis supervisors Dr. Dermot Brabazon and Dr. Lisa Looney, Lecturers, School of Mechanical and Manufacturing Engineering, Dublin City University for their constant guidance, enthusism, constructive criticism, valuable suggestions, encouragement, benevolent help and practical hand on assistance in carrying out the research work as well as in writing this thesis.

The author would like to express her heartiest gratitude and profound indebtness to Professor M.S.J. Hashmi, Head, MME, DCU, Dublin, who not only funded this project but also providing the laboratory facilities and inspiration without whose support and encouragement this thesis would not have been completed.

The author wishes to express her heartfelt gratitude and sincere thanks to her husband Dr. Monjur Morshed for providing his valuable time, suggestions and encouragement during the project work as well as in writing this thesis. Author also like to thank her son Mufid Morshed who was born during this study and made her life full by providing unconditional love and endless inspiration.

Author has greatest respect and admiration for Professor Ehasanul Hoque, MME, BUET for his guidance, encouragement and support over the years.

Sincere thanks are due to school teachers and technicians for their generous assistance, especially appreciation goes to Mr. Christopher Crouch, Mr. Keith Hickey and Mr. Micheal May. Thanks are also due to the officers and staff of the school for their help in various stages of the study. Author would like to thank all friends and colleagues namely, Abu Raihan Rashid, Abu Hena, Ahmed Elfiki, Ahmed Imhamed, Ali Shah, Ekhlasur Rahman, Jufikar Haider, Mafizur Rahman, Mahbub Hasan, Mahfujur Rahman, Shafiqur Rahman, Tarik Chowdhury and Taslima Akter for their friendship and support.

Finally the author wishes to express her gratitude to her mother, siblings and well wishers for their continued encouragement and inspiration throughout her life as well as this research work. Without one name this acknowledgement would remain incomplete that is Dr. Kashmiri Hashmi whose valuable time, advice and support made life in Ireland easier and enjoyable. She owes them a lot.

Abstract

This work examined the influence of processing parameters on the production of Al-SiC metal matrix composites (MMC) by batch compocasting process. Processing parameters investigated include stirring speed, stirring time, stirrer geometry, stirrer position, metal fluid temperature (viscosity). Room temperature (25°C) visual simulations, computer simulations and validation Al-SiC MMC production tests were performed.

In the visual and computer simulations, water and glycerol/water were used to represent liquid and semi-solid aluminium respectively. The effects of viscosities of 1, 300, 500, 800 and 1000 mPas and stirring speeds of 50, 100, 150, 200, 250 and 300 rpm were investigated. A 10 vol. % reinforced SiC particulate, similar to that used in the aluminium MMC's, was used in the visualisation and computational tests. The visualisation tests were carried out in a transparent glass beaker. The computational simulation was performed with Fluent (CFD software) and an add on package MixSim. This consisted of a 2D axisymmetric multiphase time dependent simulation of the production route using an Eulerian (granular) model. The dependence of particle dispersion times, settling times and vortex height on stirring geometry and stirrer speed was found. A blade angle of 60 degrees was found better for the flat blade stirrer, to obtain uniform particulate dispersions quickly. From these tests a stirring speed of 150 rpm for water-SiC and 300 rpm for the glycerol/water-SiC system were found to be necessary in order to obtain a uniform distribution of the SiC. A viscosity increase from 1 mPas (for liquid metal) to 300 mPas (for semi-solid metal) was found to have a tremendous effect on the SiC dispersion and settling times. However, a further increase from 300 mPas to 1000 mPas had negligible effect on this time. A significant part of the work consisted of the design, construction and validation of a specialised quick quench compocaster for this high temperature processing method. This machine consisted of a stirrer with four 60 degree angled flat blades and a crucible in a resistance heated furnace chamber. An actuator was integrated to this rig to enable quick quenching of the processed mixture. This device was used to produce Al-SiC composites. Generally, good agreement was found between the visualisation, computational and validation experimental results.

Contents

List of Tables

List of Figures

Chapter 1

Literature review

1.1 Background

Metal matrix composites (MMCs) are a relatively new range of advanced materials providing properties hithertofore not achieved by conventional materials. The benefit of MMCs is that they can be tailored to produce various combinations of stiffness and strength. The most attractive properties of MMCs is their potential availability of high specific stiffness at high temperatures. MMC materials have a combination of different, superior properties to an unreinforced matrix, which can result in a number of service benefits, among which are: increased strength, higher elastic modulus, higher service temperature, improved wear resistance, decreased part weight, better fatigue resistance, high toughness and impact properties, high electrical and thermal conductivity, low coefficient of thermal expansion [1]. The excellent mechanical properties of these materials, together with weight saving make them very attractive for a variety of engineering applications in the automotive [2] and aerospace [3] industries. Some MMC parts are shown in figure 1.1 (a). An example of some of the discontinuous silicon carbide aluminium cast parts may be seen in figure 1.1 (b).

There are several liquid fabrication techniques available to manufacture MMC materials [5,6]. According to the type of reinforcement, the fabrication techniques can vary considerably. These techniques include stir casting [7–12], liquid metal infiltration [13–15], squeeze casting [16, 17], spray co-deposition [18] and compocasting [19]. Compocasting in composite production is the present research interest. Compocasting involves the addition of particulate reinforcement into semi-solid metal (SSM) by means of agitation. The advantage of compocasting lies in a low processing temperature [20, 21] compared to conventional casting. High fluidity can be achieved in SSM by means of shearing [22]. The more laminar flow that can then be produced reduces solidification shrinkage, making the

(a) (b)

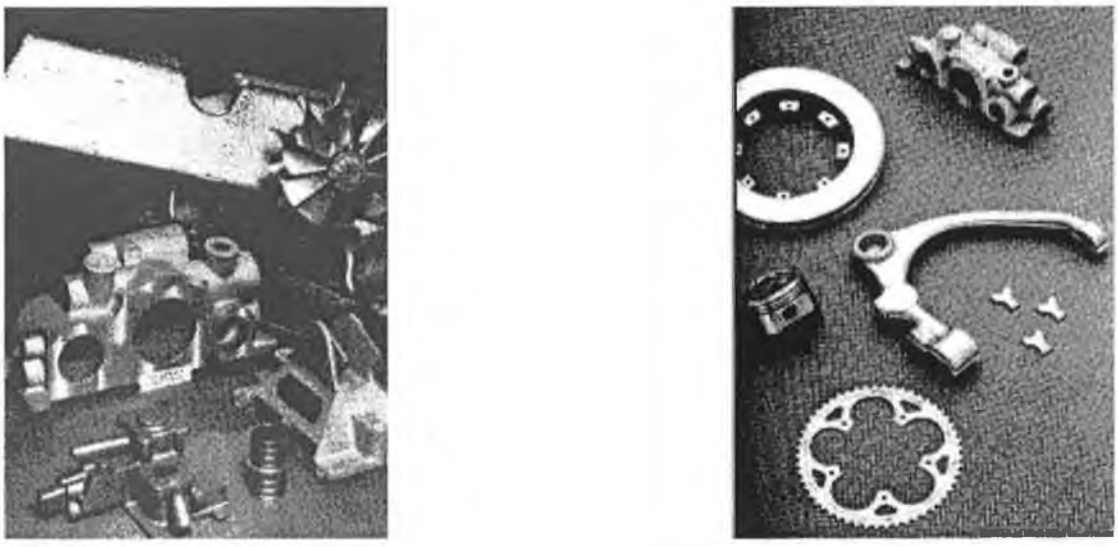

Figure 1.1: (a) Various parts made from aluminium MMCs. (b) Discontinuous silicon carbide/aluminium castings: automotive disk brake rotor, upper control arm, piston, bicycle sprocket, aircraft hydraulic manifold, three engine cylinder inserts. [4]

fabrication of structural components with tight tolerance possible [23]. The production can be carried out by conventional foundry methods [24]. Disadvantages with the method, if process parameters are not adequately controlled, include the fact that non-homogeneous particle distribution results in sedimentation and segregation [25].

In this research, A356 aluminium alloy was used as the matrix material and SiC_p as the reinforcement material. The specific research focus is to achieve a uniform distribution of SiC_p throughout the A356 aluminium alloy by the compocasting method. To reach this research goal, firstly some physical simulations were carried out and then computational simulation and finally the results from both physical and computational simulation were applied to the quick quenched compocasting system.

This thesis contains six chapters. Those are accordingly,

1. Literature review
2. Visualisation modeling experiments
3. Computational modeling
4. Stir-casting validation experiments

5. Discussion

6. Conclusion

The first chapter deals with the introduction to the present research work, and literature review carried out for this research includes the topics of material selection, MMC fabrication methods, challenges in stir casting and mechanical properties of cast, particulate reinforced MMC. Physical and computer simulation of the MMCs fabrication process are described in Chapter 2 and Chapter 3. Chapter 4 includes experimental equipment and procedure carried out, including designing of rig, sample preparation, metallographic examination and image analysis. Chapters 2, 3, and 4 also contain results. Chapter 5 consists of discussion based on the simulation and experimental works. Finally, chapter 6 contains the conclusions from this present research, and provides suggestions for future work related to this field of study.

1.2 Composite materials

Unlike alloys, composites must be a combination of at least two chemically distinct materials with a distinct interface separating the constituent materials. MMCs basically consist of a non-metallic reinforcement incorporated into a metallic matrix [4].

The matrix main function is to transfer and distribute the load to the reinforcements or fibres. This transfer of load depends on the bonding at the interface between the matrix and the reinforcement; however bonding depends on the type of matrix, the reinforcement and the fabrication technique [17,26]. In general the prime role of the reinforcement material in the matrix metal is to carry load. Reinforcement increases strength, stiffness, and temperature resistance capacity, but generally lowers the fracture toughness and ductility of the MMCs.

There are a number of criteria to consider before appropriate selection of materials for a composite system. Some of these criteria are inter-related. Several criteria for the selection of matrix and reinforcement materials are as follows [26,27]:

- Compatibility
- Thermal properties
- Fabrication method
- Application

- Cost
- Properties
- Recycling

1.2.1 Selection of matrix materials

Many of the matrices used in MMCs are well known metals or alloys [28], selected mainly on the basis of their already known mechanical properties which, in turn, can be further enhanced by means of suitable heat and/or working treatment. For the matrix material, factors such as density, and strength retention at elevated temperature and ductility are considered to be important [17]. The matrix can also be selected on the basis of oxidation and corrosion resistance or other properties [4].

Matrix selection depends not only on desirable properties but also on which material is best suited for a particular composite manufacturing technique [29]. For example powder is used in powder metallurgy techniques [30] and liquid matrix material is used in liquid metal infiltration [13,14], squeeze casting [16,17] and compocasting [19]. In liquid based techniques, it is necessary to give careful consideration to the matrix chemical compatibility with the reinforcement or its coating, to its ability to wet, its own characteristic properties and processing behavior. Generally Al, Ti, Mg, Ni, Cu, Pb, Fe, Ag, Zn, Sn and Si are used as the matrix materials, but Al, Ti and Mg are most widely used [14,31].

Currently the main focus is given to aluminium alloys as the matrix material because of its unique combination of good corrosion resistance, low electrical resistance and excellent mechanical properties [4]. This is also because aluminum has low density, which is the first requirement in most potential applications of MMCs. Additionally; it is inexpensive in comparison to other low density metals such as Ti and Mg. Aluminium has a density of only of 2700 kg m^{-3}, approximately one third that of steel (7830 kg m^{-3}), copper (8930 kg m^{-3}), or brass (8530 kg m^{-3}) [4]. It can display excellent corrosion resistance in most environments, including atmosphere, water (including salt water), petrochemicals, and many chemical systems. In recent years, Al-Li [32], and Al-Si [33], alloys have received considerable attention.

Titanium has been examined for use in aero-engines, mainly for compressor blades and discs, due to its higher elevated temperature resistance property [34]. The melting point of titanium is relatively higher than aluminium, so the strength of Titanium is retained to higher temperatures than for aluminium. Corrosion and oxidation resistance of Ti is also good. Magnesium is the lightest structural metal,

approximately 35 % lighter than aluminum, and is a potential matrix material for composites [17].

Inter-metallic compounds have also been developed as matrix materials. Their high temperature capability and oxidation resistance is higher than those of titanium matrix composites. Among them are Ni_3Al, Ti_3Al and $MoSi_2$. These intermetallic materials have high strength, high elastic moduli and good creep resistance. The major disadvantage of these materials is their low ductility at room temperature, and this makes the processing method of structural components more difficult. However, this problem can be reduced by addition of certain alloying elements.

1.2.2 Selection of reinforcing materials

The correct selection of reinforcement type, geometry or shape is important in order to obtain the best combination of properties at relatively low cost. For instance, the use of spherical reinforcements instead of angular reinforcements could be advantageous in certain components [35]. When selecting the reinforcement materials the following aspect must be considered:

1. Shape - Continuous fibre, chopped fibre, whiskers, spherical or irregular particles, or flakes
2. Size - diameter and aspect ratio
3. Surface morphology - smooth or corrugated and rough
4. Surface defects - voids
5. Inherent properties - such as strength, moduli and density
6. Chemical compatibility with the matrix

In terms of size and shape, the reinforcement material may be subdivided into three major categories [17]:

1. Continuous fibres
2. Whiskers
3. Particles or platelet

Figure 1.2 shows schematic diagram of different kinds of reinforcing elements.

Figure 1.2: Schematic diagram of different kinds of reinforcing elements.

Continuous fibre

Continuous fibres exhibit highest strength when they are oriented unidirectionally, but the composite then has low strength in the direction perpendicular to the fibre orientation. Carbon (C), boron (B), silicon carbide (SiC) and alumina (Al_2O_3) are the most researched continuous reinforcements [36]. The density of carbon fibre is the lowest; accordingly, it can offer significant weight savings. Boron fibres show the greatest strength in comparison with other fibres, however the cost of these fibres is very high.

The continuous fibre reinforced composite offers the best combination of strength and stiffness, compared to other types of reinforcement. Among the greater benefits is the increased strength with increased temperature. Aluminium based fibre MMCs have useful strength up to 400 °C [37]. However the cost of these systems are very high, mainly because of high costs of the continuous fibres and the composite production cost [38]. These expensive materials have military applications, where weight saving is of greater importance than the production cost. However, continuous fibres suffer from fibre damage, especially during secondary processing [39], such as rolling and extrusion. These materials are non recyclable.

Whiskers

Numerous materials, including metal, oxides, carbides, halide and organic compounds have been prepared under controlled conditions into the form of whiskers. Whisker based composites are more costly than particle based ones, but in general they offer higher strength than particle based composites. Compared to other discontinuous reinforcement, such as poly crystalline flake, particle or chopped fibres, single crystal whiskers usually have a much greater tensile strength. Whisker reinforced composites offers the potential for enhanced properties, but suffer from whisker breakage and damage during secondary fabrication [40]. Discontinuous fi-

bres and whiskers are not as expensive as continuous fibres, however the whiskers have a higher cost than discontinuous fibres. The whisker reinforced material retains strength up to 250 °C [41].

Particles

A major reason for using particles is to reduce the cost of the composite. Particles are the most common and cheapest reinforcement. These are readily available in the quantities, size and shape required. This type of reinforcement material produces discontinuous reinforced composites with isotropic properties. Another advantage is that conventional fabrication methods may be used to produce a wide range of product forms, making them relatively inexpensive compared to composites that are reinforced with continuous fibre or filaments. Because of their relatively low cost, these materials are likely to find extensive application [41].

Particle shape and size can play an important role since angular particles can act as stress raisers, whereas rounded or globular particles are favored for their impact properties. Spherical particles should give better ductility than angular shapes [41]. It has been found that fine particles are more effective in strengthening the composites than coarse particles of the same volume fraction [42].

More coarse particles are, in general, easily incorporated in liquid melts but are more susceptible to gravity settling and can result in a heavily segregated casting [43, 44]. These particles are more susceptible to cracking under stress, resulting in poor mechanical properties of the composite [45]. Larger particles show a greater propensity to crack than smaller particles, having a higher probability of containing defects. However, fine particles in a matrix pose difficulty due to the clustering of the particles and other problems associated with the large surface area of the particles, such as increased viscosity of a melt, making processing more difficult. Most molten metal processing uses ceramic particles in the size range of 10-20 μm [43].

The preferred and most used of the particle materials, for aluminium alloy matrix composites is silicon carbide (SiC), due to its favorable combination of mechanical properties, density and cost [46, 47]. Another widely used particle reinforcement in aluminium matrix composites is Al_2O_3. In comparison to SiC, it is more suitable for high temperature fabrication and use. Some other particle reinforcement have also been investigated. For example, graphite can give the composite specific tribological properties, and B_4C reinforced materials may have nuclear application because of neutron capturing properties of boron [48]. It is well established that uniformly distributed reinforcements of finer size and clean interface are essential for improvement of mechanical properties [49].

Initial interest in whiskers and particle reinforcements has declined because of realization of the health hazard posed in their handling [17]. Skin, eye and respiratory protection must be used during the handling of these powders to minimise exposure in the event of accidental spillage during mixing [10,50]. Very fine whiskers in particular may cause respiratory disorders, and can be carcinogenic.

1.2.3 Properties of MMCs

Metals have a useful combination of engineering properties such as good strength, high ductility and toughness and high temperature resistance, but they have relatively low stiffness. Ceramics are stiff and strong, but brittle. Aluminum and silicon carbide have very different mechanical properties, for example Youngs moduli of 70 GPa and 400 GPa, coefficients of thermal expansion (CTEs) of $24 \times 10^{-6}\ ^{\circ}C^{-1}$, and $4 \times 10^{-6}\ ^{\circ}C^{-1}$, and yield strengths of 350 MPa and 600 MPa respectively [51,52]. The concept involved in the design of MMC materials is to combine the desirable attributes of metals and ceramics.

In general the addition of reinforcement phase to the matrix metal will yield several advantages such as increases in elastic modulus, yield and tensile strength, creep and wear resistance, and also an increase in elevated temperature strength. If the elastic moduli are increased, it is usually possible to decrease the component thickness and therefore reduce the weight for any given design. An increase in moduli indicates an increase in stiffness, and the specific stiffness for aluminum composite is high since the density is low.

The properties of metals reinforced with short fibres (whiskers) or particulates, although still superior to those of the respective matrix alloy, are modest compared to those of continuous fibre reinforced MMCs.

In general, with increasing volume fraction of reinforcement, the strength of the composite will increase. According to Mohn and Gegel [53] by increasing the content of SiC particles in composite materials, increase in tensile strength, yield strength and elastic modulus can be attained. Tensile tests [54] of Al-SiC particle MMC indicate that for high volume fraction samples (20 % SiC_p), the fracture process is very localized. According to Wang [54] as the volume fraction of the reinforcement decreases, the deformation region spreads out. The Young's modulus of A356/SiC composites increases with increasing content of SiC particles, up to 100 % for 20 vol. % of SiC. Addition of SiC decreases the thermal expansion coefficient of the composites [55]. An increase of SiC particle size did not improve crack initiation toughness of SiC/Al composite. Crack initiation toughness was independent of SiC particle size up to 20 μm average size [56].

Lim and Dunne [57] studied the effect of volume fraction of reinforcement on

the elastic response of Al-SiC composite. They found that the elastic modulus of the composites increase with increasing content of the reinforcement, and the yield strength also increase with increasing content of the reinforcement [58]. Figure 1.3 (a) shows the effect of silicon carbide particle percentage on elastic modulus [59]. Figure 1.3 (b) shows the effect of temperature on elastic modulus. Table 1.1 shows the mechanical properties of SiC particle reinforced aluminium matrix composites (AMCs).

With smaller size particles, the fracture toughness will increase as the particle size increases; whereas the toughness decreases with increasing the particle size when the size is very large [60, 61].

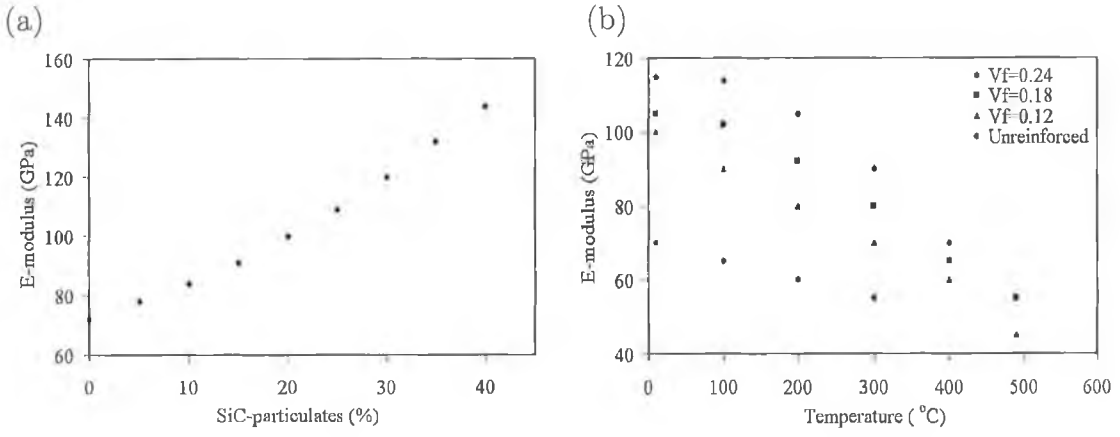

Figure 1.3: (a) Elastic modulus versus SiC particle content for A2124-T6 [59], (b) Elastic modulus versus temperature for Al-9Si-3Cu alloy with varying quantity of alumina fibres [62].

Table 1.1: Mechanical properties of SiC_p reinforced AMCs.

Composite system	Yield strength (MN m^{-2})	Ultimate tensile strength (MN m^{-2})	Percentage of elongation (%)	Elastic modulus (GN m^{-2})	Reference
A356(as cast)	96.6	165.6	6–7	-	[50]
A356-T6	205	280	6	76	[63]
A356/15 %SiC_p-T6	-	295	1.5	95	[64]
A2124/17 %SiC_p-T6	230	342	9.7	95	[65]
A6061/5 %SiC_p-T6	271.4	293.6	8.7	75.3	[66]

The tensile properties of sand cast and permanent mould cast bars of A356-SiC_p composites are given in Table 1.2. It is clear that the addition of SiC particle

results in substantial increases in the tensile yield strength, the tensile ultimate strength [67]. These results also illustrate that as the strength and stiffness is improved, the tensile ductility is decreased with the addition of SiC.

Table 1.2: Tensile properties of A356-SiC composite for different percentage of SiC at T6 condition (solutionised at 540 °C, aging at 160 °C) [67].

Volume percentage of silicon carbide (%)	Ultimate strength (MN m^{-2})	Yield strength (MN m^{-2})	Elongation (%)
0	227.50	199.93	4.0
10	255.078	241.29	0.7
15	289.55	296.44	0.4
20	296.44	296.44	0.5

1.3 MMC fabrication methods

There are several fabrication techniques available to manufacture MMC materials. Depending on the choice of matrix and reinforcement material and on the type of reinforcement, the fabrication techniques can vary considerably. According to the matrix materials processing phase, fabrication methods can be divided into three types.

1. Solid phase processes: Diffusion bonding, Hot rolling, Extrusion, Drawing, Explosive welding, Powder Metallurgy (PM) route, Pneumatic impaction
2. Liquid phase fabrication methods: Stir casting, Liquid metal infiltration, Spray co-deposition [68]
3. Semi-solid fabrication process: Squeeze casting, Compocasting, Pressure casting

1.3.1 Solid state fabrication methods

There are several ways to fabricate MMCs using solid phase materials but among them diffusion bonding and the powder metallurgy (PM) route are most widely used [17]. Diffusion bonding is normally used to manufacture fibre reinforced MMC using sheets of foils of matrix materials, but this is the most expensive method to fabricate MMC materials [34,69]. The PM route is the most commonly used for the preparation of discontinuous reinforced MMCs [70–73]. The technique used to produce MMC by powder metallurgy is similar to those used for powder

metallurgy processing of unreinforced materials. But because of the need for hot pressing, it is also very expensive method.

Solid state processes are generally used to obtain the best mechanical properties in MMCs, particularly in discontinuous MMCs. This is because segregation effects and brittle reaction product formation are at a minimum for these processes, especially when compared with liquid state processes [74].

Secondary processing of discontinuously reinforced metal matrix composite (DRMMC) such as extrusion and rolling, leads to break up of particle (or whisker) agglomerates, reduction or elimination of porosity, and improved particle to particle bonding, all of which tend to improve the mechanical properties of these materials [75].

1.3.2 Liquid phase fabrication methods

Normally liquid phase fabrication methods are more efficient than solid phase fabrication methods, because solid phase fabrication requires longer time [61]. Liquid phase fabrication will be inexpensive if it can be successfully undertaken by conventional casting methods. Among the variety of manufacturing processes available for discontinuous MMC production, stir casting is generally accepted, and currently practiced commercially. Its advantages lie in its simplicity, flexibility and applicability to large scale production and, because in principle it allows a conventional metal processing route to be used, its low cost. This liquid metallurgy technique is the most economical of all the available routes for MMC production, allows very large sized components to be fabricated, and is able to sustain high productivity rates. According to Skibo et al. [39], the cost of preparing composite materials using a casting method is about one third to one half that of competing methods, and for high volume production, it is projected that costs will fall to one tenth [1]. Potentially this is a relatively inexpensive [1] way of making a broad range of MMCs whereby the dispersoid is added to the surface of the melt and then becomes entrained in the melt by agitation and/or mechanical work [37, 76]. Variations of this process involve SSP (compocasting/rheocasting/thixoforming) [38].

In general stir casting of MMCs involves producing a melt of the selected matrix material, followed by the introduction of a reinforcing material into the melt, obtaining a suitable dispersion through stirring. The next step is the solidification of the melt containing suspended particles to obtain the desired distribution of the dispersed phase in the cast matrix.

The application of high temperature processing methods is limited by poor wettability and a tendency for chemical reaction of the reinforcement with liquid

metal. However, there are a number of techniques used to control these phenomena. Normally this type of fabrication method is carried out under vacuum or using an inert gas atmosphere to minimize the oxidation of the liquid metal. Generally there are three liquid phase fabrication methods or casting routes, which are currently in practice: vortex method [25, 40–42], liquid metal infiltration [77] and spray co deposition [17].

The vortex method is one of the variations in the stir casting method [78]. In the vortex method, the reinforcement is introduced into a vortex created in the liquid metal by stirring. Reinforcement is efficiently distributed throughout the melt, and the resulting composites can be cast. However, the vortex method of introducing particles into the melt is efficient only up to about 10-12 % of reinforcement addition by volume [79, 80].

Introducing reinforcement particles to the stirred molten matrix sometimes will entrap, not only the particles, but also other impurities such as metal oxide and slag, which is formed on the surface of the melt. In addition, during pouring air envelopes may form between particles, which can alter the interface properties between particles and the melt, retarding the wettability between them. In the case where the temperature of the particles added is not at the same as temperature of the molten slurry, the viscosity of the slurry increases very rapidly. In the vortex method the reinforcement particles are added to the top of the stirred liquid, and are drawn toward the center of the vortex. In other words, the vortices formed tend to concentrate particles added to the surface at the center of the mould. A pressure difference between the inner and outer surface of the melt sucks the particles into the liquid [74]. However, air bubbles are also sucked by the same mechanism into the liquid metal, resulting in high porosity in the cast product. Vigorously stirred melts will also entrap gas, which is extremely difficult to remove as the viscosity of the slurry increases.

The injection of a liquid metal through a fibrous or porous preform is known as liquid metal infiltration and is used to manufacture MMCs [27, 81]. Current research work done in this area is reported by a number of workers [15, 81, 82]. Spray co-deposition is also a liquid metal processing technique applied to produce MMCs [83].

1.3.3 Semi-solid fabrication methods

Incorporation of the reinforcement particles within a semi-solid alloy is claimed to be advantageous, because the solid mechanically entraps the reinforcement and agglomeration, and settling or flotation is avoided [84]. This involves adaptation of a technique called rheocasting [2, 85, 86]. This casting process of metallic al-

loys produces a unique cast structure with non-dendritic, globular primary solid phase. In this process, vigorous shearing is applied to a molten alloy as it cools into the solidification range. The shearing breaks the dendrites into individual round particles, which become more or less spherical by coarsening [86]. A casting becomes stiff when the solid fraction of primary phase is about 15 % in conventional casting. However, the rheocast slurry maintains very low viscosity at much higher solid fractions, depending on the shear rate and cooling rate. This enables the slurry to be cast at a lower temperature and provides many advantages over conventional liquid casting such as reduced hot cracking and reduced shrinkage.

When the rheocast ingot is reheated to a temperature at which it is semi-solid, it still maintains the cast shape and becomes soft enough for further processing. Then the reheated ingot may be die cast or forged to final dimensions with better microstructure and properties than those obtained by conventional processing. This is called Thixocasting and Thixoforging.

The rheocasting technique was extended to produce metal matrix composites [2, 85, 86]. Since reinforcements such as ceramic particulates, short fibers, or whiskers have poor wettability to molten metals, it is very difficult to fabricate such MMCs by mixing reinforcements and liquid metal. However, the reinforcement may be incorporated into a semi-solid alloy slurry of a matrix formed by rheocasting. Once the reinforcements are introduced into the semi-solid slurry, they are entrapped mechanically by primary solid particles. Then the chemical interaction between the reinforcements and liquid matrix proceeds with time, and finally the reinforcements are trapped in the composite slurry. This is called compocasting. The compocasting process is very effective in making cast composites with higher particle content [43, 45, 66, 87]. The reinforcement particles are added gradually, while stirring continues at a constant rate.

Vogel et al. [88] gave the term 'stir-casting' to the production of metals with spheroid like microstructure by a shearing action induced by stirring. The term stir-casting and compocasting are used interchangeably in this work.

1.3.4 Heat treatment of MMCs

Procedures

Solution heat treatment homogenizes structure and minimizes segregation of alloying elements in a cast material [89]. The eutectic Si morphology plays a vital role in determining the material's mechanical properties. Under normal cooling conditions the phase is present as coarse needles. The needles act as crack initiators and lower mechanical properties.

In most cases, the A356, A357, A359 type alloys are solutionized at 540 °C [4].

Following solution treatment, the casting is quenched in water. The purpose of quenching is to suppress the formation of equilibrium Mg_2Si retained in solid solution, and the highest strength is obtained with fast quench rates. In most cases, the samples are quenched in water between 25 °C to 100 °C.

Quenching is followed by aging treatment, either natural or artificial aging. The purpose of this treatment is to precipitate constituents, which were dissolved during solution treatment. The microstructural changes occurring during this phase of heat treatment of A356 samples are illustrated in Figure 1.4 [89].

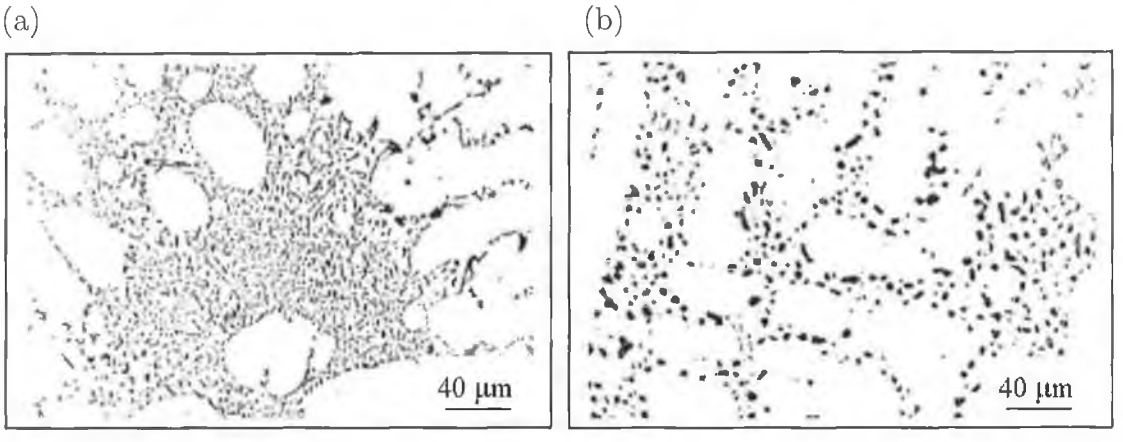

Figure 1.4: Microstructure depicting the morphology of eutectic Si as a function of aging time of 540 °C (500×) (a) as cast (b) after 2 hrs [89].

Initially Si is broken down into smaller fragments, and is gradually spheroidized. Prolonged solution treatment leads to coarsening of the particles and as the solution time is increased, there is coarsening of Si.

Effect of reinforcement particles

A number of investigators have reported that the presence of SiC particles accelerates the aging response in the matrix when compared to the unreinforced alloy [90–95]. Ribes and Suery [96] found that the addition of SiC particles to the Al-7Si-3Mg alloy accelerates aging during thermal treatment at 185 °C, and this is primarily due to the thermal mismatch between the reinforcement and the matrix. The aging behavior also depends on the nature of the surface of the particles. For oxidized particles, spinel forms at the interface leading to magnesium depletion in the matrix, and subsequently to less age hardening.

Yamada et al. [19] found that the addition of fibre or particles usually changes the aging response of the matrix due to the presence of high dislocation densities and residual stresses generated close to the reinforcement matrix interface. The

addition of SiC_p to Al-Si-Mg alloy accelerated the aging response during heat treatment. They also concluded that this is primarily due to the thermal mismatch between the reinforcement and the matrix. Salvo et al. [97] investigated the effect of reinforcement on the age hardening of cast 6061-SiC_p MMC, and found that the precipitation sequence in the unreinforced matrix and the composites is identical. The precipitation kinetics is accelerated in the composites by the higher dislocation density and enhanced nucleation, and this occurs at any aging temperature. The hardening behavior of the composites and unreinforced 6061 seems to be identical when the phase transformation occurs. Composites reach their maximum hardness when the aging temperature is beyond the critical temperature.

In general the hardness of the MMC is better than that of an unreinforced matrix, and this is more pronounced in the heat treated condition. The increase of hardness in heat treated MMCs, is primarily a result of precipitation microstructure changes, such as increase in dislocation density in the matrix, and the presence of the residual stress that is caused by the incorporated particles. The hardness in both the matrix and composite materials are shown in figure 1.5. This figure is from the work of Dutta and Surappa [98].

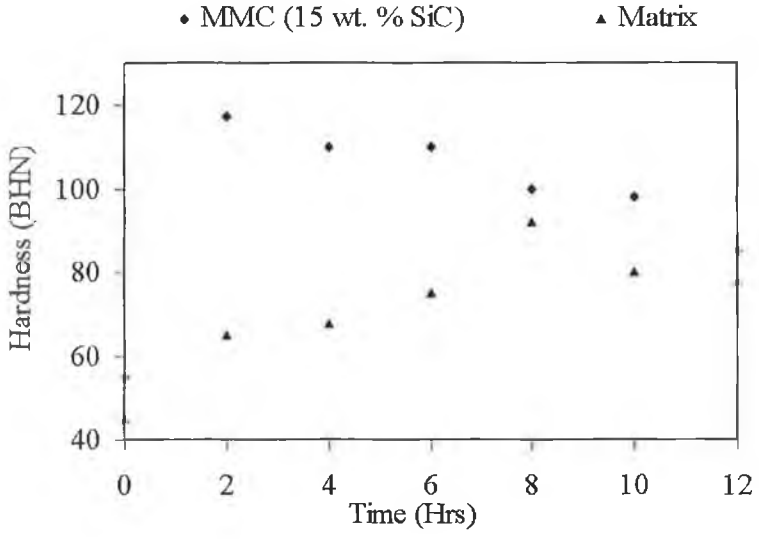

Figure 1.5: Aging studies on Al-15 % SiC materials [98].

1.4 Solidification

Solidification is a key stage of metal processing. Some important industrial processes in which solidification takes place include casting, welding, sintering, and metal coating. In each case, subsequent material properties are related to the

structure and composition of the material, mainly depending on the solidification process. Solidification is a phase transformation process from liquid to solid; liquid solidifies when cooled below a certain temperature, the process beginning with the formation of nuclei, followed by their subsequent growth. The nucleus is a simple unit of the appropriate crystal lattice structure for the metal, with atoms arranged accordingly. Slow cooling during solidification often develops an interesting structure made up of tree-like forms called dendrites. Dendritic solidification is the most common form of solidification in casting and an example of dendrites in an Al-4 % Si alloy may be seen in figure 1.6 (a). The shearing action during cooling reduces the dendritic microstructure into a spheroidal morphology, and a reduced viscosity of the semi-solid. The spheroids of solid in the liquid could easily flow over each other providing a non-restricting microstructural network and a fluid semi-solid metal. Such a spheroidal microstructure may be seen in figure 1.6 (b). As the liquid changes phase into solid, heat is lost in the process. Undercooling is the temperature drop below the equilibrium freezing temperature at which, in practice, a metal begins to solidify [99, 100]. In practice, nuclei are formed but are dissolved back into the liquid metal unless considerable supercooling occurs. In the absence of growth of these nuclei, solid grain structure is not generated. The energy of the crystal structure is less than that of the liquid, that is the main reason for solidification. Volume and surface free energy are associated with nucleation and growth phenomena and are shown in figure 1.7.

(a) (b)

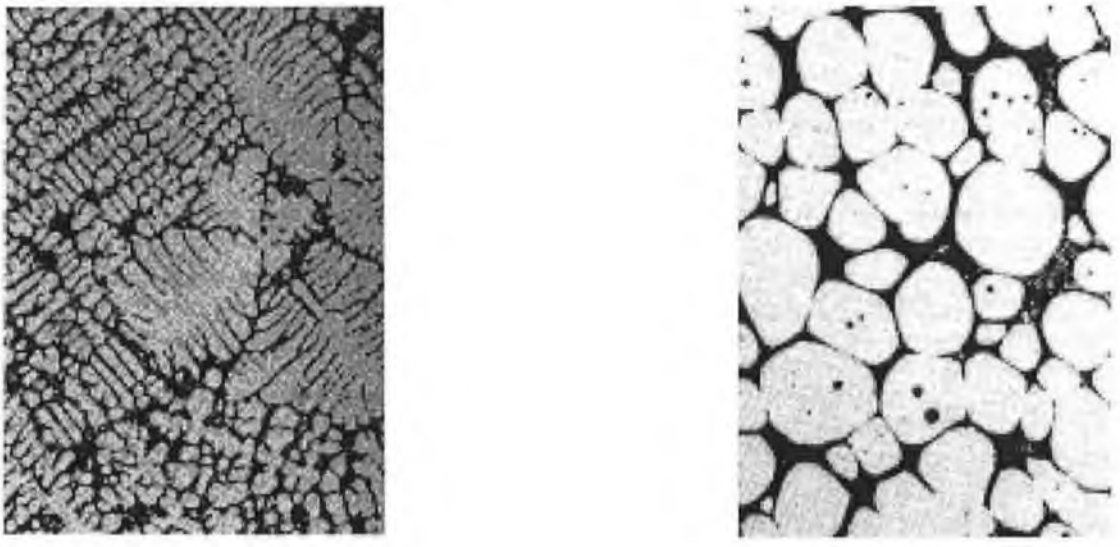

Figure 1.6: (a) Dendritic microstructure of conventionally cast Al-4 % Si, (b) Spheroidal microstructure of stir-cast Al-4 % Si [4].

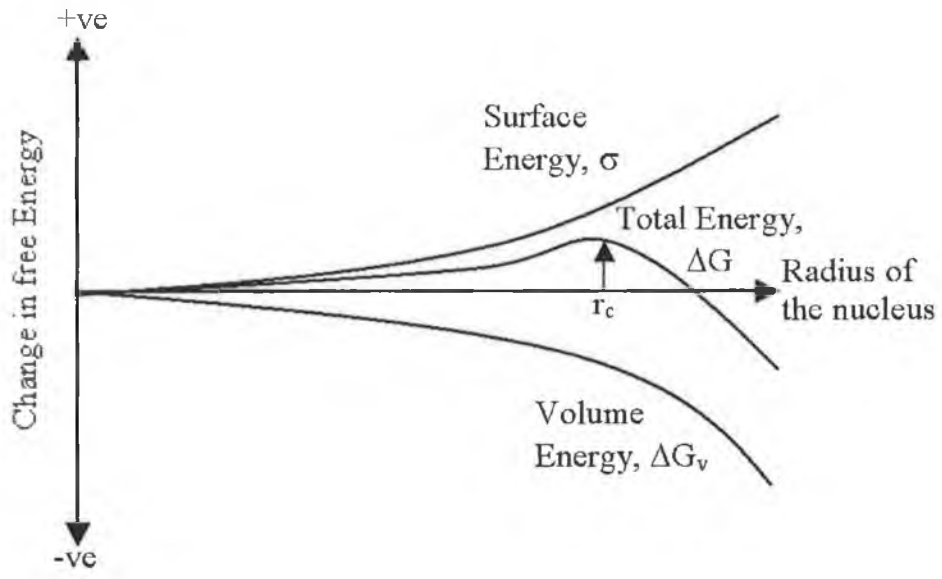

Figure 1.7: Total free energy of a solid liquid system.

As the solid grows in size (r is the radius of the solid nucleolus), the magnitude of the total volume free energy (ΔG_v) increases with a negative value. But, when solids form in a liquid there is an interface created, and the surface free energy (σ) is associated with this interface. As the solid grows, the total surface free energy increases with a positive value. That means, the total change in free energy for the system is the sum of the two factors. Presuming a spherical solid, the total free energy,

$$\Delta G = \frac{-4\pi r^3 \Delta G_v}{3} + 4\pi r^2 \sigma \tag{1.1}$$

The implication of equation 1.1 is that if the nucleus radius is less than a critical radius (r_c), it will redissolve and if the radius is greater than r_c, the embryo will grow.

The formation of nuclei may be homogeneous or heterogeneous. Spontaneous nucleation, known as homogeneous nucleation, may occur when an alloy is cooled rapidly to a temperature well below its equilibrium freezing temperature [101]. Homogeneous nucleation occurs without the help of foreign particles, and only occurs if the material is very pure. Heterogeneous nucleation occurs with the help of foreign particles such as the mold material or impurities in the molten metal. Inoculants are impurities or may form crystalline structures with a higher melting point than the melt to which they are added. Their presence increases nucleation sites, and therefore number of grains. Titanium carbide is known to act as a grain refiner in aluminium. Some of the inoculants are listed in Table 1.3.

Inoculants act as nucleation sites and are often added to alloys in order to increase the amount of nucleation. Higher undercoolings in both homogeneous and

Table 1.3: A list of inoculants for different metals and alloys.

Metal	Nucleation agent
Al alloys	Ti compounds such as $TiAl_3$, TiB_2, TiC
Plain carbon steel	Al compounds such as AlN, Al_2O_3
Stainless steel	Ca and Mg cyanides
Mg alloys	ZrC, ZrN, Zr oxides
Cast iron	Sulfur compounds

heterogeneous nucleation also produce a larger number of nucleations [101, 102]. High cooling rates are therefore associated with a finer grain size (a larger number of grains per unit volume). This is generally desirable within the solidified metal as larger grain boundary surface areas more effectively block the slip of crystal structure defects, resulting in better mechanical properties [103]. The grain size in a casting is determined by the nucleation rate which results in grain multiplication as well as the presence of fluid flow during solidification. The nucleation rate is influenced by the cooling rate and by the presence of heterogeneous nucleation catalyst.

Pure metals solidify at a single temperature. Alloys on the other hand solidify over a temperature range during which they are in the semi-solid state. To understand the solidification of Al-Si alloys, the phase diagram of Al-Si alloys, shown in figure 1.8, is important. From the phase diagram it is easy to get the solidus and liquidus temperatures for an alloy like A356 (line 10) and other necessary information like, percentage solid with the processing temperatures. A schematic of solidified microstructure at point a, b and c of figure 1.8 are shown in figure 1.9.

It is now established that the formation of solidification microstructure in cast particulate composites is mainly influenced by a number of factors: the nucleation, solidification rate, particulate pushing or being engulfed, and chemical reactions between particles and the matrix [17, 35, 63, 71, 105, 106]. The particulate reinforcement can influence nucleation rate as well as solidification rate, and hence modify the resulting grain size in the matrix. If the reinforcement surface serves as a propitious site for heterogeneous nucleation of the matrix, a much finer grain size will result.

1.4.1 Nucleation effects

It is normally expected that surfaces of ceramic particles suspended in solidifying melts would be favorable sites for the heterogeneous nucleation. However according to Jin and Lloyd [107], the reinforcement does not normally nucleate

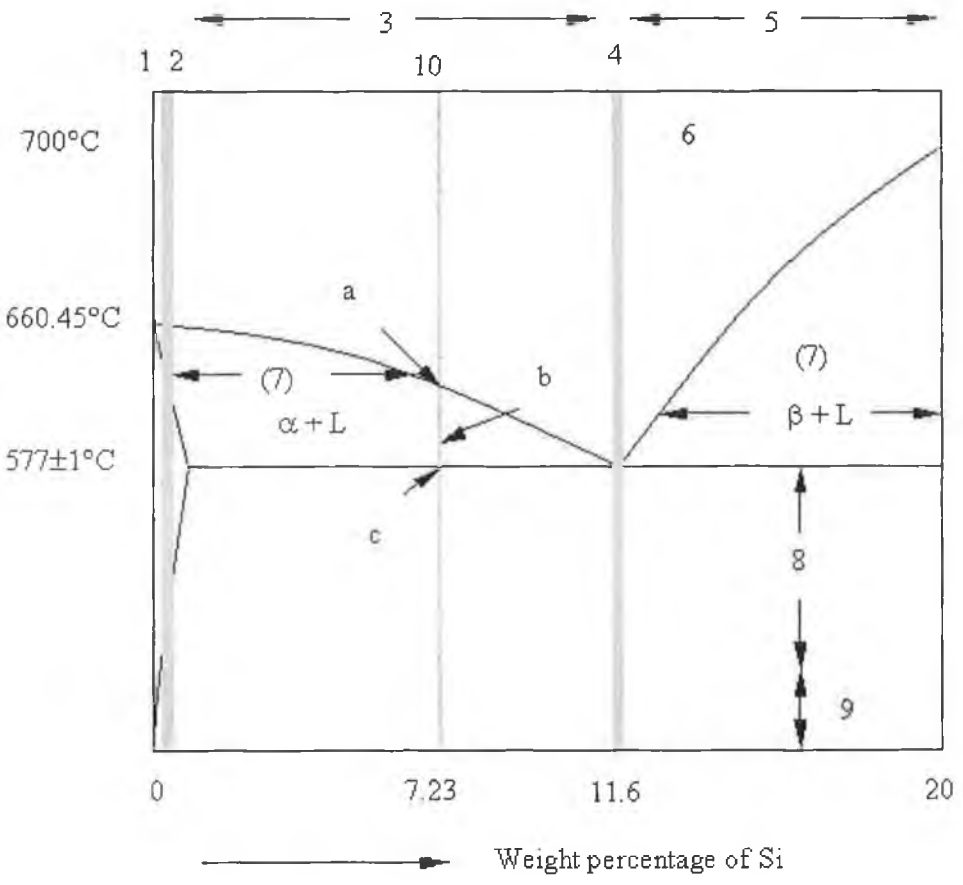

Figure 1.8: Schematic of the Al-Si phase diagram indicating (1) pure metal, (2) solid solution alloys, (3) hypoeutectic alloys (4) eutectic alloy, (5) hypereutectic alloys, (6) liquid metal, (7) semi-solid metal, (8) hot working temperature range, (9) cold working temperature range [101, 103, 104] (10) 7.23 % Si alloy (a) start of the solidification (b) semi-solid stage (c) completion of solidification.

Al dendrites, and does not affect the as cast grain size. Generally, the particulate reinforcements used to date are polycrystalline, and the crystallographic planes constituting their surfaces may not always be suitably oriented with respect to the solidifying phase. This inhibits forming a low energy interface with it and therefore it also inhibits substrates acting as sites for heterogeneous nucleation. During the solidification of hypoeutectic Al-Si alloys reinforced with SiC particulates, the particles are rejected by the growing Al dendrites. However, the effect of this on particle segregation in the solidified material depends on the cooling rate during solidification. At lower cooling rates, where the dendrite arm spacing is larger than the particle size, the particles segregate into the inter dendritic arm region. At the high cooling rates, where the dendrite arm spacing is smaller than the particle size, particles become virtually immobile and no solidification

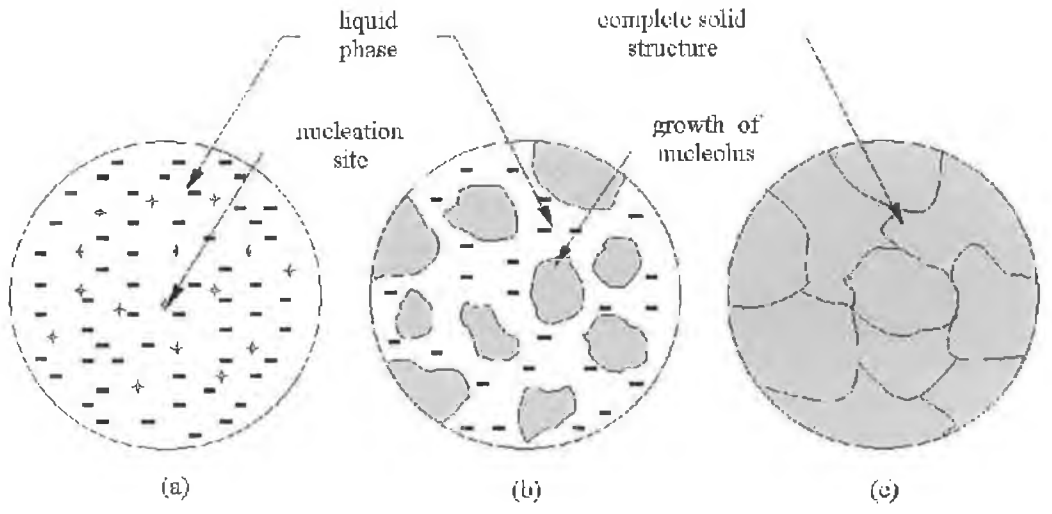

Figure 1.9: A schematic of solidified microstructure at point a, b and c of figure 1.8 (a) Nucleation sites (b) Growth of nuclei (c) completion of solidification.

induced segregation results [108]. α-aluminium dendrites in hypoeutectic Al-Si alloys do not nucleate on the surfaces of graphite, SiC, alumina, and silica particles [35]. The primary aluminium phase of the Al-Si hypoeutectic alloy does not nucleate on the SiC reinforcement particles and pre-oxidation of SiC particles does not have any effect on the nucleation process [78]. On the other hand, observations have confirmed that there is some indication that secondary silicon nucleates preferentially on the surface of the graphite, alumina, and silicon carbide particles. Zhou et al. [109] found that SiC particles were observed to act as substrates for heterogeneous nucleation of Si crystals in one of the composites produced (A356-10 % SiC).

Nucleation taking place away from the fibre surface can be explained in terms of the surface energy and thermal considerations. For example, it is known that alumina fibre is not wettable by an Al-Cu alloy matrix [17]. Any formation of solid within the melt will reduce the system energy, whereas the formation of the solid on the surface of the fibre will possibly lead to an increase in the system energy. From the thermal point of view, the conductivity of alumina is much less than that of the molten Al alloy, but since their temperatures were the same before solidification, and when it solidifies the alumina is slightly hotter than the molten metal, therefore nucleation must start at places away from the fibre. Nucleation takes place away from the fibre surface and starts within a large interstice first, and then proceeds in a small interstice. A schematic of nucleation and particle pushing solidification of SiC reinforced Al alloy matrix is shown in figure 1.10.

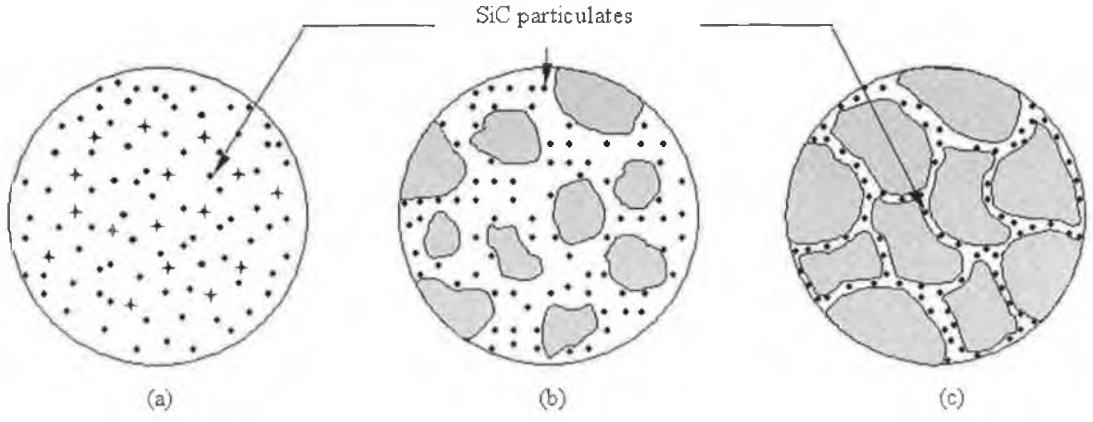

Figure 1.10: Schematics of nucleation of MMCs in SiC reinforced aluminium matrix, particle pushing; (a) starting of nucleation with solid embryo, (b) solidification started (c) solidification finished.

1.4.2 Interactions between particles and matrix solidification front

It is now well established that depending on the interfacial energies, a growing crystal can either engulf or reject particles [110–113]. Engulfment of the reinforcement means reinforcement wetting has taken place, and that the interfacial bonding between the particles and the matrix must be good. Two mechanisms have been suggested for particle pushing from flow [114, 115]. In the first mechanism, the particle is in contact with the solid and it is moved by the surface by the fluid flow as the solid grows. Whereas in the second mechanism, the particle which is located a small bit away from the solidification front and then moved. When a particle is rejected by the growing crystals and pushed ahead of the advancing interface, a viscous force is generated and this tends to work against the pushing of particle. Hence, it is the balance of these counteracting forces which decides the rejection or engulfment of the particle. It is parameters such as relative density difference, relative difference in thermal conductivity and heat diffusivity between the particle and metallic melt, and alloy composition which will effect the shape of the solidification front and determine the magnitude of these forces [110, 112]. Particle pushing [116] suggests that the solid metal has no affinity for reinforcement, and that the interfacial bonding is weak.

1.5 Challenges in stir cast MMC fabrication

Although compocasting is generally accepted as a commercial route for the production of MMC's [117], there are however technical challenges associates with producing a homogeneous high density composite. In preparing MMCs by stir casting, there are several factors that need consideration including:

1. The effect of poor wettability between the two substances,
2. The propensity for porosity in the cast metal matrix composite,
3. The possible chemical reactions between reinforcement material and matrix alloy,
4. The difficulty of achieving a uniform distribution of reinforcement material.

In order to achieve the optimum MMC properties, the distribution of the reinforcement materials in the matrix alloy must be uniform, and the wettability of bonding between these two substances should be optimized. The chemical reaction between reinforcement materials and the matrix alloy and porosity must be avoided or minimized.

1.5.1 Wettability

Good wetting of the reinforcement particle is an essential condition for the generation of a satisfactory bond between a solid ceramic phase and a liquid metal matrix during casting of a composite [118]. The mechanical properties of metal MMCs are controlled to a large extent by the structure and properties of the reinforcement metal interface [106, 118–120]. It is believed that a strong interface permits transfer and distribution of load from the matrix to the reinforcement, resulting in an increase elastic modulus and strength. From metallurgical considerations the desired interfacial region in a composite relies on several factors [121]:

1. An intimate contact between the reinforcement and matrix to established satisfactory wetting of the reinforcement by the matrix.
2. A very low rate of chemical reaction at the interface, and no or little interdiffusion between the component phases so that the reinforcement is not degraded.

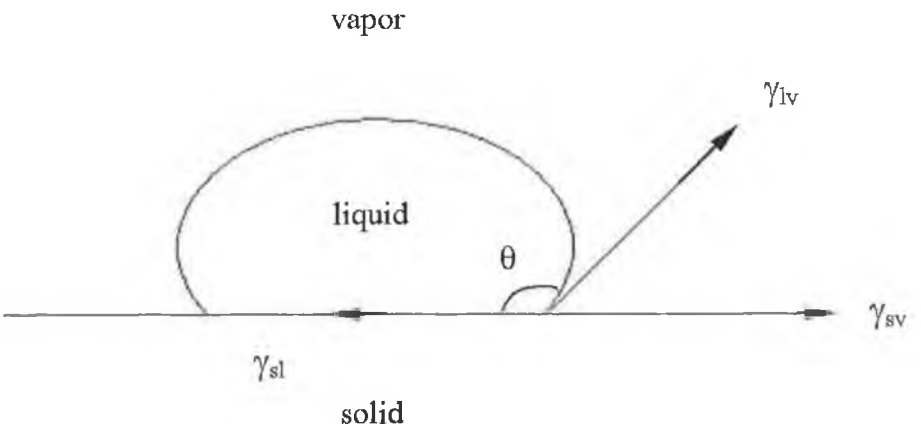

Figure 1.11: Schematic diagram of the wetting angle [118].

Definition of wettability

Wettability can be defined as the ability of a liquid to spread on a solid surface. Wettability also describes the extent of interface content between the liquid and solid. Consider a drop of liquid resting on a solid substrate as shown in figure 1.11.

The contact angle at equilibrium is determined by equation 1.2 often referred to as Young-Dupre equation [122]:

$$\gamma_{sv} = \gamma_{sl} + \gamma_{lv} \cos\theta \tag{1.2}$$

where, γ_{sv} is the specific energy of the solid vapour interface, γ_{sl} is the specific energy of the liquid solid interface, γ_{lv} is the specific energy of liquid vapour interface and θ is the contact angle.

The three forces are the specific energies of surface tension, such as energy per unit area. When a liquid drop is put on a solid substrate, it will replace a portion of solid vapour interface by a liquid solid and liquid vapour interface. The spreading of liquid will occur only if this results in a decrease in the free energy of the system. The work of adhesion, W_a, such as the bonding force between the liquid and the solid phase is defined as [122]:

$$W_a = \gamma_{lv} + \gamma_{sv} - \gamma_{sl} \tag{1.3}$$

Combining equation 1.2 and 1.3 gives

$$W_a = \gamma_{lv}(1 + \cos\theta) \tag{1.4}$$

The bonding force between the liquid and solid phase can be expressed in

terms of the contact angle and surface tension of the liquid as shown in equation 1.4.

The magnitude of the contact angle will describe the wettability;

1. $\theta = 0°$, for perfect wetting

2. $\theta = 180°$, for no wetting; condition of homogeneous nucleation

3. $0° < \theta < 180°$, for partial wetting

This means that low contact angle indicates good wettability. A liquid is said to wet a solid surface when $\cos\theta > 0°$, i. e. when $\gamma_{sv} > \gamma_{sl}$. According to Dellanay et al. [123], in a vacuum, the driving force for wetting is affected by only two factors. These are surface tension of the liquid and the strength of the solid-liquid interaction at the interface. If the wettability is considered as one of the factors, the critical free energy for nucleation, ΔG^*, can be given by

$$\Delta G^* = \frac{16\pi\gamma_{sl}^3 f(\theta)}{3\Delta G_v^2} \tag{1.5}$$

where $f(\theta) = (2 - 3cos\theta + cos^3\theta)/4$, ΔG_v is the chemical free energy change for the liquid solid transition [124]. It can be seen from equation 1.5 that the condition for a foreign material acting as the substrate for nucleation depends on the wettability between them. However, fibre distribution also affects nucleation.

Usually wetting properties are measured by the Sessile drop method [63], which is based on the measurement of the work of adhesion. This technique involves the placing of a liquid drop of metal on a solid substrate. Generally the Sessile drop technique is used in the 400-2000 °C temperature range [40,125,126].

For the measurement of the dihedral angles, the system is rapidly cooled in order to freeze the equilibrium shapes. In measuring the contact angle θ, great care must be exerted to control several important parameters. These measurements require very precise control of experimental conditions including the composition of the solid (particularly its surface), the melt, and the surrounding atmosphere. The chemical purity of all phases present may be tightly controlled. The composition and pressure of the vapor phase can exert a significant influence on θ, as can deviations of the substrate geometry from a plane; also, oxide formation at the metal drop surface prevents proper contact between metal and substrate.

Wetting of contact angle of various phases by liquid aluminium in a Sessile Drop test is summarized in Table 1.4. It shows that, in general, the value of contact angle decreases with increase in aluminium liquid temperature, or, in other words, the wettability is improved at a higher temperature, above 900 °C.

Table 1.4: Contact angles between liquid aluminium and different ceramics at different temperatures [127].

Ceramic Phase	Temperature (°C)	Angle (°)
SiC	900	150
	1100	34
	1100	42
B_4C	900	135
	1100	120
	1100	119
Al_2O_3	900	90
	900	120
	1100	70
	1100	80
	1100	83

Factors that retard wettability

Generally the presence of oxide films on the melt surface or, adsorbed contaminants on the ceramic substrate, lead to non-wetting by molten alloys on reinforcement particles. This oxide layer also creates a resistance to reinforcement particles penetrating into the molten matrix, especially when the particles are added from the top of a cast. It is well known that aluminium has a high oxygen affinity, and therefore, oxide formation in aluminium based systems is difficult to avoid without special treatment. For example at 400 °C, a 50 nm thick layer is formed on aluminium alloy in 4 hours. To ensure good wetting the contamination or formation of aluminium oxides on the surface of the ceramic should be minimized during the fabrication of a composite [40].

Generally it has been observed that the particle surface is normally covered with a gas layer. This prevents the molten matrix coming into contact with the surface of the particle. In addition, when the particle concentration in the melt reaches a critical level, these gas layers can form a bridge, leading to total rejection of particles from the melt [128]. Hence it is essential that these gasses from the surface of the particles be removed prior to composite synthesis. Zhau and Xu [109] have also proposed that the gas layer surrounding the particles might be the main reason for poor wettability. Therefore it is necessary to break the gas layers in order to achieve good wettability. When the gas layers are broken and the particles are wetted, the particles will tend to sink to the melt bottom, rather than float to the surface.

Properties of the particle surface also affect wettability. The wetting of the

SiC by metals is often hindered by the presence of a layer of silicon oxide on the solid surface. As a result, a sharp transition from non-wetting is observed at a certain threshold temperature [129]. This transition temperature is determined by the kinetics of diffusion of the metal through the oxide layer. In their work, they suggested that wetting is not usually observed below 900 °C (Table 1.4). For example, the contact angle for a SiC system decreases significantly from 150 to 34 °C when the temperature of the melt is raised to 1100 °C [130]. Naidich et al. [130] showed that this phenomenon is due to the presence of the aluminium oxide layer preventing the direct contact of aluminium and carbon.

Methods used to promote wettability

Several methods have been used by researchers [40, 131–133] to promote wettability of reinforcement particles with a molten matrix, such as:

1. Addition of alloying elements to the molten matrix [134–143]
2. Treatment of the particles [40, 126, 138]
3. Coating of the particles [110, 123, 144, 145]

The basic principles involved in improving wetting are increasing the surface energy of the solid, decreasing the surface tension of the liquid matrix alloy, and decreasing the solid-liquid interface energy at the particle-matrix interface.

To improve wettability addition of alloying elements is very popular. In certain processes, reactive elements like magnesium or lithium [134] are added to the melts to promote their wettability of the reinforcement. The formation of a solidification microstructure under this type of process involving the interaction of magnesium with the atmosphere and the liquid, as well as the formation of aluminium nitride, needs to be further investigated [35].

The composites produced by liquid metallurgy techniques generally show excellent bonding between ceramic and molten matrix when reactive elements are added to induce wettability [135]. For example, the addition of magnesium [136,137], calcium, titanium, or zirconium to aluminum melt may promote wetting by reducing the surface tension of the melt, decreasing the solid liquid interface energy of the melt, or reducing wettability by chemical reaction.

It has been found that for aluminum based composites, magnesium has a greater effect in incorporating reinforcement particles in the melt, and improving their distribution, than other elements tested including: cerium, lanthium, zirconium, titanium, bismuth, lead, zinc and copper [146]. The addition of magnesium

to molten aluminum has been found to be successful in promoting wetting of alumina [140, 141], and indeed it is though that magnesium is suitable in aluminum with most reinforcements [142, 143].

Magnesium is a powerful surfactant. The addition of magnesium to an aluminium melt improves wetting because of the lower surface tension of magnesium (0.599 N m^{-1}) compared to with that of pure aluminum (0.760 N m^{-1}) or aluminum 11.8 wt. % Si (0.817 N m^{-1}) [147]. The addition of 3 wt. % magnesium to aluminum reduces its surface tension from 0.760 to 0.620 N m^{-1} at 720 °C [148]. The reduction is very sharp for the initial 1 wt. % magnesium addition. For example, with 1 wt. % magnesium, the surface tension of an aluminum alloy has been found to drop from 0.860 N m^{-1} to 0.650 N m^{-1} [72]. In the work of Sukumaran et al. [149] they concluded that the addition of magnesium is necessary during the synthesis of A356-SiC particle composites by a stir casting route, and found the optimum addition of magnesium for obtaining the best distribution and maximum mechanical properties to be around 1 wt. %. The addition of magnesium lower than the optimum value results in the formation of agglomerates of reinforcement particles, and their non-uniform dispersion in the melt.

Heat treatment of particles before dispersion in the melt aids their transfer by causing desorption of adsorbed gasses from the particle surface. Agarwala and Dixit [138] observed the importance of preheating in the incorporation of graphite particles in aluminum alloy. There was no retention when the graphite particles were not preheated, whereas the particles were retained when preheated. Heating silicon carbide particles to 900 °C assists in removing surface impurities, desorption of gases, and alters the surface composition due to the formation of an oxide layer on the surface. The ability of an oxide layer to improve the wettability of SiC particles by an alloy melt has previously been suggested by other investigators. The addition of preheated alumina particles in Al-Mg melt has been found to improve the wetting of alumina.

A clean surface provides a better opportunity for melt particle interaction, and thus enhances wetting. Ultrasonic techniques, various etching techniques and heating in suitable atmosphere could be used to clean the particle surface [40]. The silica layer grown naturally or artificially on the surface of SiC particles used in aluminum based matrix composites, which is achieved through particle treatment, has two functions: protection of the SiC from aluminum attack to form Al_4C_3, and improvement of wettability of SiC by aluminum which results from the reaction between aluminum and SiO_2 [126].

In general, the surface of some non-metallic particles are difficult to wet by metallic alloy. Wetting has been achieved by coating the particles with a wettable metal. This is because liquid metals almost always wet solid metals, and the wet-

tability is the highest in the case of mutual solubility or formation of intermetallic compounds. Infiltration is thus made easier by desorption of a metallic coating on the surface of the reinforcing solid [123]. Coatings are applied in a variety of ways including chemical vapour deposition (CVD), several forms of Pressure vapour deposition (PVD), electroplating, cementation, plasma spraying and by sol gel processes. Nickel and copper are wet well by many alloys, and these metal have been used as a coating material. However, nickel is the most frequently used metal for coating reinforcement particles, which are normally used for aluminum based composites. Silver, copper and chromium coatings have been proposed [145].

Metal coating on ceramic particles increases the overall surface energy of the solid, and improves wetting [110] by enhancing the contacting interfaces to metal-metal instead of metal-ceramic. However, the interaction of coatings with a liquid metal during infiltration or stirring, and the influences of this interaction on the solidification microstructure and the mechanical properties of a coating are not well understood.

A mechanical force can usually be used to overcome surface tension to improve wettability. However, in the experimental work of Hashim et al. [136], it was found that mechanical stirring could not solve poor wettability, when the matrix alloy is in a completely liquid state. Stirring in a semi-solid state while slurry is solidifying improves incorporation of the particles into the matrix alloy.

Ultrasonic vibration was applied to liquid MMC processing to improve apparent wettability of Al_2O_3 particles with molten aluminum. Prior to the ultrasound-assisted processing, it was found that the application of ultrasonic vibration made the contact angle of the system change from non-wetting to a wetting system [135, 150].

Mixing time is one of the important processing variables, which is often not adequately recognized or reported. Many of the metal-ceramic systems of commercial interest are made wettable by promoting interfacial reaction. Since these processes effecting the interfacial energy balance, progress with time, the contact angle, θ is often a function of time. Therefore if the processing time is short, the particles may appear non-wetting but with an increase in time, these particles become wettable. For example, for Al-SiC composites, at a holding temperature of 800 °C, the contact angle is 125 ° for a holding time of 125 minutes, this value drops to 55 ° for holding time of 160 minutes [151]. Similar time dependence of contact angle may also be observed for coated particles if the coating is soluble in the melt. The processing time should be controlled so that coating does not dissolve completely [152].

Particle incorporation

In general there are two types of barrier to particle incorporation into a liquid melt. These are mechanical barriers such as a surface oxide films, and thermodynamic barriers, which are usually referred to in terms of wettability. Mechanical barriers can be reduced by good foundry practice, but overcoming thermodynamic barriers is more difficult. Generally ceramic reinforcements used in MMCs are non-wettable by the metallic melt, requiring an external driving force to overcome the surface energy barriers. This force is provided by stirring the melt with a mechanical stirrer or using electromagnetic stirring. It has been shown that alloy chemistry, temperature of particle addition and stirring rate are some of the parameters controlling wetting of the reinforcement by the melt [153]. Once the particles are transferred into the liquid and the energy barrier is overcome, the surface energy or surface forces will not change with position inside the melt. The dynamics of particles in the melt will be governed by other forces including gravity, buoyancy or by stirring action. Two problems complicate the incorporation process:

1. Particle agglomerates must be broken up before complete dispersion and wetting can occur, and

2. It is energetically conducive for the particles to become attached to gas bubbles.

The method of particle incorporation to the matrix melt is a very important aspect of the casting process. There are a number of techniques [42, 110] for introducing and mixing the particles. However, some of these methods have several disadvantages. Gas injection of particles for example will introduce a quantity of gas into the melt. Some methods are not very effective in dispersing the particles and some, such as the ultrasonic technique are very expensive, and are difficult to scale to production level. By using centrifugal action, the distribution of particles varies from the inner to outer part of a billet because of the differences in centrifugal force [154].

1.5.2 Porosity

Porosity, as is well known, is one of the biggest problems in the production of premium quality aluminium castings; it is always a case for concern because, in addition to affecting the surface finish, its presence can be detrimental to the mechanical properties [80] and corrosion resistance [155, 156] of the casting. Porosity levels must therefore be kept to a minimum in order to produce sound casting

with optimum properties. Porosity cannot be fully avoided during the casting process, and so the mechanical properties of the cast materials are commonly correlated to the volume fraction of its porosity [157]. For MMCs, in particular, reinforcements provide the sites for cavity formation and development [158]. For MMCs, excessive cavities are expected to be formed at the interfaces and to give rise to larger damage. It is very important to understand cavitations mechanism in MMC.

Sources of porosity

In general porosity comes from three different sources:

1. Gas entrapment during stirring
2. Hydrogen evolution,
3. Shrinkage during solidification

The porosity of the composite primarily results from air bubbles that normally enter the slurry either independently, or as an air envelopment on particles. The air trapped in a cluster of particles also contributes to porosity. Oxygen and hydrogen are both sources of difficulty in light alloy foundry process, the affinity of aluminum for oxygen leads to a reduction of the surrounding water vapor and the formation of hydrogen, which is readily dissolved in the aluminum.

The occurrence of porosity can be attributed to the amount of hydrogen gas present in the melt, the oxide film on the surface of the melt that can be drawn into it at any stage of stirring, and gas being drawn into the melt by certain stirring methods. Vigorously stirred melt, or vortex tends to entrap gas and draw it into the melt. It has been found that the presence of a vortex inhibits wetting.

According to Ghosh and Roy [80] the stirring parameters such as holding time, stirring speed, size and the position of the stirrer in the slurry will influence the formation of the porosity. Their experimental work showed that there is a decrease in porosity level with an increase in holding temperature. It has been recommended that the turbine stirrer should be so placed as to have 35 % liquid below and 65 % liquid above. According to Lloyd and Samuel et al. [28], structural defects such as porosity, particle clusters, oxide inclusion, and interfacial reactions are found to arise from unsatisfactory casting technology. It was observed that the amount of gas porosity in casting depends more on the volume fraction of inclusions than on the amount of dissolved hydrogen. This is because, in general composite casting will have a much higher volume fraction of suspended non-metal solid than even the most dirty conventional aluminium casting, so the potential

for nucleation of gas bubbles is enormous. It has been observed that porosity in cast composite increases almost linearly with particle content.

Prevention of porosity

Cleanliness of the matrix and reinforcement prior to casting is chiefly determined by the hydrogen and inclusion content of the melt. The deleterious effect of both hydrogen and inclusions on the quality of the cast product is amply recorded in the literature. While removal of hydrogen is accomplished by various melt procedures (such as degassing and fluxing), inclusions can be removed by the use of filtration and a properly designed gating system. Filtration allows for removal of non-metallic and intermetallic inclusions whose presence in the melt can otherwise reduces the melt fluidity and mechanical properties, and increases the internal porosity of the casting giving rise to poor surface, reduced mechanical properties and machinability. In addition, inclusions can also induce premature failure in the cast component. With the present-day demands on product integrity, filtering the metal prior to casting has become the norm on most cast shop floors [28].

Samuel and Samuel [28] found that the porosity level decreases with increasing the mould temperature and that will improve the soundness of casting. The porosity shape and size were affected by the presence of the SiC reinforcement particles through the tendency these particles display to block or restrict the growth of the pore. As a result, a more uniform distribution of porosity was obtained compared to the unreinforced matrix alloy, where the porosity was seen to occur in the inter-dendritic region, spreading across several dendrites.

Cocen and Onel [159], producing aluminum silicon alloy based composite containing different volume fraction of SiC particles, found that the volume fraction of porosity in all samples including the matrix alloy varied between 0.7 % and 6.8 %. It was indicated that the porosity content increased with the total mixing time or with the volume fraction of SiC particles [159], or alumina.

Pouring distance from the crucible to the mould should be as short as possible [160]. Shrinkage that occurs on solidification is the primary source of porosity formation in solidifying casting. Shrinkage porosity also occurs on a micro level as micro-shrinkage, or micro-porosity, which is dispersed in the interstices of dendrite solidification region [161]. When the temperature reaches the eutectic temperature the growth of the pores is limited by their ability to expand in a viscous media, by their edges being surrounded by the silicon carbide particle.

There are several strategies that have been used to minimized porosity. These includes:

1. Vacuum treatment

2. Degassing

3. Casting under pressure

4. Postprocessing

There are several methods that can be used to minimize the porosity in the cast MMCs, such as vacuum [162] or inert atmosphere processing [43,163], purging the slurry by chlorine or nitrogen [40], or preheating of ceramic particles [138]. Most of gas absorbed on the surface of the particles is in the form of H_2O. Miwa et al. [46] found that the evolution process of H_2O gas with temperature is mostly finished at temperatures between 200 °C to 600 °C. Therefore it is suggested that most of the H_2O gas absorbed on the surface of the particles can be liberated by heat treatment at 600 °C.

It is necessary to avoid gas pick up during melting, since any gas taken into solution will be difficult to remove [74]. It is recommended to melt under a protective cover of dry argon or nitrogen to reduce significantly the possible of oxidation, therefore degassing and fluxing are unnecessary [164]. This can be achieved by placing a fire proof blanket such as kaowool, over the furnace or crucible, in which a small hole has been made for the reception of a simple piece of gas pipe. The protective gas is fed through a suitable flexible hose from a cylinder fitted with a pressure regulator and flow indicator. In order to get a clean melt, the matrix material must be well dried to over 200 °C and added to a preheated crucible, and stirrer, ladles and sampling spoon must be also be well preheated before being put into the melt. Richardson [164] recommended that any steel utensil introduced into the melt must be well coated with ceramic adhesive before use, to prevent iron contamination and must be well dried and preheated to prevent the possibility of hydrogen generation, the stirring action must be slow to avoid the formation of vortex in the surface of the melt. Care must be taken not to break the surface skin into the melt.

It has been observed that increasing the mould temperature will improved the soundness of the casting, as shown by a decrease in porosity levels [69].

Degassing liquid aluminum alloy is a usual step in the casting procedure. When reinforcement materials are incorporated into a melt in air, the molten compound must be treated to remove the dissolve gases. Although various out-gassing treatments are available (based on nitrogen gas, chlorine or vacuum treatment) it is difficult to reach a very low hydrogen content corresponding to the saturation of solid aluminum alloys. Girot et al. [165] have developed a procedure for gas removal. In this process the usual cleaning, deoxidizing and refining treatments are done before degassing. The degassing is carried out in a vacuum chamber. At the

end of the degassing steps, the formation of bubbles is enhanced by an injection of nitrogen gas. However, the application of vacuum to the molten mixture of metal and particles during the mixing step can reduce the atmospheric gasses available for introduction into the melt, and also tend to draw dissolved, entrapped and adsorbed gasses out of the melt during mixing. Porosity problem could be solved by the use of a vacuum technique or squeeze casting. Fluxing treatments which have long been applied to cast aluminium alloys (to accelerate inclusion removal, retard oxidation and clean oxide build up from the crucible), cannot be used to process molten composite material, as these procedures also remove the particles from the melt, and negate the very purpose of the reinforcement. For the same reason, neither can degassing be applied to reduce the melt hydrogen content [28].

Cavity formation during tensile straining of particulate and short fibre MMC is very interesting. Spherical reinforcement generate voids less readily than angular particles of the same size. Cavitation occurs more readily in material produced by a powder route than with cast material [166].

Postprocessing includes compressing, extruding or rolling the materials after casting to close the pores. This secondary processing can reduce particle porosity [167]. Extrusion [168] rapidly homogenize the distribution of particles as well reduces the porosity content at quite low extrusion ratios, [169].

1.5.3 Chemical reactions

When MMC is produced by powder metallurgy, generally the reinforcement is not exposed to molten metal, except for a short period of time during liquid phase sintering. However, in molten metal processing, the reinforcement particles are mixed directly into the liquid, and exposure times to liquid metal are relatively long. As a result, the reinforcing particles may react with the liquid metal, which can degrade the reinforcement as well as final MMC product [63]. Chemical reactions between a liquid metal and ceramic particles leave their products in the solidification microstructure of the composite.

The reaction between silicon carbide particles and liquid aluminium is believed to take place in several steps including the following [170]:

1. Diffusion of silicon and carbon atoms away from the silicon carbide particle surface into the molten aluminium pool.

2. The formation of compounds when the aluminium and carbon concentration exceed the equilibrium constants of Al_4C_3, and/or

3. Further precipitation of compounds on cooling due to a decrease in solubility.

The carbon atoms go into solution and react with aluminium to form Al_4C_3. Following the dissolution of silicon carbide, Al_4C_3 grows and silicon will diffuse into the melt around the Al_4C_3. According to the various theoretical and experimental studies carried out so far [12, 171], SiC reacts with Al to form Al_4C_3 and Si:

$$4Al + 3SiC \longrightarrow Al_4C_3 + 3Si \tag{1.6}$$

These reactions basically involve redox type chemical reactions [35]. The dissolution of the silicon caused by chemical reactions between SiC and Al has been confirmed by measuring the changes in the liquidus temperatures that accompany dissolution of silicon in aluminium and also by X-ray diffraction studies on the formation of aluminium carbide at the interface between the particles and the matrix [35].

The formation of aluminium carbide is bad for several reasons [63, 75, 120, 172]. This reaction is known to have several undesirable effects on the overall composite properties:

1. Mechanical properties of the SiC reinforced composites will degraded due to the formation of Al_4C_3 [63].

2. Since the reaction product Al_4C_3 is unstable in some environments such as water, methanol, hydrochloric acid [173, 174] the composite can be susceptible to corrosive environments; and in addition, Si formed as an interfacial reaction product, will produce the Al-Si eutectic at the interface and grain boundary regions, resulting in reduced mechanical properties of the composite.

Control of reaction

Fabrication of SiC/Al composite devoid of Al_4C_3 has long been a major concern. Among various methods which have been proven to be effective in achieving such a goal, two methods have been accepted widely:

1. Si addition into the Al matrix

2. Artificial oxidation of SiC to produce a SiO_2 layer on the surface of SiC [144, 168, 175–178].

The basic principle behind both methods is to enhance the Si activity and thereby reduce the Al activity, by dissolving Si into the Al matrix. However, considering that the interface reaction given by equation 1.6 is also dependent on

the temperature and holding time, the use of adequate combinations of processing parameters, such as process temperature, holding time, etc. can be the alternative solution to suppress the interfacial reaction [176]. The aluminium carbide reaction can be avoided by using high silicon alloys for the matrix [63] but this restricts the choice of the matrix alloy. Increasing the amount of silicon in the matrix can reduce the dissolution of silicon carbide and prevent the formation of Al_4C_3 [167]. Usually 7-15 wt. % silicon in necessary to prevent the reaction [34, 167, 170, 179].

Another method of controlling the aluminium carbide reaction is to oxidize the surface of the silicon carbide, forming an outer layer of SiO_2. In this case the early stages of the reaction involves reducing the SiO_2, rather than dissolving the silicon carbide [177]. According to Heuer et al. [180] the SiO_2 layer on silicon carbide can easily be thickened by heat in air. From their research, it is estimated that heating in air at 700 °C for one hour increases the thickness of the oxide layer by between 30 and 50 nm from the original thickness of between 2 and 4 nm.

Wang et al. [121] studied the interfacial microstructure in a aluminium-silicon carbide system composite produced by molten mixing. In their work, magnesium aluminate $MgAl_2O_4$ was found at the interface as a reaction product after processing. Several studies of the aluminium alloy-alumina composite system also indicate that the $MgAl_2O_4$ spinel may be formed at the reinforcement-matrix interface [41, 143]. Levi et al. [142] found that in the case of an aluminium-magnesium alloy based composite, the bonding between the reinforcement and the matrix metal is achieved through the formation of an $MgAl_2O_4$ (spinel) layer, by reaction between the reinforcement and the magnesium in the aluminium. The chemical reaction between ceramic and metal, which occurs at the interface, generally improves the wetting and bonding, especially the spinel chemical reaction product. Table 1.5 shows examples of interaction in selected reinforcement-matrix system.

Table 1.5: A list of interaction product and approximate temperature of significant interaction in selected reinforcement-matrix systems [176]

System	Interaction	Approximate temperature °C
C-Al	Formation of Al_4C_3	550
B-Al	Formation of borides	500
B-Ti	Formation TiB_2	750
SiC-Al	Formation of Al_4C_3	Melting point, 660
SiC-Ti	$TiSi_2$, Ti_5Si_3 and TiC	700
SiC-Ni	Formation of Nickel silicides	800

Thickness of the interfacial reaction layer can be controlled by varying the temperature of the slurry and the residence time of particles in the slurry. The interface reaction may stop once a sufficiently thick layer of a stable reaction product has formed at the interface. The effects of wetting and interface chemistry on the structure formation and property evolution in metal ceramics system has been reviewed by several researchers. Chemical reactions have also been used to generate in-situ reinforcements in the matrix phase. Controlled solidification of eutectic liquids which decomposed into two solids has been used to produced MMC. Likewise, chemical reactions within the liquid, between gas and liquid, or between elements dissolved in liquids, have been used to produce reinforcements that form a part of the solidification microstructure [35].

Lloyd et al. [167] studied the thermodynamic stability of the reinforcement in aluminium and magnesium alloy, and concluded that in a silicon free alloy, silicon carbide is thermodynamically unstable above the melting temperature of the matrix alloy, reacting to form aluminium carbide, Al_4C_3 and, a subsequent increase in the silicon level of the matrix occurs. The silicon that forms is relatively harmless, however the precipitation of aluminium carbide as crystals can substantially degrade the quality of the casting. For high Si content aluminium alloy, these phenomena can be easily prevented by keeping the melt temperature below 773 °C at all the times, because below this value, the reaction proceed too slowly to be a problem. Samuel and Samuel al. [28], studied melt holding times and temperatures for aluminium and the A356 alloy-silicon carbide particle composite system, and found that Al_4C_3 forms rapidly at temperature above 790 °C. The reaction can also occur below this temperature but at much lower rates, and in their study, no significant Al_4C_3 was formed below this temperature (for holding times less than 30 minutes).

1.5.4 Distribution of reinforcement material

The distribution of the particle reinforcement in a matrix alloy is significantly influenced by three stages: the melt stage, solidification and post solidification process. Melt and solidification stages are interrelated. Post solidification processing can help to homogenize the distribution of the particles in the final product.

Particle distribution in the matrix material during the melt stage of the casting process mainly depends on the viscosity of the slurry, particle wetting, the extent to which particles are successfully incorporated in the melt, how the characteristics of the reinforcement particles influence settling rate, the effectiveness of the mixing and breaking up of agglomerates, and the minimizing of gas entrapment.

Particle floating or settling

Particle settling or floating may occur because of density differences. If the original distribution of particles in the melt is uniform, the theoretical prediction of settling can be made by using Stokes's Law [181], which assumes that the particles are spherical, and that no interaction occurs between particles. Stokes predicts that is the settling rate of particles using [181]:

$$V_\gamma = \frac{2R_p^2(\rho_p - \rho_m)g}{9\mu} \tag{1.7}$$

where, V_γ is the settling velocity of the particles, R_p is the particle radius, ρ_p is the particle density, ρ_m is the matrix density, g is the gravitational force and μ is the viscosity of the molten metal.

Particle enriched zones may form either as a consequence of gravity segregation of particles in melts during holding or during slow solidification, or as a consequence of selective segregation under the action of the centrifugal acceleration in centrifugal casting. At sufficiently long holding times, when the particles have higher density than the melt, the top part of the casting becomes completely denuded of particles, which settle to the lower parts of the casting, as a function of time [34, 39]. Therefore the melt must be restirred prior to casting, if long holding times in the molten state are used. Clustering of the particles is a contributory problem, making the particles settle more quickly. Therefore, the particles may be unevenly distributed macroscopically (denuded region due to settling) and microscopically (clusters of particles) [29, 76].

According to Geiger et al. [181] the settling rate will be a function of the particle density, shape and size. At high volume fractions, particles interact with each other and settling is hindered [182]. Hindered settling for spherical particles has been modelled by Richardson and Zaki [183, 184] with the particle velocity, V_c given by:

$$V_c = V_0(1 - f)^n \tag{1.8}$$

where, V_0 is the Stokes's velocity, f is the volume fraction of the particles, and n is a factor depending on the Reynolds number. The particle diameter and the container diameter, increases with increasing particle diameter. The studies on settling indicate that the finer the dispersions and the higher their volume fraction, the slower the rate of settling. Hanumanth et al. [11] using an average particle size of 90 μm found a slurry of 0.2 volume fraction of SiC particles settled completely in about 300 seconds, resulting in loosely packed particles at the bottom of an aluminium alloy matrix. At lower volume fraction of particles the settling times were lower. So, it is apparent that a slurry with large size

(90 μm) particles will have to be stirred continuously until casting. In practice the situation is complicated by the fact that there is a range of particle shapes and sizes. As large, irregular particles sink, the liquid they displace can influence the settling rate of other particles.

According to Ray [185] when the flow velocity is above a critical value for a given size of particle, the suspension will remain homogeneous during flow. If the flow velocity is further reduced, the particles will sediment at the bottom of the channel and move by tumbling over each other.

The result of the settling experiments of Sekhar et al. [186] indicate that the silicon carbide particles show a tendency to segregate in aluminium alloy as a result of settling. It was concluded that as holding time in the molten state increases, the particle settling would also be increased.

The specific gravity of most of the reinforcements used in aluminium MMCs production is usually higher than that of molten aluminium, which leads to settling of the particulate reinforcement in the melt. In Al-SiC composites, sedimentation of the SiC particles to the bottom of the melt crucible normally occurs during melting, once the melt material reaches the mushy zone. As the temperature of the melt rises, the sedimentation increases with increasing fluidity of the molten material. With settling, the upper region of the melt become denuded of reinforcement, which can result in large differences in melt viscosity and temperature in different parts of the melt. Many reinforcements are not thermodynamically stable in molten aluminium matrix and there is a tendency to form Al_4C_3, which adversely affects the fluidity of the melt. Therefore it is important that mechanical stirring be commenced as soon as the metal is sufficiently fluid in order to get homogeneous distribution. Another factor contributing to SiC sedimentation is the dead time between castings, when there is no mechanical stirring. This should be minimized [35]. Continuous stirring is necessary between castings to avoid sedimentation of particles in the melt [187].

Mixing

Stirring is a complex phenomena, and it can be a problem to control the process so that a uniform distribution of particles is achieved. Mechanical stirring is usually used during melt preparation and holding. The stirring condition, melt temperature, and the type, amount and nature of the particles are some of the main factors to consider when investigating this phenomenon [63, 111]. Settling and segregation are both to be avoided. In creating a homogeneous distribution of particles in a molten alloy, the high shear rate caused by stirring the slurry should result in a fairly uniform particle distribution in the radial direction, and

also prevent particles from settling. Secondary flow in the axial direction results in transfer of momentum from high to low momentum regions and causes lifting of particles.

1.5.5 Review of published processing parameters

Most previous researchers have used the matrix metal alloy in the ingot form [19, 48, 74, 171] or extruded bar [171]. As a starting point the ingot is generally melted to above the liquidus temperature, for example to 50 °C above the liquidus temperature [48]. Composite melt may be prepared in a graphite, [10, 72, 74] silicon carbide [61, 171], alumina [127], concrete [84], or clay graphite crucible [109]. In order to keep the melt as clean as possible the ingot is melted under a cover of an inert gas such as nitrogen, in a vacuum chamber [74], or in a pressure chamber [171]. This also helps to minimize the oxidation of the molten metal [66], or reduces porosity (under pressure). McCoy et al. [84] prepared composite with the whole apparatus being sealed within a close container which was filled with nitrogen gas. According to Yamada et al. [19] the molten aluminium should be subjected to a high vacuum atmosphere to degas hydrogen, before the reinforcement materials are completely added. Gupta and Surappa [66] treated the metal ingot in different ways. In their work the metal ingot, before melting, was treated with a warm alkaline solution and washed with a mixture of acids, in order to reduce the thickness of the oxide film and to eliminate other surface impurities. Zhou et al. [109] preheated the scrap alloy at 450 °C for 3 to 4 hours before melting.

The reinforcement particles used normally are one of two types: either in as received condition, or heat-treated (artificially oxidized). For SiC oxidation has taken place at 1000 °C for 1.5 hours in air [10] at 1100 °C for 1 to 3 hours [109], or one and half hours [61], at 850 °C for 8 hours and at 1200 °C for 1 hour [188]. Additionally, gas absorbed on the surface of SiC, which was prepared in air, can be removed by preheating at a certain temperature for a certain period of time. For example, particles have been heated to 554 °C for 1 hour, or at the temperatures of 900 °C [66], 799 °C [74, 80] and 1100 °C [171] for 8 hours.

According to Miwa [46], in order to get good incorporation, the addition rate needs to be reduced with a decrease in size of the particles. Lee and Kim [48] introduced particles at 4-5 g/hour, and Salvo et al. [171] takes about 5-10 minutes to incorporate silicon carbide particles into the melt. In some cases the particles were introduce through a nitrogen gas stream [72, 74].

One significant requirement when using a stir casting technique is the continuous stirring of the melt with a motor driven agitator to prevent settling of

particles. If the particles are more dense than the host alloy, they will naturally sink to the bottom of the melt [152]. This means that some method of stirring the melt must be introduced before casting to ensure that the particles are properly distributed throughout the product. Dispersion by stirring with the help of a mechanical stirrer has become widely used. This external force is used to mix a non-wettable ceramic phase into a melt, and also to create a homogeneous suspension in the melt. The uniformity of particle dispersion in a melt before solidification is controlled by the dynamics of the particle movement in an agitated vessel. The composite slurry may be agitated using various types of mechanical stirrer [25]. Example include graphite stirrer [10], steel stirrer coated with ceramic [84], and alumina stirrer. Stirrer speeds previously investigated range from 100 to 1500 rpm [10, 19, 72, 74, 75, 78, 84, 127, 137]. The vortex method is the most frequently used [10, 19, 66, 72, 80, 84] since any stirring of a melt naturally results in a formation of a vortex. Ceramic particles are introduced through the side of a vortex which is created in the melt with the mechanical impeller. Particles have, for examples been continuously stirred after being incorporated into the melt, for 45 minutes [84], or for 15 minutes [75]. Gibson et al. [189, 190] dispersed graphite powder in agitated slurry of Al-Si alloys by using a special rotor designed to prevent surface agitation of the melt and consequent air entrapment.

The utilization of fine particles in large volume fraction will reduce the settling rate [140]. If a mixture of fine and coarse particles is used in slurry, the coarse ones will settle faster than the fine particles. In a large mass of liquid, such as in the furnace or crucible, there may be thermal current flowing through the melt, which helps to keep the particles in suspension. However, if the melt is not continuously stirred, it is important to stir it immediately before pouring, whether or not it was stirred while melting and holding [164]. The particle distribution or homogeneity will be maintained if the settling of particles has been controlled.

After the incorporation of the particles in the melt is completed (in the case in which the stirring action was preformed in semi-solid condition) the slurry has to be remelted to a temperature above the liquidus before being poured into the mould. For aluminium the remelted temperature used varies from 700 °C for one minute [19, 61, 171] to 720 °C for 5 minutes [61]. The composite slurry is then poured into a steel mould [80,171], copper mould [84] graphite moulds [127] or cast iron mould [66]. Normally the mould is preheated, and has been to 300 °C [61,171], 370 °C [191] and 565 °C [127]. In some cases the casting is solidified under pressure to prevent porosity [19, 48, 61, 171]. The viscosity of the melt-particle slurry is higher than that of the base alloy, and this may offer greater resistance to flow in the mould cavity.

The main advantages of stirring the melt between the solidus and liquidus is

that the partly solidified structure drags the particulates along into the melt even if they are not wetted. This mechanical entrapment is favoured by a vigorous agitation, which is also supposed to promote wetting by the abrasive cleaning effect on the particulate surfaces. As the reinforcement is forced into the matrix without being wetted, it is essential to continue mixing after the addition is completed, in order to ensure proper interface bonding [139, 146].

Even when stirring in the liquid condition, poor wetting was seen when SiC particles were used in an as-received condition, without magnesium. Microscopic observations show no wettability in case of treated particles without magnesium. During stirring some of the particles tended to float to the top of the melt, and the others accumulated at the base of the crucible. This occurred irrespective of speed of stirring [192].

The high effective viscosity of the metal slurry prevents particles from settling, floating, or agglomerating [193]. With increasing mixing times after addition, interaction between the particles and the liquid matrix promotes bonding. Particles and fibres of a variety of materials, including SiC, $A1_2O_3$, MgO, boron, mica, carbon (anthracite), and glass have been incorporated into aluminium alloys in this way [139]. Sizes have ranged from sub-micrometers to one hundred or more micrometers. The composites, thus prepared, can be cast when the alloy is partially solid or after re-heating to above the alloy liquidus [187]. This ease of blending, and the fact that there are similar trends in semi-solid viscous flow behaviour compared with un-reinforced semi-solid metal [194] promotes bulk production of MMC structures. The lower temperatures associated with semi-solid state can also act to inhibit interfacial reactions between the second-phase particles and the molten metal which could become sites of weakness in the casting. Second-phase particles are generally not entrapped within primary phase particles. They are more commonly entrapped by the eutectic between dendrite arms [107]. Best particulate distribution can be achieved if the particulate size is chosen based upon the secondary dendrite arm spacing characteristic of the casting process [195]. The viscosity of semi-solid composites changes with volume fraction, shape, and size of the reinforcing phase, in addition to those factors that affect viscosity in stir-casting, such as shear rate, stirring time, volume fraction of the primary solid and cooling rate [196]. A large portion of the flow resistance of SSM slurries derives from the dissipative interaction of the primary particles. The viscosity of the semi-solid slurry may be lowered by the addition of the second-phase particles. These particles are normally smaller than the primary metal particles and remain between them in the liquid matrix preventing particle to particle collisions. Shearing during the formation of a composite can act to align particles or fibres in the semi-solid providing the opportunity for tailored anisotropy. This has the poten-

tial of producing a variety of composite materials for improved wear resistance, damping characteristics, increased stiffness, and greater strength. These MMCs have been shown to possess adequate hot-working characteristics and encouraging post extrusion properties [197]. The process may also provide a practical way of lowering the cost or weight of die castings that do not need to exhibit high strength. One can envisage diluting an energy-expensive metal such as aluminium with a material such as recycled glass, slag, or sand [86]. Al-Si composite alloys in particular have been examined. Composites of the widely used A356 (A1Si7Mg) alloy have received a lot of investigation. Work by Cornie et al. [195], discusses the particle insertion process in relation to particle-matrix wettability, the surface energies that control wettability, and fluid velocity required to drag a particle below surface of the liquid matrix. Brute force methods such as vigorous stirring in an evacuated crucible vessel or pressure infiltration followed by shear dilution were seen by Cornie et al. [195] as the most successful methods of slurry formation.

1.6 Modeling of SSM processing

Although semi-solid processing (SSP) has existed as a net shape forming technology for many years, the flow behaviour of semi-solid metal (SSM) alloys is still poorly characterized. With recent major advances in computational hardware and software and perhaps most important, with the rapidly developing experience base, fluid flow tools are becoming broadly accessible. There are only a small number of commercial software packages that describe the flow of SSM. These include Magma, ANSYS, Deform, and Abaqus [198]. A number of studies have shown the general characteristics of flow of SSM [199–203]. At low solid concentrations the slurry behaves as a history dependent, non-Newtonian fluid and at high solid concentrations the SSM may act as a viscoplastic, nonlinear solid. At moderate solid fractions the flow behaviour of these slurries is highly nonlinear. A number of simulations have been developed that focus on SSP [198, 204–211]. There are few works to date however that have examined the effect of the SSM rheology on the segregation or sedimentation of solid phases during the batch compocasting process.

1.6.1 Rheological modeling

Rheology is the branch of physics that studies the deformation and flow of matter. Models of SSP currently utilize constitutive equations to describe slurry rheology. Using the techniques of molecular dynamics it may be possible to go beyond this

approach to obtain direct relationships between applied shear rates, the resultant microstructural changes and the rheology of the SSM [212].

Kumar et al. [200, 201] studied the constitutive flow behaviour of SSM alloy slurries. They presented a constitutive model for predicting the flow behaviour of SSM alloy slurries for low (0.1) to moderate solid fraction (0.5 to 0.6). To validate their model they carried out experimentation on two alloy systems, Sn-15 % Pb and AlSi7Mg0.6, using a computer controlled, high temperature Couette rheometer. They applied their model to semi-solid composites. The results of a simple simulation of semi-solid flow within a Couette rheometer were presented in their later study and compared with experimental data for the Sn-15 % Pb system. It was found that the model correctly predicted the apparent viscosity under steady state conditions, up to a solid fraction of 0.4. It can be shown that even with a very simple interparticle potential function, a molecular dynamic model can reproduce many of the features of semi-solid slurries under steady state conditions. The same model was able to give quantitative predictions of the apparent viscosity for slurries of less than 0.4 solid fractions. It was apparent that the agreement between the model and experiment was very good for less than 0.35-0.40 fractional solid. Above 0.35-0.40 the model appears to seriously underestimate the apparent viscosity of the suspension, with the discrepancy being particularly evident for the continuously cooled material. The authors of this work later noted that the discrepancy between model and experiment at high solid fraction was probably due largely to the direct transfer of stress through the solid, although hydrodynamic interactions between the particles, and the simplified potential model utilized may also be responsible. At high solid fraction there will be many solid-solid contacts, even under steady state conditions. These contacts become broader as a function of contact time, giving rise to a stronger interparticle bonding.

Martin et al. [199] studied the rheological behaviour of the semi-solid dendritic structure under various stress states for high solid volume fractions (> 0.6). Different compositions of Sn-Pb alloys were solidified to obtain a coarse dendritic structure. A microstructural observation was conducted after each experiment which revealed that no significant primary phase structural evolution occurred during deformation and reheating induced some Ostwald ripening. No axial or radial liquid segregation was discernible in deformed specimens. Damage was observable for the smallest applied strain. Damage was characterized by voids created in the liquid part of the semi-solid (figure 1.12). The size of voids varied from approximately 10 μm up to 1 mm when coalescence of voids has started. The majority of the voids were localized between two primary dendrite arms. More rarely they were observed between secondary dendrite arms, or at the initial lo-

cation of the entrapped liquid in a solid grain. The liquid entrapped in between secondary arms was not expected to participate in the macroscopic liquid flow. This would explain why very little damage was observed between secondary arms. These observations confirmed that damage initiation was related to liquid flow in the semi-solid. Using image analysis the authors determined the extent of damage for the deformed specimens, and were able to approximate the relationship between the volume of extracted liquid, and the volume of porosity left in the deformed specimen.

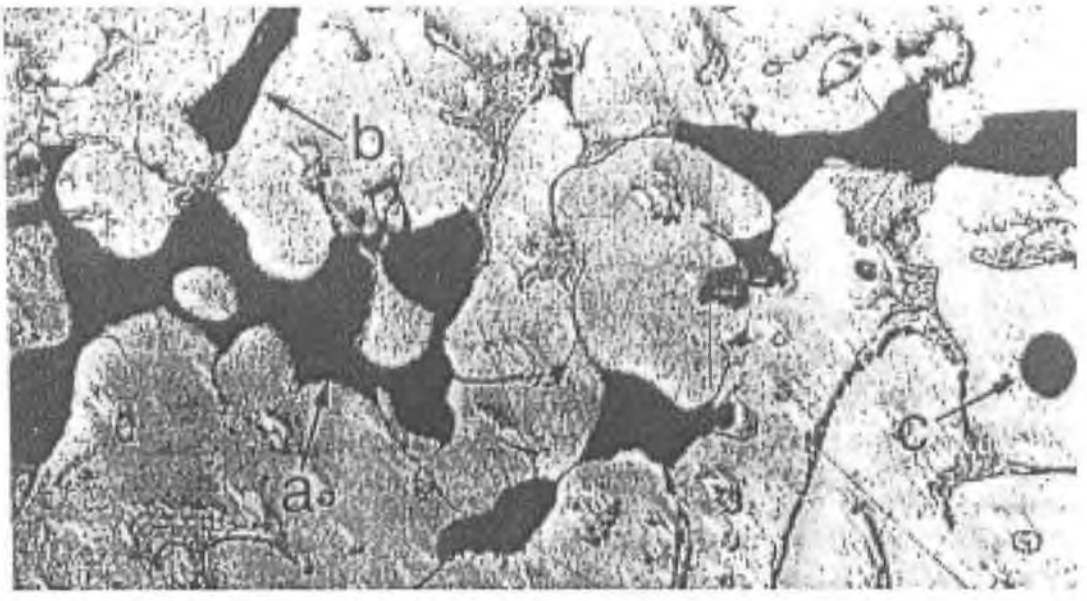

Figure 1.12: Micrograph of damage microstructure after applied strain. Damage is visible (a) between primary dendrite arms (b) between secondary dendrite arms and (c) inside solid particles (at the prior location of entrapped liquid) [199].

The semi-solid primary phase structure at rest for a previously sheared semi-solid A356 alloy, has been successfully modelled [203]. The researchers used an analogous approach to the kinetics of structure dissociation or reconstitution of agglomerate. The reconstitution of the structure of semi-solid composite at rest can be described by the following equation:

$$\frac{d\lambda}{dt} = g(\lambda, \dot{\gamma}) \tag{1.9}$$

where λ is the structural parameter, and $\dot{\gamma}$ is the shear rate of the composite prior to the rest period. This equation describes the kinetics of the variation of the semi-solid structure in terms of the structural parameter λ (such as its time dependent behaviour). From their work it can be concluded that the kinetics of reconstitution at rest are much slower than the kinetics of dissociation of the structure during shear. The structural parameter λ increases as a function of

the duration of the rest period. The kinetics of reconstitution are more rapid for decreasing primary solid fractions. Again it was seen that the reinforcing particles play an important role in the reconstitution kinetics, slowing down the process with respect to non reinforced alloys. The kinetics of reconstitution was more rapid for larger reinforcing particles because they are not as mobile as the small ones in surrounding the primary phase particles. This facilitates primary phase particle contact, and causes an agglomerate structure to reform more quickly.

1.6.2 Compocasting modeling

The complete description of the rheology of SSM requires a two-phase model that can separately model the flow of the liquid and solid phases [213]. By using the Algebraic Slip Model of commercial code PHOENICS^{TM}, Bui et al. [214] developed a 3D two phase model to simulate the stirring of a solid liquid mixture in a tank. They optimized various operational and design parameters and consequently, the conditions that will give the best mixture in terms of homogeneity. Another two phase model of the flow of SSM was studied by Burgos et al. [215]. Two-phase model requires extensive computational time. In order to perform the analysis more quickly, various researchers established a one phase mixing model for an Al-SiC composite melt [216, 217]. Comparison of one and two phase approaches for numerical simulation of semi-solid processing were investigated by Gebelin et al. [218]. A complete description of the processing requires a two phase model. Liquid segregation which can be detrimental to the mechanical properties of the processed parts can therefore be predicted. The unknowns are the liquid and solid velocities, the solid fraction and the temperature. The aim of their work was to develop the equations and to compare them to the single phase case.

A rheological model for semi-solid alloys was proposed and tested experimentally on A356 reinforced with SiC particle by Mada and Ajersch [202]. Their model described the kinetics of the structural degradation of the primary solid phase particles of the alloy as a function of shear rate, duration of shear and solid fraction of the composite. The thixotropic nature of these materials was confirmed experimentally using a concentric cylinder viscometer. The decrease in apparent viscosity at constant shear rate was described as occurring in two stages, resulting in an exponential decrease. Initially, the rapid decrease was the result of the break up of interaggregate bonds, releasing the entrapped liquid within the agglomerates. This increased lubrication between the particles, and hence reduced viscosity. The second stage of degradation of the structure was seen to be slower and was attributed to the break up of interparticle bonds. During this stage the size of agglomerates was seen to decrease and particles became

more spherical and of a more uniform size. Their experimental results show that the kinetics of the degradation increase with increasing shear rate, decreasing solid fraction of the primary solid phase and decreasing volume fraction of SiC particles. It became evident that the primary solid fraction had a much larger influence on the kinetics of the degradation than the SiC concentration, confirming that the primary particle interactions were the principal mechanisms which define the thixotropic nature of these composites. Finally, the effect of the reinforcing particle in the composite were found to oppose the agglomeration of the primary particles, which results in a more rapid degradation of the agglomerate structure as compared with the nonreinforced semi-solid alloy. The practical implications of this finding were that the reinforced alloys may require shorter stirring times, as compared with non-reinforced alloys, in order to achieve the desired fluidity for casting or forming.

1.6.3 Thixoforming modeling

Thixoforming is a novel process of manufacturing near net shape component from SSM which is currently competing with traditional manufacturing processes. The rheology of thixotropic slurries is not a simple matter. The apparent viscosity has been shown to be a function of shear rate, length of time being sheared, temperature of the semi-solid, solidification rate, composition and processing history [219]. The modeling of the flow of SSM is by no means trivial [220]. More research in this field is therefore needed. For example, a better understanding is needed of disagglomeration and reagglomeration behaviour of the primary particles during forming and recovery cycles. The cost effective production of near net shape thixoformed parts possess significant potential, not only for good mechanical properties but also for the development of complete new geometries of formed parts that were formerly impossible or difficult to achieve.

Previous SSM modeling work largely focused on the simulation of the die filling process [220–222]. A very important variable in the thixoforming process is the flow behaviour of the semi-solid slurry. It is particularly important to investigate the factors that influence this flow behaviour. Temperature has the most influence, because it determines the relative liquid and solid fractions [223]. Particle morphologies will dictate the exact solid fraction where the transition into the network deformation regime takes place. The prior shear rate and temperature history is also a strong determinant of particle morphologies and hence the semi-solid flow behaviour. The aim of Wahlen's modeling work [220] was to combine all these influences with the help of a microstructure based approached which incorporated an image analysis parameter, called the agglomeration ra-

tio, of the near globulitic primary particles. Hot deformation experiments with a cast (A356) and a wrought aluminium alloy (AA6082) were conducted [220]. The experimental work showed good agreement with the developed constitutive model. The constitutive model was able to predict the transition temperature at approximately 570 °C for A356, where the forming behaviour changed from the deformation of a connected particle network to viscous flow of a suspension of solid particles. There were some errors at lower forming temperatures that the predicted forces were too high because the simulation proceeds from a homogeneous initial temperature distribution in the specimen that could not be achieved with the radiation furnace geometry that was used.

Although considerable researches were done on optimizing the forming technologies and the appropriate initial microstructure of the input material, much less is known about how the flow behaviour of the semi-solid slurries influences the quality of the formed part. The objective of Wahlen and Tong [224] work was to implement a thixotropic flow model in the special purpose FE software ThixoForm for the optimization of thixoforming manufacturing. In order to verify the constitutive model and the simulation technique, cylindrical specimens of a rheocast aluminium billet (A359) with a globular microstructure were formed in a backward extrusion process at different temperatures in the semi-solid range. The specimens were heated up using a furnace of a metal heated source of infrared radiation. The temperatures of the specimens were measured using K type thermocouples. The measured forces were then compared with the simulation.

Modelings of thixoforming process were performed in 3D for the thixocasting process parameters, mould optimization and mixture approach [221,225–229]. Simulating the injection of thixotropic material required the viscosity to be specified as a function of both temperature and the shear rate history [225]. Experiments were performed using an industrial die casting machine that was instrumented with sensors to measure the pressure and temperature during the injection of semi-solid aluminium alloy through a small tube. This industrial scale capillary flow viscometer was used to determine the effect of fraction of liquid, piston velocity and die temperature on the pressure during filling of the die and to provide results for the development of a model that would correctly predict the shear rate history dependent flow response of thixotropic alloys. Simulations incorporating slip at the boundary between the SSM were tested. Numerical modeling of mould filling and solidification were used to optimize the thixoforming production moulds [221]. Rheological data and boundary conditions for the modeling were deduced from several sets of instrumented experiments.

The simulation results were correlated by Imwinkelried [230] with several types of known defects. He optimized the geometries of gates, parts, overflows and vents

of a mould. For the determination of the gate location and the gate geometry, the numerical simulation tool was used. Gating geometry and the piston velocity are linked and those need to be chosen together. The fill behaviour itself should be looked at if cold shuts and gas inclusions are identified. During the filling of the overflow, the local velocity distribution inside the part helped to identify other defects such as sticking. The flow behaviour of the thixotropic aluminium alloy A356 was modelled by a one phase Navier-Stokes model with a non-Newtonian power law viscosity.

A multiphase numerical model was presented by Binet and Pineau [226] for semi-solid flows. The proposed methodology, based on mixture theory, was also applied to the casting of MMCs, for which the matrix was assigned as one phase and the reinforcements on the other. The hydrodynamic part of the model was written in the same form as in most incompressible CFD codes. The computed velocity field represented the velocity of the mixture, and a source term was added to the momentum equations in order to take into account the diffusion velocities of the individual phases. Algebraic relations were also used to compute relative velocities, based on the interaction force between the phases. The proposed methodology was implemented in a finite element code and the constitutive equation was derived from a set of experimental rheological data. The model was then used in a simple test case of interest in thixocasting. From their study, a numerical solution of the flow of solid liquid mixtures using this multiphase constitutive model was presented. One of the achievements of their work was that phase segregation was lower, at lower pressure gradients. Even though the cases studied were highly simplified, they allowed a better understanding of segregation in the mixture during the flow. A full material characterization was required for truly predictive simulation capabilities. Rapid transient rheology in particular was investigated.

The work of Nohn and Hartmann [229] included the simulation of the thixoforming process and described the determination of appropriate material properties of the alloy A356. They established that the physical and flow properties of SSM were strongly dependent on the filling velocity and temperature. These were very important for the numerical simulation as input parameters. Experimental investigations were carried out to determine these properties by extruding semi-solid slugs. These tests helped to verify their modeling work. The investigations showed strong velocity dependence in the mould filling behaviour. Good agreement between experiments and simulations for the filling of a connecting rod and pump housing was found. The different velocity ranges between the parts investigated showed the broad applicability of the model to different patterns and circumstances.

Kang and Kang [231] studied the numerical analysis of semi-solid filling with solid fraction of 0.3 in A356 aluminium alloy. Their analysis gives die filling patterns and final solidification area, and also can predict mechanical properties of semi-solid forging components indirectly. In their study, a numerical analysis on semi-solid filling was investigated with two gate types and two associated die temperatures.

The microstructure evolution of aluminium alloys during isothermal holding at a temperature in the semi-solid range were simulated and experimentally investigated by Prikhodovsky et al. [232]. The particle size distribution of α-Al grains as a function of holding time was analyzed for several rheocast aluminium alloys. A new model for the simulation of Ostwald ripening in multicomponent systems, with high volume fraction of secondary phase, was also used. The analysis of the experimentally obtained particle distributions confirms the theoretical prediction that the asymptotic value of coarsening is approached only approximately one hour after the beginning of the isothermal holding.

Kiuchi et al. [233] studied a new mathematical model to simulate flow of semi-solid alloy where they presented a new yield criteria for SSM. This model, which incorporated grain size effects allowed working force and the distribution of the solid fraction in the work piece to be predicted.

Yang et al. [222] investigated the influence of die geometric parameters (such as gate dimensions) and process conditions (such as shot velocity, initial billet temperature, die and shot sleeve temperature, etc.) on SSM flow. A new die with varying wall thickness and five gate designs were used in their work. Regardless of the effect of various gate areas on the metal flow, it was shown that 100 % full casting with varying wall thickness between 0.8 and 5.6 mm were almost always achieved. This clearly displayed the ability of SSM to fill very thin sections by selecting proper process parameters. A general tendency among all gate combinations indicate a difficulty to fill heavier sections after the metal passes a very thin section. This depends mainly on the thermal conditions in the die, and the length of the flow path through the thinner section. Also, all gates illustrated a higher part integrity. These factors include the size of the solid grains in the preformed billet, the initial solid fraction, temperature distribution, ram speed and load, and the mold temperature.

Wang et al. [234] determined the optimal semi-solid forming process parameters by using simulation. Computer based and analytical simulation techniques were developed to assist in the design of the heating, material handling, and forming process steps of the SSM process. The forming process step analysis integrates experimental data, simplified analytical methods, and comprehensive 3D computer simulations. The general process was initiated with simplified analy-

sis, using empirical and analytical techniques to develop recommendations for minimum part thickness, gating and venting geometries, and the piston velocity profile. This was followed by 3D computer simulations to design the die heating and cooling system, calculate the die temperature after preheat, and evaluate the effect that the shot cycle time has on die temperatures. A 3D die filling computer simulation was then performed to confirm that the part geometry and rigging were appropriate for complete die filling with minimal solid-liquid segregation. Finally, a 3D solidification analysis was performed to assess the part solidification history and probability of defect formation. These techniques were used to successfully design a number of dies and parts.

The application of analogue casting systems to SSP were investigated by Mullis et al. [235]. Ammonium chloride was precipitated from aqueous solution under conditions of constant applied shear and controlled cooling rate. Experiments were performed in a glass reaction vessel so that insitu observations of dendrite size and morphology can be made as a function of cooling rate. At the fastest cooling rate employed (1 °C min^{-1}) large dendritic crystals were observed with extensive secondary branching. Under these conditions mean crystal size increased as solidification proceeded. As the cooling rate was decreased, secondary branching became less frequent until at the slowest cooling rate employed (0.2 °C min^{-1}), the observed crystallites had a cross shaped morphology with no obvious secondary branching. Under these conditions the mean crystallite size was approximately constant throughout solidification. No evidence of the rosette or spheroidal structures characteristic of metallic systems solidified under applied shear was found, even at the slowest cooling rates employed.

Kirkwood et al. [227] found that modeling die filling during thixoforming considered two aspects in FLOW-3D software. The constitutive equations were used to describe the thixotropy and to solve the flow equations. The first aspect was studied by examining the rheological behaviour of Sn-15 % Pb under equilibrium flow conditions and after shear rate jumps. Experimental work on Sn-15 % Pb indicated thixotropic model which was most applicable to semi-solid alloy slurries. They noted that shear rate jump experiments carried out on semi-solid alloy in a conventional viscometer were revealed short transients (greater than 0.1 s) in shear stress before a steady state was reestablished, which were interpreted as thixotropic behaviour in their modeling.

The thixotropic behaviour of semi-solid slurries was modelled by Alexandrou et al. [228] using conservation equations and the Herschel-Bulkley fluid model. Their model was implemented into a computer code to predict die filling. Results showed that the final quality of the products depends on the processing conditions and the geometry of the die. The model accounts for the existence of yield stress

in the material. The time dependent rheological parameters were found to be a function of the alpha phase volume fraction and an internal variable that changes with the processing history.

1.6.4 Stirring and sedimentation modeling

The effect of the impeller clearance off the bottom of a closed container on the minimum agitation speed for complete suspensions of solids in stirred tanks was presented by Armenante and Nagamine [236]. Considerable attention has been given in the past to determine the minimum agitation speed required to just suspend solids in mechanically stirred tanks [236]. The effect of the impeller off-bottom clearance has not been well established, particularly when the impeller is positioned very close to the tank bottom. Another investigation [204] was focused on the determination of the minimum agitation speed and power dissipation required to completely suspend solid particles in tanks provided with impellers having small clearances off the tank bottom. In their work, the effect of impeller off bottom clearance on the agitation speed was experimentally determined. They also established that mixed-flow and axial-flow impellers are more energy efficient than radial-flow impellers to completely suspend solids in the region very near to the tank bottom. Their work established a good agreement between the experimental data and the predicted data derived from mathematical equations.

The settling of silicon carbide particles in cast MMC has been studied by some researchers [193, 216, 237]. It is well known that an important factor influencing the microstructure is the settling of the particles during liquid processing of these composites. Latsa et al. [238] also presented a two-phase modeling of batch sedimentation. Numerical simulations of a typical batch sedimentation process for monodispersed particles were carried out, and they predicted sedimentation of a monodispersed suspension and the position of the sludge, suspension and clear liquid zones were in agreement with experimental results. The extension of the model to 2D was also verified qualitatively.

Kolsgaard and Brusethaug [193] studied the settling of SiC particles in an AlSi7Mg melt. The effect of SiC particle size and volume fraction on the settling behaviour were studied by isothermal holding of particulate MMC melts with initially homogeneous distributions of particles. The melts were held in cylindrical steel crucibles at 700 °C from which one crucible was quenched every minute. Longitudinal sections of the solidified samples were polished, and sharp transition between particle free and particle enriched areas could be observed. The distance from the bottom of the sample to the particle free area was measured, and used for calculating the settling rate. The effects of particle sizes ranging from 9 to 23

μm and volume fractions from 0.1-0.2 were studied. The observed settling rate varied from 3 to 26 mm min^{-1}, depending on the combination of particle size and volume fraction. For particle of size 23 μm and 10 % vol. reinforcement the settling rate was 26 mm min^{-1}; increasing the vol. % of reinforcement to 20 % reduced the settling rate to 3 mm min^{-1}. On reducing the particle size to 9 mm, a settling rate of 3 mm min^{-1} was observed for 10 % vol. fraction reinforcement. Measured settling rates were approximately 5 times higher than what is predicted from Stokes law. This deviation could be due to non spherical particles which can minimize the flow resistance and interaction between particles. Their findings indicated that the selection of the proper combination of size and amount of SiC reinforcement is important for obtaining a homogeneous distribution of the SiC particles in castings. When the objective was to obtain local reinforcement at the bottom of the casting, large particle size and reduced volume fraction should be used.

A two phase model for metal alloys in semi-solid state was studied by Modigell et al. [239]. In their paper a model is presented, which predicts the phase segregation in SSM owing to inclusion of the solid fraction with a proper balance equation (momentum conservation equation, continuity equation and power law equation) in addition to the thixotropic behaviour. The mixture of solid and liquid phases is described by the balance equations for the liquid and the averaged solid phase. Experiments were performed for different fractions of solid and basically consisted of isothermal step changes of shear rate. The model equations were employed into FEM software and simple flow cases like the Couette rheometer experiment and the compression of a cylindrical specimen were simulated. The results were in good qualitative agreement with experimental observations. A simple numerical model was presented for thixotropy in addition to the two phase character of SSM alloys.

A multiphase model for MMC solidification was developed and applied to sedimentation and solidification in various 1D and 2D Al-SiC systems [235]. Good agreement was found between simulation and experimental sedimentation results in A356 systems containing nonclustering and clustering particle systems. 1D composite solidification results illustrated the effect of particle clustering and cooling direction on the final macroscopic particle distribution, with the greatest concentration of particles found to occur near the wall opposite the chill. 2D simulations examined macroscopic particle transport and its effect on buoyancy driven melt flow, macrosegregation, and eutectic formation. They found that for the unreinforced alloy, macrosegregation was widespread with several channel segregates formed due to thermosolutal convection within the mushy zone. They also found that for the reinforced alloy with small particles, very little particle settling

prior to entrapment was observed, since the drag was relatively high (such as, the particles closely follow the motion of the liquid). In contrast, large particles resulted in a large amount of settling and packing prior to entrapment, due to the smaller drag and relatively large particle liquid relative velocity. They also found that in the presence of particles, convection during solidification was found to be substantially reduced due to the relatively large interfacial drag exerted on the liquid by the stationary mush and particles, which effectively acts to decrease the permeability of the mushy zone due to the increased viscosity in the liquid particle zone. As a result, macrosegregation was negligible where reinforcement was present, and solidification behaviour that predicted by the Scheil model. Buoyancy driven convection in the melt was generally significant, and consideration of settling alone was not sufficient, since particle motion occurs due to melt convection. Their model predicted the particle and melt velocities at the front, which were primary ingredients in any particle rejection model that accounts for flow. More solidification experiments over a larger range of cooling rates are required before many of these issues can be addressed.

Drenchev et al. [240] established a mathematical description for sedimentation phenomenon and the viscosity of a water SiC suspension under gravity conditions. They described it as a water model study for composite synthesis. In their work the nature of particle movement was discussed on the basis of sedimentation experiments carried out with water-SiC suspensions.

According to Stokes' law, the drag force, f_D, acting on a sphere moving in a liquid can be written as [240]:

$$f_D = 6\pi\mu_o r v \tag{1.10}$$

where, μ_0 is the dynamic viscosity of the liquid, r is the radius of the solid particle, v is the relative velocity of fluid with respect to the solid.

In the real case, the assumptions for the Stokes' law do not strictly apply, and to save the simplicity of the expression above an additional term is inserted

$$f_D = 6\pi\mu_o\mu_v r\nu, \mu_v \geq 1. \tag{1.11}$$

where μ_v expresses the effects of multi-particle movement, non-spherical particles shape and the influence of vessel's walls in an integral manner.

Most of the calculations devoted to composite synthesis use the following relationship [240]:

$$\mu_\nu = 1 + 2.5V_f + 10.05V_f^2 \tag{1.12}$$

where V_f is the volume fraction of the particle.

Drenchev et al. [240] showed that this formula generates large errors in numerical simulations when compared to real composite casting. Their water model experiments also proved this equation to be erroneous.

A new formula for viscosity, which takes into account the movement of many particles and provides quite good coincidence of measured and calculated values for parameters of sedimentation was presented in their work is as follows:

$$\mu_\nu = 1 + 18.5V_f + 4.5V_f^2 + 170V_f^3 \tag{1.13}$$

According to their work, in the sedimentation experiments the particle size distribution of the SiC particles were measured by light microscopy is shown in figure 1.13 (a). The variation of suspension height that they measured as a function of time for an initial particle volume fraction of 0.25 is shown in figure 1.13 (b). Above these heights it was noted that a clear liquid had formed.

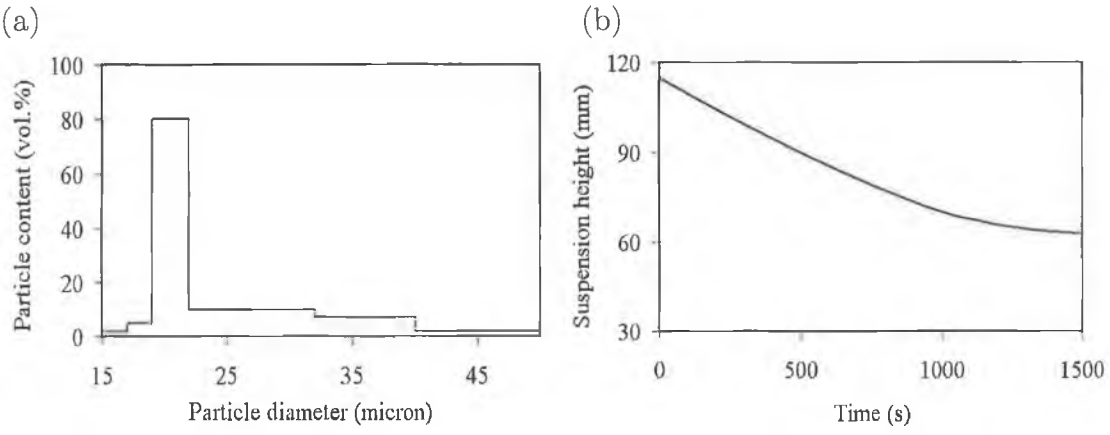

Figure 1.13: (a) Distribution of SiC particles contents of nominal diameter 20 μm measured by light microscopy (type Reichert) as a function of particle diameter, (b) Variation of suspension height (such as movement of the boundary between particles-free zone and particle-rich zone) measured as a function of time for initial particles of volume fraction 25% [240].

In the above section previous one and two phase rheological SSP models were presented. Some of these two phase models examined particle distribution and sedimentation in the compocasting process. Only a few of these focused on the batch compocasting process and none of the modeling work done above has verified either the visualization or the computational simulation results with actual MMC (Al-SiC) production. This present work is concerned on the stir-casting process. In order to analysis this, visualisation and computational simulation were performed and results were compared to compocasting with similar operating parameters.

Chapter 2

Visualisation modeling experiments

In every MMC fabrication technique, wettability and uniform distribution of the reinforcement particles in the matrix materials are among the main problems. Unfortunately, in normal practice the effect of the stirring action on the flow patterns can not be observed as they take place in non-transparent molten metal within a furnace. As such, and because of the fact that direct measurements of metal flow characteristics can be expensive, time consuming and dangerous, the current research focuses on methods of simulating fluid and particle flow during stirring. Simulation work involves visualization experiments and computational simulations. Both simulations were carried out to optimise SiC particle distribution in aluminium alloys during the mechanical batch compocasting process.

In the visualisation experiments liquid and semi-solid aluminium are replaced by other fluids with similar characteristics. Water and transparent glycerol/water solutions were used to provide fluids of a varying viscosity. Viscosities similar to those of SSM of 300, 500, 800 and 1000 mPas were produced from glycerol/water solutions [86]. Viscosity was measured by RI viscometer (model no. RI:2:L) with the accuracy of 1 % Water provided a viscosity of 1 mPas, similar to that of liquid aluminium [147]. SiC reinforcement particulate similar to that used in aluminium MMC's was used in the simulation fluid mixtures. Two levels of 13 μm sized SiC particles, 0.1 % or 10 %, were added to these fluids. The lower level allowed internal flow patterns to be observed whereas the upper level, simulating a typical quantity of SiC in a MMC, showed external flow patterns and allowed measurement of dispersion rates. Water, glycerol and SiC densities were 1000, 1260, and 3210 kg m^{-3} respectively.

Variables taken into account in simulation include fluid viscosity, speed of shearing and position of stirrer. Viscosity variations with fraction solid are also

important. Different viscosity levels (1, 300, 500, 800 and 1000 mPas) were taken into account in order to simulate these effects. Optimum conditions for obtaining and sustaining a uniform suspension of solid particles were established.

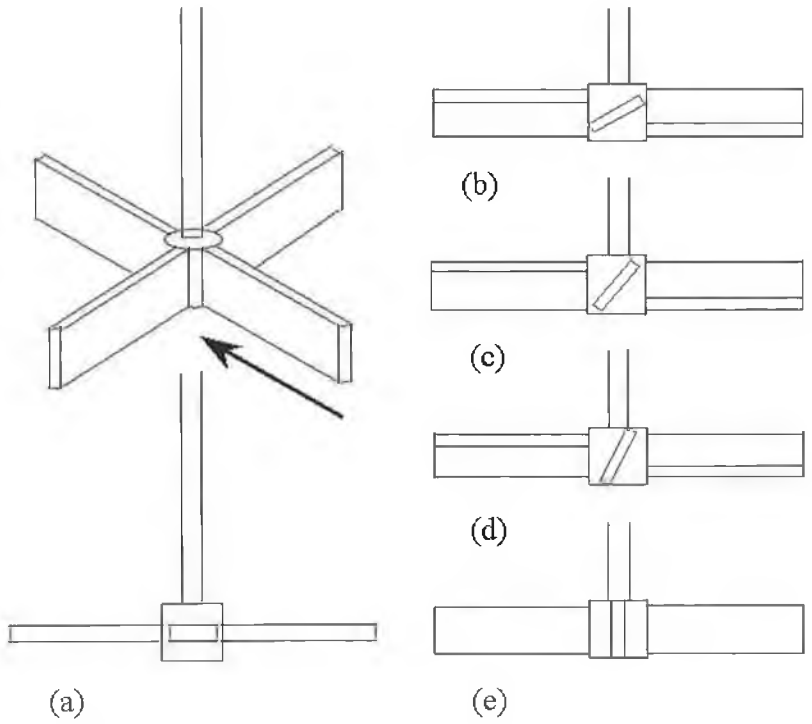

Figure 2.1: Four blades stirrer, showing different blade configurations (a) 0 ° (b) 30 ° (c) 45 ° (d) 60 ° and (e) 90 ° [241].

2.1 Experimental model set-up

Scaled-up stirring experiments were carried out in a transparent crucible with the percentage of reinforcement material being varied. Optimum conditions for photographing flow patterns were established. The dependence of the photography conditions (shutter speed, aperture control, lighting), particle dispersion and settling times and vortex height on stirrer geometry and speed were found. A 400 ml quantity of each of these solutions was prepared in a 10.5 cm diameter Pyrex beaker. This resulted in a solution height of 6.5 cm. The height of the solution was chosen so that one stirrer is sufficient enough to disperse the SiC uniformly throughout the crucible and a uniform mixture of SiC could be achieved for maximum amount of liquid. The SiC particles were resting at the bottom of the beaker as an initial condition of dispersion set-up. Agitation was provided by three different stirrer types. Three and four bladed stirrers with blades normal to the axis of rotation as well as a fixed bladed turbine stirrer were used. Flat blades

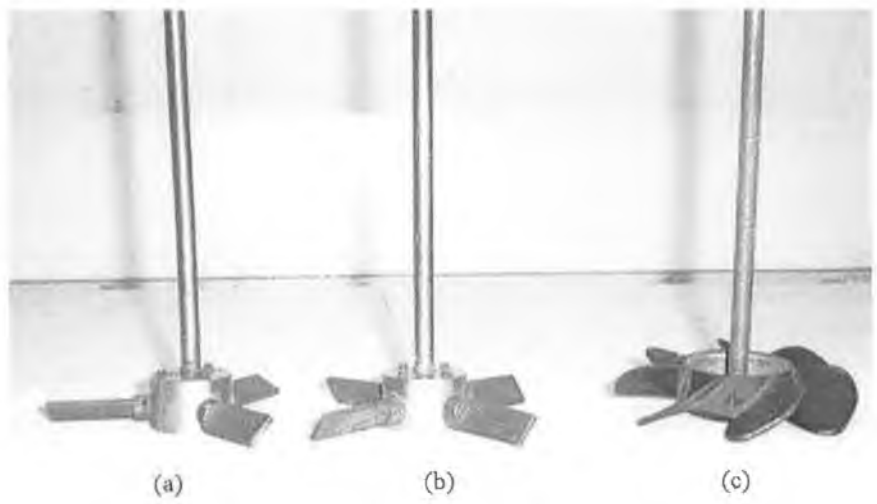

Figure 2.2: Different stirrer (a) three blade stirrer (b) four blade stirrer (c) turbine blade stirrer.

could be rotated about their longitudinal axis (figure 2.1). A speed controlled DC motor enabled accurate control of the stirring speed. Height of the stirrer from the bottom of the beaker, H, was adjustable. A schematic of the experimental set up is shown in figure 2.3.

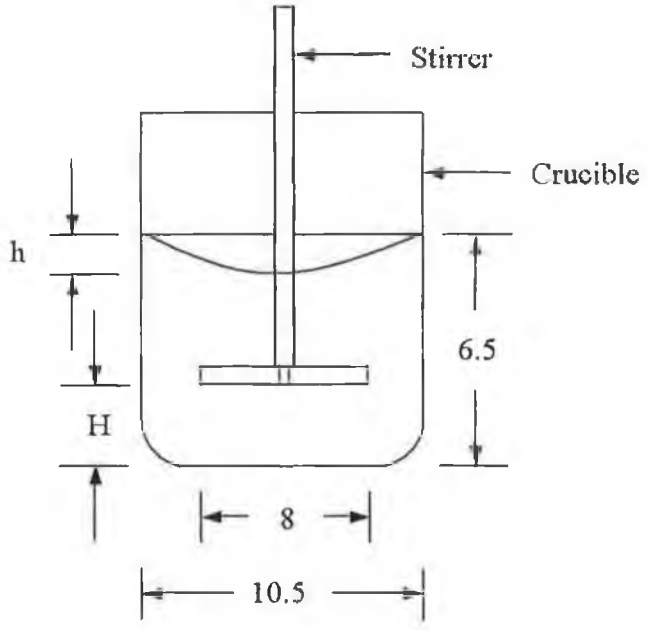

Figure 2.3: Schematic of the experimental set up; all dimensions are in cm. [241].

A camera was mounted along the same horizontal plane as the beaker. Shutter speed, aperture, and lighting settings were adjusted to optimise the picture quality. During these tests, shutter speeds were varied from 1/15 s to 1/2000 s while the aperture was automatically controlled. Conversely, the aperture was varied from F 5.5-38 while the shutter speed was automatically adjusted.

Steady state flow patterns were set up in the fluids with stirring speeds of 50, 100, 150, 200, 250 and 300 rpm. With the SiC particles initially resting at the bottom of the beaker, time required from shearing commencement, for a uniform dispersion of particles were recorded. When shearing was stopped, settling times for uniformly dispersed particles in the different fluids were measured. Uniform dispersion and settling were completely judged by eye. The effects of different stirrer heights on different solutions were also observed. In addition, vortex height, h (figure 2.3), was recorded for water and glycerol/water with different stirrer types and stirring speeds.

2.2 Experimental model results

2.2.1 Dispersion results

Camera shutter speeds at least greater than 1/60 s were required to capture the flow pattern in the stirring speed range investigated (50-300 rpm). Faster shutter speeds up to 1/2000 s did not affect captured image quality. Aperture control with automatic shutter speed settings did not produce good photographs due to the low shutter speeds recorded for the aperture range investigated ($< 1/60\ s$). Integral camera flash, with a white background to the Pyrex beaker, proved the best lighting solution. With this set-up internal flow pattern were captured in 0.1 % SiC fluids and external flow of the fluid could be observed in the 10 % SiC fluid mixtures. Some visualisation photograph are shown in figure 2.4.

At 50 rpm no dispersion of the particles occurred irrespective of blade angle or fluid. Uniform particulate dispersion times for a 10 % SiC water mixture, for different stirring speeds above 50 rpm are listed in Table 2.1. Below 150 rpm no dispersion occurred for the higher viscosity glycerol/water mixtures. Uniform particulate dispersion times for a 10 % SiC glycerol/water mix (with 300 mPas viscosity), for the different stirring speeds are shown in Table 2.2.

Uniform dispersion times for 10 % SiC particles in glycerol/water solution for different stirrer types and stirrer heights, H, are listed in Table 2.3. Due to high vortex formation in water at higher stirring speeds and the lack of dispersion in the glycerol/water mixture at lower speeds, a stirring speed of 150 rpm was used in water and 200 rpm in the glycerol/water mixture. With increase in the height of the stirrer in the melt, the dispersion times increase. Indeed, for stirrer heights of 30 mm and above in the glycerol/water mixtures, the particles are not dispersed into the solution. From Table 2.1, 2.2 and 2.3 a general result observed is the strong tendency for the turbine to produce a faster dispersion time than the other stirrer types. A less pronounced tendency for the 4 blade stirrer to produce

Table 2.1: Uniform dispersion time for 10 % SiC particles for different stirrer types and stirring speeds in water of viscosity 1 mPas. Stirrer height was 20 mm from the base of the beaker.

Stirring speed (rpm)	Blade angle (°)	Uniform dispersion time (s)		
		3 Blade stirrer	4 Blade stirrer	Turbine Blade stirer
100	0	N/A	N/A	180
	30	N/A	N/A	
	45	300	180	
	60	180	180	
	90	180	120	
150	0	120	120	27
	30	90	25	
	45	30	29	
	60	25	12	
	90	28	27	
200	0	120	29	17
	30	60	17	
	45	20	16	
	60	19	16	
	90	25	16	
250	0	60	16	16
	30	30	16	
	45	16	16	
	60	15	16	
	90	14	18	
300	0	60	15	15
	30	19	15	
	45	15	15	
	60	13	15	
	90	13	15	

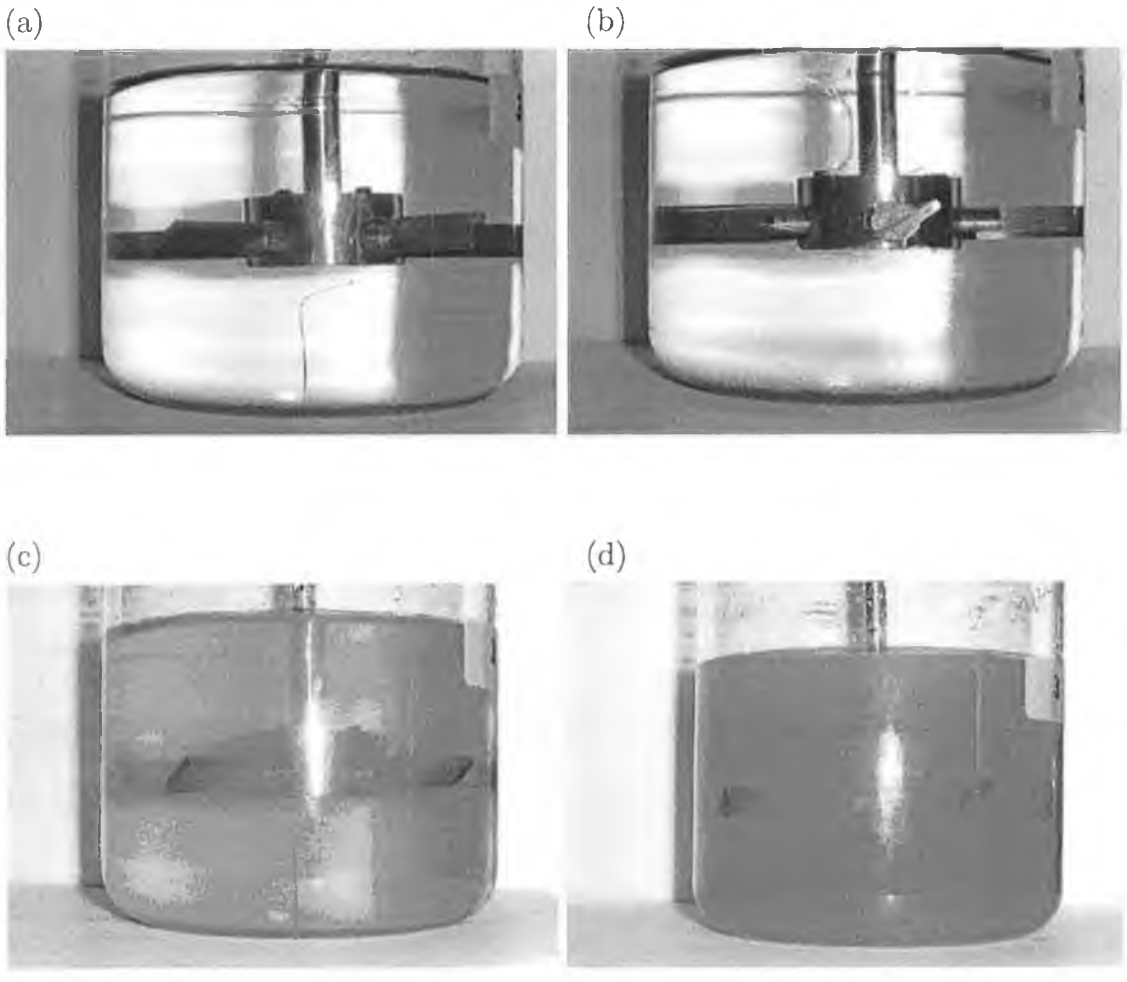

Figure 2.4: (a) Transparent glycerol/water mixture in a pyrex beaker, 0.1 % SiC (b) velocity traces in the glycerol/water for four bladed and pyrex beaker with 0.1 % SiC, (c) distribution pattern of SiC with velocity of the stirrer (d) full dispersion of 10 % SiC in the glycerol/water mixture.

shorter stirrer times than the 3 bladed stirrer is also observed.

Table 2.4 compares the vortex depth of different viscosities solutions, stirrer types, and stirring speeds. It is evident from this table that at higher stirring speed in water the vortex height increases. Much greater vortex height is also observed in the water compared with the glycerol/water. No vortex was present in glycerol/water for stirring speeds below 150 rpm. Air entrapment was also observed in all fluids at speeds above 250 rpm, though this was more evident in the higher viscosity fluids.

Table 2.2: Uniform dispersion time for 10 % SiC particles for different stirrer types and stirring speeds in glycerol/water solution of viscosity 300 mPas. Stirrer height was 20 mm from the base of the beaker.

Stirring speed (rpm)	Blade angle (°)	Uniform dispersion time (s)		
		3 Blade stirrer	4 Blade stirrer	Turbine Blade stirer
200	0	2700	2520	2340
	30	2520	2460	
	45	2400	2400	
	60	2100	1920	
	90	2640	2460	
250	0	1980	1800	1680
	30	1800	1800	
	45	1800	1740	
	60	1740	1680	
	90	1920	1800	
300	0	1320	1200	900
	30	1200	1140	
	45	1080	1080	
	60	900	900	
	90	1200	1200	

2.2.2 Settling results

In all cases, particulate settling times measured were independent of stirrer types and stirring speed. Approximately 90 % of all particles settled within 60 seconds in water and complete settling was recorded after 180 seconds. The time at which particulate settling occurred in the glycerol/water mixtures was evident from the emergence a clear layer, absent of SiC particles, at the top of the mixture. For all glycerol/water mixtures the uniform dispersion of SiC remained for one hour, and complete particulate settling only occurred after 20 hours. Figure 2.5 shows the graphical settling results.

Table 2.3: Uniform dispersion time in different solution for 10 % SiC particles for different stirrer types and height for 45 degree blade angle

Solution	Stirring Speed (rpm)	Stirring height (mm)	Uniform dispersion time (s)		
			3 Blade stirrer	4 Blade stirrer	Turbine Blade stirer
Water, viscosity 1mPas	150	10	30	25	24
		20	30	29	27
		30	50	45	40
		40	120	90	60
		50	180	120	70
Glycerol, viscosity 300mPas	200	10	1500	1500	1320
		20	2400	2400	1740
		30	N/A	N/A	N/A
		40	N/A	N/A	N/A
		50	N/A	N/A	N/A

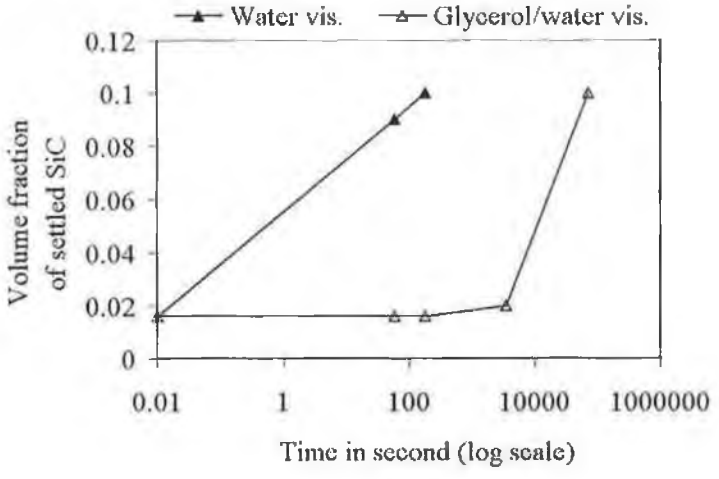

Figure 2.5: Visualisation results in settling. Volume fraction of settled SiC versus time in seconds in log scale.

Table 2.4: Comparison of the vortex height for different stirring speeds and stirrer types in solutions of viscosities 1, 300, 500, 800 and 1000 mPas. Stirrer height was 20 mm from the base of the beaker.

Solution	Stirring speed (rpm)	Vortex Depth (mm)		
		3 Blade stirrer (45 degree blade angle)	4 Blade stirrer (45 degree blade angle)	Turbine Blade stirrer
Water viscosity 1 mPas	100	4	5	6
	150	12	13	14
	200	22	25	30
	250	35	40	45
	300	40	50	55
Glycerol viscosity 300 mPas	100	No Vortex	No Vortex	No Vortex
	150	No Vortex	No Vortex	1
	200	2	1	5
	250	5	5	7
	300	7	6	10
Glycerol viscosity 500 mPas	100	No Vortex	No Vortex	No Vortex
	150	No Vortex	No Vortex	No Vortex
	200	1	No Vortex	1
	250	2	3	3
	300	4	5	6
Glycerol viscosity 800 mPas	100	No Vortex	No Vortex	No Vortex
	150	No Vortex	No Vortex	No Vortex
	200	No Vortex	No Vortex	No Vortex
	250	1	1	1
	300	2	3	4
Glycerol viscosity 1000 mPas	100	No Vortex	No Vortex	No Vortex
	150	No Vortex	No Vortex	No Vortex
	200	No Vortex	No Vortex	No Vortex
	250	2	1	1
	300	2	2	3

Chapter 3

Computational modeling

3.1 Model set ups

The mathematical model was built as a two-phase fluid flow model where the first phase was water or a glycerol/water mixture and the second phase was the particulate SiC. These phases were chosen as they would enable the model to be validated using previous visualisation simulations. The water and glycerol/water mixture were used in this previous work to simulate the liquid and semi-solid aluminium in the Al-SiC MMC system [241]. The physical parameters of the model were chosen in order to match this previous work in which a compocasting mixing vessel held the fluid. Dimensions of this vessel and the four bladed stirrer used are shown in figure 2.3. All the measurements were made in a standard flat-bottomed cylindrical vessel of 105 mm diameter. A flat bladed impeller was set at 45 degree to the vertical and arranged to pump in the up-wards direction. The dimensions of the impeller used in the model are shown in figure 3.1. Water, glycerol and SiC densities were set at 1000, 1260, and 3210 kg m^{-3} respectively. The SiC particulate size was set at 13 μm and the volume fraction of this phase at 10 %. The viscosity of the first phase was set at 1 mPas to simulate liquid aluminium and at 300 mPas to simulate semi-solid metal. An Eulerian (Granular) multiphase model was chosen in Fluent in order to model the multiphase flow.

Initial velocity distributions along the stirrer blade for this model were obtained from a 3D velocity model of the flow at the investigated stirring velocity (100, 150, 200, 250 and 300 rpm), stirrer height (13, 20 and 26 mm) and stirrer diameter (50, 60, 70, 80 and 90 mm). The four flat bladed impeller was used for this modeling set-up. 2D numerical simulations were examined for dispersion and settling. Detail theory of multiphase model is in Appendix A.

All of the measurements reported here were taken in the plane mid way between the impeller blades. This is represented in figure 3.2 (a) as plane AA. The

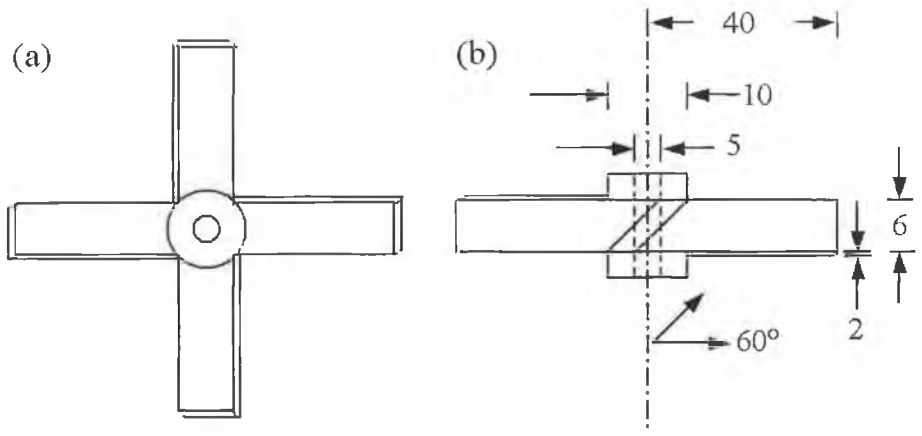

Figure 3.1: Schematic of the impeller used in the modeling, all dimensions are in mm. (a) top view (b) side view.

three directions of measurement were axial, x, radial, r, and circumferential θ as shown in figure 3.2. These measurements showed that the flow inside the crucible was symmetrical about the impeller axis. The height positions at which measurements were taken in the crucible are marked by P, Q, R, S, T and Z (figure 3.2 (b)).

Results that were recorded and presented in this thesis were the velocity components, the kinetic energy dissipation, the eddy dissipation, and the percentage of SiC. The axial, radial and circumferential velocity, the kinetic energy dissipation, the eddy dissipation, and the volume percentage of SiC around in the vessel has been estimated by using a 3D velocity model in Fluent. For water $k-\epsilon$ model and for glycerol/water system laminar flow model were chosen. $k-\epsilon$ model is generally used for turbulent model. Stirring velocity, stirrer height and stirrer diameter were established by these two models. The 2D Eulerian multiphase model was used for dispersion and settling times set-up. The Grid generated in FLUENT for 2D simulation and 3D simulation can be sen in Appendix B.

Axial velocity in the upward direction, radial velocity towards the periphery of the vessel, and clockwise (when viewed from the above) circumferential velocity were taken as the positive velocity directions. Impeller rotation was set to be in the clockwise direction (also viewed from above) so that a pumping action in the upward direction was set-up.

3.1.1 Stirring velocity

To investigate the effect of velocity of the impeller, the impeller was positioned at a fixed distance of 20 mm from the bottom of the crucible and the speed was

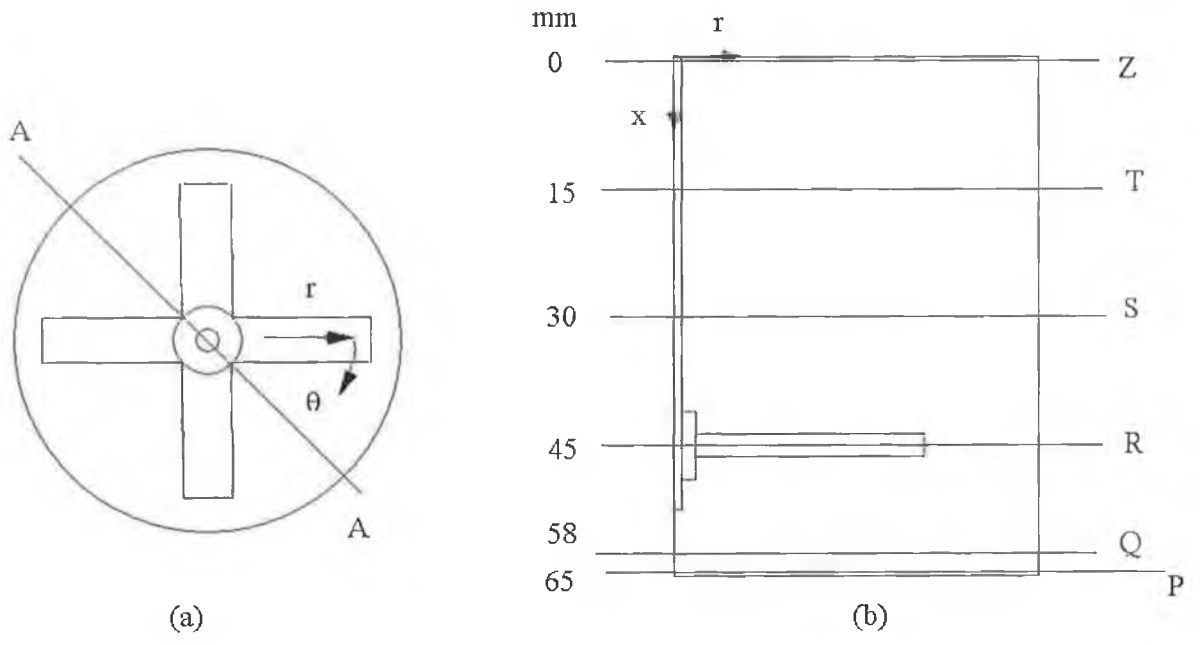

Figure 3.2: Arrangement of the measuring points in the mixing crucible (a) Plan view (b) elevation on A-A: Z is at the top of the liquid surface, T is 15 mm inside the liquid from the position Z below the liquid surface, S is 30 mm from the liquid surface, R is 45 mm away from the liquid surface, Q is 58 mm from the top surface, and P is at the base of the crucible.

varied. Velocity distributions for different rotational speeds ranging from 50 to 300 rpm in water of viscosity 1 mPas and glycerol/water solution of 300 mPas were investigated. During these modeling stirrer diameter used was 80 mm.

3.1.2 Stirrer height

The effect of stirrer height on the velocity distribution were investigated. The impeller was positioned in the tank as different height at different time to investigate the effect of height on the velocity distribution of the liquid. Impellers were positioned at 20 %, 30 % and 40 % of the liquid height. For 20 %, 30 % and 40 % liquid height it was 13 mm, 20 mm and 26 mm respectively from the bottom of the crucible. During these modeling stirrer diameter used was 80 mm.

3.1.3 Stirrer diameter

To understand the effect of diameter on flow patterns five different diameters of 50, 60, 70, 80 and 90 mm were taken into consideration. Each time height of the stirrer was kept constant at position 20 mm and rotational speed was kept constant at 300 rpm.

3.1.4 Dispersion

The SiC was positioned at the base of the mixing vessel at the start of these simulations. A packing volume fraction of 0.6 for SiC particles were assumed (figure B.3a) Velocity and SiC distributions at different times after the commencement of stirring were then examined. SiC distributions at different times after the commencement of the model were then noted. During these modeling stirrer diameter used was 80 mm.

3.1.5 Settling

This type of simulation examined the settling times for SiC in the absence of stirring. As an initial condition for this simulation a uniform distribution of the particulate of 0.1 volume fraction was set throughout the fluid (figure B.3b). SiC distributions at different times after the commencement of the model were then noted. During these modeling stirrer diameter used was 80 mm.

3.2 Model velocity field results

3.2.1 Stirring velocity

Figure 3.3 (a) shows the axial velocity around the impeller as a function of radial position for various stirring speeds. This figure shows that the axial velocities are small and very random in nature. From 50 to 150 rpm the axial velocity distribution pattern were found to be similar with different magnitude. For 150 rpm the magnitude was found to be higher and for 50 rpm the magnitude was lower. Below 150 rpm, velocities have positive values. From 200 rpm the axial velocity distribution becomes very much dissimilar than the lower velocities. The random pattern of the velocity distribution above 200 rpm suggest the great turbulent flow in the system. For 200, 250 and 300 rpm, the velocities found to have both positive and negative values. The velocity magnitude was ranging from -0.1 to +0.15 m s^{-1}. For the axial velocities in water it was found that the random fluctuations were almost entirely due to the periodic nature of the turbulent flow imposed by the blades of the impeller in water.

Figure 3.3 (b) shows the radial velocity also as a function of radial position for various stirring speeds. For 50-150 rpm, the radial velocity distribution was found to be the same pattern with different magnitude. For 150 rpm the magnitude was higher and for 50 rpm the magnitude was lower. Up to 150 rpm, the conventional linear velocity formula $v=\omega r$ can be seen to work and above 150 rpm, this formula was invalid. The values for radial velocities were all positive.

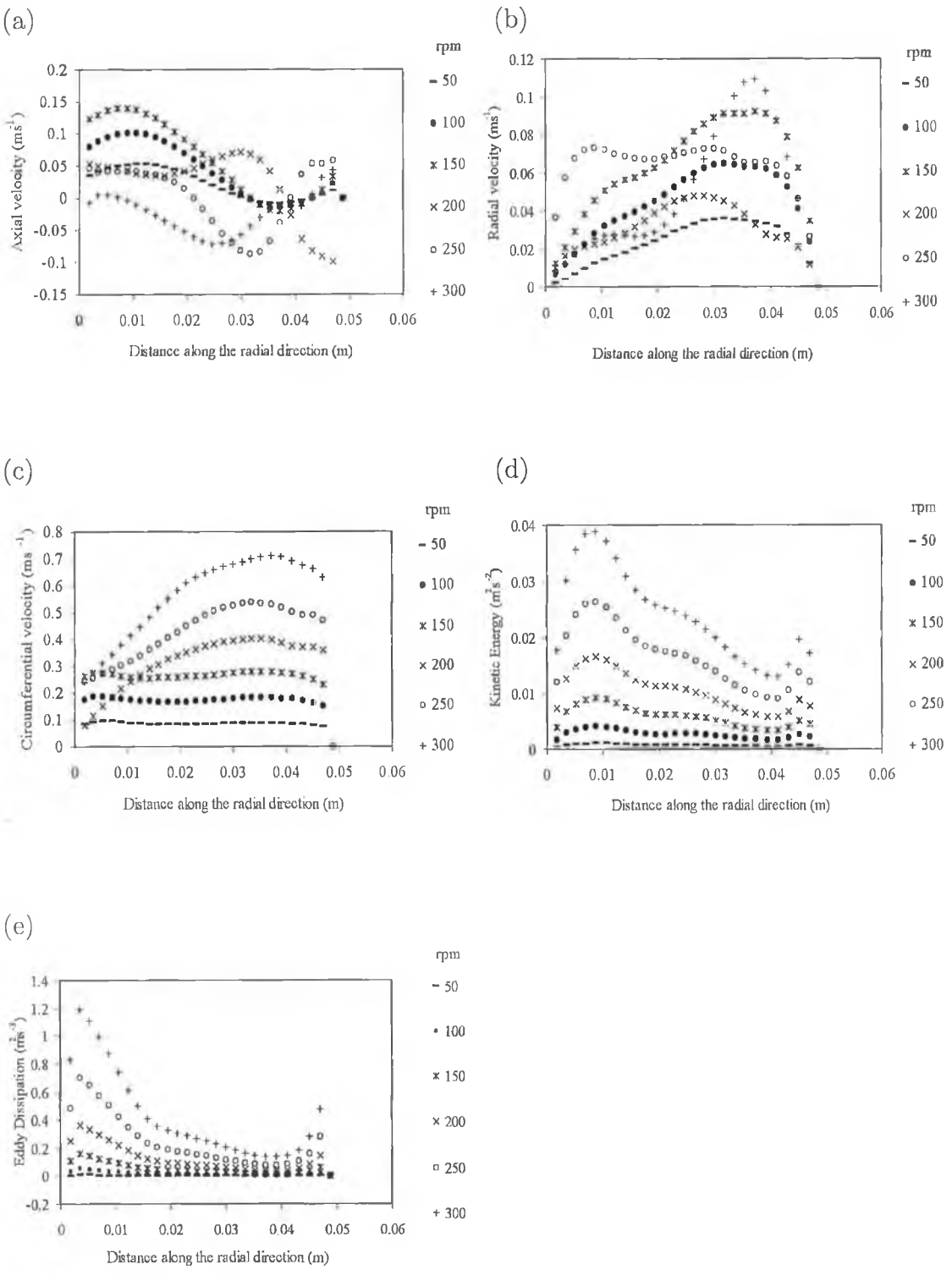

Figure 3.3: (a) Axial velocity, (b) radial velocity, (c) circumferential velocity, (d) kinetic energy and (e) eddy dissipation distribution of fluid along the blade at various stirring speeds for water of viscosity 1 mPas. Stirrer height was 20 mm from the base of the beaker.

The maximum velocity magnitude recorded was 0.1 m s^{-1} at 0.038 m from the centre of the crucible for 300 rotational speed. It is noted that the blade edge was at 0.04 m.

Figure 3.3 (c) shows the circumferential velocity distribution for water of viscosity 1 mPas at various stirring speeds at given distances from the centre of the crucible. The found distribution of circumferential velocities on the centreline of each impeller fitted with expectation. The velocities in this direction is much greater than either axial or radial velocities. For lower velocities, a linear velocity magnitude was observed along the blade. For 50, 100 and 150 rpm the velocity magnitude were around 0.1, 0.2 and 0.25 m s^{-1} respectively. There were sharp changes in the velocity distribution along the blade above 200 rpm. For 200 rpm the velocity distribution was non-linear with increasing pattern and it was increasing from 0.1 m s^{-1} to 0.35 m s^{-1}. The velocity was increasing up to 0.02 m of blade length, after that it reaches a uniform value of 0.35 m s^{-1} magnitude. For 250 rpm the velocity magnitude was recorded within 0.25 to 0.5 m s^{-1}. Velocity distribution was recorded from 0.25 to 0.7 m s^{-1} for 300 rpm rotational speed. For both 250 and 300 rpm at 0.038 m distance from the centre of the stirrer, the velocity magnitude was found to be maximum. It is noted that the blade edge was at 0.04 m.

Figure 3.3 (d) shows the kinetic energy distribution for various stirring speeds at given distances from the centre of the crucible. The patterns for kinetic energy distribution were same with different magnitude. The values for the graphs were distinct. For higher velocity the magnitude of the kinetic energy was maximum and for lower velocity the kinetic energy was minimum. For 50 to 150 rpm the kinetic energy recorded was under 0.01 value m^2 s^{-2} and above 200 rpm, the maximum kinetic energy recorded was at 0.01 m from the centre of the blade. For 300 rpm the maximum recorded kinetic energy was 0.04. Figure 3.3 (e) shows eddy dissipation distribution for various stirring speeds at given distances from the centre of the crucible. Again, the patterns were similar with different magnitude. It was noted that the maximum eddy dissipation was 1.2 m^2 s^{-3} for 300 rpm near the shaft of the stirrer and the eddy dissipation was nearly zero for 50 rpm.

The axial velocity distribution in the axial position in the radial directions for various stirring speeds in glycerol/water solution of 300 mPas are shown in Figure 3.4 (a). From 50 to 150 rpm the axial velocity distribution was similar with different magnitude with negligible velocity value. For 150 rpm the magnitude was higher and for 50 rpm the magnitude was lower. Below 150 rpm all the velocities were found to be positive. From 200 rpm the axial velocity distribution becomes very much dissimilar than the lower velocities. For 200, 250 and 300

rpm, the velocities found to be with both positive and negative values. There was no significant random fluctuations, confirming that the fluid was in laminar flow in the glycerol/water solution.

Figure 3.4 (b) shows the fluid velocity distribution for radial directions in glycerol/water solution at various stirring speeds at given distances from the centre of the crucible. The radial velocity distribution pattern were similar with different magnitude. For 300 rpm the magnitude was higher and for 50 rpm the magnitude was lower. Radial velocities were positives. The maximum radial velocity magnitude recorded was 0.15 m s^{-1} at 0.03 m from the centre of the crucible for 300 rotational speed.

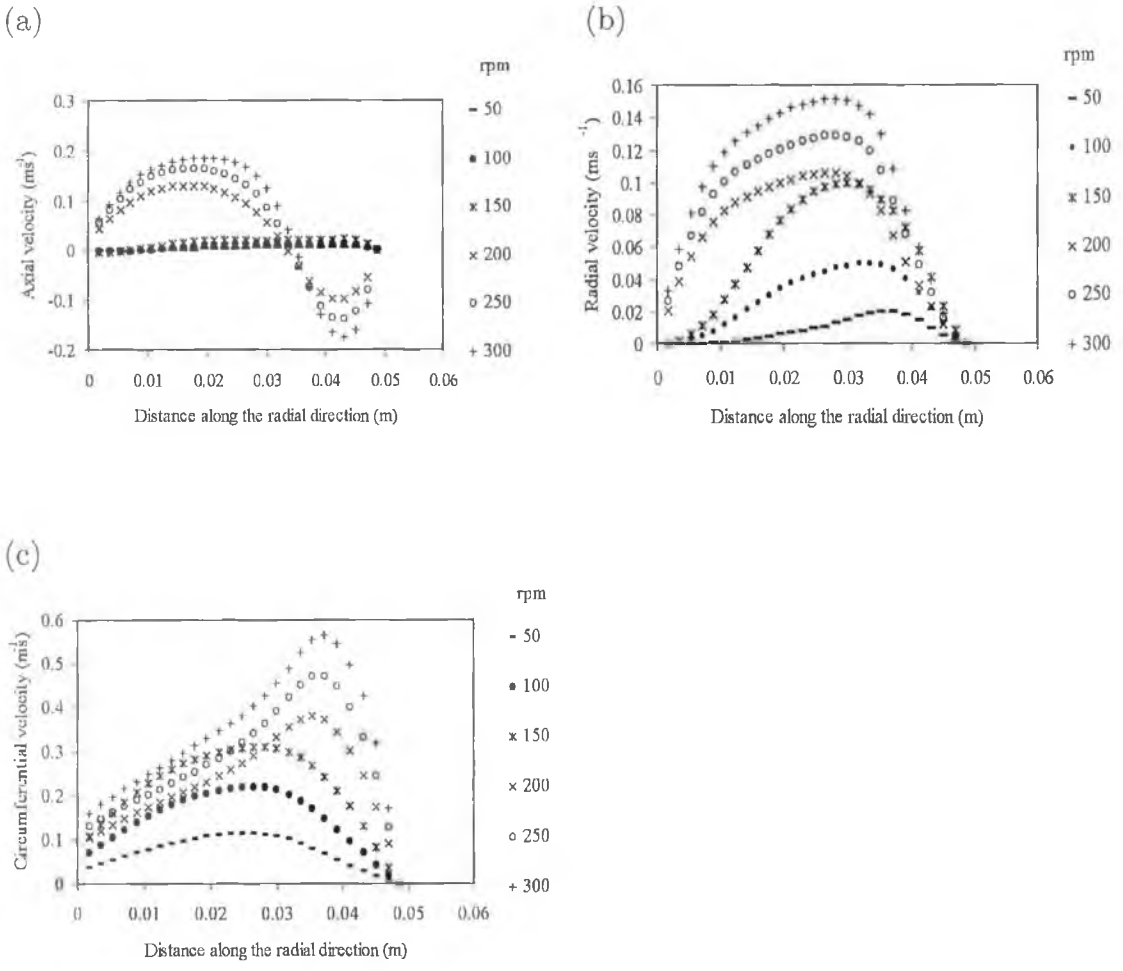

Figure 3.4: (a) Axial velocity, (b) radial velocity and (c) circumferential velocity distribution of fluid along the blade at various stirring speeds for glycerol/water of viscosity 300 mPas. Stirrer height was 20 mm from the base of the beaker.

Figure 3.4 (c) shows the velocity distribution for axial directions at various stirring speeds at given distances from the centre of the crucible. With lower

velocities, a linear velocity magnitude was observed along the blade. For 50, 100 and 150 rpm the maximum velocity magnitude was found to be around 0.08, 0.2 and 0.28 m s^{-1} respectively. There were a sharp change in the velocity distribution along the blade above 200 rpm. For 200 rpm the velocity distribution was non-linear with increasing trend which was increasing from 0.1 m s^{-1} to 0.35 m s^{-1}. Up to 150 rpm the velocity increase and decrease was axisymmetric. The pattern of velocity profile was same with different magnitude for 200, 250 and 300 rpm rotational speeds. The velocities were increasing up to 0.038 m of blade length then decreases to zero value. For 250 rpm the velocity magnitude was recorded 0.1 near the shaft and increases to 0.48 m s^{-1} at 0.038 m length of the blade. For 300 rpm the velocity magnitude was recorded 0.1 near the shaft and increases to 0.58 m s^{-1} at 0.038 m length of the blade. For 200, 250 and 300 rpm at 0.038 m distance from the centre of the stirrer, the velocity magnitude were found to be maximum. It is noted that the blade edge is 0.04 m.

3.2.2 Stirrer height

A divergent result for 10 % liquid height was obtained and then there was no effort given to get a model below 20 % height. During investigating the effect of height of impeller, the main focus was held at a position of Z and P. Axial velocity at P is more important than position Z, during dispersion. To get a uniform suspension sufficient velocity is required at position P. After suspension, to keep the suspension uniform velocity at Z should be considered. Axial, radial and circumferential velocity profiles were carefully examined for different stirrer height and the velocity profiles were carefully examined for the different position in the crucible. Axial, radial, circumferential velocity and kinetic energy distribution as a function of radial distance in water for 300 rpm and 13 mm height of the impeller are shown in figure 3.5 (a), (b), (c) and (d) respectively. In this case, axial velocity at position Z is nearly zero. In all the positions, circumferential velocities are similar with negligible differences. At position R, kinetic energy was maximum at 0.01 blade lengths and then decreasing and for Q position; kinetic energy was maximum at 0.02 m^2 s^{-3}. Except R and Q, all the other position P and Q, the eddy dissipation is dramatic. For position P, eddy dissipation decreases sharply along the shaft of the impeller from a value of 0.35 m^2 s^{-3} to 0.05 and then again increases to a value of 0.03 m^2 s^{-3} at a position of the 0.03 m of the blade length and then decreases to zero at the wall.

At 20 mm height of the impeller of base in the liquid height, axial, radial and circumferential velocities in water are shown in figure 3.6 (a), (b), (c) and (d) respectively. Compared to 13 mm height, for 20 mm height, there is a significant

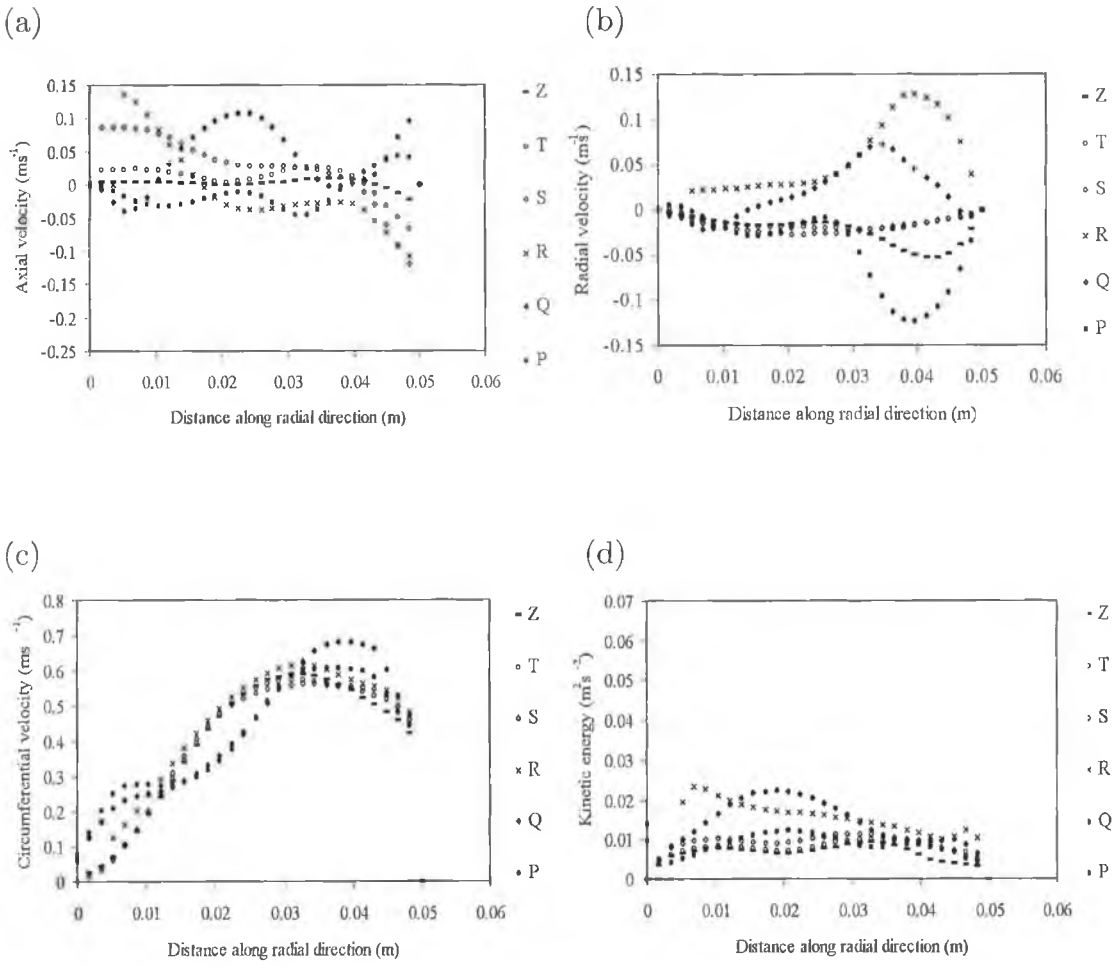

Figure 3.5: (a) Axial velocity, (b) radial velocity, (c) circumferential velocity and (d) kinetic energy distribution in water of viscosity 1 mPas for a stirring speed of 300 rpm and with the base of the impeller 13 mm off the base of the vessel.

axial, radial velocity at position Z. At position R, circumferential velocity is maximum. The circumferential velocities in the rest of the positions are dissimilar with pattern and magnitude. It is very interesting to note that for the same rotational speed with only variation of height in figure 3.5, there is a significant increase in kinetic energy. Values at kinetic energy at position R, for 13 mm height it was found to be 0.025 m^2 s^{-2} and for 20 mm height it was found to be 0.04 m^2 s^{-2}. It should be noted here that for 20 mm height at position R was found to be the higher kinetic energy because of the impeller position.

At 26 mm height of the impeller in the liquid height, axial, radial and circumferential velocity and kinetic energy distribution in water are shown in figure 3.7 (a), (b), (c) and (d). It is important to note that for 26 mm height of the impeller all the values of axial, radial and circumferential velocity, kinetic energy (figure 3.7) and dissipation rate at position P was found to be zero. So,

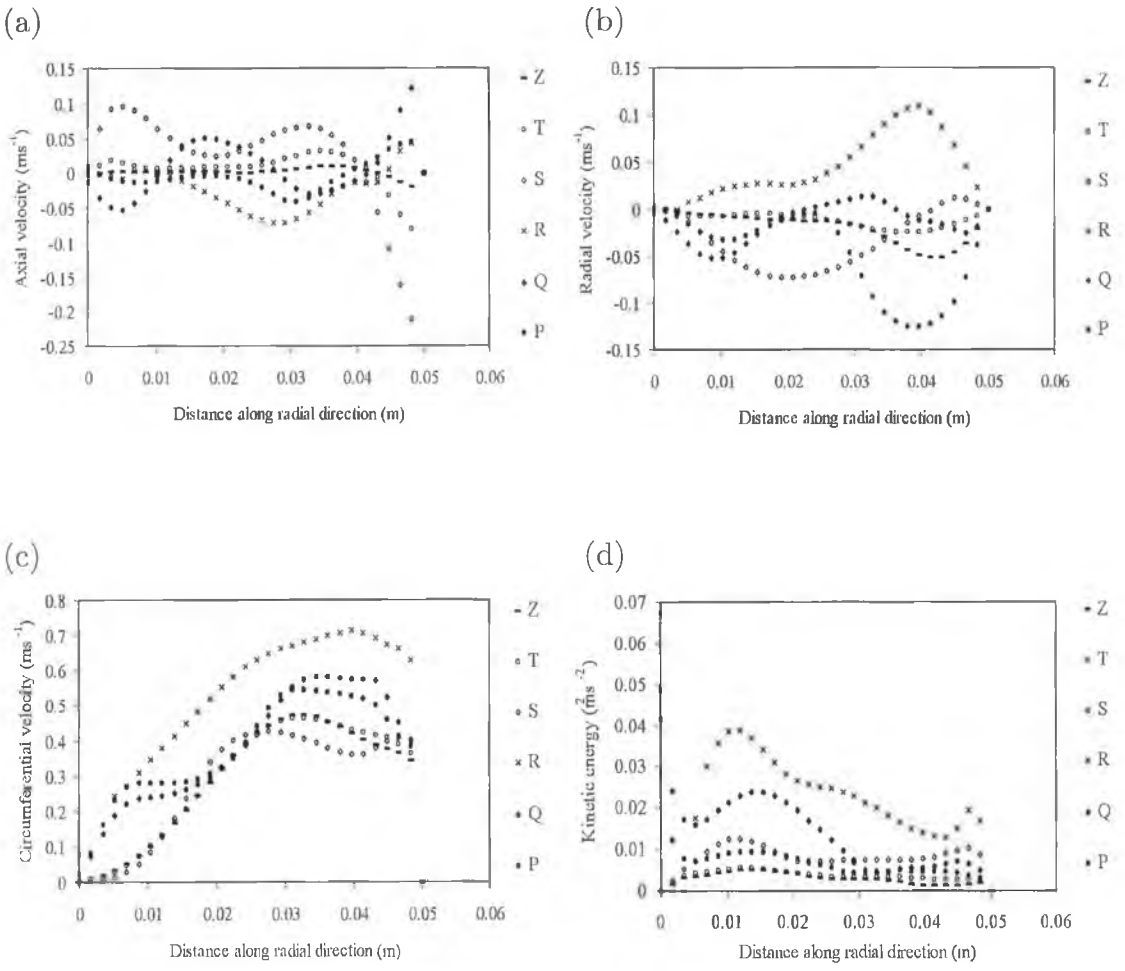

Figure 3.6: (a) Axial velocity, (b) radial velocity, (c) circumferential velocity and (e) kinetic energy distribution in water of viscosity 1 mPas for a stirring speed of 300 rpm and with the base of the impeller 20 mm off the base of the vessel.

it is impossible to disperse SiC from the bottom of the crucible when impeller is in a position of 26 mm height of the liquid. For 20 mm height, there was a wide range of axial velocity distribution than 13 mm height position. It is important to note that for 26 mm height, there was no velocity distribution at the bottom of the crucible. So, 26 mm height is not suitable for a stirrer position to up lift SiC particles from the bottom of the crucible. The radial velocity distribution at position P, R is same for both 20 mm and 26 mm height. The significant difference in radial velocity was noticed at position S and T. For 20 mm height radial velocity are almost zero at S and T. For 13 mm height, there was noticeable velocity distribution still found at that position. For 26 mm height, at position P, there was no velocity which was completely undesirable.

Effect of stirrer height on the velocity distribution at 300 rpm in glycerol/water solution was much more prominent than in water. It was noted that the model for

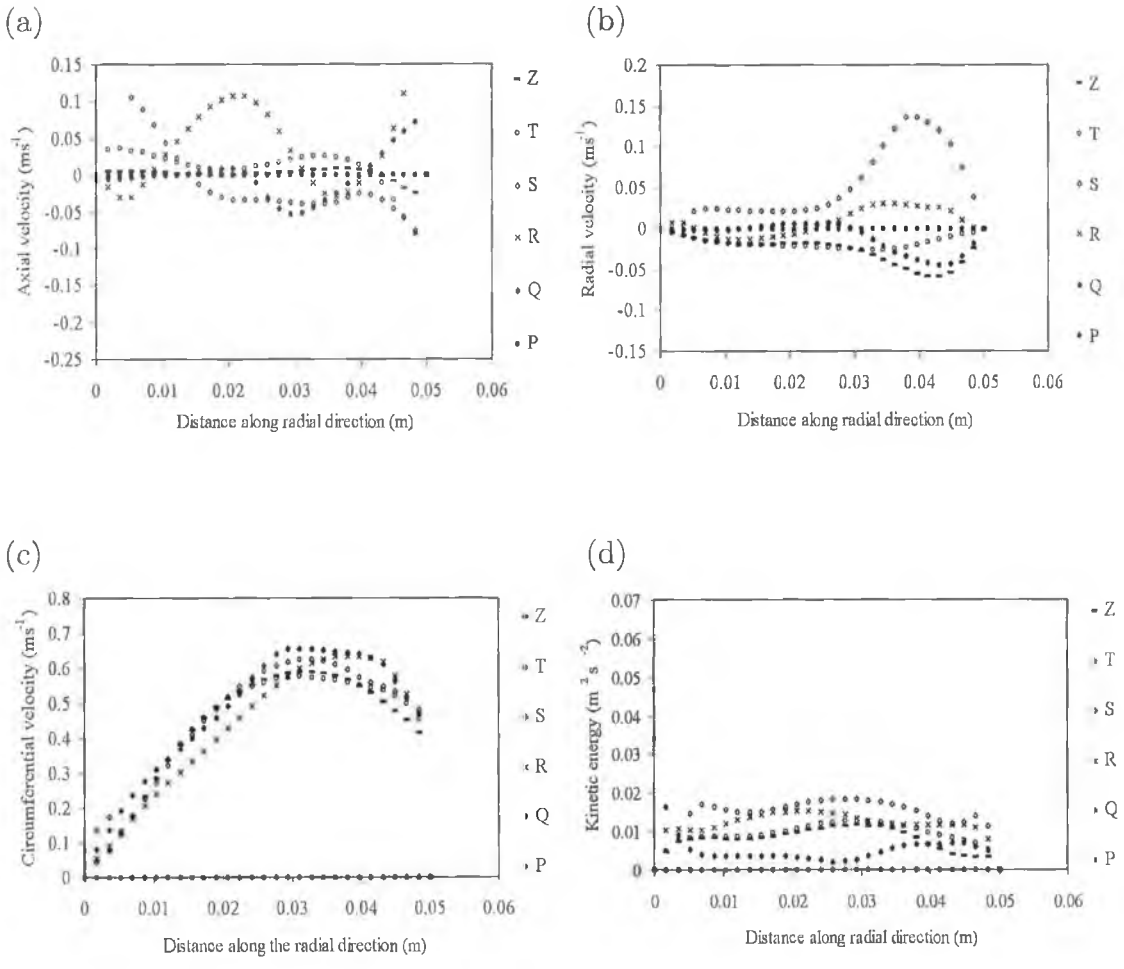

Figure 3.7: (a) Axial velocity, (b) radial velocity, (c) circumferential velocity and (e) kinetic energy distribution in water of viscosity 1 mPas for a stirring speed of 300 rpm and with the base of the impeller 26 mm off the base of the vessel.

glycerol/water at 300 rpm, was laminar. So, the velocity profile were steadier in these modelings. Axial velocity distribution in glycerol/water solution of viscosity 300 mPas at 300 rpm rotational speeds for 13 mm height of the impeller from the bottom of the crucible is shown in figure 3.8 (a). In this case at position Z, the axial velocity was almost zero. The velocity patterns at position T and Z were with similar pattern with different magnitude. The maximum axial velocities were found for position S is both with positive and negative values of 0.15 and -0.15 m s^{-1}. Radial velocity distribution in glycerol/water solution of viscosity 300 mPas at 300 rpm rotational speeds for 13 mm height of the impeller from the bottom of the crucible is shown in figure 3.8 (b). For position R, the radial velocity was found to be with positive values and for other positions, it was found to be a negative values. Circumferential velocity distribution in glycerol/water solution of viscosity 300 mPas at 300 rpm rotational speeds for 13 mm height

of the impeller from the bottom of the crucible is shown in figure 3.8 (c). For position Z, circumferential velocities were found to be with minimum magnitude. In all of the other cases, stirrer was positioned in between positions of Q and R. Axial, radial and circumferential velocity distribution in glycerol water solution of 300 mPas viscosity for 20 mm height of the base of the crucible are shown in figure 3.9 (a), (b) and (c) respectively. Axial, radial and circumferential velocity distribution in glycerol water solution of 300 mPas viscosity for 26 mm height of the base of the crucible are shown in figure 3.10 (a), (b) and (c) respectively. From these above mentioned figure of 3.10 (a), (b) and (c), it is clear that for 26 mm height of the stirrer there are no flow parameters at position P.

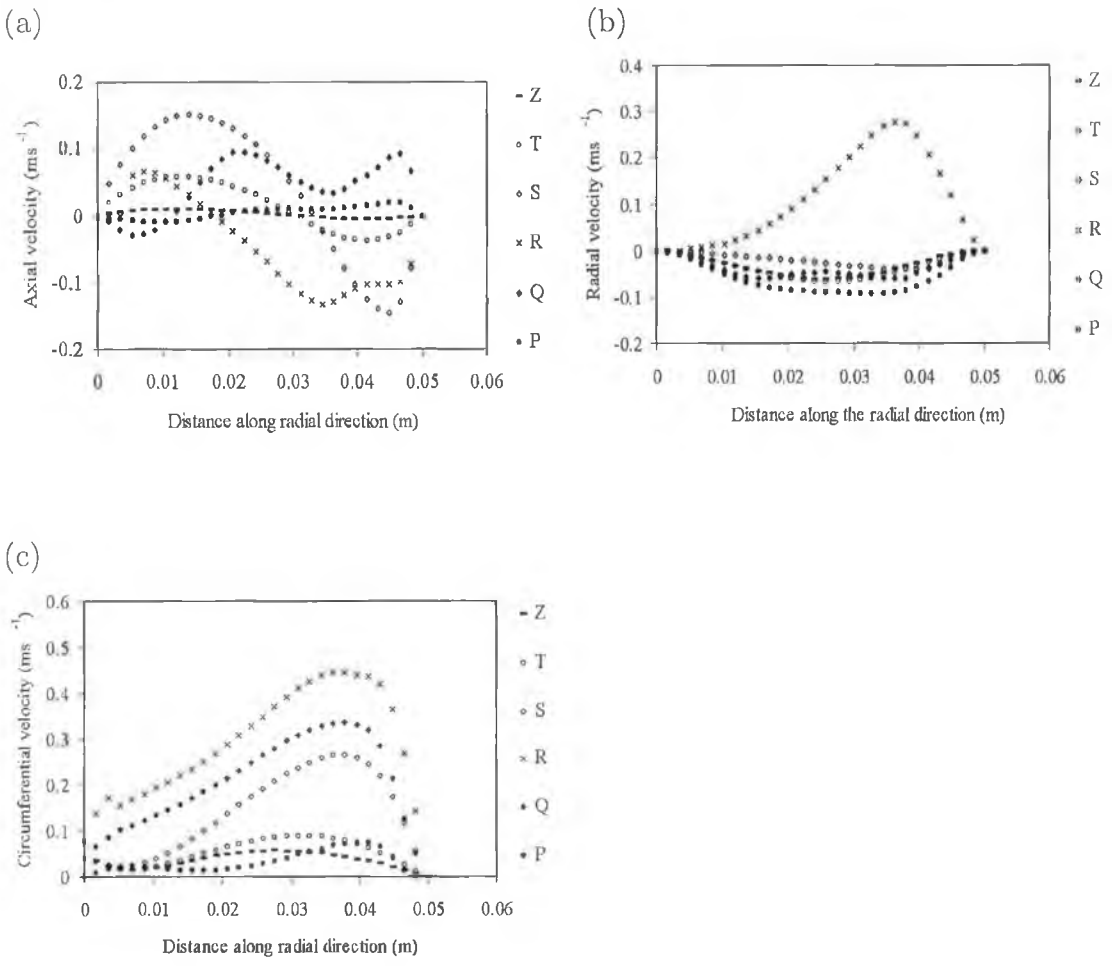

Figure 3.8: (a) Axial velocity, (b) radial velocity and (c) circumferential velocity in glycerol/water solution of viscosity of 300 mPas for a stirring speed of 300 rpm and with the base of the impeller 13 mm off the base of the vessel.

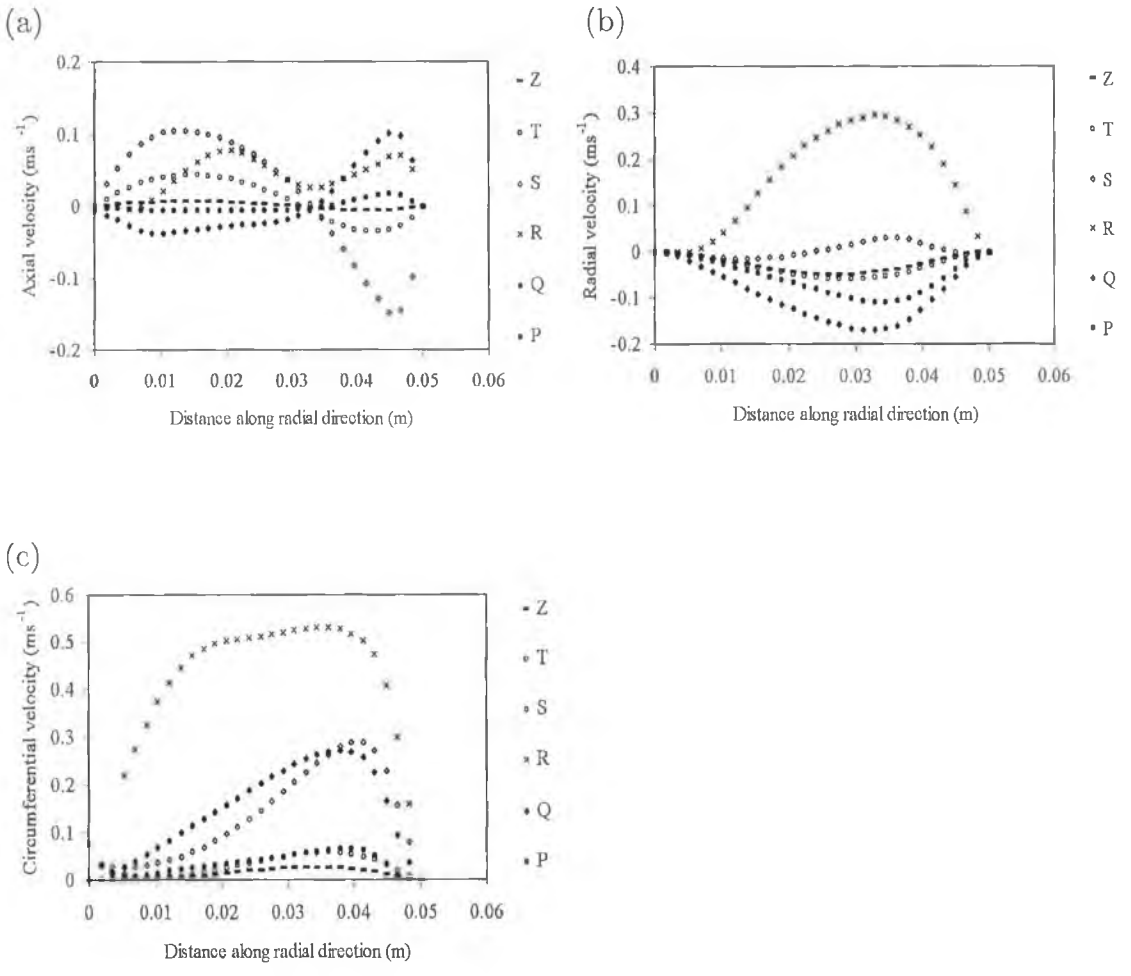

Figure 3.9: (a) Axial velocity, (b) radial velocity and (c) circumferential velocity in glycerol/water solution of viscosity of 300 mPas for a stirring speed of 300 rpm and with the base of the impeller 20 mm off the base of the vessel.

3.2.3 Stirrer diameter

Axial velocity distribution for different stirrer diameter are shown in Figure 3.11 (a). From this figure it is clear that for 60 and 70 mm diameter impeller, the axial velocity distribution was very wide and with maximum magnitude. Radial velocity distribution for different stirrer diameter are shown in Figure 3.11 (b). From this figure it is clear that 50 mm diameter stirrer gave the lower radial velocity. 80 and 90 mm diameter impellers gave the medium velocity and 60 mm and 70 mm stirrer gave the maximum radial velocity distribution with a magnitude of 0.18 m s^{-1}. Circumferential velocity distribution for different stirrer diameter are shown in Figure 3.11 (c). With increasing stirrer diameter, the circumferential velocity was responsible for swirl and higher vortex. 50 mm diameter gave the lower circumferential velocity and 60 mm and 70 mm diameter stirrer gave in-between results. All these results were only for position R.

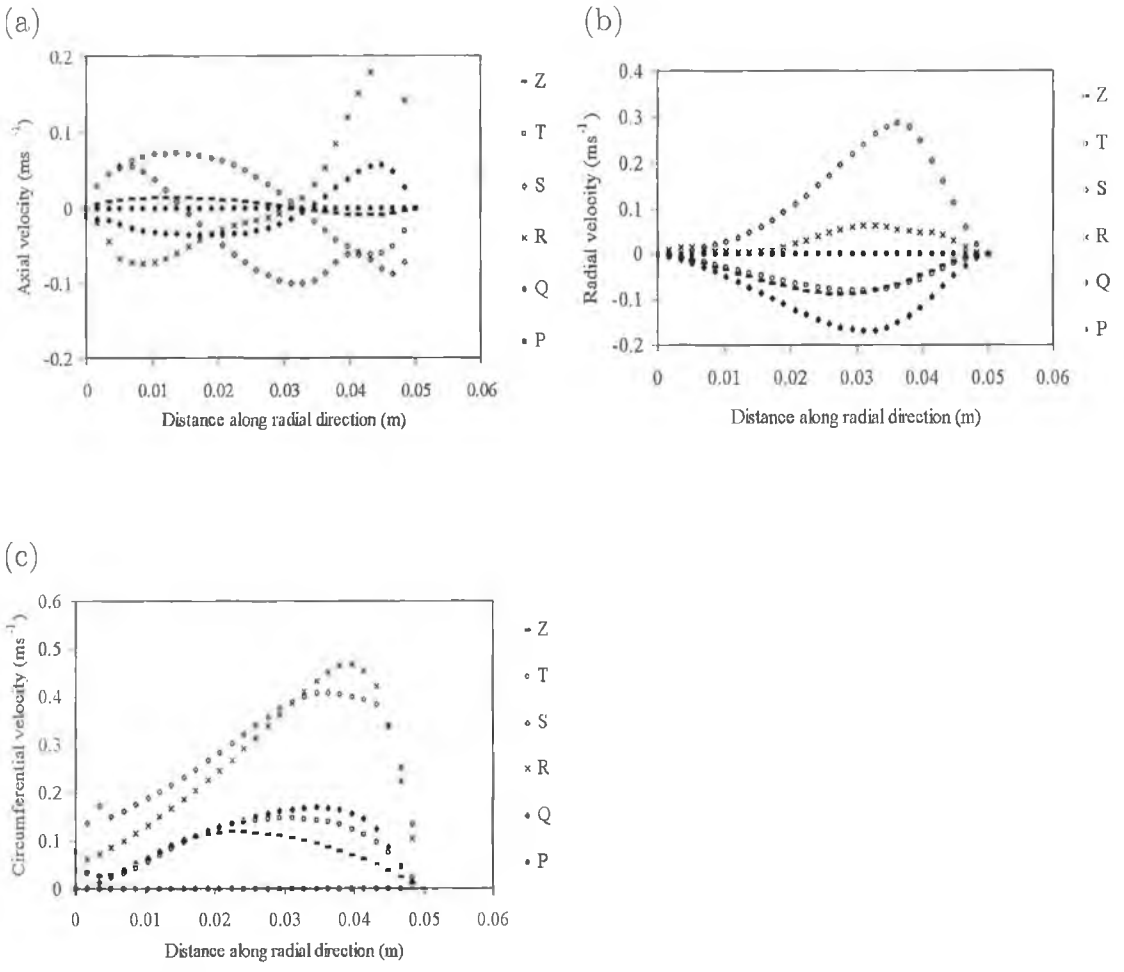

Figure 3.10: (a) Axial velocity, (b) radial velocity and (c) circumferential velocity in glycerol/water solution of viscosity of 300 mPas for a stirring speed of 300 rpm and with the base of the impeller 26 mm off the base of the vessel.

3.3 Model dispersion results

3.3.1 Stirring velocity

In analysis of the results of the dispersion experiments 10 % vol. of SiC was initially positioned at the base of the crucible. The time taken to obtain a stable uniform dispersion of SiC particulate in the crucible was termed and noted as the dispersion time. For the uniform dispersion to occur, the agitator has to rotate at a speed that is great enough for the solid material to be kept in suspension rather than accumulate at the bottom of the crucible. The base of the stirrer was 20 mm off the base of the crucible. Stirring speeds from 50 to 300 rpm and from 200 to 500 rpm were investigated for the water and the glycerol/water systems respectively. Some results are presented in Table 3.1 and Table 3.2. For data presented the stirrer height in both cases was 20 mm from the base of the crucible.

Above 300 rpm the vortex created in the water system was excessively high

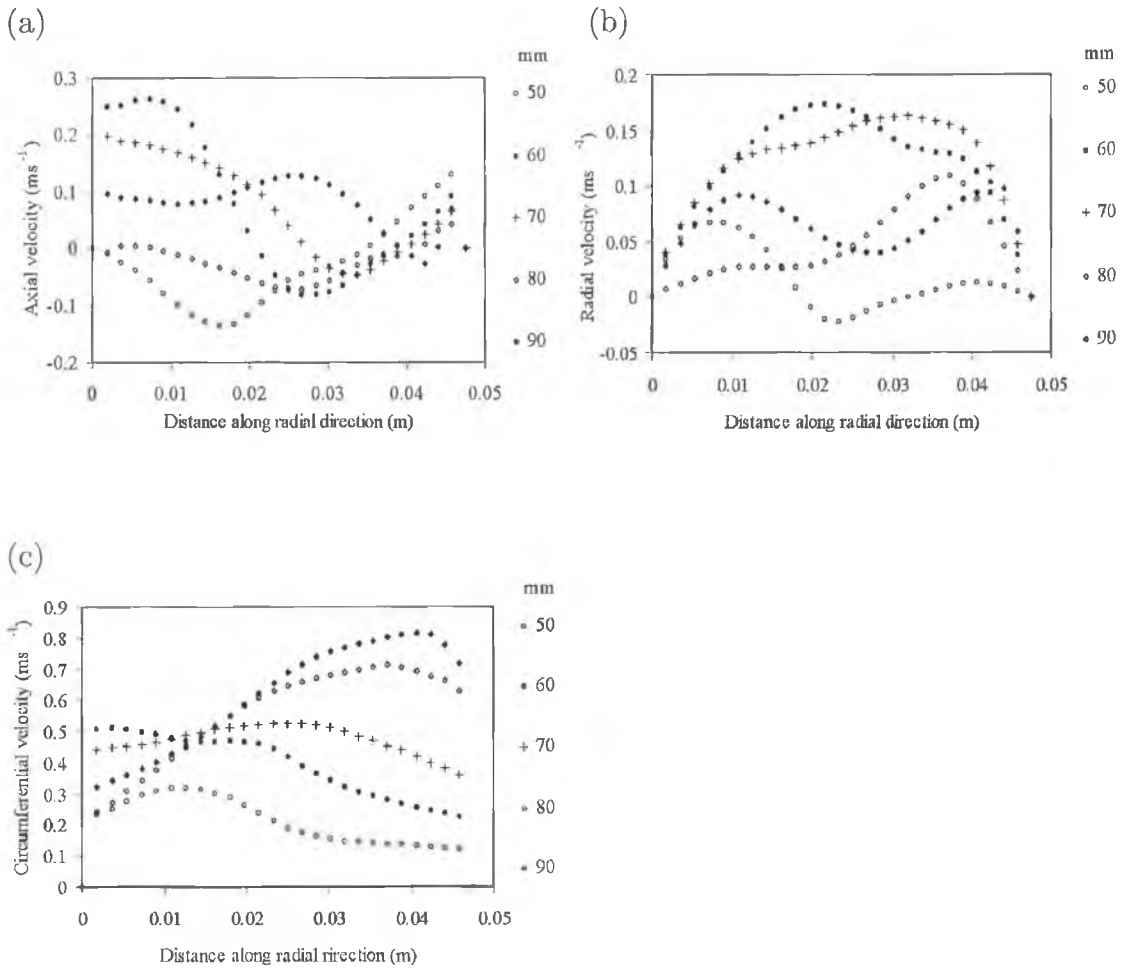

Figure 3.11: (a) Axial velocity, (b) radial velocity and (c) circumferential velocity in water of viscosity of 1 mPas for a stirring speed of 300 rpm and with the base of the impeller 20 mm off the base of the vessel.

and speeds below 200 rpm the dispersion times were too long in the glycerol/water system. Due to the higher viscosity of this system. In addition, no solution convergence could be obtained in the computer simulation of the glycerol/water system at speeds below 200 rpm. At 50 rpm no dispersion was detected in any of the models or in the visualisation tests. Rapid solution divergence was detected in these models.

The steady state fraction of SiC results at the various stirring speeds and locations in the crucible, is presented in figure 3.12 and 3.13. Figure 3.12 (a) to 3.12 (e) present the fraction of SiC results versus the radial distance from the central axis of the crucible for the water system. The key on the left of the graphs P, Q, S, T indicates the height at which the radial fraction of SiC was computed. Figures 3.13 (a) and 3.13 (e) represent similar results but for the glycerol/water system.

From figure 3.12 (a) and (b), it is can be seen that approximately 0.22 and

Table 3.1: Uniform dispersion time for 10 % SiC particles for different stirring speeds in water of viscosity 1 mPas. Stirrer height was 20 mm from the base of the beaker.

Stirring speed (rpm)	Uniform dispersion time (s)
100	170
150	28
200	16
250	15
300	14

Table 3.2: Uniform dispersion time for 10 % SiC particles for different stirring speeds in glycerol/water solution of viscosity 300 mPas. Stirrer height was 20 mm from the base of the beaker.

Stirring speed (rpm)	Uniform dispersion time (s)
200	2335
250	1700
300	1030
400	720
500	540

0.16 fraction of SiC remains near the base of the crucible (P), under the stirrer position. From figure 3.12 (c), (d) and (e) it can be seen that at stirring speeds of 200 rpm and above a very uniform fraction of SiC is present throughout the crucible. The rest uniform fraction of SiC (approximately 10 %) was obtained, as expected, at the highest stirring speed of 300 rpm, see figure 3.12 (c).

Sedimentation of the SiC can be seen in the glycerol/water system at the base of the crucible (position P), see figure 3.13 (a) and (b). This sedimentation occurred mainly in the center and at the outer wall of the crucible. At stirring speeds of 300 rpm (figure 3.13 (c)), 400 rpm (figure 3.13 (d)) and 500 rpm (figure 3.13 (e)), a very uniform fraction of SiC was noted throughout the crucible.

3.3.2 Stirring period

To investigate the effect of agitation period, a vertical plane was taken through the fluid at a distance of 8.5 mm from the outer wall. The fraction of SiC along this plane at an agitation speed of 300 rpm is shown in figure 3.14.

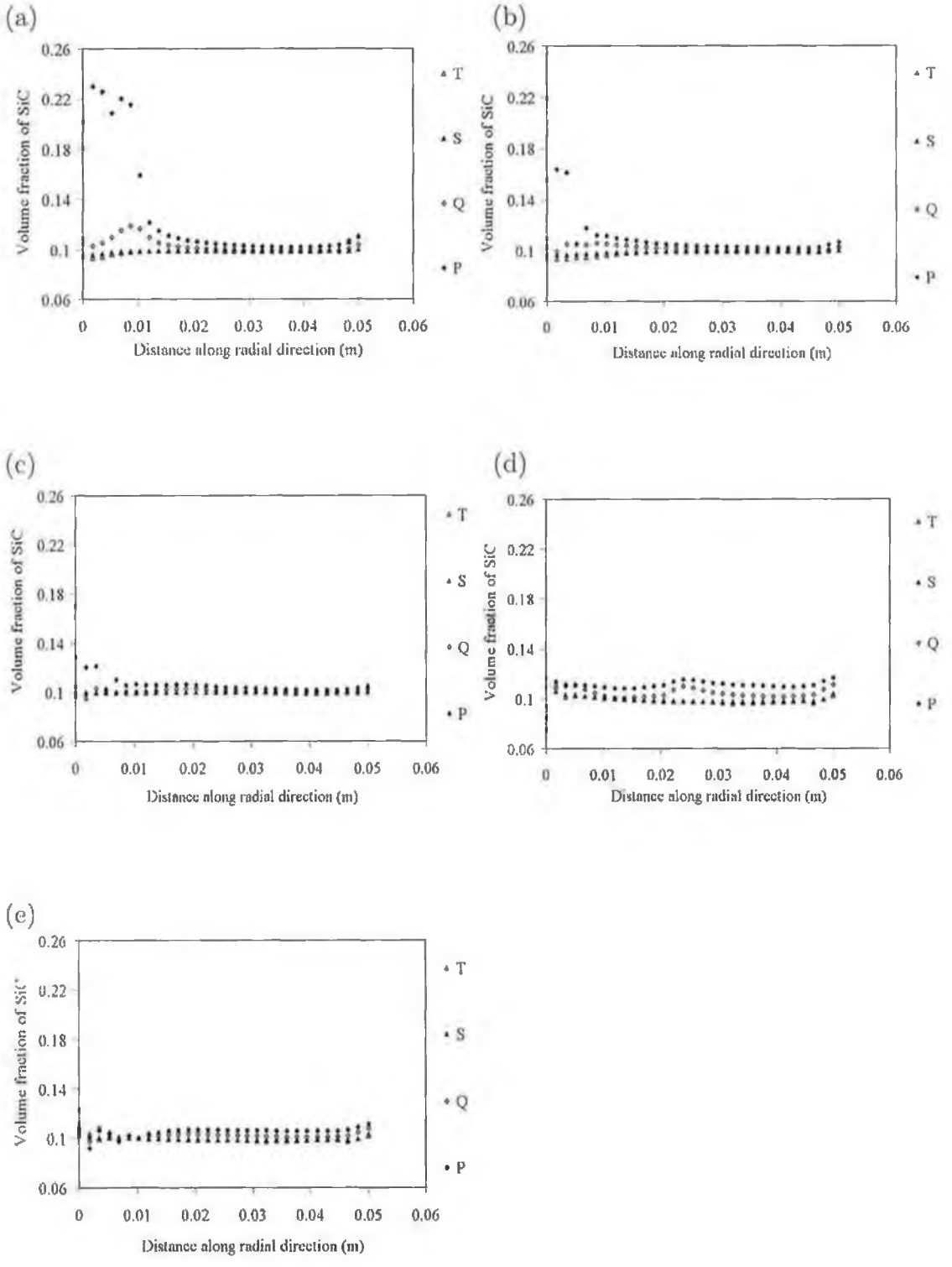

Figure 3.12: Steady state distribution of SiC in water for stirring speed of (a) 100 rpm (b) 150 rpm (c) 200 rpm (d) 250 rpm and (e) 300 rpm. Stirrer height was 20 mm from the base of the beaker.

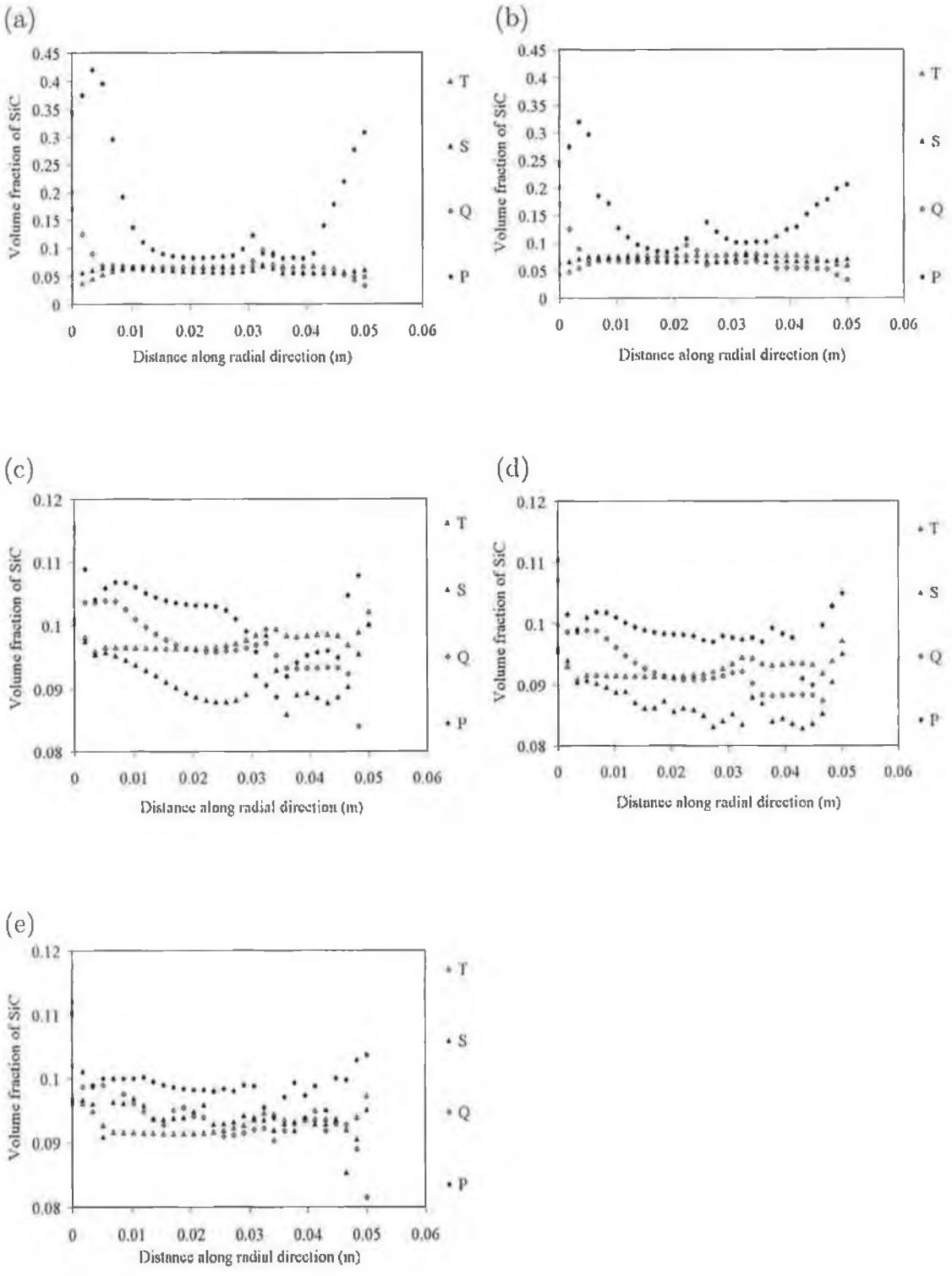

Figure 3.13: Steady state distribution of SiC in glycerol/water for stirring speed of (a) 200 rpm (b) 250 rpm (c) 300 rpm (d) 400 rpm and (e) 500 rpm. Stirrer height was 20 mm from the base of the beaker.

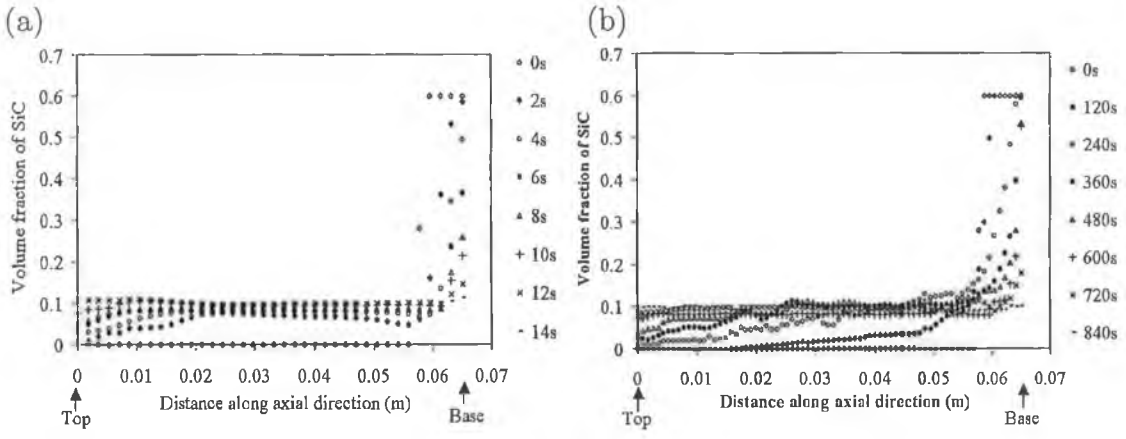

Figure 3.14: Volume fraction of SiC particles as a function of axial distance along the crucible at different times during settling in (a) water and (b) glycerol/water system. The legend on the left of these graphs represents the time after commencement of agitation.

A fast dispersion rate can be seen for the water system, figure 3.14 (a). Even after just 2 seconds, a significant amount of SiC was found along the vertical fluid section. After 14 seconds in this system a relatively uniform SiC distribution along the section can be seen. In contrast, a relatively uneven distribution of SiC is present even after 480 seconds in the glycerol/water system at this agitation speed, see figure 3.14 (b). It is not until 840 seconds have past that a relatively uniform distribution of approximately 10 % SiC is present along the vertical section.

3.4 Model settling results

The model was used to investigate the time taken for the uniformly dispersed SiC particles to settle to the bottom of the crucible when stirring was halted. This was done for both water and the glycerol/water mixture. A significant difference emerged. Settling was predicted to be much faster in water than in the glycerol/water mixture (60 sec as compared to 3,600 sec). This relationship is expected from the higher viscosity of glycerol/water.

3.4.1 Settling in water

From figure 3.15 to 3.17 detailed settling fractions of SiC results presented at position P, Q, S and T for various settling periods. Figures 3.15 (a) to (d) present the settling fractions of SiC for the water system. In all the settling simulations

the model was commenced with a uniform distribution of 10 % SiC particulate throughout the fluid. From these graphs it can be seen that settling commenced rapidly in the water system and almost complete settling occurred after 60 seconds.

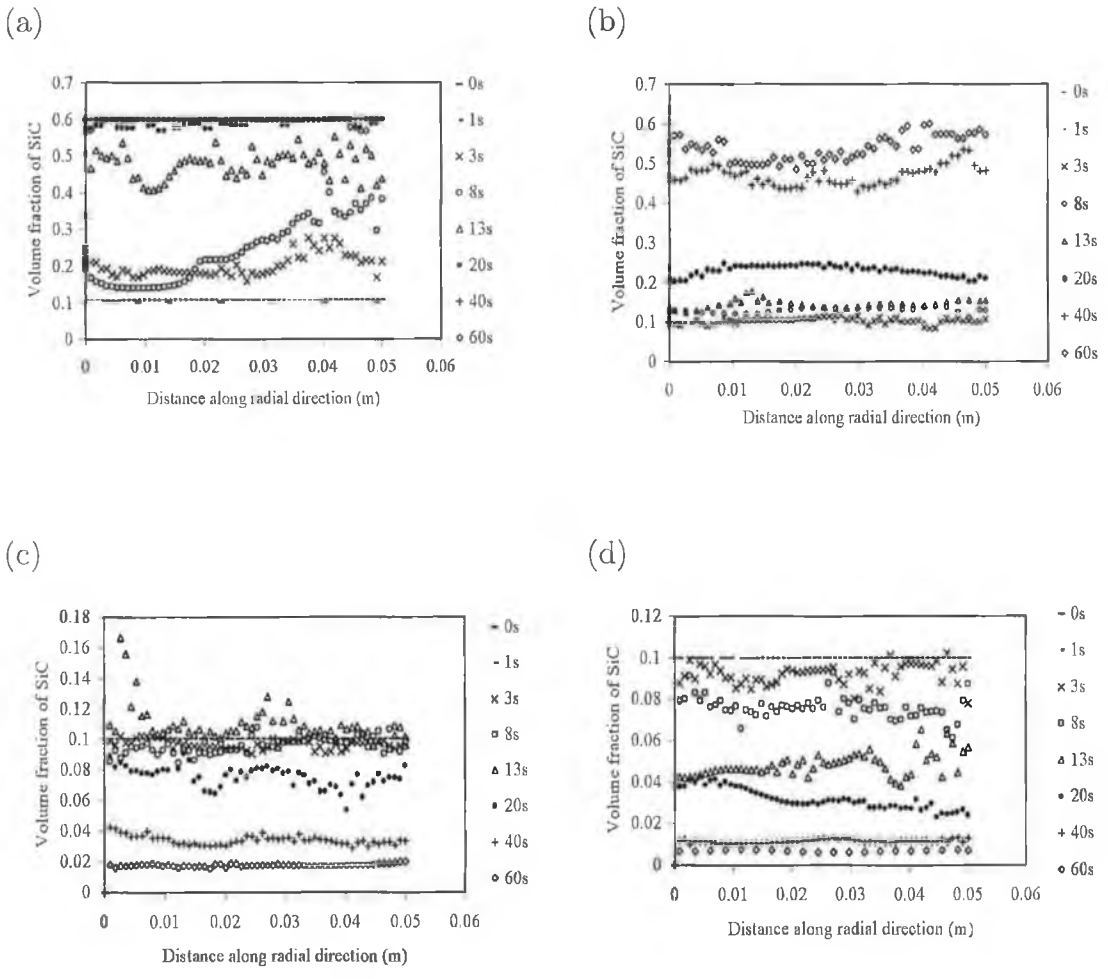

Figure 3.15: Volume fraction of SiC particles as a function of radial distance along the crucible in water at position (a) P, (b) Q, (c) S and (d) T.

In water the model predicts very rapid initial settling of most of the particles, followed by slower settling of remaining particles. Figure 3.16 (a) illustrates the volume distribution of particles during settling in water. The random distribution of particle concentration is evident in this figure. Some more color Fluent graphics can be seen in Appendix B.

3.4.2 Settling in glycerol

Figures 3.17 (a) to (d) present the settling fractions of SiC for glycerol/water system. From these figures it is clear that no appreciable settling occurs after 120

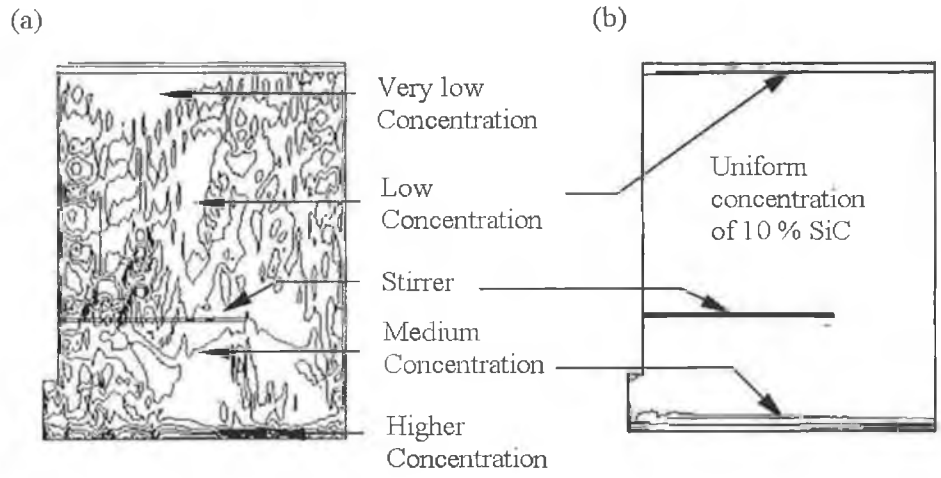

Figure 3.16: Settling pattern of SiC particles (a) in water after 1.5 s and (b) in glycerol/water after 40 s.

seconds and only a small amount of sedimentation was present after 3020 seconds. Appreciable settling was noticeable after 3920 seconds. The present work focused to analysis the possible processing times, the simulation was stopped after 3920 seconds. In the visualisation experiments complete settling took 20 days. With the glycerol/water predictions where little or no settling occurs for quite a while, followed by a period of relatively fast settling. In glycerol/water mixture particle distribution during settling is also more uniform than in water (figure 3.16 (b)). Some more color Fluent graphics can be seen in Appendix B. It is clear from figure 3.17 that after 2120 s, the volume fraction of SiC is still constant and there is no significant settling. After 3020 s, there is a clear sedimentation at the bottom of the crucible. After 4120 s, the volume fraction of SiC at the bottom of the crucible was 0.6. So significant settling was observed after this time.

Figure 3.18 (a) and (b) represent the settling fractions of SiC along a vertical plane in the fluid 8.5 mm from the outer wall in the water and glycerol/water system respectively. The legend along the left of these graphs represents the time since the settling commenced. Settling again can be seen to commence immediately in the water system and approach a almost complete settling after 60 seconds. The theoretical maximum packing fraction of solid spheres is evident at the base at this time.

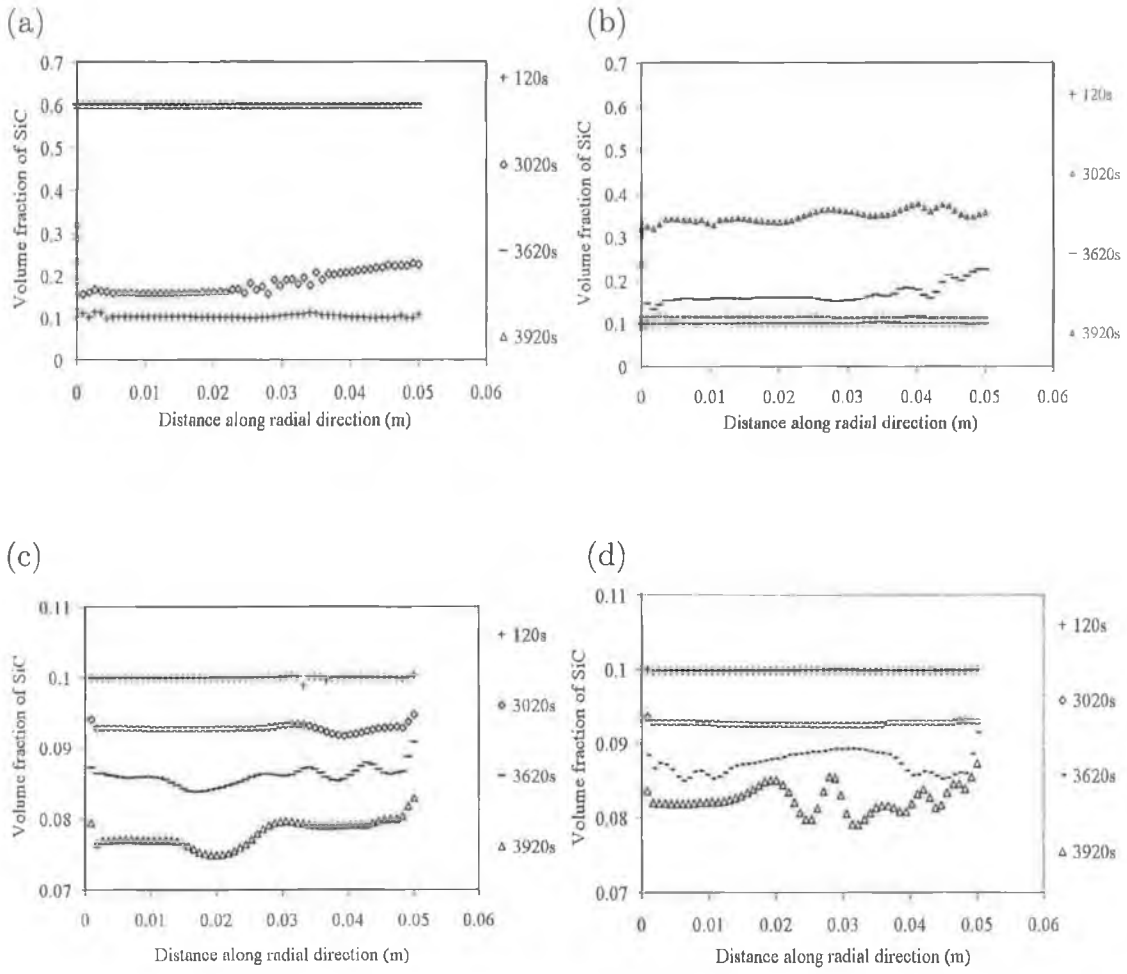

Figure 3.17: Volume fraction of settled SiC as a function of radial distance along the crucible in glycerol/water at position (a) P, (b) Q, (c) S and (d) T.

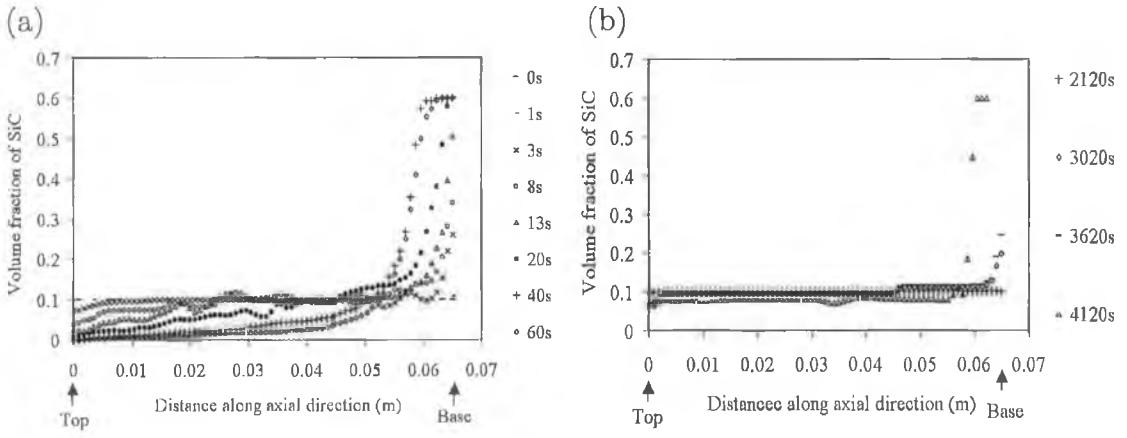

Figure 3.18: Volume fraction of settled SiC particles as a function of axial distance along the crucible at different times during settling in (a) water and (b) glycerol/water system.

Chapter 4

Stir-casting validation experiments

4.1 Experimental equipment

In this study, a new quick quenched compocasting method was used to fabricate MMC ingot. This device was redesigned around a previously compocaster used by Hashim et al. [242] where the rig had a bottom pouring unit to facilitate the casting. Bottom pouring prevented impurities from being entrapped which instead floated on the top of the melt. The stirrer was connected to a DC motor which was used to stir the molten matrix material. A temperature controlled resistance heating element was placed around the crucible unit. In order to minimise the heat loss during processing, two layers of 50 mm thick ceramic board insulation was placed around the heater band. A graphite crucible was used in their work. The stopper and stirrer were made of steel because graphite was too brittle and was not strong enough to mix the composite slurry, particularly at high speed.

This rig that was used in this work for the initial compocasting trials was altered to allow the steel crucible to be quickly lowered beneath the furnace. The crucible could then be placed directly in a quench tank in an attempt to trap and allow analysis of the SiC distribution. The overall design and operation of this commissioned rig is described in the subsequent paragraphs.

4.1.1 Design overview

The constructed stir-caster, used in this work is schematically illustrated in figure 4.1. A more detailed engineering drawing of the stir-caster may be found in appendix C. The stir-caster furnace was mounted on four legs. This in turn was attached to a welded steel table. A screw driven actuator lift was bolted vertically under the table. The crucible was mounted on a ceramic spacer which is in

turn attached to the actuator. This arrangement allowed rapid extraction of the crucible from the furnace. The top plate of the actuator rotated as it descended. A free rotational bearing on top of this plate prevented rotation of the crucible.

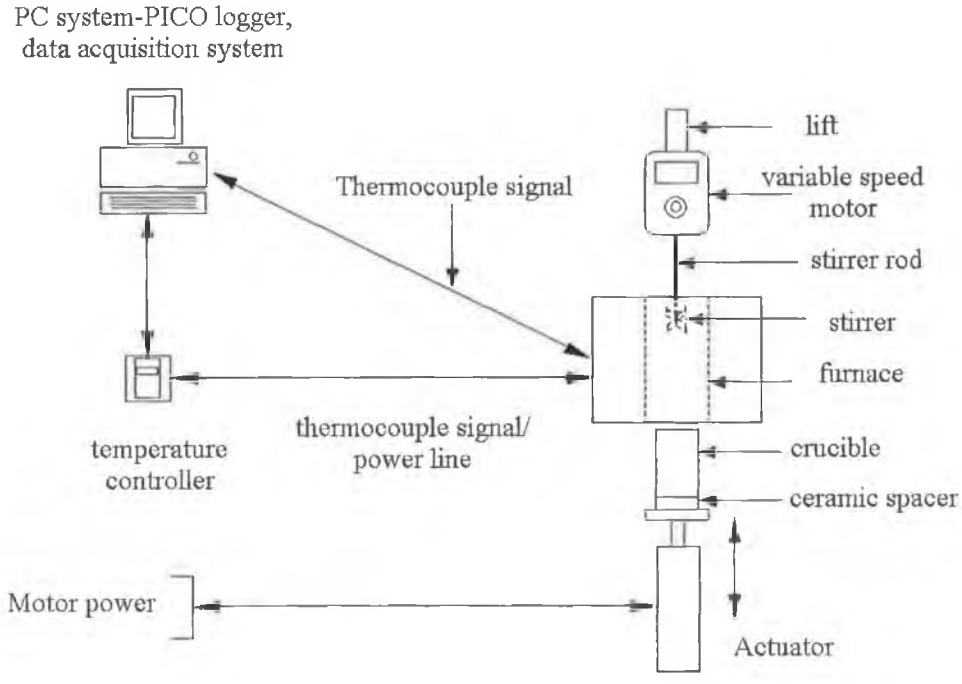

Figure 4.1: Schematic of constructed stir-caster.

4.1.2 Furnace

The temperature within the stir-caster had to be precisely measured and accurately controlled (1 °C), in order to control the fraction solid of the semi-solid alloy. One calibrated K type mineral insulated thermocouple provided the control inputs to a Eurotherm 2216 PID temperature controller. A temperature range of 100°C from the bottom to the top of the crucible was present in the charged crucible. A more detail temperature profiling of the furnace experiment can be found in Appendix D. These profiles enabled the melt temperature to be controlled by inserting a control thermocouple placing 170 mm from the top plate of the furnace.

4.1.3 Data acquisition and control system

PICO^{TM} software with thermocouple data logger facilities was used to read the temperature and display it on a computer monitor. Another thermocouple was connected to the PICO data logger system. The temperature inside the crucible could then be displayed and recorded against time. A sampling rate of one reading per second was used.

4.1.4 Crucible

Stainless steel (Ovar Supreme^{TM}, Uddeholm) was chosen for crucible material. This material would resist corrosion with a suitable (boron nitride) oil coating, not contaminate the melt, and has a high thermal shock resistance and strength. This coating also provide facility for easy removal of the MMC production from the crucible. This is a common tool material for the die casting of aluminium. The crucible material would also allow the melt to be quickly quenched. Here, the crucible is acting as a chill mould. Dimensions of the crucible were chosen so that they corresponded to the visualisation and computational tests. The crucible used in these MMC production tests was scaled down by a factor of 0.6 from the visualisation and simulation tests, in order to fit in the furnace.

4.1.5 Rotational drive unit

During experimental work, a four flat bladed stirrer was chosen as it was found from the visualisation test that the turbine blade stirrer introduced more air to the melt and may result more porosity in the final castings. Another consideration was the difficulty of fabricating the turbine. The stirrer had to be chosen of a suitable material such that it would resist corrosion, not contaminate the melt, and have a low moment of inertia, and a high thermal shock resistance and strength. Ovar Supreme was again used for the stirrer rod and impeller. The stirrer was designed to help uniformly disperse the SiC particulate throughout the melt. Dimensions of the stirrer were also chosen so that they corresponded to the visualisation tests. The stirrer and crucible used in these MMC production tests was scaled down by a factor of 0.6 from the visualisation and simulation tests, in order to fit in the furnace. Full hydrodynamic similarity can not be achieved in geometrically similar scaled up vessels [243]. This suggests that the hydrodynamic regime for attainment of a given suspension speed would be vessel size dependent. A four bladed 60 degree angle stirrer was made for this purpose. A uniformly thin coating of boron nitride was introduce with the stirrer to avoid contamination of iron in to the melt and to prevent corrosion of the stirrer materials. The stirrer was connected to a DC motor which was used to stir the molten matrix material.

4.1.6 Rack and pinion mounted stirring motor

A lifting mechanism for the rotational drive unit, stirrer assembly was used to extract the stirrer from the melt before quenching of the melt and to facilitate the stirrer positioning, cleaning and replacement. A stroke length of 240 mm was used in this lifting mechanism.

4.1.7 Crucible actuator

A Servomech acme thread linear actuator ATL101 was purchased from Lenz for the lifting mechanism. This required a 70W, 24V power supply and was capable of 0.22 Nm and a linear speed of 93 mm s^{-1}. The actuator had a total stroke length of 273 mm. The crucible dropped 270 mm in total during the experimental operation.

4.2 Investigated materials

A356 alloy and alpha silicon carbide were chosen for experimental testing in this work. A356 aluminium ingots were purchased from P.J. Carney Ltd., Crossakeil, Kells, Co. Meath, Ireland. Certificates of composition were supplied for the A356 ingots purchased. The composition of the A356 aluminium ingots can be seen in Table 4.1. A356 was used as it provided clear microstructural detail and is of great commercial interest. A356 was also highlighted by previous researchers as an alloy which could be easily stir cast [114, 202, 244, 245]. More recently, it has been shown that it is possible to successfully thixoform A356 alloy [23, 246]. The synthesis of the MMCs used in the present study was carried out according to the following procedure. The A356 matrix material was received in the form of 1.2 kg ingot. In order to fit into the crucible, the ingots were cut into smaller pieces of about 3-5 grams weight. Theoretically the A356 matrix alloy melts completely at about 614 °C.

Table 4.1: Composition of A356 aluminium alloy.

Alloy	Si	Cu	Mg	Fe	Mn	Ti	Ni	Zn	Pb	Sn	Al
A356	7.23	0.127	0.408	0.355	0.135	0.113	0.012	0.059	0.01	0.011	bal.

The Alpha silicon carbide used was of 320 mesh and was purchased from Elite Thermal System Ltd. (product number SCB-320). The composition of the purchased SiC was investigated by spark emission spectrometer. A typical composition of the silicon carbide can be seen in Table 4.2 and a typical size distribution curve for F320 SiC is shown in figure 4.2. The weighing of the matrix alloy and silicon carbide were carried out using an analytical balance with an accuracy of 0.01 grams. The amount of SiC particles used was 10 % SiC particulates, preheated to 900 °C for 4 hours. At volume percentage of SiC [135] particles higher than 10 % in the matrix alloy the wettability decreases and the agglomeration and settling tendencies increases. Therefore, 10% vol. percentage of SiC was chosen for the present research.

Table 4.2: Typical chemical analysis of SiC.

%SiC	% free C	% free SiO_2	% free Si	% free Fe_2O_3
99.1	0.1	0.4	0.2	0.06

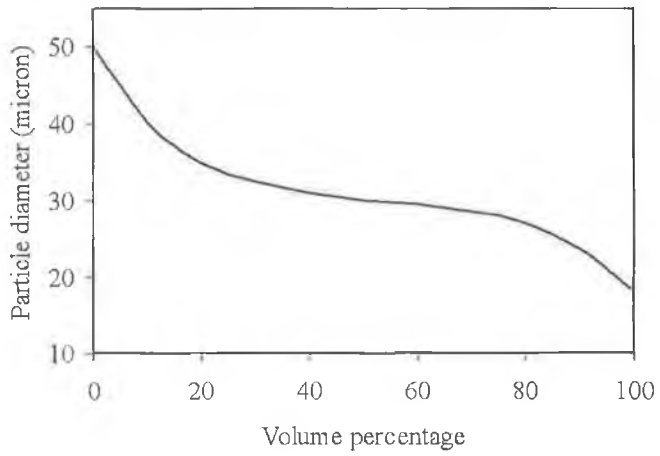

Figure 4.2: Typical size distribution curve for F320 SiC.

4.3 Stir-caster operation

When setting up the stir-caster before an experiment, the crucible was charged with aluminium and SiC particles. Then it was attached to the ceramic spacer on top of the actuator. A locking mechanism was engaged to ensure the height and lateral position of the crucible remained constant throughout the tests. The temperature was then raised to 630 °C to melt the charge. A continuous purge of nitrogen gas was used in order to minimize high temperature oxidation problems. When the metal was fully melted, the stirrer was lowered into the crucible and pushed into contact with a bearing pin at the base of the crucible. This ensured that the height of the stirrer off the base (12 mm) was consistent throughout the test and that it was held concentrically.

The charge temperature was raised to 630 °C within 130 minutes at the start of each experiment. The stirring was then started and continued for specified periods for the liquid state experiments. After the specified shearing periods the crucible was lowered and quenched. In the semi-solid experiments the stirring was again started at 630 °C and continued for five minutes to promote wettability. Stirring was then stopped and the temperature was continuously lowered to 605 °C (0.30 fraction of solid), the stirring was recommenced. This corresponds to a viscosity of about 300 mPas in the semi-solid metal [247]. After shearing the alloy at a specified shear rate and for a specified length of time, the stirring was stopped,

the stirrer raised, the lock on the actuator released, and the crucible containing melt was lowered. The crucible was immediately lifted off the ceramic spacer with steel tongs and quenched into water.

All the experimental parameters are mentioned in the Table 4.3. A flow chart for the MMCs fabrication method is shown in figure 4.4. Time-temperature diagram for liquid and semi-solid state experiments as recorded from PICO logger for control T/C are shown in figure 4.3 (a) and (b) respectively.

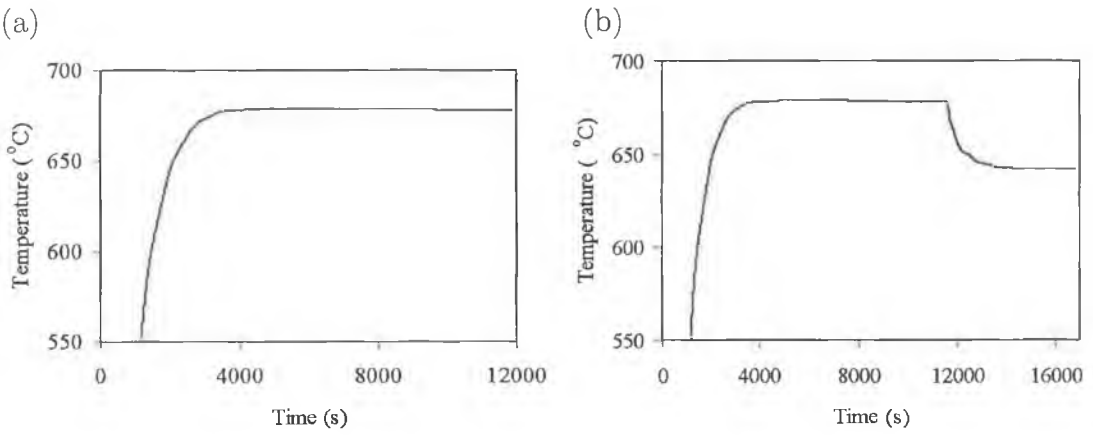

Figure 4.3: Time-temperature diagram for (a) liquid and (b) semi-solid processing, recorded by the control thermocouple.

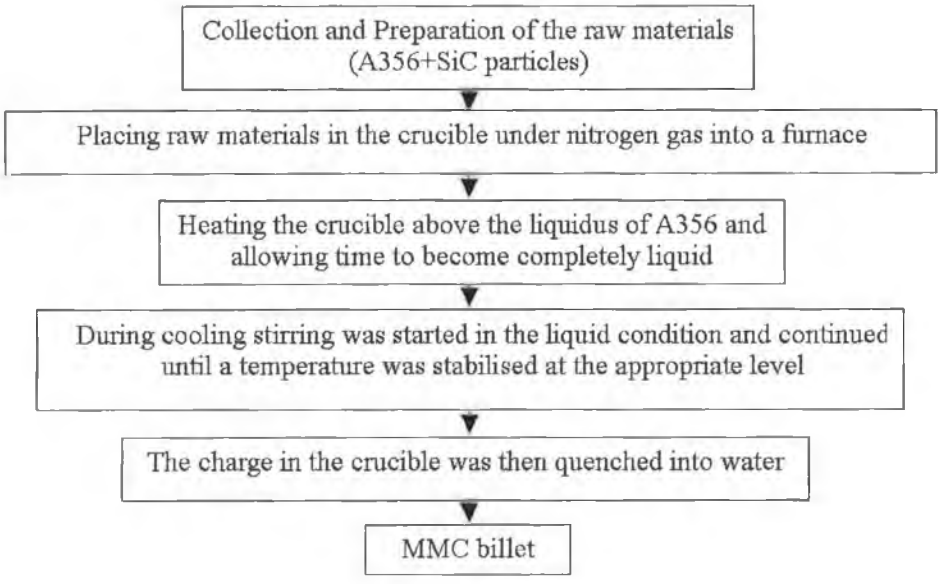

Figure 4.4: Flow chart used for the MMCs fabrication.

Table 4.3: The experimental parameters.

Experiment Number	Stirring speed (rpm)	Stirring time (s)	Approximate viscosity (mPas)
1	200	16	1
2	300	16	1
3	200	2335	300
4	200	1030	300
5	300	1030	300
6	300	540	300
7	500	540	300
8	500	120	300

4.4 Some cast MMCs product

Some casting photograph are shown in figure 4.5. In figure 4.5 (a), an impingement of four bladed stirrer is evident at the top surface of the semi-solid compocast product of experiment number five. The easy removal of the stirrer after processing bears the evidence of the semi solid state of the melt during quenching. In figure 4.5 (b), there are no stirrer impingement as this was processed in the liquid state, instead of that a solidification pipe is visible on the top. A very smooth external appearance was found for semi-solid product figure 4.5 (c), whereas a non-smooth surface was found for liquid products (figure 4.5 (d)). At the bottom of the liquid casting, the SiC settled position after removal of the casting at the bottom was evident.

4.5 Metallography

MMC ingots were cut into small pieces with a dimension of 250 mm diameter and 1 mm thick by Struers cut off machine to produce the samples for metallographic examinations. Oil coolant was used for avoiding any overheating of the ingot and the Struers HHH cutting wheel. Cutting materials may cause surface damage, such as pull-out of silicon carbide particles. During cutting, it is essential to reduce the damage of the surface to a minimum. To minimise this damage, a very low feeding speed and a high cutting speed with constant medium pressure were used.

Metallographic preparation of particle-reinforced MMC was quite a challenge,

as the reinforcement particles are very hard and fragile compared to the matrix materials. This combination of respectively hard and soft materials makes it difficult to avoid damages like cracks and broken reinforcement particles, and relief between the particles and the soft matrix during preparation. A Struers Prestopress-3 was used to mount the specimen. A Struers DAP-V grinding machine was used for the grinding and polishing operations. The objective of the plane grinding is to make the sample surface plane, whereas fine grinding must reduce the surface damage introduced by plane grinding to a level to make polishing possible. SiC paper is often used for grinding of metal, and this must be avoided when the MMC is reinforced with SiC particles. This is because the soft matrix will quickly be removed whereas the SiC particles will in general remain intact. Plane grinding was performed with a Struers TEXMET grinding disc with 30 mm diamond. This grinding was done manually and only very light pressure was applied. The plane grinding took about 5-10 minutes. This was followed by polishing using TEXMET grinding disc with 9, 6, 3 and 1 mm diamond suspended in water as a lubricant. Some scratches left were believed to be as a result of silicon carbide particle pull out during polishing. The optical microscope was attached to a digital camera and video printer which was capable of photograph printing and also to a PC for image capture and image analysis (IA). The prepared samples were viewed using a 'Reichert MeF2' metallurgical microscope

4.6 Image analysis

Liquid and semi-solid stir-cast microstructures were investigated by image analysis (IA) techniques to determine, the area percentage of SiC, SiC count, spherical diameter (μm), perimeter (μm), aspect ratio and sphericity. Analysis was performed on an Avent Pentium III computer using the Beuhler Omnimet Enterprise software. Cross section examination areas with a minimum size of 1.26 mm^2 were used to perform IA on each cast product. SiC particles that did not connect with neighbouring particles or porosity were analysed as 'isolated particles'. The equivalent average circular diameter (D) of isolated particles, for a given material type, was calculated from their average area (A) according to: $D=(4A/p)^{0.5}$, where, p was the particle perimeter. This is the diameter of a circular particle with the same area as the average area of the isolated particles. An edge detect image processing filter was used to approximate the total number of SiC. This included all SiC particles within agglomerates as well as unagglomerated isolated particles.

The area percentage of SiC was measurement as the area of a particular mi-

crostructure picture divided by the area of the SiC represented in that picture. This result is expressed as percentage. Count measurement gives the total number of SiC in the selected microstructure picture within the measurement frame. Spherical diameter is defined as the circular diameter, multiplied by 1.22474. This measurement gives the total equivalent spherical diameter of all the SiC in a microstructure picture of an image. Aspect ratio is the ratio of length and width of the SiC particles. The result is provided as a dimensionless number. Sphericity measures the sphericity of each SiC in a selected microstructure picture in a range of 0 to 1.0. If the shape of the particle is a perfect circle, the sphericity of this particle is 1. The more bumps a particle has, the lower sphericity value. The result is provided as a dimensionless number.

4.7 Results

4.7.1 Metallography

The microstructure of composites produced are presented in figure 4.6 to figure 4.9. These microstructures were obtained from the compocasting performed according to the processing variables outlined in Table 4.3. Micrographs from the liquid state castings are shown in figure 4.6 and those from the semi-solid state castings are in figures 4.7 to 4.9. A range of SiC distribution was observed in these microstructures depending upon the chosen compocasting state and parameters. A quick quenched small dendritic primary aluminium phase was observed in liquid state process and a larger primary Aluminium phase was observed for semi-solid state processing. These micrographs represent typical examination areas used for IA of the alloys. Microstructural analysis from the metallographic samples of experiments one and two, it was found that there was only small sized and volume fraction of SiC is presents. During metallographic examination of the sample from experiment one, there were too many gas porosity observed all through the specimen in all places over top, middle and bottom parts. Some small particles were also surrounded by the air holes. This type of phenomena was more prominent at the top part of the specimen. It is believed to be the flocculation behaviour of the small SiC particles. Porosity content is higher in this specimen is due to the vortex and turbulent nature of the liquid metal flow during the experiments. The main effects of the processing parameters on the microstructure evolution are also seen from a qualitative examination of the presented micrographs.

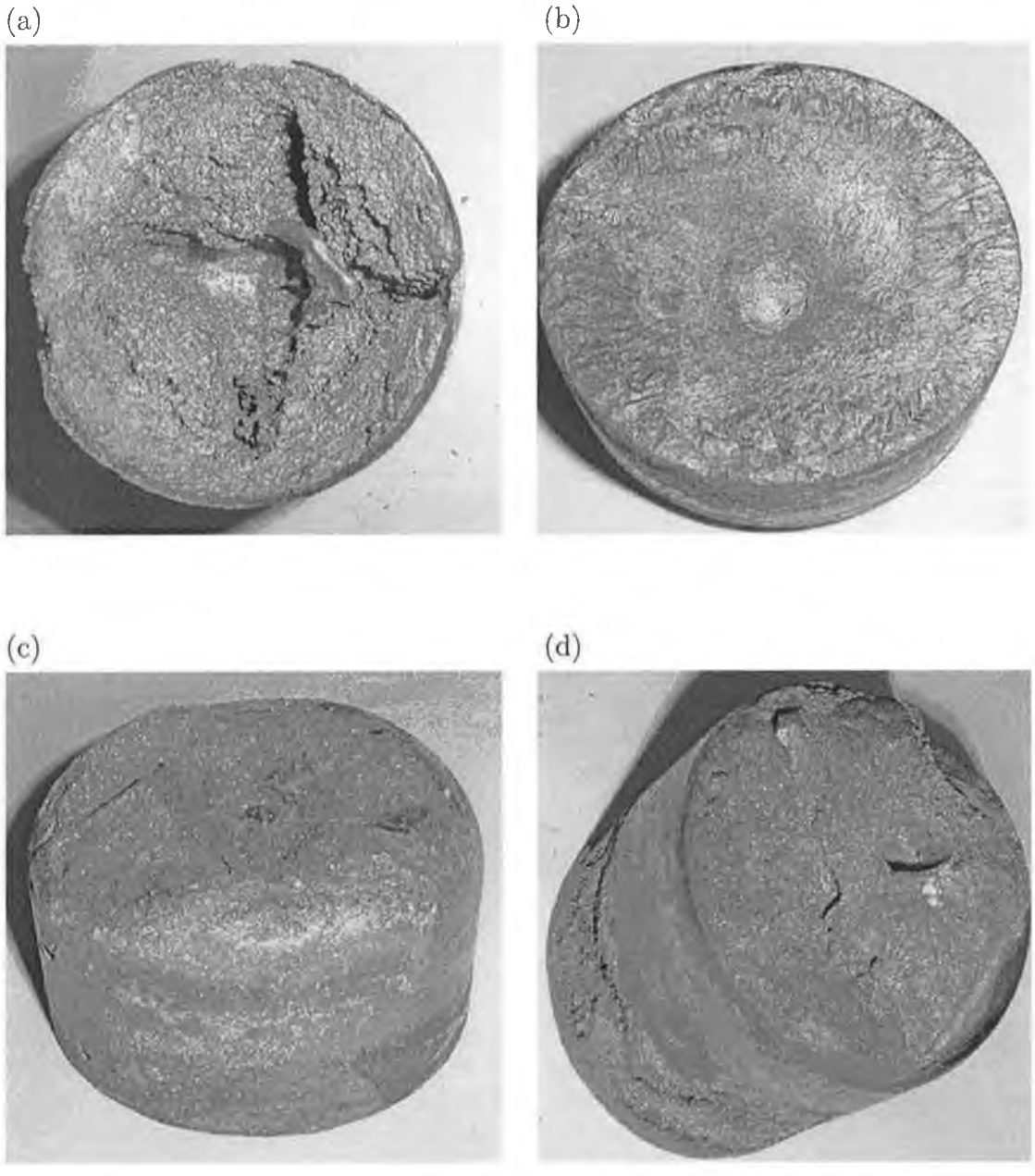

Figure 4.5: Top view of the compocasting; (a) semi-solid casting (Experiment 5), (b) liquid state casting (Experiment 1), Bottom and side view of experiment; (c) semi-solid casting (Experiment 7), (d) liquid state casting (Experiment 2).

(a)

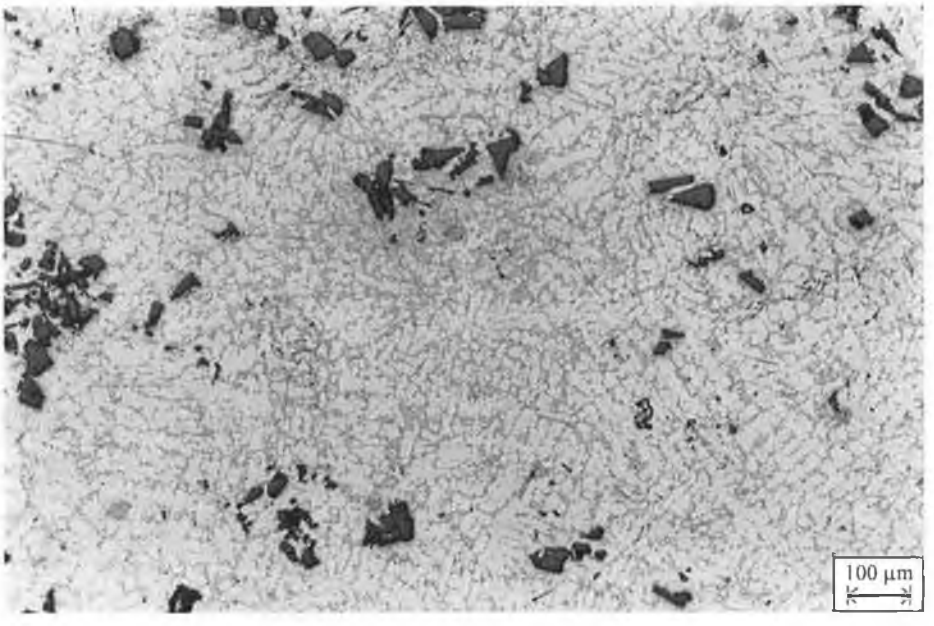

(b)

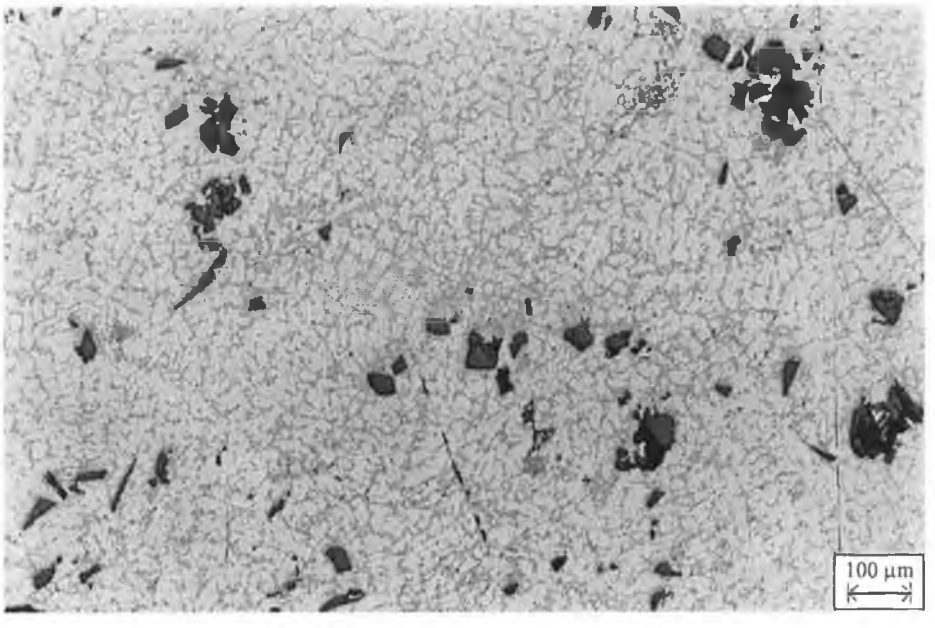

Figure 4.6: (a) Micrograph of experiment one. Processing parameters: Stirring speed 200 rpm, stirring time 16 seconds and viscosity is 1 mPas. (b) Micrograph of experiment two. Processing parameters: Stirring speed 300 rpm, stirring time 16 seconds and viscosity is 1 mPas.

(a)

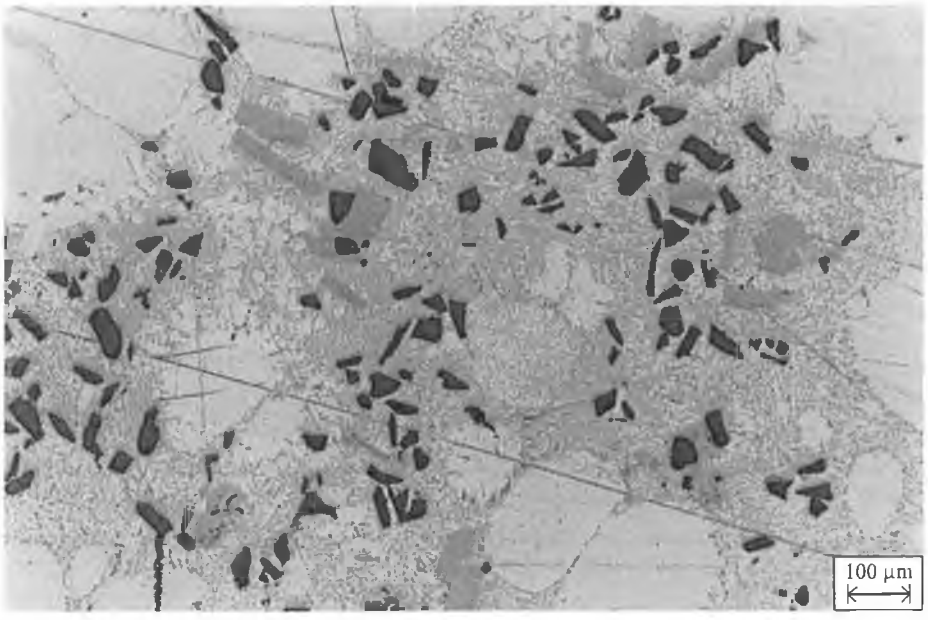

(b)

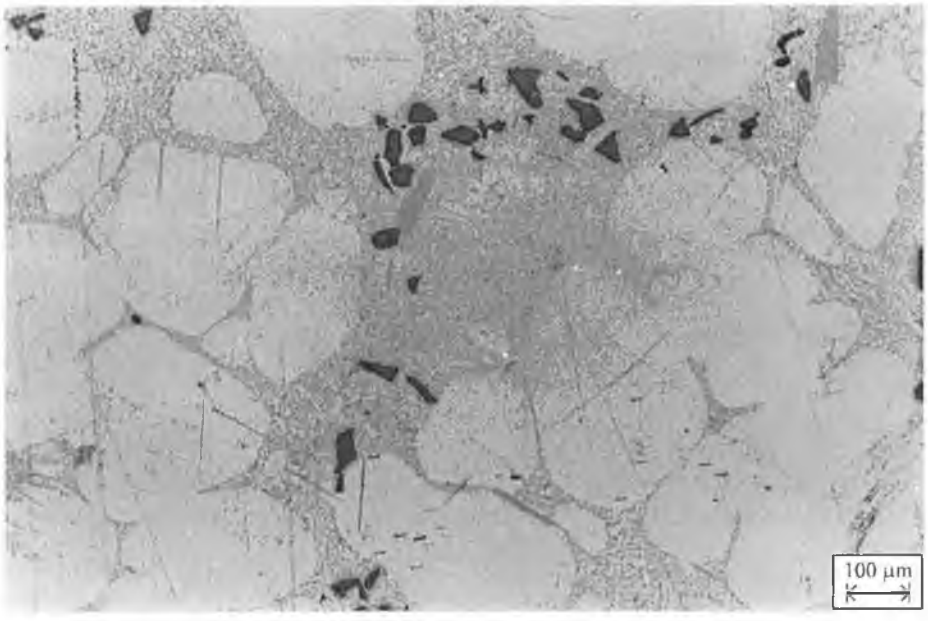

Figure 4.7: (a) Micrograph of experiment three. Processing parameters: Stirring speed 200 rpm, stirring time 2335 seconds and viscosity is 300 mPas. (b) Micrograph of experiment four. Processing parameters: Stirring speed 200 rpm, stirring time 1030 seconds and viscosity is 300 mPas.

(a)

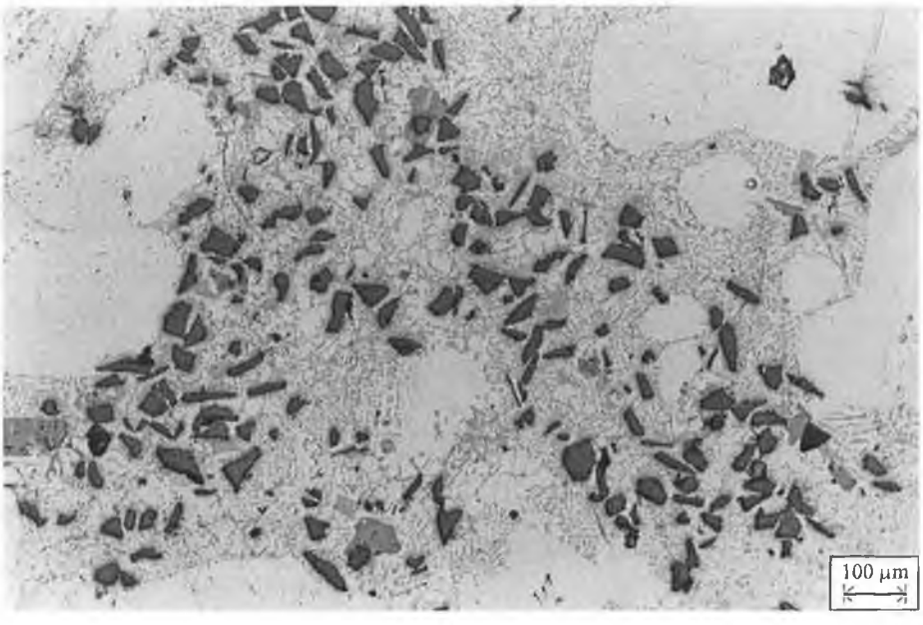

(b)

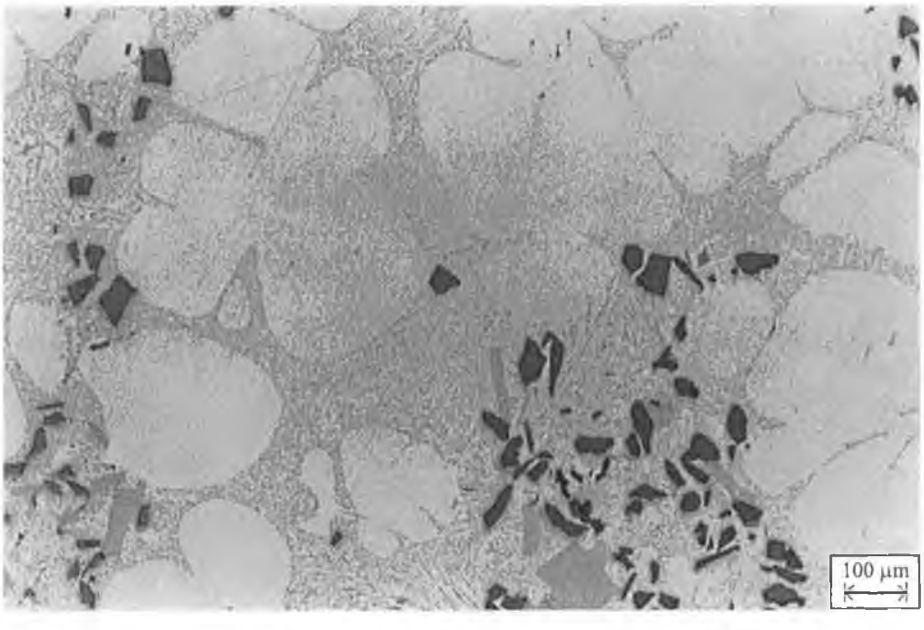

Figure 4.8: (a) Micrograph of experiment five. Processing parameters: Stirring speed 300 rpm, stirring time 1030 seconds and viscosity is 300 mPas. (b) Micrograph of experiment six. Processing parameters: Stirring speed 300 rpm, stirring time 540 seconds and viscosity is 300 mPas.

(a)

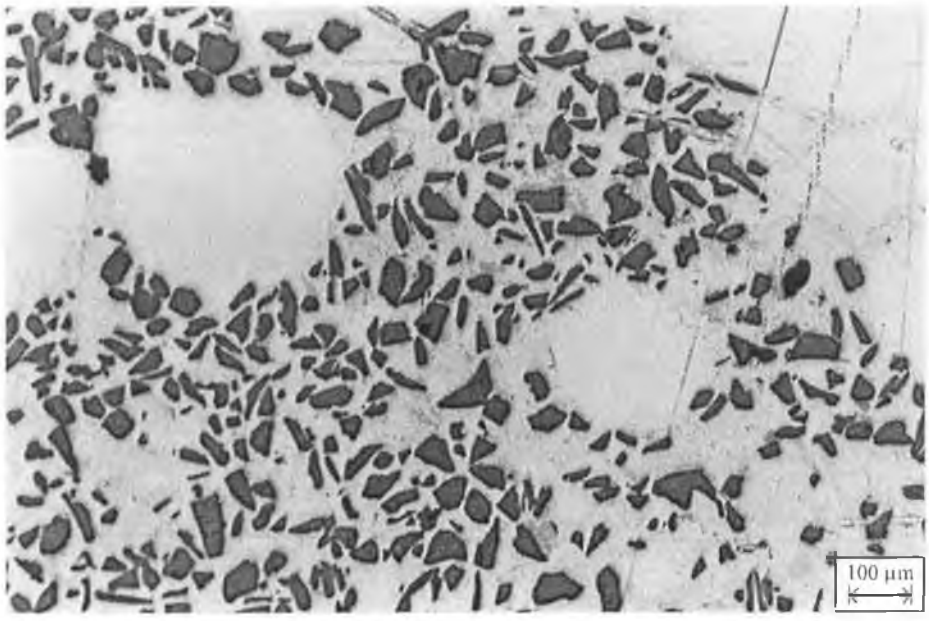

(b)

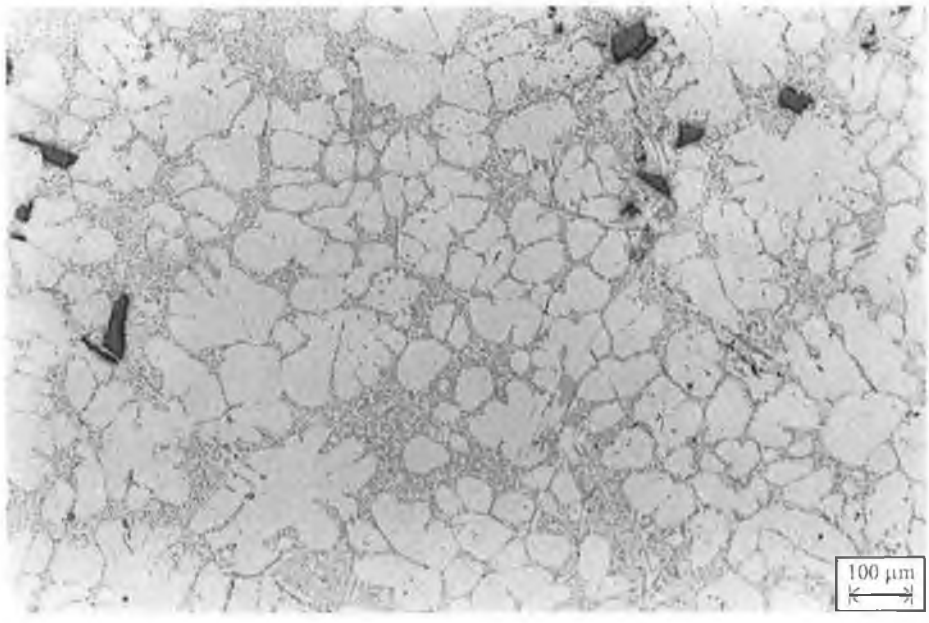

Figure 4.9: (a) Micrograph of experiment seven. Processing parameters: Stirring speed 500 rpm, stirring time 540 seconds and viscosity is 300 mPas. (b) Micrograph of experiment eight. Processing parameters: Stirring speed 500 rpm, stirring time 120 seconds and viscosity is 300 mPas.

4.7.2 Image analysis

The average area percentage of SiC determined in the indicated parts of the compocasting are shown in Table 4.4. Table 4.3 lists the processing parameters for the each experiment in Table 4.4 and 4.5. From Table 4.4 it is clear that experiment 5 and 7 resulted in the highest percentage of SiC content. Experiment 1, 2, 3, 5 and 7 were conducted allowing the time, according to the computer simulations, for a steady state distribution of SiC to be produced. Experiment 4, 6 and 8 were done allowing less time than the required steady state distribution time than was found in the previously done visualization and computational simulation experiments. According to this Table, the samples from experiment one and two contain less volume fraction of SiC than the other samples. It can be seen from this that semi-solid processing of Al-SiC, is better for retaining the SiC particulate than liquid state processing. It is also noted that experiment two contains less SiC particles than experiment one.

These results also gives us an idea about the effect of stirring time at a particular stirring speed. For example, casting number 3 was processed for the steady state time period at 200 rpm and 300 mPas before quenching whereas casting 4 was processed for only half this period at 200 rpm and 300 mPas. It was found that the 200 rpm stirring velocity is not enough for 300 mPas viscosity to disperse the SiC particle from the bottom of the crucible. This is evident in area percentage of SiC. At around half stirring time with the same stirring speed 3.7 % SiC content was found in the sample produced from the compocasting four.

The results for the other SiC IA parameters calculated are shown in Table 4.5. The SiC count was found to be less for experiment 8 and higher for experiment 5. The maximum perimeter was found for experiment 5 and minimum perimeter was for experiment 8. These latter two results correspond with the % of SiC present. For liquid state processing, the aspect ratio was found to be approximately 2 whereas for SSP the aspect ratio of the SiC particles are ranging from 1.68 to 1.88. The SiC particles entrapped in the liquid state processing, were less spherical than in the semi-solid state. In the liquid state processing, the sphericity of SiC particles were 0.35 and for semi-solid state it was ranging from 0.50 to 0.57. The more spherical nature of the SiC particles from the semi-solid compocastings is possibly due to the additional drag produced by irregularly shaped particles with relatively large surface area, compared with the quicker settling of the spherical particles in the semi-solid state.

Table 4.4: IA results showing the area percentage of SiC for different experiments and casting position.

Experiment Number	Area percentage of SiC		
	Position Q	Position S	Position T
1	6.1	6.3	5.3
2	4.1	3.8	3.3
3	7.9	7.1	7.4
4	3.6	3.6	2.8
5	10.6	11.9	11.7
6	5.9	6.9	4.8
7	10.6	11.6	9.9
8	1.6	1.4	1.1

Table 4.5: IA results showing the SiC count, average SiC spherical diameter, perimeter, aspect ratio, and sphericity.

Experiment Number	Count	Diameter spheric (μm)	Perimeter (μm)	Aspect ratio	Sphericity
1	87	29	4.9	2.03	0.35
2	51	27	3.01	2.01	0.35
3	103	30	7.54	1.85	0.56
4	49	30	3.32	1.68	0.54
5	116	30	12.09	1.88	0.57
6	100	30	6.4	1.85	0.51
7	115	30	10.2	1.86	0.50
8	14	30	1.01	1.87	0.53

Chapter 5

Discussion

5.1 Visualization experiments

5.1.1 Dispersion

From the results presented it is apparent that the stirring velocity, blade angle and stirrer height have a significant effect on particle distribution in the water-SiC mixture. These effects are dampened by the higher viscosity glycerol/water mixtures. In this regard, even the relatively low viscosity glycerol/water mixture (300 mPas) has a significant effect.

Stirring velocity

With increasing stirring velocity dispersion time decreases. At 200, 250 and 300 rpm, in the glycerol/water system, the range of dispersion times for 3, 4 and turbine bladed stirrers are 1920-2700, 1680-1980 and 900-1320 seconds respectively. The turbine blade also produced dispersion times similar to the best found for the flat bladed stirrers. The geometry of the turbine blade allowed much greater axial flow within the crucible which enable quick and uniform particle dispersion.

Blade angle

From Table 2.1 it is observed that at 100 rpm and with 0 and 30 degree blade angles no uniform dispersion resulted, but with 45 and 60 degree blade angles there was full particulate dispersion. It is further observed for all stirring speeds that dispersion rates increase with increasing blade angle, up to 60 degree. A further blade angle increase to 90 degree did not significantly appear to change the dispersion rates, but lead to increased dispersion times particularly for the glycerol/water mixture, see Table 2.2. A similar trend with blade angle to that noted for the water suspension was also noted for the dispersion time in glyc-

erol/water. Though there was a tendency for reduced dispersion time with higher blade angle, it was found that for most cases the 60 degree angle produced the lowest dispersion times. Very similar results were observed for the higher viscosity (300, 500, 800 and 1000 mPas) glycerol/water mixtures tested, see section 2.2.1.

Stirrer height

The height of the stirrer was also seen to have an important effect for the distribution time of the SiC. This was again particularly true for the higher viscosity glycerol/water solutions, see Table 2.3.

Vortex generation

Excessive vortex height was recorded for some processing condition, see Table 2.4. This can result in air entrapment, however brute force has also been shown to provide the best method for incorporating particles in SSM [195]. For batch casting then, the stirrer should only produce strong currents in the bottom region of the SSM to encourage particle entrapment and discourage air entrapment. Air entrapment leads to internal voids and oxides within the casting which deteriorate the mechanical properties. Non-reactive argon or nitrogen gas atmospheres mitigate the problems of oxide formation. However these gases may also form pores when present within the SSM during solidification. In contrast to the constant viscosity simulation fluids used in this work, the viscosity of SSM changes during processing. Lower fractions solid, higher shear rates, or longer shearing periods result in lower viscosity in the SSM which could help prevent retention of these gases [22].

Comparison with other work

Hashim et al. [248], in an effort to investigate the flow pattern of particles in SSM used glycerol with small polystyrene particles to visualise the flow pattern of particles. Both their visualization and computational simulations were focused on studying the effect of stirrer position in the crucible and stirring speed on the flow pattern of the particles. The use of the glycerol and polystyrene was arbitrarily selected to give some idea of the mixing flow pattern. Their simulation results ended up with the findings that turbulence at the base of the crucible could give effective mixing, without a vortex at the surface, thus avoiding gas/impurity entrapment. This corresponds well with the effect of stirring speed and stirrer height noted in this work. A number of other similarities between this work and the work of Hashmi et al. were also noted. When the impeller was placed excessively high within the fluid, little flow occurs at the base of the vessel where

it is required to lift particles into the melt. It was also observed that the predicted flow pattern in the computational simulation and the observed flow pattern in visualization showed a good agreement.

Experimental results from Rohatgi et al. [249] examined the homogeneity of SiC distributions during stirring in water-SiC mixtures. An experimental study was conducted on the mixing quality of two phase slurries in the model water-SiC system. A gravimetric technique was used to determine the influence of impeller geometry on the uniformity of distribution of SiC in the mixture. Their work indicated that the minimum rotational speed to disperse SiC in water should be 225 rpm. They also found that blade angle has a significant effect on dispersion, increased homogeneous mixing can be obtained by increasing blade angle from 20 to 60 degree. With the radial flow impeller at high rotational speeds, the particles are concentrated more at the wall and the bottom of the tank but gives a low rotational speed of 115 to 140 rpm for homogeneous suspension. So, according to them, the minimum speed required for a completely homogeneous suspension of SiC in water was found to be in the range 200 to 300 rpm. A comparison between parameters in the real Al-SiC system, the water SiC system and current water-SiC system are shown in Table 5.1.

Table 5.1: Comparison of some dynamic parameters between the real Al-25 % SiC system and the model water 25 % SiC system [249] and current water-10 % SiC system for 300 rpm rotational speed.

Property	Al-25 % SiC [249]	Water-25 % SiC [249]	Water-10 % SiC (Current)
Mixture Density (kg m^{-3})	2591	1562	1321
Dynamic viscosity (mPas)	2.6	1.8	1.25
Temperature (°C)	700.00	30	22
Reynolds number	3.94×10^4	3.37×10^4	3.2×10^4
Froude number	0.22	0.22	0.20

5.1.2 Settling

Particulate settling times, see section 2.2.2 and figure 2.3, were in general longer than dispersion times though they were of similar order of magnitude. Settling times, in contrast to dispersion times, showed no variation with stirring speed but were strongly dependent on fluid viscosity. From the results with the liquid aluminium simulation fluid (water) it was seen that settling occured within seconds of stopping shear within the fluid. In the context of compocasting MMC

materials, solidification would then have to be immediate in order to retain the uniform SiC distribution, see figure 2.3. A slight increase in viscosity (from 1 to 300 mPas) however allows for much longer time before processing (one minutes to 60 minutes). Such a viscosity increase could be obtained from lowering the melt temperature to within an alloy's semi-solid range. A disadvantage of higher viscosities however is their increased lack of fluidity. A compromise is then required in the casting temperature. It was seen from the results above that at a viscosity of 300 mPas would sufficiently increase the time available for SSM processing, potentially up to 20 hours, see section 2.2.2.

5.2 Computational simulation

5.2.1 Model velocity field simulation

Over the years, many researchers [250–253] have measured the mixing time for different impeller designs, vessel geometries, etc.

Stirrer velocity

A lower velocity magnitude was found in the water model, compared to the glycerol/water model, for axial and radial velocity components and a relatively high circumferential velocity component was evident (figures 3.3 and 3.4). Appreciable turbulence, kinetic energy and eddy dissipation components were found in the water model (figure 3.3) but were absent in the glycerol/water model (figure 3.4). It is clear from the velocity results that the circumferential component of the velocity was the highest for both liquids, and that this is significantly greater in water than in glycerol/water (figures 3.3 and 3.4). However, in glycerol for a viscosity of 300 mPas there was no turbulence and kinetic energy and eddy dissipation values were zero. From 50 to 300 rpm no turbulence was evident in glycerol/water and all the velocity distributions in glycerol/water for these rotational speed were laminar.This is consistent with results from the visualisation tests, which showed a much higher vortex in water than glycerol/water.

It is well known that based on Reynold number, the flow can be classified as laminar or turbulent. For mixing tank simulation, the Reynold number [254] is defined as

$$R_e = \frac{\rho N D^2}{\mu} \tag{5.1}$$

where, ρ is fluid density, kg m^{-3}
N is the stirrer speed, rev sec^{-1}

D is the stirrer diameter, m

μ is the fluid viscosity, kg m^{-1} s^{-1}

In mixing tanks, flow with Reynold numbers greater that 2,000 are generally considered turbulent, although the line of demarcation is somewhat flexible. In water for a viscosity of 1 mPas, and for a 80 mm diameter stirrer, and for a stirring speeds of 50, 100, 150, 200, 250 and 300 rpm, the calculated Reynold numbers are 5,312, 10,624, 16,000, 21,120, 26,624 and 32,000 respectively. On the contrary, for a glycerol/water mixture of 300 mPas viscosity the same impeller diameter Reynold numbers are 134, 179, 224 are found respectively for stirring speeds of 300, 400 and 500 rpm. For the same system to have a Reynold number greater than 2,000 should need a stirring speed of greater than 4,464 rpm. So, below that rpm any stirring speed for the glycerol/water mixture will provide a laminar flow. El-Kaddah and Chang during semi-solid Al-SiC composite production, stiring speed ranging from 1,000 to 2,000 rpm were investigated [255].

As the Reynold number is squarely proportional to the stirring daimeter, increasing the diameter of the stirrer increases the Reynold number and hence the chance of turbulence occuring at lower speeds. This is consistent with the computational simulation findings.

Stirrer height

Analysing the axial, radial and circumferential velocity and kinetic energy components with impeller positions of 13, 20 and 26 mm off the base of the vessel, it was found that at 20 mm off the base, there was a wide distribution of axial velocity, radial velocity and kinetic energy distribution (figure 3.5 to 3.7). These suggested that 20 mm height off the base of the vessel was the best position to disperse the SiC in water. A similar conclusion can be drawn from the results in the glycerol/water solution (figure 3.8 to 3.10). According to Nagata [256], the stirrer should be placed no more than 30 % of height from the base, to avoid accumulation of particles at the botom of the mixture. Hashim [242] also suggested the same.

Stirrer diameter

One objective of the computer modelling work presented in this thesis was to use the predicted flow field to estimate the mixing time for different stirrer diameters. From the results of the diameter effect analysis, it was found that a 50 mm diameter stirrer performed better than the others. Other researchers [257] found that an optimum ratio of the stirrer diameter, d, and vessel diameter, D, should be, $d/D = 0.3 - 0.35$, for an axially discharging stirrer suspending concentrated

solids. In the MMC compocastings, in this work, a ratio of 80 mm/105 mm(= 0.76) was used. Therefore based on their work [257] stirrer diameters as low as 35 mm could also be used in producing homogeneous suspensions.

5.2.2 Dispersion simulation

An analysis of particulate suspension during the mixing was performed in these experiments. The agitator should be rotated at a speed that is great enough to keep the solid material in suspension, rather than allowing it to accumulate on the base of the vessel. The degree of suspension is influenced by the fluid flow pattern and stirring speed. A measure of the degree of suspension that is often used in the literature is the quantity of remaining particulate on the base of the vessel [243]. The time at which this is measured is an important parameter.

Zwietering [258] proposed, on the basis of a dimensional analysis, the following empirical correlation for the minimum agitation speed, N_m, required to disperse the particulate,

$$N_m = \frac{s D_p^{0.2} \mu_L^{0.1} (g\Delta\rho)^{0.45} B^{0.13}}{\rho_L^{0.55} D^{0.85}} \tag{5.2}$$

where,

s is a constant for a given system geometry

D_p particle diameter, 13×10^{-6} m in this work

μ_L is the viscosity of the liquid phase, 0.001 and 0.3 Pas

g is the gravity acceleration, 9.81 ms^{-2}

$\Delta\rho = \rho_S - \rho_L$, $\Delta\rho$ for water-SiC is 2210 and for glycerol/water-SiC is1950 kg m^{-3}

ρ_S is the density of the solid phase, kg m^{-3}, 3210 kg m^{-3} for SiC

ρ_L is the density of the liquid phase kg m^{-3}, 1000 kg m^{-3} for water and 1260 kg m^{-3} for glycerol/water

B is the solid concentration, 0.1

D is the stirrer diameter, m, calculated for both 0.08 and 0.07 m

Using this formula, a minimum agitation speed for water of about 50 rpm was found and and 315 rpm for glycerol/water is around 315 rpm. By changing the blade diameter, this result can be changed. In the water-SiC system for an 80 mm blade diameter, N_m was around 50 rpm and for a 70 mm blade diameter, N_m was 98 rpm. The computational and visualisation gave different rotational speed for the water-SiC system. In water the stirring speed should be above 100 rpm and should not be more than 150 rpm and in glycerol, the stirring speed should not be less than 300 rpm and not more than 500 rpm for stirrer diameter of 80 mm. It should be in between 300 rpm and 500 rpm.

In spite of the turbulent flow field observed in the water-SiC system a very uniform distribution of SiC was found at steady state, see figure 3.12. Distribution times noted at the various stirring speeds in water and the corresponding visualisation results are shown in figure 5.1 (compilation of results from Table 2.1 and 3.1). From this figure it can be seen that for the visualisation experiments (vis.) and at 100 rpm the dispersion times were 300 and 180 seconds for three and four blade stirrers respectively. The computer simulation (cs) model predicted 170 seconds for complete dispersion with the four bladed stirrer. At higher stirring speeds the difference between the dispersion times from the two visualisation experiments and the computer simulation reduced. The magnitude of these times also reduced at the higher stirring speeds.

Distribution times at the various stirring speeds in glycerol/water and the corresponding visualisation results are shown in figure 5.2 (compilation of results from Table 2.2 and 3.2). From this figure it can be seen that at 200, 250 and 300 rpm the dispersion times were approximately 2400, 1750 and 1050 seconds respectively for the three bladed and four bladed visualisation and computer simulation results. For these speeds the computational simulation results were slightly lower than the visualisation results. Dispersion times of approximately 720 seconds (12 minutes) and 540 seconds (9 minutes) were noted from the Fluent simulation at agitator speeds of 400 and 500 rpm respectively.

It can be seen from figure 5.1 and figure 5.2 that the model is in good agreement with results from the physical simulation, with agreement within 5 % in most cases. Given the margin for error in visualisation tests, this was an encouraging correlation. In both cases faster, rotational speeds gave much shorter dispersion times.

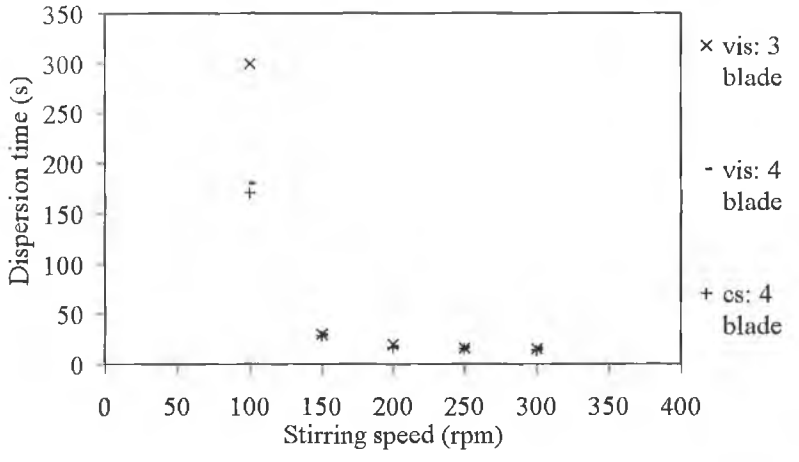

Figure 5.1: Dispersion time for 10 % SiC particles in water for various stirring speeds. Here vis means visualisation and cs means computer simulation.

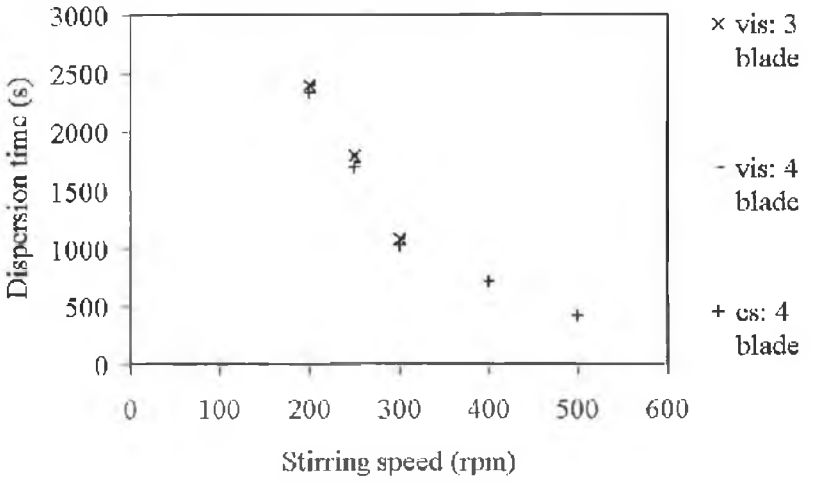

Figure 5.2: Dispersion time for 10 % SiC particles in glycerol/water solution for various stirring speeds. Here vis means visualisation and cs means computer simulation.

The computational and visualisation results suggest that for quick dispersion of SiC in water, 200 rpm should be the minimum speed for liquid state processing (Table 2.1 and 3.1). Higher vortex and air entrapment was however observed at rotational speeds higher than 100 rpm. This presents a problem in that a stirring speed of 250 rpm or above, see figure 3.12, is needed to obtain a ful distribution in the water-SiC system. The computer simulation, figure 3.13, suggests that for complete dispersion of SiC in the glycerol/water system, a minimum stirring speed of 300 rpm is needed. Even at 200 rpm and 250 rpm, all the SiC was not dispersed from the bottom of the vessel. A relatively small vortex height of 6 mm, see Table 2.4, was noted for the 300 mPas fluid at a stirring speed of 300 rpm.

More complex models of homogeneous solid suspensions based on total energy balance, phase change during solidification would be difficult to solve and may have a lower chance of success. Another model, during phase change, that could be used to determine the required stirring speed to obtain a uniform particulate dispersion based on equating the particle settling velocity and the mean upward velocity [243].

5.2.3 Settling simulation

Where the solid fraction is relatively high, particle settling rates are strongly influenced by the presence of the surrounding particles. This situation is called hindered settling. Finer particles tend to behave differently than larger or coarse particles, since the fine particles usually exhibit a high degree of flocculation due to the dominance of the surface force and high surface areas. Course particles

(such as 100 μm or larger) have a specific surface area that is much smaller, so flocculation is not common.

Stokes' law gives an equation for the relative velocity, V_0, between the particle and the fluid in terms of the density of the solid, ρ_s, the density of the liquid, ρ, the gravitional force, g, the diameter of the particle, d, and the viscosity of the liquid, μ [181].

When the solids are relatively fine and/or the slurry is sufficiently concentrated, settling is extremely slow. The slurry can usually be approximated as a uniform continuous medium with properties (viscosity and density) that depend upon the solids loading, particle size and density, and interparticle forces (surface charges, conductivity, etc.). If a significant fraction of the particles are fine (such as less than about 30 μm or so), the suspending fluid and particles can be considered to be a continuous medium, with increased viscosity and density, through which the larger particles must move. The viscosity of the suspension (μ_θ) is modified by the presence of the solids. For uniform spheres at a volumetric fraction of 2 % or less, Einstein showed [259] that

$$\mu_\theta = \mu(1 + 2.5\varphi) \tag{5.3}$$

where, μ is the viscosity of the suspending fluid. For more concentrated suspensions, a wide variety of expressions have been proposed in the literature [260]. If the volume fraction of solids are relatively low (such as below about 10 % solids by volume) and/or the particle size and/or density are relatively large, the system will be heterogeneous and the larger particles will settle readily [260].

Measured settling times from the visualisation experiments were compared to those predicted by the model, see figure 5.3. The model predicted shorter times in both the water and the glycerol/water mixture than those measured. One reason for this discrepancy may be the fact that in the visualisation tests, a subjective view of when settling was used. This tended to be conservative. Probably more significant is the fact that the starting condition for the settling model was zero fluid velocity, whereas in the actual stirring the fluid has some momentum after the stirrer is stopped. This momentum and additional circumferential velocity would be expected to prolong settling. The same pattern of settling predicted in the model was however seen in the visualisation tests.

All the modelling and simulation experiments were done for 13 μm SiC particle size. Due to availability, SiC particles of 30 μm in size were used in the validation experiments. To examine the effect of particle size on the dispersion and settling, simulation experiments were performed for 13 μm, 30 μm and 100 μm sized 10 % SiC particles. For a lower viscosity of 1 mPas, the particle size has a greater

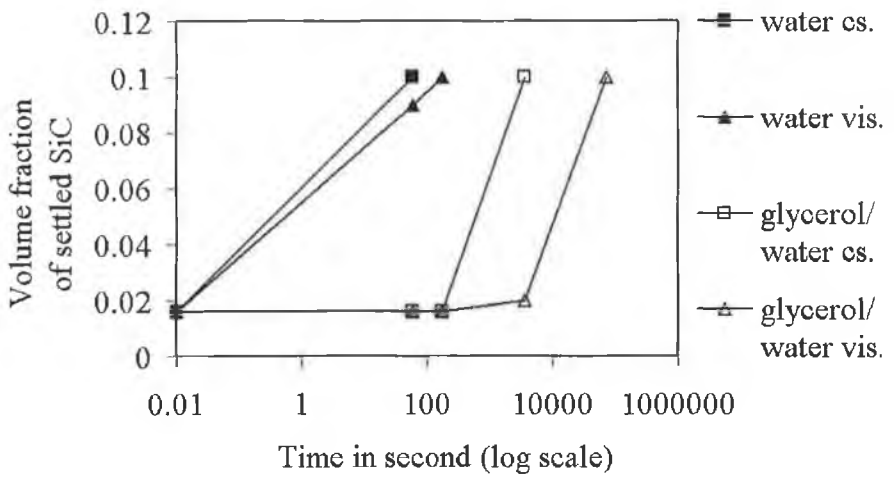

Figure 5.3: Comparison of visualisation and simulation results in settling (Volume fraction of settled SiC versus time in seconds in log scale).

effect as shown in the simulation figure 5.4. The closer sized particles, 13 μm and 30 μm, have less effect on the particulate distribution than the 100 μm sized particle. Figure 5.4 shows the settling distribution after 9 minutes in water. This simulaton was repeated for the glycerol/water system, however after 9 minutes no noticeable setling occured for any of the particle sizes examined (13 μm, 30 μm and 100 μm).

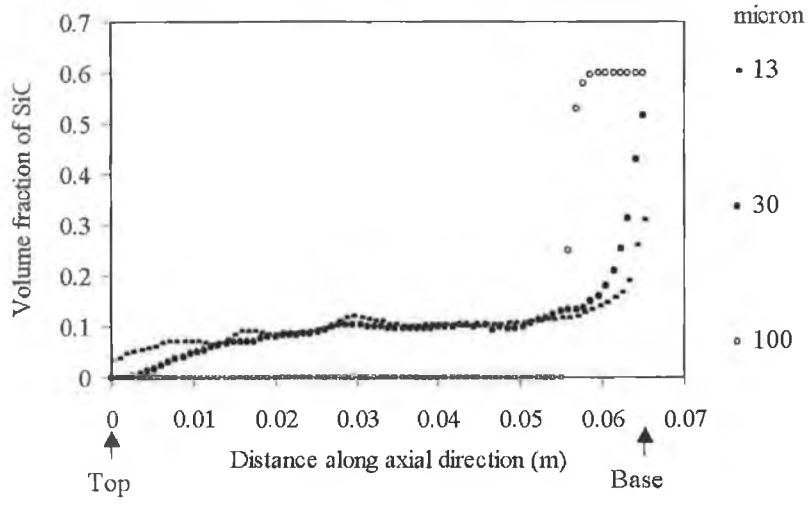

Figure 5.4: Effect of particle size 9 minutes after the commencement of settling in a uniformly mixed water-10 % SiC system.

5.3 Stir-casting validation experiments

In the liquid state experiments all the grain sizes were very small and it is clear that these were quick quenched castings. The aluminium crystals were larger for the semi-solid casting than for the liquid state castings. As a quick quenched structure, solidification time was very short. It would therefore seem that these large primary aluminium grains were formed during stirring. These grains were also globular rather than dendritic which also occur due to the stirring action and holding period. Shear rate would be expected to affect the grain size. A higher shear rate during processing should produce smaller grains [219]. In this experimental work, at higher shear rates (500 rpm), smaller grains were observed (figure 4.8 ($\sim$40μm) versus figure 4.6 through 4.7 ($\sim$110μm)).

From the metallography, it was clear that liquid state samples contained much porosity than semi-solid state. This is a viscosity effect. It is noticeable that 300 rpm stirring speed (Experiment 2) generated bad sample than 200 rpm stirring speed (Experiment 1). It indicate that with increasing stirring speed the dispersion of SiC and incorporation of these particles will not increase. For a melt of particular viscosity, there are critical speed of stirring to achieve better results.

From experiment 3 it was found that even at 200 rpm and after 2335 seconds, see Table 4.4, not all the SiC was dispersed from the bottom of the tank, see Table 4.5. Only 7.5 % SiC was recorded instead of 10 %. At half this stirring period but for the same other processing parameters, see Table 4.4, only 3.7 % SiC was dispersed.

The viscosity of the melt generally increases with fractional solid. The incorporation of the reinforcement particles will immediately increase the viscosity of the matrix melt [219]. For example, if 15 volume percent of reinforcement particles is added into the fully melted matrix mixture, this means that the melt will be occupied by 15 % of solid particles, or in other words, the slurry becomes partially solidified [64]. Kaufmann et al. [261] made a comparison between the cooling curve of the A356 alloy and its composite which was reinforced by 15 vol. % SiC. They noted that liquidus temperature of the composite was 5.5 °C higher than that of un-reinforced A356 and concluded that this was due to the addition of ceramic particles in the molten metal reduces the effect of under-cooling. It was established in that work that the composite slurry with the matrix in the semi-solid state, exhibited a lower viscosity than the matrix alloy slurry with an equivalent total volume fraction of solid. The composite slurry in his work contained 13 μm size particles in the liquid state. However, it has been shown by Moon that the addition of SiC can also reduce the viscosity [219] in the semi-solid metal.

The viscosity reduces as the shear rate caused by stirring increases. At higher shear rates, the clusters of particle are broken, reducing the resistance to flow. Also the apparent viscosity increases with the volume fraction of particles in the slurry. Higher viscosity helps to enhance the stability of the slurry by reducing the settling velocity, but also creates resistance to flow in mould channels during casting [85, 262].

A comparison of results from the computer simulation and the castings for the liquid state experiments is shown in figure 5.5 (a) and (b). Comparison of the results from the computer simulation and the compocasting for semi-solid experiments are shown in figure 5.6 (a) to (f). The computer modeling was done assuming that the water and glycerol/water solution was a Newtonian fluid. Molten metals and alloys generally behaves as Newtonian fluids [219], but semi-solid metals behave as non-Newtonian fluids. It was therefore not expected that computer model results would correspond exactly with those from the semi-solid castings. The homogeneous SiC particle distribution set up in the computer simulation can not be expected to be match with the actual castings. There are lots of other factors that could lead to differences between these results, as discussed in the literature such as wettability, particle pushing during solidification etc. [35, 109, 116, 118, 128]. However, in most cases the experimental work was supported by the visualisation and simulation results.

From figure 5.5, it can be seen that the simulation and actual experimental results were different somewhat but especially for the results in figures 5.5 (b) where the processing parameters were 200 rpm and 16 s stirring time. This may be because of the fact that in the liquid state, the wettability of SiC with liquid aluminum is very low. So, the behaviour of water with SiC with the viscosity of 1 mPas, is not responding exactly as in the case of the liquid aluminum. Computer and visulisation simulation indicate that there should be no difference between the dispersion rate of SiC particle at 200 and 300 rpm. However, the casting validation experiments one and two indicate that a lower % of SiC is distributed at the lower stirring speed of 200 rpm. One reason for difference between the cs and the casting validation is that there is a difference in the surface tension between the water and glycerol/water of the cs compared to the liquid Al of the casting experiment. This is however does not account for the difference between experiment one and two. A more probable explanation is that the slight time difference in quenching these two castings resulted in this volume percentage difference.

Selection of stiring speed and period is essential for the effective incorporation of particles to occur [135]. These researchers found that when there was no stirring, the particles were not wetted and remained out of the melt, irrespective

of the presence of magnesium or heat treatment of particles. They also found that with stirring in the liquid condition, poor wetting occured when the SiC particles were used in an as received condition, without magnesium. Microscopic examination of their sample showed no SiC particles within the matrix alloy or, in other words, zero wettability. This was also the case for the heat treated particles, without magnesium. Another point noted by these workers, that was also confirmed during the course of this work, was that if particles are poured from the top, during stirring some of the particles tended to float to the top of the melt, and others accumulated at the base of the crucible.

Mechanical stirring is necessary to help to promote wettability. Stirring in a fully liquid condition gives poor incorporation of the particles into the matrix. The particles tend to float to the top of the molten alloy, regardless of the speed of stirring. On the other hand, stirring while the slurry is solidifying improves incorporation of the SiC particles into the matrix alloy by entrapment.

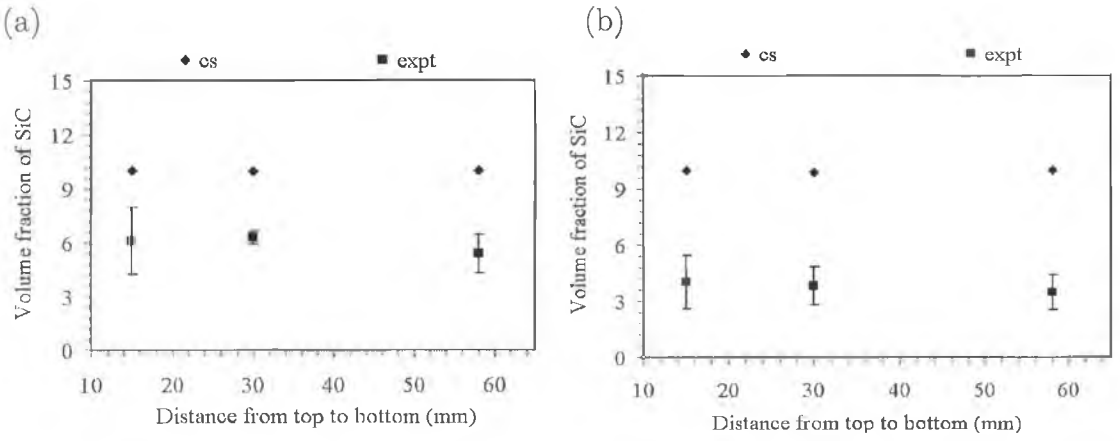

Figure 5.5: Comparison of computer simulation and experimental work for the volume fraction of SiC particles as a function of distance from top to bottom for liquid state experiment (a) Experiment one (b) Experiment two.

Placing all the substances together for melting is experimentally a very convenient process. During the initial stage of heating to about 600 °C any moisture in the ceramic particles, and the matrix materials is burnt off and thus reduce the level of porosity. This advantage can not be achieved by other methods in which the ceramic particles are introduced in the molten matrix materials from the top.

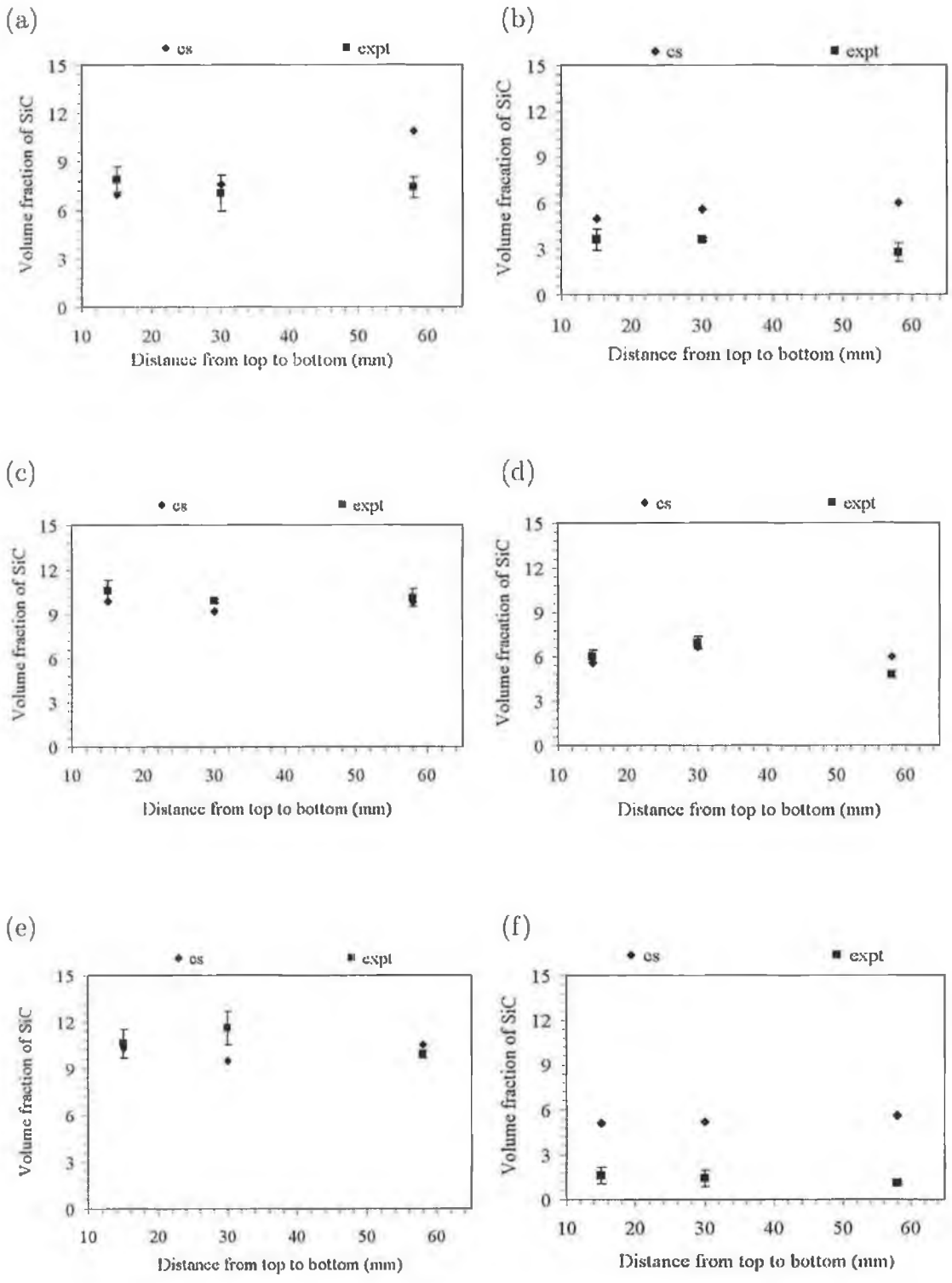

Figure 5.6: Comparison of computer simulation and experimental work for the volume fraction of SiC particles as a function of distance from top to bottom for semi-solid state experiment (a) Experiment three (b) Experiment four (c) Experiment five (d) Experiment six (e) Experiment seven (f) Experiment eight.

Chapter 6

Conclusion

6.1 Visualisation experiments

- Up to a point, higher blade angles and lower viscosities result in reduced particulate dispersion time.
- A minimum stirring speed of 100 rpm for water and 200 rpm for glycerol/water-10 % SiC mixtures is required for uniform dispersions to be produced.
- A viscosity increase from 1 mPas (for liquid metal) to 300 mPas has a tremendous effect on SiC dispersion and settling times. However a further increase from 300 mPas to 1000 mPas has negligible effect on this time.

6.2 Computational simulation

- A 3D velocity model has been develop to describe fluid flow patterns with stirrer speed, stirrer diameter and position effects identified.
- A 2D multi-phase computational model of stirring of solid particles in a fluid has been developed. Dispersion and settling time predictions of the model have been found to compare well with physical simulations. This model was applied and validated with a specific compocaster geometry. The model can now be extended to 3D and applied to other compocaster geometries.
- Measured dispersion times were compared to those predicted by the model. The model predicted shorter times in both the water and the glycerol/water mixture than those measured.
- Measured settling times were compared to those predicted by the model. The model predicted shorter times in both the water and the glycerol/water mixture than those measured.

6.3 Stir-casting validation experiments

- A novel quick quenched stir-caster has been designed and built for processing Al-SiC composites in liquid and semi-solid state. Temperature controlled compocasting experiments were performed on Al-10 % SiC.
- Stirring the MMC slurry in semi-solid state, at a temperature in the solidification range of the alloy matrix, during the solidification process, helps to incorporate ceramic particles into the alloy matrix.
- The quick quenched compocasting were found to be successful to fabricate Al-SiC metal matrix composite.
- One of the successes of the present study lies in the fact that without any addition of a wetting agent, a full incorporation of SiC particles into the aluminium matrix was obtained in the semi-solid state.
- Microstructural observation suggested that the stirring action of the slurry produces a cast MMC with globular structure. Stirring produces globular structures rather than dendritic structures.

6.4 Comparison of visualization, computational simulation and validation experiments

- Liquid phase fabrication technique was found to be less correspond with computational simulation due to the lack of wettability in real case.
- Semi-solid phase fabrication technique was found to be well correspond with computational simulation due to the increase of wettability in real case.
- Vortex formation in liquid state was found to be well agreed with the visualisation and validation experiments.
- Porosity incorporation was higher in the liquid state than semi-solid state which also corresponds well with visualisation and validation experiments. Highly dispersed, microporosity was observed all through the liquid state samples and well defined big but less in number were found in the semi-solid state samples.

6.5 Further work

- More detail results could be achieved during visualisation test by using modern techniques like, laser-Doppler anemometry, scanning laser microscopy.
- The present computational model could be applied to the problem of semi-solid processing of Al/SiC particle metal matrix composites by changing model parameters and to validate this new model experimentally. Computer simulation incorporating phase change criteria could also be performed to analysis this effect.
- The dispersion results from the computational simulation have been validated against actual casting. Similarly, the computer simulation settling results could be validated.
- Stirrer diameter could be lower than those used in this work. Smaller diameter stirrer of 50-60 mm or even less could be tested in future experiments.
- The mechanical and chemical property evaluation of the produced composite would be advantageous to better describe the quality of the composites produced.
- To investigate chemical reaction and oxidation of SiC after heat treatment, SEM and TEM study could be done.
- With different shearing action, in high temperature, viscosity of the melt could be studied.

Chapter 7

References

[1] B. Ralph, H.C. Yuen, and W.B. Lee. The processing of Metal Matrix Composites-an overview. *Journal of Materials Processing Technology*, 63:339–353, 1997.

[2] A. Mortensen, J.A. Cornie, and C. Flemings. Solidification processing of Metal Matrix Composites. *Materials and Design*, 10:69–76, 1989.

[3] D.E. Hammond and W.R. Hoover. Advances in castable Al-SiC composites. In K. Hirano, H. Oikawa, and K. Ikeda, editors, *Science and Engineering of Light Metals*, pages 447–452, Tokyo, Oct. 1991. Japan Institute of Light Metals.

[4] *ASM Handbook, Properties and Selection: Nonferrous alloy and special purpose materials*, volume 2. ASM International, Metals Park, OH, 1996.

[5] D. Huda, M.A. El Baradie, and M.S.J. Hashmi. Metal-matrix composites: Manufacturing aspects. part I. *Journal of Materials Processing Technology*, 37(1-4):513–528, February 1993.

[6] C. William and Jr. Harrigan. Commercial processing of metal matrix composites. *Materials Science and Engineering A*, A224:75–79, 1998.

[7] Y.H. Seo and C.G. Kang. Effects of hot extrusion through a curved die on the mechanical properties of SiC_p/Al composites fabricated by melt-stirring. *Composites Science and Technology*, 59:643–654, 1999.

[8] S. Skolianos. Mechanical behaviour of cast SiC_p-reinforced Al-4.5 % Cu-1.5 %Mg alloy. *Materials Science and Engineering*, A210:76–82, 1996.

[9] C.G. Kang, J.H. Yoon, and Y.H. Seo. The upsetting behavior of semi-solid aluminium material fabricated by a mechanical stirring process. *Journal of Materials Processing Technology*, 66:30–38, 1997.

[10] M. Yilmaz and S. Altintas. Properties of Al-Mg-SiC composites produced by a modified compocasting technique. In *Proceeding of the 2nd Bienniel*

European joint conference on Engineering Systems, pages 119–124, London, UK, 1994.

[11] G.S. Hanumanth and G.A. Irons. Particle incorporation by melt stirring for the production of Metal Matrix Composites. *Journal of Materials Science*, 28:2459–2465, 1993.

[12] J.C. Lee, J.Y. Byun, C.S. Oh, H.K. Seok, and H.I. Lee. Effect of various processing methods on the interfacial reactions in SiC_p/2024 Al composites. *Acta Materialia*, 45:5303–5315, 1997.

[13] Y. Xu and D.D.L. Chung. Low volume fraction particulate preforms for making metal matrix composites by liquid metal infiltration. *Journal of Materials Science*, 33(19):4707, 1998.

[14] C.S. Lim and A.J. Clegg. The production and evaluation of Metal Matrix Composite casting produced by a pressure-assisted investment casting process. *Journal of Materials Processing Technology*, 67:13–18, 1997.

[15] V. Michaud and A. Mortensen. Infiltration processing of fibre reinforced composites: governing phenomena. *Composites: Part A*, 32(8):981–996, 2001.

[16] Y.H. Seo and C.G. Kang. The effect of applied pressure on particle-dispersion characteristic and mechanical properties in melt-stirring squeeze-cast SiC_p/Al composites. *Journal of Materials Processing Technology*, 55:370–379, 1995.

[17] D. Huda, M.S.J. Hashmi, and M.A. El Baradie. MMC's: Materials, manufacturing and mechanical properties. *Key Engineering Materials, Metal-matrix composites: Manufacturing aspects. Part II*, 104-107:37–64, 1995.

[18] Q. Xu, R.W. Hayes, W.H. Hunt, and E.J. Lavernia. Mechanical properties and fracture behaviour of layered 6061/SiC_p composites produced by spray atomization and co-deposition. *Acta Materialia*, 47:43–53, 1998.

[19] K. Yamada, S. Sekiguchi, and T. Matsumiya. The optimum condition of compocasting methods for particulate metal matrix composites. *34th International SAMPE Symposium*, pages 2266–2277, 1989.

[20] G. Bartos-Tausig and K. Xia. Rheocasting and semisolid forming of a usually wrought aluminium alloy. [263], pages 290–295.

[21] M.P. Kenney and J.A. Courtois et al. *Metal Handbooks.* 15, Casting, ASM International, OH, USA, 30th March 1998. 9th Ed.

[22] D. Brabazon, D.J. Browne, and A.J. Carr. Fracture toughness of aluminium rheocast alloys: an experimental comparison of test methods. In Chiarmetta and Rosso [264], pages 331–336.

[23] T. Witulski, A. Winkelmann, and G. Hirt. Thixoforming of amuminium components for lightweight structures. In *Proc. 4th Int. Conf. on Semi-Solid Processing of Alloys and Composites*, pages 242–247, University of Sheffield, UK, 1996.

[24] M. Gupta, M. K. Surappa, and S. Qin. Effect of interfacial characteristics on the failure-mechanism mode of a SiC reinforced Al based Metal Matrix Composite. *Journal of Materials Processing Technology*, 67:94–99, 1997.

[25] A.K. Surappa and P.K. Rohatgi. Preparation and properties of cast aluminium ceramic particle composites. *Journal of Materials Science*, 16:981, 1981.

[26] T.W. Clyne and P.J. Withers. *An Introduction to Metal Matrix Composites.* Cambridge University Press, 1993.

[27] D. Huda, M.A. El Baradie, and M.S.J. Hashmi. Metal-matrix composites: Manufacturing aspects. part II. *Journal of Materials Processing Technology*, 37(1-4):529–541, February 1993.

[28] A.S. Samuel and F.H. Samuel. Foundry aspects of particulate reinforced aluminium MMCs: Factors controlling composite quality. *Key Engineering Materials*, 104-107:65–98, 1995.

[29] D.J. Lloyd. Aspect of fracture in particulate reinforced metal matrix composites. *Acta Metallurgica*, 39:59–71, 1991.

[30] R.B. Bhagat. Emerging P/M Metal Matrix Composites. *Advances in powder metallurgy and particulate materials*, 9:139–146, 1992.

[31] R.D. Carnahan, R.F. Decker, N. Bradley, and P. Frederick. New manufacturing process for metal matrix composite synthesis. In J. Masounave and F.G. Hamel, editors, *Fabrication of Particulates Reinforced Metal Composites*, pages 101–106. ASM International, 1990.

[32] A. Eftekhari, J.E. Talia, and P.K. Mazumdar. Influence of surface condition on the fatigue of an Aluminium-Lithium alloy (2090-T3). *Materials Science and Engineering*, A199:L3–L6, 1995.

[33] J.U. Ejiofor and R.G. Reddy. Characterization of pressure-assisted Al-Si composites. *Materials Science and Engineering A*, 259:314–323, 1999.

[34] D.J. Lloyd and B. Chamberlain. Properties of shape cast Al-SiC matrix composites, in cast reinforced metal composites. *World materials Congress*, Chicago:265–269, 1988.

[35] P.K. Rohatgi. Future directions in solidification of Metal Matrix Composites. *Key Engineering Materials*, 104-107:293–312, 1995.

[36] M.H. Stacey. Production and characterisation of fibres for Metal Matrix Composites. *Materials Science and Technology*, 4:227–230, 1988.

[37] M.K. Surappa. Microstructure evolution during solidification of DRMMCs (discontinuously reinforced metal matrix composites): State of art. *Journal of Materials Processing Technology*, 63:325–333, 1997.

[38] F. Bonollo, R. Guerriero, E. Sentimanti, I. Tangerini, and V.L. Yang. The effect of quenching on the mechanical properties of powder metallurgically produced Al-SiC (particles) metal matrix composites. *Materials Science and Engineering*, A144:303–309, 1991.

[39] M. Skibo, P.L. Morris, and D.J. Lloyd. Structure and properties of liquid metal processed SiC reinforced aluminium. *World Materials Congress*, Chicago:257–262, 1988.

[40] W.H. Hunt. *Interfaces in Metal Matrix Composites.* TMS-AIME, New Orleans, 1986.

[41] B.F. Quigley, G.J. Abbaschian, R. Wunderlin, and R. Mehrabian. *Metallurgical Transaction A*, 13A:93, 1982.

[42] B.P. Krishan, M.K. Surappa, and P.K. Rohatgi. The UPAL process: a direct method of preparing cast aluminium alloy-graphite particle composite. *Journal of Materials Science*, 16:1209–1216, 1981.

[43] M.C. Flemings and R. Mehrabian. Casting of semi-solid metals. *AFS Transactions*, 102:81–88, 1973.

[44] C.B. Lin, C.L. Ma, and Y.W. Chung. Microstructure of A380-SiC_p composites for die casting. *Journal of Materials Processing Technology*, 84:236–246, 1998.

[45] M.C. Flemings, R.G. Riek, and K.P. Young. Rheocasting processes. *Int. Cast Metals Journal*, pages 11–22, 1976.

[46] K. Miwa. Fabrication of SiC_p reinforced aluminium matrix composites by compocasting process. *Journal of Japan Foundryman's Society*, 62:423–428, 1990.

[47] D. Charles. Metal matrix composites-ready for take-off? *Metal and Materials*, pages 78–82, 1990.

[48] H.C. Lee and M.S. Kim. A fabrication method of aluminium short fibre aluminia matrix composites by compocasting. *Proceddings of the KSME-JSME Joint Conference*, pages 471–475, 1990.

[49] M. Suery and G. L'Esperance. Interfacial reaction and mechanical behaviour of aluminium matrix composites reinforced with ceramic particles. *Key Engineering materials*, 79-80:33–46, 1993.

[50] A. Labib, H. Liu, and F. Samuel. Effect of solidification rate (0.1-100 $°Cs^{-1}$) on the microstructure, mechanical properties and fractography of two Al-Si-10 vol. % SiC particle composite castings. *Materials Science and Engineering*, A(160):81–90, 1993.

[51] H. Lilholt. Aspects of deformation of metal matrix composites. *Materials Science and Engineering*, A(135):161–171, 1991.

[52] J. Eliasson and R. Sandstrom. Applications of aluminium matrix composites. *Key Engineering Materials*, 104-107:3–36, 1995.

[53] W.R. Mohn and R.A. Gegel, editors. *Dimensionally stable metal matrix composites for guidance systems and optics application*, USA, 1987. ARCO Chemical Advanced Materials.

[54] I. Wang R.J. Arsenault, N. Shi and C.R. Feng. Localized deformation of SiC-Al composites. *Materials Science and Engineering*, A131:55–58, 1991.

[55] J. Luo, R. Stevens, and N. Han. The stress-strain relationship in Al356/SiC particulate composites. *Key Engineering Materials*, 127-131:1159–1166, 1997.

[56] Y. Flom and R.J. Arsenault. Effect of particle size on fracture toughness of SiC/Al composite material. *Acta Metall.*, 37:2413–2423, 1989.

[57] L.G. Lim and F.P.E. Dunne. The effect of volume fraction of reinforcement on the elastic-viscoplastic response of metal matrix composites. *Int. Jour. of Mech. Sci.*, 38:19–39, 1996.

[58] H. Sekine and R. Chen. A combined microstructure strengthening analysis of SiC_p/Al metal matrix composites. *Composites*, 26:183–188, 1995.

[59] I.C. Stone and P. Tsakiropoulos. *Materials Science and Technology*, 11:222–227, 1995.

[60] L. Sun, S. Li, Z. Zhu, and Z.G. Wang. Dependence of fracture behaviors on SiC_p size of Al matrix composites. volume Canada, pages II295–II300, 1995.

[61] W.M. Zhong, G. L'Esperance, and M. Suery. Interfacial reaction in Al-Mg (5083)/SiC composite-a fabrication and remelting. *Metallurgical and Materials Transactions*, 26A:2637–2649, 1995.

[62] J. Dinwoodie, E. Moore, C.A.J. Langman, and W.R. Symes. The properties and applications of short staple aluminium fibre reinforced aluminium alloys. In *5th Int. Conf. on Composite Materials*, 1995.

[63] D.J. Lloyd. Particle reinforced aluminium and magnesium matrix composites. *International Materials Review*, 39:1–23, 1994.

[64] D.J. Lloyd. The solidification microstructure of particulate reinforced aluminium/SiC composites. *Composites Science and Technology*, 35:159–179, 1989.

[65] S.J. Harris, H.W. Cai, and P.C. Weatherburn. Structure, properties relationships in Al_2O_3, short fibre and SiC particle reinforced aluminium alloys. *International Conference on Advanced Composites Materials*, pages 1301–1307, 1993.

[66] M. Gupta and M.K. Surappa. Processing-microstructure-mechanical properties of Al based Metal Matrix Composites synethesized by casting route. *Key Engineering Materials*, 104-107:259–274, 1995.

[67] W.R. Hoover. Recent advances in castable metal matrix composites. In J. Masounave and F.G. Hamel, editors, *Fabrication of Particulate Reinforced Metal Composites*, volume Montreal, Quebec, Canada, Sept., pages 115–124. ASM International, 1990.

[68] M. Vedani, F. Santos, F. Brossa, G. Piatle, and G. Donzell. Particulate reinforced Al metal matrix composites produced through a plasma spray co-deposition technique: processing and microstructural aspect. In *Advanced Al and Mg Alloys, ASM*, 1990.

[69] E.A. Feest. Exploitation of the metal matrix composites concept, 1988.

[70] V.K. Lindroos and M.J. Talvitie. Recent advaces in Metal Matrix Composites. *Journal of Materials Processing Technology*, 53:273–284, 1995.

[71] R.L. Trumper. *Metal and Materials; Metal Matrix Composites-Application and Prospects.* Pergamon, Oxford, 1989.

[72] C. Milliere and M. Suery. Fabrication and properties of metal matrix composites based on SiC fibre reinforced aluminium alloys. *Materials Science and Technology*, 4:41, 1988.

[73] G. O'Donnell. *Process optimisation and numerical modelling of powder metallurgical Aluminium Matrix Composites.* Ph.D Thesis, Dublin City University, 1999.

[74] P.K. Ghosh and S. Ray. Fabrication and properties of compocast aluminium-aluminiuma particulate composites. *Indian Journal of Technology*, 26:83–94, 1988.

[75] K. Miwa, I. Takashi, and T. Ohashi. Fabrication of SiC whisker reinforced aluminium matrix composites by compocasting process. *Proceedings of the 2nd International Conference on the semi-solid alloys and composites*, Eds: S.B. Brown and M.C. Fleming:398–405, 1993.

[76] D.J. Lloyd, editor. *Factors influencing the properties of particulate reinforced composites produced by molten metal mixing*, Roskilde, Denmark, 1991.

[77] Y. Chen and D.D.L. Chung. Si/Al network composites fabricated by liquid metal infiltration. In M.Gilbert, P. Tremblay, and E. Ozberk, editors, *Proceedings of the International Symposium Recent Developments in Light Metals*, pages 61–68. Metallurgical Society of the Canadian Institute of Mining, Metallurgy and Petroleum, 1993.

[78] W. Wang and F. Ajersch. Particle interaction of melt-stirred Al-Si/SiC_p composites. In M.M Avedesian, L.J. Larouche, and J. Masounave, editors, *Advances in Production and Fabrication of Light Metals and MMCs*, pages 629–640, Alberta, Canada, 23rd-27th August 1992.

[79] T. Hikosaka and T. Imai. Effect of hot rolling on superplasticity of a SiC/6061 aluminium alloy composite made by a vortex method. *Scripta Materialia*, 36:145–150, 1997.

[80] P.K. Ghosh and S. Ray. Effect of porosity and alumina content on the high temperature mechanical properties of compocast aluminium alloy-alumina particle composite. *Journal of Materials Science*, 22:4077–4086, 1987.

[81] E. Lacoste, O. Mantaux, and M. Danis. Numerical simulation of metal matrix composites and polymer matrix composites processing by infiltration: a review. *Composites*, A(33):1605–1614, 2002.

[82] O. Mantaux, E. Lacoste, and M. Danis. Numerical prediction of microporosity formation during the solidification of a pure metal within a porous preform. *Composites Science and Technology*, 62(14):1801–1809, 2002.

[83] S. Zhang, F. Cao, Y. Chen, Q. Li, and Z. Jiang. Microstructure and damping properties of 2024Al/SiC_p metal matrix composite produced by spray codeposition. *Acta Materiae Compositae Sinica*, 15(1):88, 1998.

[84] J.W. McCoy, C. Jones, and F.E. Wawner. Preparation and properties of cast ceramic/aluminium composites. *SAMPE Quarterly*, 19:37–50, 1988.

[85] H.K. Moon, J.A. Cornie, and M.C. Flemings. Rheological behavior of SiC particulate (Al-6.5wt %Si) composite slurries at temperatures above the liquidus and within the liquid solid region of the matrix. *Materials Science and Engineering*, A144:253–265, 1991.

[86] M.C. Flemings. Behaviour of metal alloys in the semi-solid state. *Metall. Trans.*, A22:957–981, 1991.

[87] R. Mehrabian, A. Sato, and M.C. Fleming. *Light metal*, 2:177, 1975.

[88] A. Vogel, R.D. Doherty, and B. Cantor. Stir-cast microstructures and slow crack growth. In *Proc. Conf. on Solidification and Casting of Metals*, pages 518–525, Sheffield, 18th - 21st July 1977. Sheffield.

[89] D. Apelian, S. Shivkumar, and G. Sigworth. Fundamental aspects of heat treatment of cast Al-Si-Mg alloys. *AFS Transactions*, 1989.

[90] J. M. G´mez de Salazar and M. I. Barrena. Influence of heat treatments on the wear behaviour of an AA6092/SiC25p composite. *Wear*, 256(3-4):286–293, February 2004.

[91] M. Y. Zheng, K. Wu, S. Kamado, and Y. Kojima. Aging behavior of squeeze cast SiCw/AZ91 magnesium matrix composite. *Materials Science and Engineering A*, 348(1-2):67–75, 15 May 2003.

[92] S.L. Dong, J.F. Mao, D.Z. Yang, Y.X. Cui, and L.T. Jiang. Age-hardening behavior of a SiCw/Al-Li-Cu-Mg-Zr composite. *Materials Science and Engineering A*, 327(2):213–223, April 2002.

[93] N.E. Bekheet, R.M. Gadelrab, M.F. Salah, and A.N. Abd El-Azim. The effects of aging on the hardness and fatigue behavior of 2024 Al alloy/SiC composites. *Materials Design*, 23(2):153–159, April 2002.

[94] M. Gu, Z. Wu, Y. Jin, and M. Koak. Effects of reinforcements on the aging response of a ZK60-based hybrid composite. *Materials Science and Engineering A*, 272(2):257–26, November 1999.

[95] B.C. Ko and Y.C. Yoo. The effect of aging treatment on the microstructure and mechanical properties of AA2124 hybrid composites reinforced with both SiC whiskers and SiC particles. *Composites Science and Technology*, 59:775–779, 1999.

[96] H. Ribes and M. Suery. Effect of particle oxidation on age hardening of Al-Si-Mg/SiC composites. *Scripta Metallurgica*, 23:705–709, 1989.

[97] L. Salvo and M. Suery. Effect of reinforcement on age hardening of cast 6061 Al-SiC and 6061 Al-Al_2O_3 particulate composites. *Materials Science and Engineering*, A177:19–28, 1994.

[98] B. Dutta and M.K. Surappa. Studies on age hardening characteristics of ceramic particle/matrix interfaces in Al-Cu-SiC_p composites using ultra low load dynamic microhardness measurements. *Journal of Materials Research*, 12:2773–2778, 1997.

[99] R.A. Higgins. *Engineering Metallurgy: Part 1: Applied Physical Metallurgy.* Edward Arnold, sixth impression edition, 1989.

[100] A. Tomer. *Structure of metals through optical microscopy.* ASM International, 1990.

[101] W. Kurz and D.J. Fisher. *Fundamentals of Solidification.* Trans. Tech. Publications, 3rd edition, 1992.

[102] M.C. Flemings and K.P. Young. Rheocasting. In *Yearbook of Science and Technology*, pages 49–58. McGraw-Hill, New York, 1978.

[103] R.E. Reed-Hill and R. Abbaschian. *Physical Metallurgy Principles.* PWS-Kent Publishing Company, Boston, USA, 1991.

[104] H. Gjestland. Thixotropic casting of Mg using a conventional casting machine. *North American Die Casting Association (NADCA), 18th Congress and Exposition*, 930753:101–106, October 1993.

[105] C. Thaw, R. Minet, J. Zemany, and C. Zweben. *Metal matrix composites for microwave packing components.* Electron packaging product, 27, August, 1987.

[106] M. Taya and R.J. Arsenault. *Metal Matrix Composites-Thermo mechanical behaviour.* Pergamon, Oxford, 1989.

[107] I. Jin and D.J. Lloyd. Solidification of SiC particulate reinforced Al-Si alloy composites. In J. Masounave and F.G. Hamel, editors, *Fabrication of Particulates Reinforced Metal Composites*, pages 47–52. ASM International, Montreal, Quebec, Canada, Sept. 1990.

[108] S.V. Kamat, J.P. Hirth, and R. Mehrabian. Mechanical properties of particulate-reinforced aluminium-matrix composites. *Acta Metallurgica*, 37:2395–2402, 1989.

[109] W. Zhou and Z.M. Xu. Casting of SiC reinforced Metal Matrix Composites. *Journal of Materials Processing Technology*, 63:358–363, 1997.

[110] P.K. Roghatgi, R. Asthana, and S. Das. Structure and properties of cast metal matrix composites. *International metal review*, 31(3):115–139, 1986.

[111] A. Mortensen and I. Jin. Solidification processing of metal matrix composites. *International Materials Review*, 37:101–128, 1992.

[112] R. Asthana and S.N. Tewari. Engulfment of forgein particles by a freezing interface. *Journal of Materials Science*, 28:5414–5425, 1993.

[113] D.M. Stefanescu, F.R. Juretzko, B.K. Dhindaw, A. Catalina, S. Sen, and P.A. Curreri. Particle engulfment and pushing by solidifying interfaces. part 1. ground experiments. *Metallurgical and Materials Transaction*, A(29):1697–1706, 1997.

[114] N. Han, G. Pollard, and R. Stevens. Interfacial structure and fracture of aluminium alloy A356-SiC particles metal matrix composite. *Materials Science and Technology*, 8:184–187, 1992.

[115] Q. Han and J.D. Hunt. Redistribution of particle during solidification. *ISIJ International*, 35:693–699, 1995.

[116] D.M. Stefanescu, B.K Dhindaw, S.A. Kacar, and A. Moitra. Particle engulfment and pushing by solidifying interfaces. part 2. microgravity experiments. *Met. Trans.*, A(19):2847–2856, 1988.

[117] J.T. Lin, D. Bhattachaaryya, and C. Lane. Machinability of a silicon carbide reinforced aluminum Metal Matrix Composite. *Wear*, 181-183:883–888, 1995.

[118] S.Y. Oh, J.A. Cornie, and K.C. Russell. Wetting of ceramic particle with liquid aluminium alloys, part II: Study of wettability. *Metallurgical transaction*, A(20):533–541, 1989.

[119] A. Kelly and N.H. Macmillan. *Strong solids.* Clarendon, Oxford, 3 edition, 1986.

[120] K.K. Chawla, editor. *Proceedings of Composite Materials-Science and processing*, Berlin, Germany, 1987. Springer.

[121] Z. Wang N. Wang and G.C. Weatherly. Formation of magnesium aluminite in cast SiC particulate reinforced Al(A356) metal matrix composites. *Metallurgical Transection*, A23:1423–1430, May 1992.

[122] K.P. Young. SSM casting process: Application and case studies in Al and Mg. In *North American Die Casting Association (NADCA), 20th Congress and Exposition*, volume 2-5, pages 403–410, Indianapolis, 2nd - 5th Oct. 1995.

[123] F. Dselannay, L. Froyen, and A. Deruyttere. The wetting of solid by molten metals and its relation to the preparation of mmcs. *Journal of Materials Science*, 22:1–16, 1987.

[124] A.J. Clegg. *Cast Metal Matrix Composites.* Foundryman, 84, 1991.

[125] B.C. Pai, G. Ramani, R.M. Pillai, and K.G. Satyanarayana. Role of magnesium in cast aluminium alloy matrix composites. *Journal of Materials Science*, 30:1903–1911, 1995.

[126] V. Laurent, D. Chatain, and N. Eustathopoulos. Wettability of SiO_2 and oxidised SiC by aluminium. *Journal of Materials Science and Engineering*, A(135):89–94, 1991.

[127] R. Warren and C.H. Anderson. Silicon carbide fibres and their potential for use in composite materials, part II. *Composites*, 15(2):101–111, April 1984.

[128] G. Ramani, T.R. Ramamohan, R.M. Pillai, and B.C. Pai. *Scripta Metallurgica*, (24):1419, 1990.

[129] D.D. Himbeault, R.A. Varin, and K. Piekarsksi, editors. *International symposium on advanced in processing of ceramic and metal matrix composites*, NS, Canada, Aug. 1989. Halifax.

[130] Y.U. Naidich. *Solid melt interfaces.* Nankova Dumba, Kiev, 1972.

[131] J. Tafto, K. Kristiansen, H. Westengen, A. Nygard, J.B. Borradaile, and D.O. Karsen, editors. *International symposium on advances in cast reinforced metal composites*, USA, Sept. 1988. Chicago, IL.

[132] B.C. Pai, K.G. Satyaranayana, and P.S. Robi. *Journal of materials science letters*, 11:779, 1992.

[133] M.D. Skibo and D.M. Schuster. *Process for preparation of composite materials containing nonmetallic particles in a metallic matrix, and composite materials made thereby.* US Patent No.: 4,786,467, Nov. 1988.

[134] S. Kennerknecht. MMC studies via the investment casting process. In J. Masounave and F.G. Hamel, editors, *Fabrication of Particulates Reinforced Metal Composites*, pages 87–100. ASM International, 1990.

[135] J. Hashim, L. Looney, and M.S.J. Hashmi. The enhancement of wettability of SiC particles in cast aluminium matrix composites. *Journal of Materials Processing Technology*, 119:329–335, 2001.

[136] J. Hashim, L. Looney, , and M.S.J. Hashmi. The wettability of SiC particles by molten aluminum alloys. *Journal of Materials Processing Technology*, 119:324–328, 2001.

[137] G.S. Hanumanth and G.A. Irons. Mixing and wetting in metal matrix composite fabrication. In J. Masounave and F.G. Hamel, editors, *Fabrication of Particulates Reinforced Metal Composites*, pages 41–46, Montreal, Quebec, Canada, Sept. 1990. ASM International.

[138] V. Agarwala and D. Dixit. Fabrication of aluminium base composites by foundry techniques. *Transaction Japan Institute of Metal*, 22:521–526, 1981.

[139] S. Caron and J. Masounave. A literature review on fabrication techniques of particulate reinforced metal composites. In J. Masounave and F.G. Hamel, editors, *Fabrication of Particulates Reinforced Metal Composites*, pages 79–86. ASM International, Montreal, Quebec, Canada, Sept. 1990.

[140] G. S. Hanumanth, G.A. Iron, and S. Lafrenier. *Met. Trans. B*, 23B:753, 1992.

[141] S.Y. Oh. Ph.D Thesis, Massachusetts Institute of Technology, 1987.

[142] C.G. Levi, G. J. Abbashian, and R. Mehrabian. *Metallurgical Transection*, 9A:697–711, 1976.

[143] L.F. Mondolfo. *Aluminium alloys: structure and properties.* Butterworth, London, 1976.

[144] Y.H. Teng and J.D. Boyd. Development of particulate coatings to control interface properties. In J. Masounave and F.G. Hamel, editors, *Fabrication of Particulates Reinforced Metal Composites*, pages 125–134. ASM International, 1990.

[145] T. Ishikawa, J. Tanaka, H. Teranishi, T. Okamura, and T. Hayase. *United State Patent*, (US No.: 440571), 1981.

[146] S. Caron and J. Masounave. Fabrication of MMCs by a bottom mixing foundry process. In J. Masounave and F.G. Hamel, editors, *Fabrication of Particulate Reinforced Metal Composites*, volume Montreal, Quebec, Canada, Sept., pages 107–113. ASM International, 1990.

[147] A.M. Korolkov. *Casting properties of metals and alloys.* Consultant Bureau, New York, 1963.

[148] Y. Kimura, Y. Mishima, S. Umekawa, and T. Suzuki. Compability between carbon fibre and binary aluminium alloys. *Journal of Materials Science*, 19:3107–3314, September 1984.

[149] K. Sukumaran, S.G.K. Pillai, R.M. Pillai, V.S. Kelukutty, B.C. Pai, K.G. Satyanarayana, and K.K. Ravikumar. The effects of magnesium additions on the structure and properties of Al-7Si-10SiC_p composites. *Journal of Materials Science*, 30:1469–1472, 1995.

[150] Y. Genma, Y. Tsunekawa, M. Okumiya, and N. Mohri. Melt stirring process with ultrasonic variation for the preparation of Al_2O_3 particle/Al-Mg composite slurry. In *4th Decennial Inter. Conf. On solidification Processing*, pages 97–100, Ranmoor House, University of Sheffield, UK, 1997.

[151] K.S. Foo, W.M. Banks, A.J. Craven, and A. Hendry. Interface characteriazation of an SiC particulate/6061 aluminium alloy composites. *Composites*, 25:677–682, 1994.

[152] S. Ray, editor. *Casting of composite components*, Banglore, India, 1996. Proceedings of the conference on inorganic matrix composites.

[153] R. Asthana and S.N. Tewari. Interfacial and capillary phenomena in solidification processing of metal matrix. *Composite Manufacturing*, 4:3–25, March 1993.

[154] L. Lajoye and M. Suery. *Solidification processing.* Sheffield, 1 edition, Sept., 1987.

[155] K.A. Lucas and H. Clarke. *Corrosion of Aluminium based metal matrix composites.* Research studies press Ltd., Taunton, Somerset, England, 1993.

[156] *Metal Handbook.* Ninth Edition, 13 edition.

[157] T. Christman, A. Needleman, and S. Suresh. An experimental and numerical study of deformation in metal ceramic composites. *Acta Metallurgica*, 37:3029–3050, 1989.

[158] M. Mabuchi and K. Higashi. Superplasticity in Metal Matrix Composites. *Key Engineering Materials*, 104-107:225–240, 1995.

[159] U. Cocen and K. Onel. The production of Al-Si alloy-SiC_p composites via compocasting: some microstructural aspects. *Materials Science and Engineering*, A221:187–191, 1996.

[160] S. Ray. Cast metal matrix composites-challenges in processing and design. *Bulletin Materials Science*, 18:693–709, 1995.

[161] A.M. Samuel, A. Gotmare, and F.H. Samuel. Effect of solidification rate and metal feedability on porosity and SiC/Al_2O_3 particle distribution in an Al-Si-Mg (359) alloy. *Composites Science and Technology*, 53:301–315, 1995.

[162] J.L. Beckers, D. Coutsouradis, and M. Lamberigts. Study of composite aluminium alloys produced by stir casting. In T. Khan and G. Effenberg, editors, *Advanced Al and Mg Alloys, ASM*, pages 719–726. ASM International, Amsterdam, Holland, 20th-22nd June 1990.

[163] P. Appendino and C. Badini. 6061 aluminium alloy SiC particulate composites: a comparison between aging behaviour in T4 and T6 treatment. *Materials Science and Engineering*, A(135):275–279, 1991.

[164] I.F. Richardson. *Casting of silicon carbide reinforced aluminium alloys.* Foundryman, 1989.

[165] L. Albingre F.A. Girot, J.M. Qeunisset, and R. Naslain. Rehological aluminium matrix composites. *Journal of materials*, 39:18–21, 1987.

[166] A.F. Whitehouse and T.W.Clyne. Cavity formation during tensile straining of particulate and short fibre Metal Matrix Composites. *Acta Metallurgica et Materialia*, 41:1701–1711, 1993.

[167] D.J. Lloyd, H. Lagace, A. Mcleod, and P.L. Morris. Microstructural aspect of Al-SiC_p composites produced by casting methods. *Materials Science and Engineering*, A(107):73-80, 1989.

[168] S. Abis. Characteristics of an Aluminium Alloy-Alumina MMC. *Composite Science and Technology*, 35:1–11, 1989.

[169] P. Kumar, K. Vedula, and A. Ritter, editors. *Microstructural effects on the fracture micromechanisms in 7XXX Al P/M-SiC particulate metal matrix composites, processing and properties for powder metallurgy composites*, Warrendale, 1987. TMS-AIME.

[170] H. B. McShane C.Y. Lin and R.D. Rawlings. Structure and properties of functionally gradient aluminium alloy 2124/SiC composites. *Materials Science and Technology*, 10:659–664, 1994.

[171] L. Salvo, G. L'Esperance, M. Suery, and J.G. Legoux. Interfacial reaction and age hardening in Al-Mg-Si Metal Matrix Composites reinforced with SiC particles. *Materails Science and Engineering*, A177:173–183, 1994.

[172] M.R. Piggot. *Load bearing fibre composites.* Pergamon press, London, 1980.

[173] T.W. Chou. *Microstructural design of fibre composites.* Cambridge University, Cambridge, United Kingdom, 1992.

[174] T. Ishikawa and T.W. Chou. Stiffness and strength properties of woven fabric composites. *Journal of Materials Science*, 17:3211–3220, 1982.

[175] K.C. Russell, S.Y. Oh, and A. Figueredo. Theoretical and experimental studies of ceramics: Metal wetting. *MRS Bulletin*, pages 46–52, 1991.

[176] R. Warren. In S.I. Andersen, editor, *9th Riso International Symposium on mechanical and physical behaviour of metallic and ceramic composite*, page 233, Denmark, 1988. Riso press.

[177] J.G. Legoux G. L'Esperance, L. Salvo, and M. Suery. Influence of particle oxidation on the interfacial structure of SiC reinforced Al-1In J. Masounave

and F.G. Hamel, editors, *Fabrication of Particulates Reinforced Metal Composites*, pages 31–40. ASM International, Montreal, Quebec, Canada, Sept. 1990.

[178] C.M. Ward-Close and P.G. Partridge. A fibre coating process for advanced metal matrix composites. *Journal of Materials Science*, 25:4315–4323, 1990.

[179] J.C. Viala, P. Fortier, and J. Bouix. Stable and metastable phase equilibria in the chemical interaction between aluminium and silicon carbide. *Journal of Materials Science*, 25:1842–1850, March 1990.

[180] I. U. Ogbuji A. H. Heuer and T. E. Mitchell. The microstructure of oxide scale on oxidised Si and SiC single crystals. *Journal of American Ceramic Society*, 63:354–355, 1980.

[181] G.H. Geiger and D. R. Doirier. *Transport phenomena in Metallurgy.* Addision Wesley Publication. Co., 1973.

[182] S. Laffreniere and G.A. Iron. Sedimentation during liquid processing of metal matrix composites. In M. Boushard and P. Tremblay, editors, *Proceedings of international Symposium on production, refining, fabrication and recycling of light metals*, pages 177–186. Pergamon Press, 1990.

[183] J.F. Richardson and W.N. Zaki. *Transaction of international Chemical Engineering*, 32:35–53, 1954.

[184] J.F. Richardson and W.N. Zaki. The sedimentation of a suspension of uniform spheres under conditions of viscous flow. *Chemical Engineering Science*, 3:65–73, 1954.

[185] S. Ray. Casting Metal Matrix Composites. *Key Engineering Materials*, 104-107:417–446, 1995.

[186] J.A. Sekhar and R Trivedi. Solidification microstructure evolution in the presence of inert particles. *Materials Science and Engineering*, 147:9–21, 1991.

[187] H. Liu and F. Samuel. Effect of some metallurgical parameters on the properties of a SiC particulate reinforced Al composite. In C. Shi, H. Li, and A. Scott, editors, *The First Pacific Rim Int. Conf. on Advanced Materials and Processing*, pages 595–600, Hangzhou, China, 23rd - 27th June 1992. The Minerals, Metals and Materials Society.

[188] V.M. Kevorkijan and B. Sustarsic. A new production technology for discontinuously reinforced Al-SiC composites. *Key. Eng. Mater.*, 127-131:471–178, 1997.

[189] P.R. Gibson, A.J. Clegg, and A.A. Das. Compocast graphitic aluminium-silicon alloys. *Foundry Trade Journal*, 25:253–263, 1982.

[190] P.R. Gibson, A.J. Clegg, and A.A. Das. Production and evalution of squeeze-cast graphitic Al-Si alloys. *Mat. Sci. Tech.*, 1:559–567, 1985.

[191] *Two phase flow behaviour and microstructure in Aluminium alloy SiC particulate composite*, 1993.

[192] D.D. Himbeault, R.A. Varin, and K. Piekarsksi. *Proceeding of international symposium on advances in processing of ceramic and metal matrix composites*, pages 312–323, 1989.

[193] A. Kolsgaard and S. Brusethaug. Settling of SiC particles in an AlSi7Mg melt. *Materials Science and Engineering*, A173:213–219, 1993.

[194] C.J. Quaak. *Rheology of partially solidified aluminium alloys and composites.* Ph.D Thesis, Technical University of Delft, 1996.

[195] J.A. Cornie, H.K. Moon, and M.C. Flemings. A review of semi-solid slurry processing of Al matrix composites. In J. Masounave and F.G. Hamel, editors, *Fabrication of Particulates Reinforced Metal Composites*, pages 63–78. ASM International, 1990.

[196] C.J. Quaak, W.H. Kool, and M. Suéry. Assessment of semi-solid state forming of Al MMCs. Part 1: Rheology. *AFS Transactions*, 30:421–426, 1995.

[197] C.J. Quaak, W.H. Kool, and M. Suéry. Assessment of semi-solid state forming of Al MMCs. Part 2: Forming. *AFS Transactions*, 31:427–430, 1995.

[198] C.G. Kang, Y.H. Moon, J.C. Choi, and J.S. Lee. Research activities of erc/nsdm on the semi-solid material processing and their application. In Chiarmetta and Rosso [264], pages 807–812.

[199] C.L. Martin, S.B. Brown, D. Favier, and M. Suery. Mechanical behaviour of course dendritic semi-solid Sn-Pb under various stress states. In Kiuchi [265], pages 27–36.

[200] P. Kumar, C.L. Martin, and S. Brown. Predicting the constitutive flow behavior of semi-solid metal alloy slurries. In Kiuchi [265], pages 37–46.

[201] P. Kumar, C. Martin, and S. Brown. Constitutive modeling and characterisation of the flow behaviour of semi-solid metal alloy slurries-I. the flow response. *Acta Metall. Mater.*, 42(11):3595–3602, 1994.

[202] M. Mada and F. Ajersch. Rheological model of semi-solid A356-SiC composite alloys. Part 1: Dissociation of agglomerate structures during shear. *Materials Science and Engineering*, A212:157–170, 1996.

[203] M. Mada and F. Ajersch. Rheological model of semi-solid A356-SiC composite alloys. Part II: Reconstitution of agglomerate structures at rest. *Materials Science and Engineering*, A212:171–177, 1996.

[204] M.L. Tims, J. Xu, G. Nickodemus, and F.R. Dax. Computer based numerical analysis of semi-solid metal working. In Kirkwood and Kapranos [263], pages 120–125.

[205] R.S. Qin and Z. Fan. Theoritical study on the evolution of grain morphology under high shear rate. In Chiarmetta and Rosso [264], pages 819–824.

[206] A. Prikhodovski, I. Hurtado, P. Spencer, and D. Neuschutz. Mathematical simulation of microstructure coarsening during preheating of aluminium alloys for thixoforming. In Bhasin et al. [266], pages 249–256.

[207] C. Geindreau and J. L. Auriault. Mechanical behaviour of metallic alloys in semi-solid state: mathematical modelling by an upscaling technique. In Chiarmetta and Rosso [264], pages 831–836.

[208] C.G. Kang, N.S. Kim, and H.K. Jung. Automatic mesh generation and remeshing for finite element simulation of semi-solid forming process. In Chiarmetta and Rosso [264], pages 801–806.

[209] D. Favier, J.C. Gebelin, and C.L. Martin. Influence of the solid skeleton deformation on the liquid segregation for semi-solid alloys under tensile stress states. In Chiarmetta and Rosso [264], pages 225–232.

[210] S. Toyoshima. A fem of densification in forming process for semi-solid materials. In Kiuchi [265], pages 47–62.

[211] Y. Chastel, J. Barlier, F. Bay, G. Lovato, and M. Bobadilla. Extrusion of semi-solid tin-lead alloys to determine the constitutive behaviour of the mushy zone. In Bhasin et al. [266], pages 257–264.

[212] A.M. Mullis. Proceedings of the fifth international conference on the semi-solid processing of alloys and composites. In Bhasin et al. [266], pages 265–272.

[213] A. Alexandrou, F. Bardinet, and W. Loue. Mathematical and computational modelling of die filling in semisolid metal processing. *Journal of Materials Processing Technology*, 96:59–72, 1999.

[214] R.T. Bui, R. Ouellet, and D. Kocaefe. A two-phase flow model of the stirring of Al-SiC composite melt. *Metallurgical and Materials transactions*, 25B:607–618, 1994.

[215] G.R. Burgos, A.N. Alexandrou, and V. Entov. Two-phase model of flow of semi-solid materials. In Bhasin et al. [266], pages 217–224.

[216] D. Kocaefe and R.T. Bui. One-phase model for stirring solid-liquid mixtures: SiC-Al melt. pages 49–60, 1993.

[217] D. Kocaefe and R.T. Bui. A one-phase model of the mixing of Al-SiC composite melt. *Metallurgical and Materials transactions*, 27B(5):1015–1023, 1995.

[218] J.C. Gebelin, D. favier, and M. Suery. Comparison of one-and two-phase approaches for numerical simulation of semi-solid processing. In Bhasin et al. [266], pages 309–316.

[219] H.K. Moon. *Rheological behavior and microstructure of ceramic particulate/aluminium alloy composites.* PhD thesis, MIT, Cambridge, MA, September 1990.

[220] A. Wahlen. Modeling the thixotropic flow behaviour of semi-solid aluminium alloys. In Chiarmetta and Rosso [264], pages 565–570.

[221] T. Imwinkelried, T. Schnorf, J.R. Gabathuler, J. Lagemenn, and H. Schelling. Mould optimization of the thixoforming process by numerical modelling. In Chiarmetta and Rosso [264], pages 515–520.

[222] X. Yang, S. Xie, M. Teller, and T. Altan. An investigation to determination the influence of geometric parameters on semi-solid metal flow. In Chiarmetta and Rosso [264], pages 789–794.

[223] *Phase diagrams:materials Science and technology.* Academic press, Inc., 1 edition, 1970.

[224] A. Wahlen and L. Tong. Thixoform: a special-purpose fe software for thixoforming process simulations. In Chiarmetta and Rosso [264], pages 825–830.

[225] C.J. Paradies, M. Rappaz, T. Imwinkelried, and J.P. Gabathuler. Simulation of the pressure die casting of a thixotropic aluminium alloy. In Kirkwood and Kapranos [263], pages 115–119.

[226] B. Binet and F. Pineau. A mixture approach to the numerical modelling of thixocasting. In Chiarmetta and Rosso [264], pages 539–544.

[227] D.H. Kirkwood, P.J. Ward, M. Barkhudarov, S.B. Chin, H.V. Atkinson, and T. Y. Liu. An initial assessment of the flow-3d thixotropic model. In Chiarmetta and Rosso [264], pages 545–552.

[228] A.N. Alexandrou, G. R. Burgos, and V.M. Entov. Modeling thixotropy and its effects on semi-solid casting. In *Proceedings of the Sixth International Conference on the Semi-Solid Processing of Alloys and Composites*, pages 553–558, Politecnico Di Torino, Italy, September 2000.

[229] B. Nohn and D. Hartmann. Use of simulation tools for optimization of the thixoforming process. In Chiarmetta and Rosso [264], pages 795–800.

[230] T. Imwinkelried, editor. *Proceedings of 9th Conf. On casting, Welding and Advanced Solidification Processes.* Aachen, Germany, August 2000.

[231] C.G. Kang and D.W. Kang. Forging process analysis of semi-solid aluminium materials. In Kirkwood and Kapranos [263], pages 142–147.

[232] A. Prikhodovsky, I. Hurtado, D. Neuschutz, H. Gorgeneck, and W. Bleck. Simulation and experimental investigations of microstructure coarsening of aluminium-alloys. In *Proceedings of the Sixth International Conference on the Semi-Solid Processing of Alloys and Composites*, pages 521–526, Politecnico Di Torino, Italy, September 2000.

[233] M. Kiuchi, J. Yanagimoto, and H. Yokobayashi. A new mathematical model to simulate flow of mushy/semi-solid alloys. In Chiarmetta and Rosso [264], pages 507–514.

[234] C.M. Wang, G.H. Nickodemus, and T.P. Creeden. Determining optional semi-sloid forming process prarameters by simulation technique. In Bhasin et al. [266], pages 327–334.

[235] A.M. Mullis, S.E. Battersby, and H.L. Fletcher. The application of analogue casting systems to semi-solid processing. In Bhasin et al. [266], pages 233–240.

[236] P.M. Armenante and E.U. Nagamine. Effect of low off-bottom impeller clearance on the minimum agitation speed for complete suspension of solids in stirred tanks. *Chemical Engineering Science*, 53:1757–1775, 1998.

[237] K.C. Chew A. Ourdjini and B.T. Khoo. Settling of carbide particles in cast Metal Matrix Composites. *Journal of Materials Processing Technology*, 16:72–76, 2001.

[238] M. Latsa, D. Assimacopoulos, A. Stamou, and N. Markatos. Two-phase modeling of batch sedimentation. *Applied Mathematical Modelling*, 23:881–897, 1999.

[239] M. Modigell, J. Koke, and J. Petera. Two-phase model for metal alloys in the semi-solid state. In Bhasin et al. [266], pages 317–326.

[240] L. Drenchev, J. Sobczak, and N. Sobczak. Sedimentation phenomenon and viscosity of water-SiC suspension under gravity conditions-a water model study for composites synthesis. *Colloids and Surface: A: Physical and Engineering Aspects*, 197:203–211, 2002.

[241] S. Naher, D. Brabazon, and L. Looney. Simulation of the stir casting process. *Journal of Materials Processing Technology*, 143-144:567–571, 2003.

[242] J. Hashim. *Production of metal matrix composites using the stir casting technique.* Ph.D Thesis, Dublin City University, 1999.

[243] M.W. Chudacek. Relationships between solids suspension criteria, mechanism of suspension, tank geometry, and scale-up parameters in stirred tanks. *Ind. Eng. Chem. Fundam*, 25:391–401, 1986.

[244] S. Chu and R. We. The structure and bending properties of squeeze-cast composites of A356 aluminium alloy reinforced with alumina particles. *Composites Science and Technology*, 59:157–162, 1999.

[245] L.N. Thanh and M. Suery. Microstructure and compression behavior in the semi-solid state of short fibre reinforced A356 aluminium alloys. *Materials Science and Engineering*, A196:33–44, 1995.

[246] N.S. Kim and C.G. Kang. An investigation of flow characteristics considering the effect of viscosity variation in the thixoforming process. *Journal of Materials Processing Technology*, 103:237–246, 2000.

[247] D. Brabazon. *Processing and properties of rheocast alloys.* PhD thesis, UCD, Dublin, Ireland, October 2001.

[248] J. Hashim, L. Looney, and M.S.J. Hashmi. Particle distribution in cast metal matrix composites-part II. *Journal of Materials Processing Technology*, 123:258–263, 2002.

[249] P.K. Rohatgi, J. Sobczak, R. Asthana, and J.K. Kim. Inhomogeneities in silicon carbide distribution in stirred liquids-a water model study for synthesis of composites. *Materials Science and Engineering*, A252:98–108, 1998.

[250] D.J. Brennan and I.H. Lehrer. Impeller mixing in vessels experimental studies on the influence of some parameters and formation of a general mixing time equation. *Chem. Engng Res. Des.*, 54:139–152, 1976.

[251] D.B. Holmes, R.M. Voncken, and J.A. Dekker. Fluid flow in turbine stirred, baffled tanks-i circulation time. *Chem. Engng Sci.*, 19:201–208, 1964.

[252] W.J. McManamey. A circulation model for batch mixing in agitated, baffled vessels. *Chem. Engng Res. Des.*, 58:271–275, 1980.

[253] R.M. Voncken, D. B. Holmes, and H.W. Den Hartog. Fluid flow in turbine stirred, baffled tanks-ii dispersion during circulation. *Chem. Engng Sci.*, 19:209–213, 1964.

[254] O.J. Ilegbusi and J. Szekely. *Computational Fluid Mechanics in Metal Processing*. ISM, 23 edition, 1991.

[255] N.E. El-Kaddah and K. E. Chang. The dispersion of SiC-Al slurries in rotating flows. *Materials Science and Engineering*, A(144):221–227, Oct 1991.

[256] S. Nagata. *Mixing principles and application*. John Wiley and Sons, 1975.

[257] F. Liepe and R. Koschek. *Chem. Tech. (leipzig)*, 29:378, 1977.

[258] T.N. Zwietering. Suspending solid particles in liquids by agitators. *Chemical Engineering Science*, 8:244–253, 1958.

[259] R. Darby and M. Dekker. *Chemical Engineering Fluid Mechanics*. Inc., 1996.

[260] R. Darby. Hydrodynamics of slurries and suspensions. *Chapter 2 in Encyclopaedia of fluid mechanics*, 5(N.P. Cheremisinoff, Ed.), Marcel Dekker 1986.

[261] A. Arnberg, O. Lahne, and N. Ryum, editors. *Aluminium Alloys.* NTH and SINTEF Trondhiem, Norway, 1992.

[262] H.K. Moon and J.A. Cornie M.C. Flemings. Rheological behavior and microstructure of ceramic particulate/aluminium alloy composites. In C. Shi, H. Li, and A. Scott, editors, *The First Pacific Rim Int. Conf. on Advanced Materials and Processing (PRICM-1)*, pages 669–674, Hangzhou, China, 23rd-27th June 1992. The Minerals, Metals and Materials Society.

[263] D.H. Kirkwood and P. Kapranos, editors. *Proceedings of the Fourth International Conference on the Semi-Solid Processing of Alloys and Composites.* University of Sheffield, England, 19th-21th June 1996.

[264] G.L. Chiarmetta and M. Rosso, editors. *Proceedings of the Sixth International Conference on the Semi-Solid Processing of Alloys and Composites.* Polytechnic di Turino, Turin, Italy, 27th-29th September 2000.

[265] M. Kiuchi, editor. *Proceedings of the Third International Conference on the Semi-Solid Processing of Alloys and Composites.* Institute of Industrial Science, University of Tokyo, Japan, 13th-15th June 1994.

[266] A.K. Bhasin, J.J. Moore, K.P. Young, and S. Midson, editors. *Proceedings of the Fifth International Conference on the Semi-Solid Processing of Alloys and Composites.* Colorado School of Mines, Denver, USA, 23rd-25th June 1998.

[267] *MixSim 1.5 User's Guide.* Fluent incorporation, September, 1998.

[268] *MixSim 1.5 Tutorial Guide.* Fluent incorporation, September, 1998.

[269] *Fluent Manual 4.5.* Fluent incorporation, November, 1998.

[270] J.D. Anderson. *Computational Fluid Dynamics the basics with applications.* Singapore, 1995.

[271] M. Syamlal and T.J. O'Brien. A generalized drag correlation for multiparticle systems. *Unpublished report*, 1986.

[272] M. Syamlal. The particle-particle drag term in a multiparticle model of fluidization. *Topical Report, DOE/MC/21353-2373, NTIS/DE87006500, National Technical Information Service*, Springfield, VA,, 1987.

[273] J. Ding and D. Gidaspow. A bubbling fluidization model using kinetic theory of granular flow. *AIChE J.*, 36(4):523–538, 1990.

Appendix A

Multiphase model

Most of these information was extracted from a number of Fluent manuals [267–269].

A large number of flows encountered in nature and technology are a mixture of phases. Physical phases of matter are gas, liquid, and solid. The concept of phase in a multiphase flow system is applied in a broader sense. In multiphase flow, a phase is defined as an identifiable class of material that has a particular inertial response to, and interaction with, the flow and the potential field in which it is immersed. For example, differently sized solid particles of the same material can be treated as different phases because each collection of particles with the same size will have a similar dynamical response to the flow field.

Some examples of complex multiphase systems are listed below for pure fluid multiphase systems and for fluid solid particulate multiphase systems.

Fluid multiphase systems

1. Gas/liquid droplet systems: Atomizers, scrubbers, dryers, absorbers, combustors, gas cooling, evaporation, cryogenic pumping

2. Liquid/gas bubble systems: Absorbers, evaporators, scrubbers, airlift pumps, cavitation, flotation, aeration, nuclear reactors

3. Liquid/gas systems: Boiling and nuclear reactor safety, surface waves of air over water

4. Liquid/liquid systems: Extraction, emulsification, separators, homogenization

Fluid/solid multiphase systems

1. Gas/solid particle systems: Cyclones, pneumatic conveyors, dust collectors, fluidized bed reactors, circulating bed reactors, fluid catalytic cracking, met-

allized propellant rockets, xerography, air classifiers, biomedical and physiochemical fluid systems, silos, dust laden environmental flows

2. Liquid/solid particle systems: Slurry transport, sedimentation, flotation, suspension, and some powder milling

A.1 Basic equations

The physical aspects of any fluid flow are governed by three fundamental principles:

1. Mass is conserved
2. Newton's second law - the acceleration of a particle is proportional to the resultant force acting on it and acts in the direction of this force.
3. Energy is conserved

These fundamental physical principles can be expressed in terms of basic mathematical equations, which in their most general form are either integral equations or partial differential equations [270]. These equations are discussed bellow. Computational fluid dynamics (CFD) is the art of replacing the integral or partial derivatives in these equations with discretised algebraic forms, which in turn are solved to obtain the flow field values at discrete points in time and/or space. The end product of CFD is a collection of numbers, in contrast to a closed form analytical solution. However, in the long run, the objective of most engineering analysis, closed form or otherwise, is a quantitative description of the problem.

Mass is conserved (Continuity equation)

The equation of continuity is really a mathematical statement of the principle of conservation of mass. In any fixed region within a fluid, in the absence of nuclear reaction, matter is neither created nor destroyed within that region:

$$\begin{aligned} &\textit{Rate at which mass enters the region} = \\ &\textit{Rate at which mass leaves the region} \\ &+ \textit{Rate of accumulation of mass in the region} \end{aligned} \tag{A.1}$$

If the flow is steady (that is unchanging with time) the rate at which mass is accumulated within the region is zero. The expression then reduces to:

Rate at which mass enters the region = Rate at which mass leaves the region (A.2)

This relation may now be applied to a stream tube whose cross-section is small enough for there to be no significant variation of velocity over it. A length δ_s of the stream tube is considered between the cross-sectional planes B and C (figure A.1), δ_s being so small that a variation in the cross-sectional area (A) along that length is negligible. The rate at which a mass of fluid enters a selected portion of a stream tube where the cross-sectional area is A_1, the velocity of the fluid u_1, and its density ρ_1, is $\rho_1(A_1)u_1$.

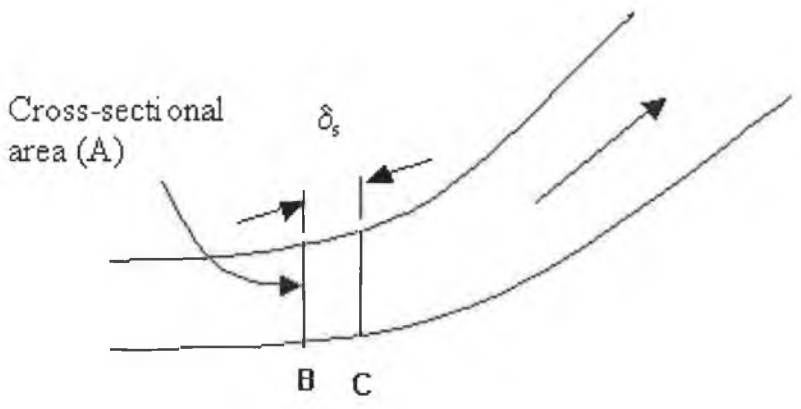

Figure A.1: Stream tube

Thus, from equation A.2 it can be written,

$$\rho_1(A_1)u_1 = \rho_2(A_2)u_2 = \ldots\cdots = constant \tag{A.3}$$

The general form for equation A.3 is

$$\rho(A)u = Constant \tag{A.4}$$

The law of conservation of mass states that matter cannot be created or destroyed; or expressing it as a time rate of change of total mass of a system of particles.

$$\frac{dM}{dt} = 0 \tag{A.5}$$

where, M is the total mass.

The rate of increase of mass in a 3D representation of a fluid element (figure A.2) is:

$$\frac{\delta}{\delta_t}(\rho\delta_x\delta_y\delta_z) = \frac{\delta\rho}{\delta_t}(\delta_x\delta_y\delta_z) \tag{A.6}$$

Let u, v, w be the velocities in the x, y, z directions and let x, y and z be a point in the center of a 3-D element. The mass flow rate across a face of the element is given by the product of density, area, and the velocity component normal to the face. From figure A.2 it can be seen that the net rate of flow of mass into the element across its boundaries is given by

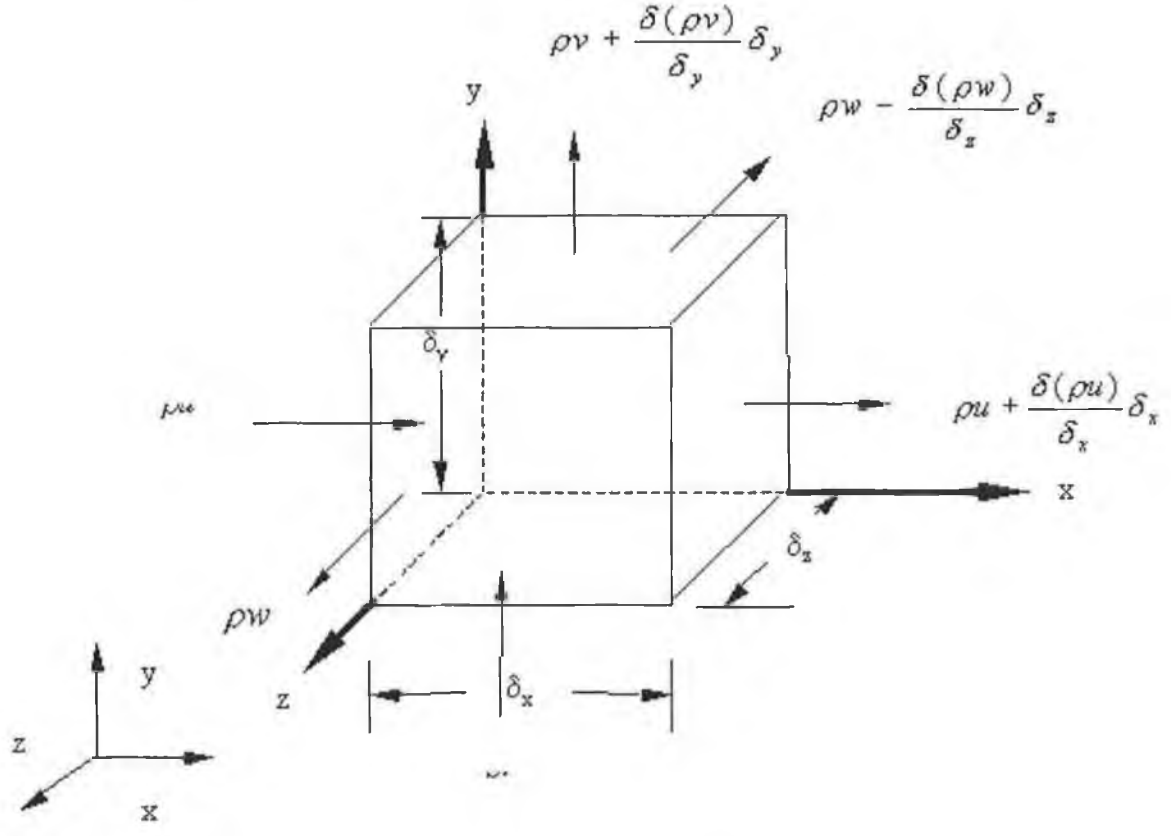

Figure A.2: Mass flows in and out of an infinitesimally small element

$$\begin{aligned}
\rho u\delta_y\delta_z - (\rho u + \frac{\delta(\rho u)}{\delta_x}\delta_x)\delta_y\delta_z + \\
\rho v\delta_x\delta_z - (\rho v + \frac{\delta(\rho v)}{\delta_y}\delta_y)\delta_x\delta_z + \\
\rho w\delta_x\delta_y - (\rho w + \frac{\delta(\rho w)}{\delta_z}\delta_z)\delta_x\delta_y = \frac{\delta\rho}{\delta_t}(\delta_x\delta_y\delta_z)
\end{aligned} \tag{A.7}$$

Flows which are directed into the element produce an increase of mass in the element and get a positive sign and those flows that are leaving the element are given a negative sign.

The rate of increase of mass inside the element which is represented by equation A.6 and the right side of equation A.7 is equated to the net rate of flow of mass into the element, across its faces which is represented by the left side of equation A.7. All terms of the resulting mass balance are arranged on the left hand side of the equals sign and the expression is divided by the element volume

This yields

$$\frac{\delta\rho}{\delta_t} + \frac{\delta(u)}{\delta_x} + \frac{\delta(v)}{\delta_y} + \frac{\delta(w)}{\delta_z} = 0 \tag{A.8}$$

or in more compact vector notation

$$\frac{\delta\rho}{\delta_t} + div(u) = 0 \tag{A.9}$$

Equation A.9 is the unsteady, three-dimensional mass conservation or continuity equation at a point in a compressible fluid. The first term on the left-hand side is the rate of change in time of the density (mass per unit volume). The second term describes the net flow of mass out of the element across its boundaries and is called the convective term.

For an incompressible fluid (i.e. a liquid) the density ρ is constant and equation A.9 becomes

$$div(u) = 0 \tag{A.10}$$

or in longhand notation

$$\frac{\delta u}{\delta_x} + \frac{\delta v}{\delta_y} + \frac{\delta w}{\delta_z} = 0 \tag{A.11}$$

A.1.1 Newton's second law (Momentum equation)

In rigid body mechanics it is customary to describe the motion of a body in terms of its position versus time. As seen in figure A.3, as the body moves along its trajectory, we can write Newton's laws of motion to determine position (s) versus time (t). For example, in the well known case of free fall of a rigid body starting from rest, Newton's law yields

$$m\frac{d^2s}{dt^2} = mg \tag{A.12}$$

where,

- m = mass of body
- g = acceleration due to gravity

- v = velocity body
- $s = s_0$ and, at $t = 0$

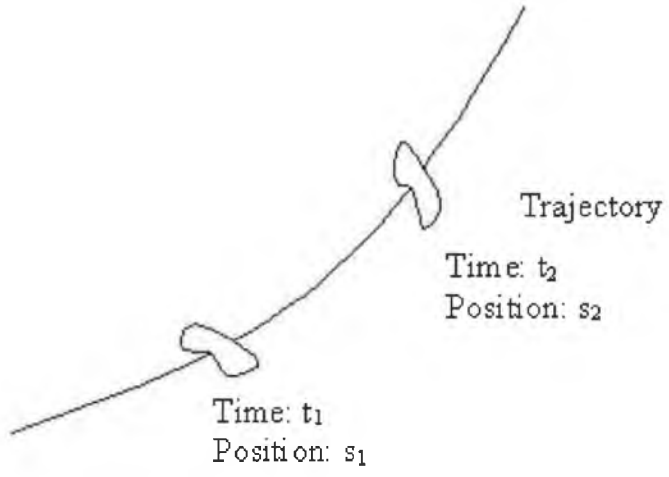

Figure A.3: Momentum equation for solid

Integrating equation A.12 twice, from s_1 to s_2 the following relationship can be obtained:

$$s_2 - s_1 = \frac{1}{2}gt^2 \tag{A.13}$$

This approach, in which the equation of motion for a moving particle is derived, is called the Lagrangian approach. However, in fluid mechanics, it is desirable to adopt a different approach, that is, to observe the motion of the fluid particles as they pass a given location in the fluid field. Unlike a rigid body, as a fluid body moves from one position to the next, it usually deforms continuously. Therefore, in order to describe completely the motion of a body of fluid, it is necessary to account for its deformation as well as its translation and rotation. Furthermore, it is often necessary to determine the velocity and pressure distribution about a body with given size and shape. Information about the flow is required at specified locations in the flow field. Thus the analysis of the motion of particles of fluid as they pass given locations is therefore necessary and is called the Eulerian or control volume approach.

Analysis of Newton's second law, which can be summarized as $F = ma$, results in the momentum equation.

Newton's second law, expressed above, when applied to the moving fluid element in figure A.4, says that the net force on the fluid element equals its mass times the acceleration of the element. This is a vector relation, and hence can be split into three scalar relations along the x, y, and z axes. Let us consider only the x component of Newton's second law,

$$F_x = ma_x \tag{A.14}$$

where F_x and a_x are the scalar x components of the force and acceleration, respectively. Firstly consider the left side of equation A.14. Considering the moving fluid element experiences a force in the x direction. There are two source of force:

1. Body forces act directly on the volumetric mass of the element. These forces act at a distance. Examples are gravitational, electric and magnetic forces.

2. Surface forces act directly on the surface of the fluid element. They are due to two sources: (a). The pressure distribution acting on the surface, imposed by the outside fluid surrounding the fluid elements, and (b). The shear and normal stress distributions acting on the surface, also imposed by the outside fluid tugging or pushing on the surface by means of friction.

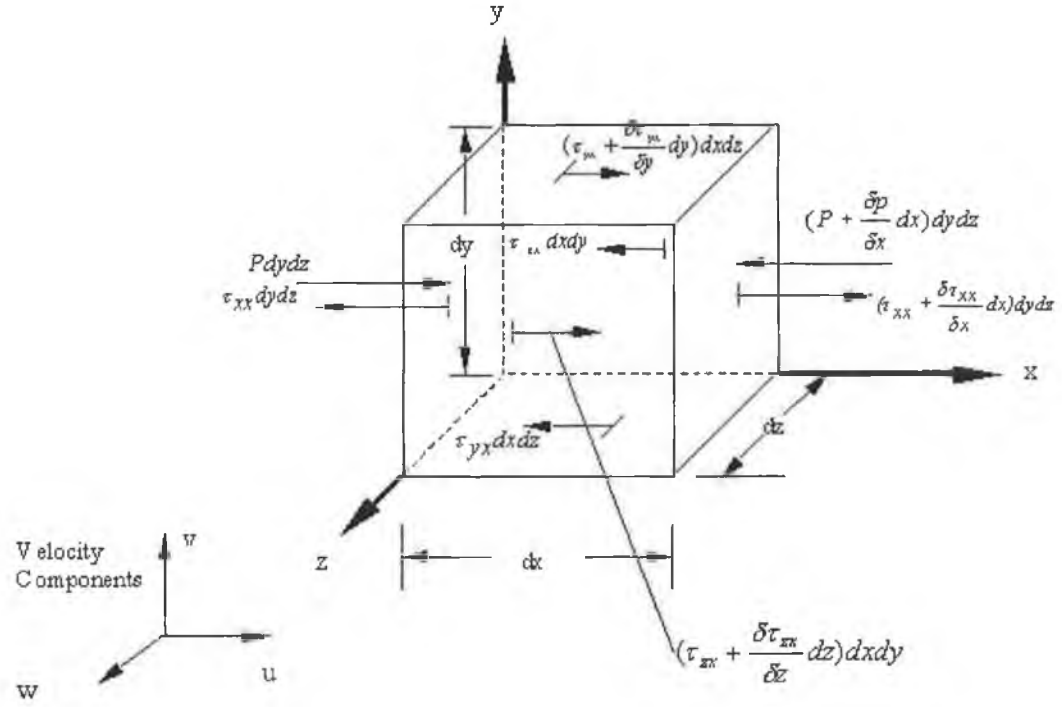

Figure A.4: Infinitesimally small, moving fluid element. Only the surface forces in the x direction are shown. The model is used for the derivation of the x component of the momentum equation.

Let us denote the body force per unit mass acting on the fluid element by f, with f_x as its x component. The volume of the fluid element is $(d_x d_y d_z)$. Hence, the body force on fluid element acting in x direction is $\rho f_x(d_x d_y d_z)$. Considering

figure A.4, for the moving fluid element it can be written the net surface force in the x direction as

$$[P-(P+\frac{\delta P}{\delta_x}d_x)]d_yd_z+[(\tau_{xx}+\frac{\delta\tau_{xx}}{\delta_x}d_x)-\tau_{xx}]d_yd_z$$
$$+[(\tau_{yx}+\frac{\delta\tau_{yx}}{\delta_y}d_y)-\tau_{yx}]d_xd_z+[(\tau_{zx}+\frac{\delta\tau_{zx}}{\delta_z}d_z)-\tau_{zx}]d_xd_y \quad (A.15)$$

where, P is the static pressure and τ is the stress

The total force in the x direction F_x, is given by the sum of equation A.14 and A.15. Adding these and cancelling out terms, we obtain,

$$F_x=[-\frac{\delta P}{\delta_x}+\frac{\delta\tau_{xx}}{\delta_x}+\frac{\delta\tau_{yx}}{\delta_y}+\frac{\delta\tau_{zx}}{\delta_z}]d_xd_yd_z+\rho f_xd_xd_yd_z \quad (A.16)$$

Equation A.16 represents the left-hand side of equation A.14. Considering the right-hand side of equation A.14, recall that the mass of the fluid element is fixed and is equal to

$$m=\rho d_xd_yd_z \quad (A.17)$$

The component of acceleration in the x direction, denoted by a_x, is simply the time rate of change of u. Since we are following a moving fluid element, this time rate of change is given by the substantial derivative.

$$a_x=\frac{Du}{Dt} \quad (A.18)$$

Thus, filling equations A.16, A.17 and A.18 into equation A.14 we obtain the following:

$$\rho\frac{Du}{Dt}=-\frac{\delta P}{\delta_x}+\frac{\delta\tau_{xx}}{\delta_x}+\frac{\delta\tau_{yx}}{\delta_y}+\frac{\delta\tau_{zx}}{\delta_z}+\rho f_x \quad (A.19)$$

which is the x component of the momentum equation for a viscous flow. In a similar fashion, the y and z component can be obtained as $\rho\frac{Dv}{Dt}=-\frac{\delta P}{\delta_y}+\delta$

$\tau_{xy}\overline{\frac{}{\delta_x+\frac{\delta\tau_{yy}}{\delta_y}+\delta}}$

$\tau_{zy}\overline{\frac{}{\delta_z+\rho f_y}}$

and

$$\rho\frac{Dw}{Dt}=-\frac{\delta P}{\delta_z}+\frac{\delta\tau_{xz}}{\delta_x}+\frac{\delta\tau_{yz}}{\delta_y}+\frac{\delta\tau_{zz}}{\delta_z}+\rho f_z \quad (A.20)$$

Equations A.19 to A.20 are the x, y and z components respectively of the momentum equation. These scalar equations are called the Navier-Stokes equations and are applicable for viscous flow. If we drop all the terms involving friction and thermal conduction, we then have the equations for an inviscid flow which

are termed the Euler equations. Considering only x-axis components from equation A.19,

$$\rho\frac{Du}{Dt} = -\frac{\delta P}{\delta_x} + \frac{\delta \tau_{xx}}{\delta_x} + \rho f_x \tag{A.21}$$

where,

$$\frac{Du}{Dt} = \frac{\delta u}{\delta t} + u\frac{\delta u}{\delta_x} + v\frac{\delta v}{\delta_y} + w\frac{\delta w}{\delta_z} \tag{A.22}$$

Considering only x axis component for equation A.22,

$$\frac{Du}{Dt} = \frac{\delta u}{\delta t} + u\frac{\delta u}{\delta_x} \tag{A.23}$$

and substituting equation A.23 in equation A.21 we obtain:

$$\rho(\frac{\delta u}{\delta t} + u\frac{\delta u}{\delta_x}) = -\frac{\delta P}{\delta_x} + \frac{\delta \tau_{xx}}{\delta_x} + \rho f_x \tag{A.24}$$

In the late seventeenth century, Newton stated that shear stress in a fluid is proportional to the time rate of strain, i.e., velocity gradients. Such fluids are called Newtonian fluids. Fluids in which shear stress is not proportional to the velocity gradients are called non-Newtonian fluids. For Newtonian fluids, Stokes in 1845 showed that,

$$\tau_{xx} = \lambda(\nabla V) + 2\mu\frac{\delta u}{\delta_x} \tag{A.25}$$

where λ is the second viscosity co-efficient and μ is the molecular viscosity co-efficient. Substituting equation A.25 into equation A.24 we obtain:

$$\rho(\frac{\delta u}{\delta t} + u\frac{\delta u}{\delta_x}) = -\frac{\delta P}{\delta_x} + \frac{\delta}{\delta_x}(\lambda(\nabla V) + 2\mu\frac{\delta u}{\delta_x}) + \rho f_x \tag{A.26}$$

Stokes made the correct hypothesis that,

$$\lambda = -\frac{2}{3}\mu \tag{A.27}$$

Substituting equation A.27 into equation A.26 we obtain:

$$\rho(\frac{\delta u}{\delta t} + u\frac{\delta u}{\delta_x}) = -\frac{\delta P}{\delta_x} + \frac{\delta}{\delta_x}(-\frac{2}{3}\mu(\nabla V) + 2\mu\frac{\delta u}{\delta_x}) + \rho f_x \tag{A.28}$$

or,

$$\rho(\frac{\delta u}{\delta t} + u\frac{\delta u}{\delta_x}) = -\frac{\delta P}{\delta_x} + \frac{\delta}{\delta_x}(2\mu\frac{\delta u}{\delta_x}) + \frac{\delta}{\delta_x}(-\frac{2}{3}\mu(\nabla V) + \rho f_x \tag{A.29}$$

This is another form of momentum equation A.19.

A.1.2 Energy is conserved

For a system of fluid particles, the law of conservation of energy states that the total energy E of the system increases, in going from state 1 to state 2, by an amount equal to the heat energy added to the system of particles less the work done by the system of fluid particles:

$$E_2 - E_1 = \dot{Q} - \dot{W} \tag{A.30}$$

Here E represents the total energy possessed by the system in a given state and thereby includes the kinetic and potential energy of the entire system mass, the internal energy associated with the random motion of the molecules comprising the system, and other forms of storable energy, such as electrical energy (such as, stored in capacitor) and chemical energy. Heat and work are not properties of a system of particles but rather are forms of energy that are transferred across the system of boundaries. Therefore, the heat and work transferred during a process are functions of the process itself, not just the end states. Energy equation A.30 in differential form becomes

$$dE = d\dot{Q} - d\dot{W} \tag{A.31}$$

A.2 Multiphase modelling in Fluent 5.4

Fluent is a state of the art computer program for modelling fluid flow and heat transfer in complex geometries. PreBFC is the name of Fluent's preprocessor. Gambit is the most common grid generation package for Fluent. Fluent can handle incompressible and compressible fluid flow simulations. An additional package from Fluent is MixSim. MixSim is used for mixing and discrete phase simulation in a closed container, the geometry and the meshing grid can be easily generated with this package.

There are different versions of the Fluent package, each of which has unique modelling techniques from other versions. Like all other software, Fluent software is unable to maintain consistency with subsequent versions. Fluent 5.4 has an Algebraic Slip Mixture (ASM) model for multiphase modelling, but in Fluent 4.5 there was no such technique. On the other hand there is a Eulerian granular technique in Fluent 4.5 which is not available in Fluent 5.4 which is a two phase simulation for multiphase modelling. Although both of these modelling methods are multiphase techniques there is little other similarity. Another point of note is that if a grid generation process for a multiphase model is necessary, MixSim rather than Gambit should be used. MixSim is specifically designed to build the

mixing geometry. For multiphase (fluid-solid) modelling with grid generated by MixSim the only choice is the Eulerian (Granular) model.

In Fluent there are options for discrete phase modelling. These modelling capabilities allow Fluent to simulate a wide range of dispersed phase problems including particle separation and classification, spray drying, bubble stirring of liquids, liquid fuel combustion, and coal combustion. In practice these issues imply that the dispersed phase must be present at a fairly low volume fraction, less than 10-12 %. When the particle volume fraction exceeds this limit, the use of the Eulerian multiphase model should be considered. Note that the mass loading of the dispersed phase may greatly exceed 10-12 %. Problems may be solved with this modelling method in which the mass flow of the dispersed phase equals or exceeds that of the continuous phase. The Lagrangian dispersed phase model is normally used to model continuous suspensions of particles which is suited for flows in which particle streams are injected into a continuous phase flow with a well-defined entrance and exit condition. The Lagrangian model does not effectively model flows in which particles are suspended indefinitely in the continuum, as occurs in solid suspensions within closed systems such as stirred tanks, mixing vessels, or fluidized beds. Such systems can be treated by Fluent using the Eulerian multiphase model.

Three models for multiphase flow are available in Fluent 5.4. These are the Volume of Fluid (VOF) model, the cavitation model and the Algebraic Slip Mixture (ASM) model. For the VOF model, two or more immiscible fluids or phases are considered where the interface between the fluids is of interest. So, no mass transfer between the fluids is allowed. A single set of momentum equations is shared by the volume fraction of each of the fluids.

In the cavitation model, two interpenetrating fluids can be modelled but this model does not assume that there is an interface between two immiscible fluids. Mass transfer between the fluids is allowed. For the cavitation model a single set of momentum equations are shared by the fluids and a continuity equation for the primary phase is solved.

Like the cavitation model, the ASM model allows for two interpenetrating phases but does not assume that there is an interface between immiscible phases. However, this model does not allow for any mass transfer between the fluids. The flow of a two phase system is simulated with the ASM model by solving the momentum equation and the continuity equation for the mixture, the volume fraction equation for the secondary phase and an algebraic expression for the relative velocity. This allows the two phases to move at different velocities. In the VOF and cavitation models, there are no facilities to model a solid phase, these only deal with fluids. So, in Fluent 5.4, simulation of the solid-liquid multi phase

system is limited to use of the ASM model. Theory and basic equations for ASM modelling are mentioned next.

A.2.1 Continuity equation for the mixture

The differential one dimensional continuity equation for the mixture is

$$\frac{\delta \rho_m}{\delta_t} + \frac{\delta(\rho_m u_{m,i})}{\delta_{xi}} = 0 \tag{A.32}$$

A.2.2 The momentum equation for the mixture

For falling or settling particles, friction force, gravitational force, and drag force are also to be considered in the momentum equation. Thus, the momentum equation for the mixture can be obtained by summing the individual momentum equations for both phases. It can be expressed as

$$\frac{\delta \rho_{m,j}}{\delta_t} + \frac{\delta({}_m u_{m,i} u_{m,j})}{\delta x_i} = -\frac{\delta P}{\delta x_j} + \frac{\delta \mu_m}{\delta x_i}\left(\frac{u_{m,i}}{}_j + \frac{u_{m,j}}{\delta x_i}\right) + \rho_m g_j + F_j + \frac{\delta}{\delta x_i}\sum_{k=1}^{n} \alpha_k \rho_k u_{Dk,i} u_{Dk,j} \tag{A.33}$$

where n is the number of phases, ρ_m is the mixture density, α is the volume fraction, α_i α_j α_k are the volume fraction at i, j and k grid in the x, y and z coordinates.

$$\rho_m = \sum_{k=1}^{n} \alpha_k \rho_k \tag{A.34}$$

μ_m is the viscosity of the mixture,

$$\mu_m = \sum_{k=1}^{n} \alpha_k \rho_k \tag{A.35}$$

$\vec{u_m}$ is the mass-average velocity,

$$\vec{u_m} = \frac{\sum_{k=1}^{n} \alpha_k \rho_k \vec{u_k}}{\rho_m} \tag{A.36}$$

and $\vec{u_{Dk}}$ are the drift velocities,

$$\vec{u_{Dk}} = \vec{u_k} - \vec{u_m} \tag{A.37}$$

A.2.3 The relative (slip) velocity and the drift velocity

The relative velocity (also referred to as the slip velocity) is defined as the velocity of the secondary phase ($\vec{u_p}$) relative to the primary-phase ($\vec{u_q}$) velocity:

$$\vec{u_{qp}} = \vec{u_p} - \vec{u_q} \tag{A.38}$$

The drift velocity and the relative velocity are connected by the following expression:

$$\vec{u_{Dp}} = \vec{v_{qp}} - \sum_{i=1}^{n} \frac{\alpha_i \rho_i}{\rho_m} \vec{v_{qi}} \tag{A.39}$$

The word 'drift' is the gradual departure from an intended course due to external influence. In hydrological engineering however, drift is also used to represent the rate of flow of a current of water, such as river. So drift velocity is the speed at which the water in a river is flowing. This also means the motion due to some current.

The basic assumption of the ASM model is that, to prescribe an algebraic relation for the relative velocity, a local equilibrium between the phases should be reached over short spatial length scales. The form of the relative velocity is given by

$$\vec{v_{qp}} = \sigma_{pq} \vec{a} \tag{A.40}$$

where is the secondary-phase particle's acceleration and $\sigma_{p,q}$ is the particulate relaxation time; the time constant of an exponential return of a system to equilibrium after a disturbance:

$$\sigma_{pq} = \frac{\rho_p d_p^2}{18 \mu_q} \tag{A.41}$$

where d_p is the secondary phase particle diameter. In this model acceleration of the particle is given by gravity and/or a centrifugal force.

A.2.4 Turbulence in multiphase

To describe the effects of turbulent fluctuations of velocities and scalar quantities in a single phase, Fluent uses various types of colour models. In comparison to single phase flows, the number of terms to be modelled in the momentum equations in multiphase flows is large, and this makes the modelling of turbulence in multiphase simulations extremely complex.

In two dimension layers the changes in the flow direction are always so slow that the turbulence can adjust itself to local conditions. If the convection and

diffusion of turbulence properties can be neglected it is possible to express the influence of turbulence on the mean flow in terms of mixing length. If convection and diffusion are not negligible as is the case for example in recirculating flows a compact algebraic prescription for the mixing length is no longer feasible. The mixing length model lacks this kind of generality. The way forward is to consider statements regarding the dynamics of turbulence. The $k-\varepsilon$ model focuses on the mechanism that effects the turbulent kinetic energy.

Fluent provides two methods for modelling turbulence in multi-phase flows within the context of the $k-\varepsilon$ model:

1. Dispersed turbulence model (default)

2. Secondary turbulence model

The choice of model depends on the importance of the secondary - phase turbulence in the application.

A.3 Multiphase modelling in Fluent 4.5

The Eulerian Multiphase model is the most effective way of modelling multi phase problems in Fluent 4.5. The Eulerian multiphase model solves a set of n momentum, enthalpy, continuity and different species for each phase. Coupling is achieved through the pressure and interphase exchange coefficients. The manner in which this coupling is handled depends upon the type of phases involved; granular (liquid-solid) flows are handled differently than nongranular (fluid-fluid) flows. For granular flows, the flow properties are obtained from the application of kinetic theory. Momentum exchange between the phases is also dependent upon the type of mixture being modelled.

The Eulerian multiphase model in Fluent allows for the modelling of multiple separate, yet interacting phases. The phases can be liquids, gases, or solids in nearly any combination. Currently, there are two approaches in Fluent for the numerical calculation of multiphase flows: the Euler-Lagrange and the Euler-Euler approach.

A.3.1 The Euler-Lagrangian approach

The Lagrangian Dispersed Phase Model follows the Euler-Lagrange approach. The fluid phase is treated as a continuum by solving the time averaged Navier-Stokes equations, while the dispersed phase is solved by tracking a large number of particles, bubbles, or droplets through the calculated flow field. The dispersed

phase can exchange momentum, mass, and energy with the fluid phase. A fundamental assumption made in this model is that the dispersed second phase occupies a low volume fraction, even though high mass loading is acceptable. The particle or droplet trajectories are computed individually at specified intervals during the fluid phase calculation. This makes the model appropriate for the modelling of spray dryers, coal and liquid fuel combustion, and some particle-laden flows, but inappropriate for the modelling of liquid-liquid mixtures, fluidized beds, or any application where the volume fraction of the second phase is not negligible.

A.3.2 The Euler-Euler approach

In the Euler-Euler approach, the different phases are treated mathematically as interpenetrating continua. Since the volume of a phase cannot be occupied by the other phases, the concept of phasic volume fraction is introduced. These volume fractions are assumed to be continuous functions of space and time and their sum is equal to one. Conservation equations for each phase are derived to obtain a set of equations which have similar structure for all phases. These equations are closed by providing constitutive relations which are obtained from empirical information, or, in the case of granular flows, by application of kinetic theory. In Fluent, the Euler-Euler model can be used in two multiphase models, the VOF (Volume of Fluid) Model and the Eulerian Multiphase Model. The Eulerian multiphase model solves momentum equations for each of the phases, which are allowed to mix in any proportion. This model differs from the Volume of Fluid (VOF) multiphase model, which solves a single set of momentum equations and tracks the phase interface explicitly with an auxiliary transport equation.

A.3.3 Features of the Eulerian multiphase (Euler-Euler) model

With the Eulerian multiphase model, the number of secondary phases is limited only by memory requirements and convergence behaviour. Any number of secondary phases can be modelled, provided that sufficient memory is available. For complex multiphase flows, however, solutions may be limited by convergence behaviour.

A.3.4 Granular (Fluid-Solid) flows

In the Euler-Euler approach if one phase is a fluid and one or more of the phases is a solid, the flow is characterized as granular. For this class of flows, the Fluent solution is based on the following:

1. The fluid is represented by the primary phase.
2. All secondary phases are solids (i.e., you cannot model a granular flow that involves more than one fluid phase).
3. The fluid pressure field is shared by all phases.
4. A solids pressure field is calculated for each solid phase.
5. Momentum, enthalpy, and continuity equations are solved for each phase.
6. The gas law can be used for the primary phase.
7. Granular temperature can be calculated for each solid phase.
8. Solid-phase shear and bulk viscosities are obtained from application of kinetic theory to granular flows.
9. Simple and fluid-solid (granular) interphase drag coefficients are used for spherical particles.
10. m species can be solved for each phase.
11. Homogeneous reactions are allowed for each phase.
12. Mass transfer is allowed between the phases.
13. The k-ϵ turbulence model is available for each phase.

A.3.5 Limitations

All other features available in Fluent can be used in conjunction with the Eulerian multiphase model, except for the following limitations:

1. The RNG $k-\varepsilon$ and Reynolds Stress models for turbulence can not be used.
2. Particle tracking (using the Lagrangian dispersed phase model) interacts only with the primary phase.
3. Specified periodic mass flow is not allowed.
4. Compressible flow is not allowed.
5. The Eulerian multiphase model cannot be used with sliding or deforming meshes.
6. Phase change (melting, freezing) is not allowed.
7. Heterogeneous reactions (i.e., reactions between phases) are not allowed, except via user-defined subroutines.

A.3.6 Theory and basic equations for Eulerian (Granular) multiphase model

To change from a single-phase model, where a single conservation equation for momentum and continuity is solved, to a multi-phase model, additional sets of conservation equations must be introduced. In the process of introducing additional sets of conservation equations, the original set must be modified.

A.3.7 Solution method for Eulerian (Granular) multiphase model

Pressure and velocities are corrected so as to satisfy the continuity constraint. In multiphase flow, this is further complicated by the following facts:

1. there are n continuity equations and usually a single pressure field,
2. phasic volume equations are a new unknown in the set of governing equations, and
3. the momentum equations are strongly coupled through the interphase momentum exchange coefficient.

The steps followed in Fluent to model granular multiphase flows are summarized below:

1. Getting initial conditions and boundary conditions.
2. Performing time-step iteration.
3. Calculating primary fluid velocity.
4. Calculating pressure correction from fluid continuity equation and correct fluid velocity, pressure, and fluid fluxes.
5. Calculating phasic volume fractions.
6. Calculating solid velocities.
7. Calculating solid pressure corrections and correct solid velocities, fluxes, and solid volume fractions. Update properties and calculate granular temperature.
8. Calculating other scalar quantities. If not converged, go to 3.
9. Advancing time step and go to 2.

A.4 Eulerian multiphase flow modelling strategies

A.4.1 Problem solving steps

Model selection is an important step for every modelling. Before beginning to solve a problem using the Eulerian multiphase model, it must be determined that this model is appropriate for the particular problem. For stratified or free surface flows the VOF model should be used, and for flows in which particle volume fractions are less than or equal to 10 % the Lagrangian dispersed phase model should be used. When phases mix and/or particle volume fractions exceed 10% the Eulerian multiphase model should be used.

Computational effort is the next important factor to consider for multiphase modelling. The required computational effort depends strongly on the number of equations being solved and the degree of coupling. For the Eulerian multiphase model, which has a large number of highly coupled transport equations (continuity equation, momentum equation and energy equation) computational expense will be high. Before setting up such a model, the problem statement should be reduced to the simplest form possible, in order to reduce computation effort and time.

Simplifying the problem statement is another important thing to keep in mind. Instead of initially trying to solve a multiphase flow in all of its complexity, simple approximations should be started with and worked up to the final form of the problem definition. Some suggestions for simplifying a multiphase flow problem are listed below:

1. Using a simplified geometry.
2. Beginning with a 2D approximation.
3. Solving a single-phase problem, using a composite density.
4. Reducing the number of phases.

It might be found that even a very simple approximation will provide useful information about specific problems. The important steps to be worked out to obtain a multiphase flow solution current simulation in MixSim and Fluent package are shown in the flow chart (figure A.5).

A.4.2 Convergence and stability

The process of solving a multiphase system is inherently difficult, and it may encounter stability or convergence difficulties. In general, mixtures involving phases

with large density differences (such as, water and air) may require more computational effort than mixtures where the densities are closer in magnitude. There are physical limitations when the volume fraction of a secondary phase increases to its maximum possible value (that is, the packing limit for a solid phase or 1.0 for a fluid phase). In such cases the momentum exchange law may not be valid and convergence problems may appear. Stratified flows of immiscible fluids can be solved more efficiently with the VOF model. Some problems involving small volume fractions can be solved more efficiently with the Lagrangian dispersed phase model. Many stability and convergence problems can be minimized if care is taken during the setup and solution processes.

Even a simplified approximation of a multiphase flow problem may require significant computational effort, so patient is needed during the solution process. If difficulty is encountered in obtaining a converged solution, the following suggestions may be tried:

1. Patching an initial guess for all variables.
2. Increasing the sweeps on the momentum equations for all phases.
3. Lowering the underrelaxation factors.
4. Solving as a pseudo-transient to approach steady-flow solution, rather than attempt a steady-state calculation.
5. Lowering the density ratio; increase it in stages.
6. Temporarily suppressing the exchange coefficient or begin a granular simulation with a non-granular model, switching after partial convergence is obtained.

A.4.3 Using the Eulerian multiphase model in Fluent

Two models for granular flows have been implemented in Fluent. One is based on the work of Syamlal et al. [271, 272] and the other is based on that of Ding and Gidaspow [273]. The main differences between the models are the expressions for the radial distribution function, the expression of kinetic particles of the solids viscosity, and the diffusion coefficient of the granular temperature. The default model is Syamlal et al.

Only the Gidaspow model was available for calculation of the radial distribution function, the kinetic part of the solids viscosity, and the exchange coefficient. Since the default model is that of Syamlal et al., it was necessary to enable the

Gidaspow model in the Multiphase Parameters panel or in the Eulerian multiphase options table. In the literature there is no unique formulation for the radial distribution function. Fluent automatically employs Syamlal et al. expressions when the number of solid phases is greater than or equal to 1.

The steps necessary to set up and run a variety of multiphase problems are as follows:

1. Turning on the Eulerian multiphase model
2. Specifying the phases
3. Setting boundary conditions
4. Setting physical properties
5. Models for granular flows
6. Time-dependent simulations
7. Modelling turbulence
8. Species transport
9. Modelling interphase heat transfer
10. Modelling interphase mass transfer
11. Solution strategies for Eulerian multiphase calculations
12. Eulerian multiphase options

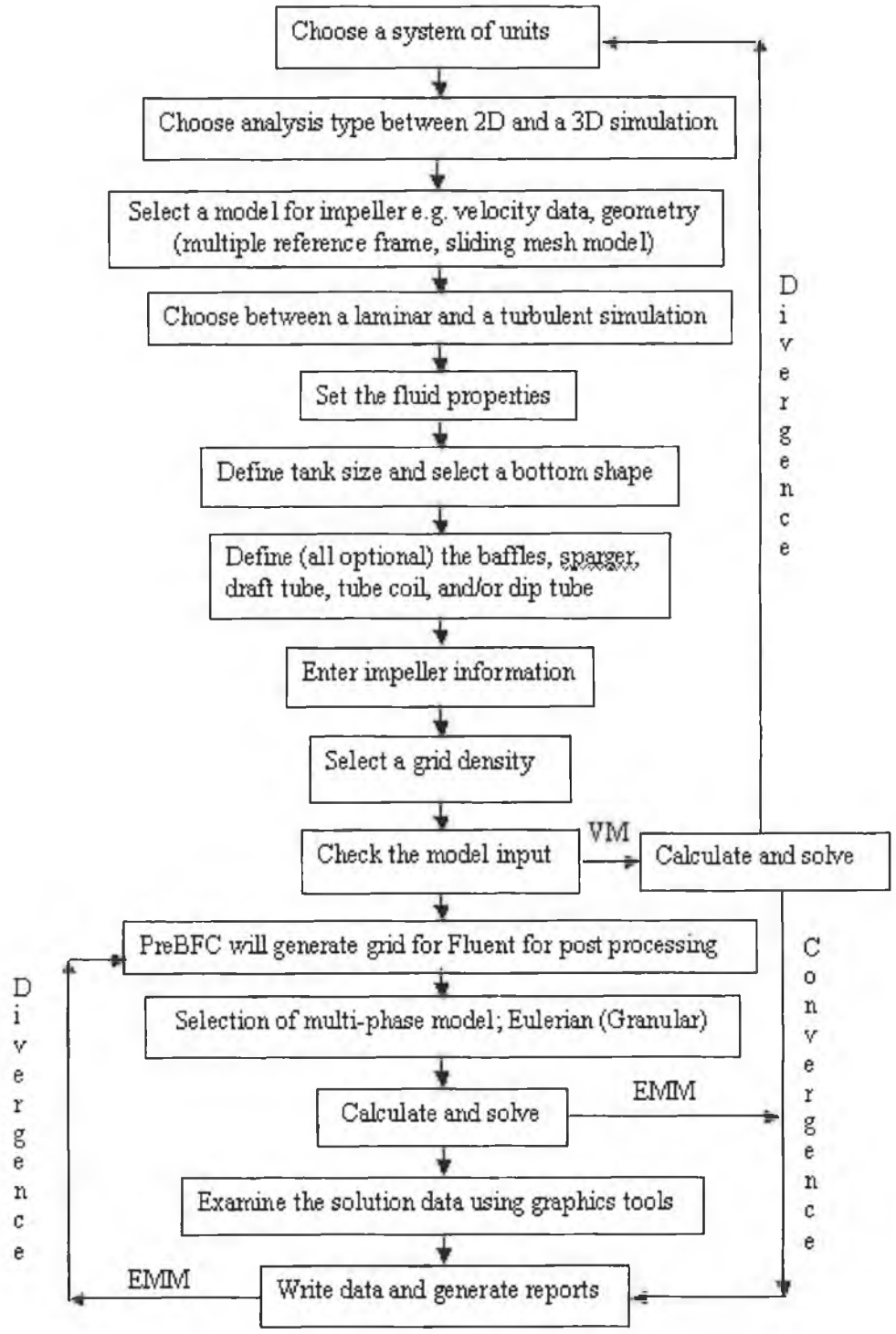

Figure A.5: Steps to be worked out to obtain a multiphase flow solution. VM stands for velocity model and EMM stands for Eulerian multiphase model.

Appendix B

Some Fluent features

This appendix consist of some Fluent features. Figure B.1 represents grids generated for 2D and 3D simulation. The pink colour outside the crucible is representing the wall and solid stirrer for stirrer geometry. Blue colour is representing the top of the crucible. Red colour representing the continuation of the same fluid field and symmetry. In figure B.1 (a) there are 1209 cells and in figure B.1 (b) there are 59241 cells.

Figure B.2 shows the Iteration-residual diagram for water and glycerol/water in Fluent solution process for 3D problems. For water turbulent and eddy dissipation are shown in these figures and for glycerol/water only pressure and velocity components were solved. Solution in water are found to be very unstable but solution in glycerol/water were very linear and stable in nature.

Figure B.3 shows the dispersion and settling simulation set-up in Fluent. Sky blue colour in figure B.3 (a) represents 0.6 volume fraction of SiC and yellow colour represents the presence of water without any SiC presence. Sky blue colour in figure B.3 (b) represent a uniform mixture of 0.1 volume fraction of SiC either with water or glycerol/water system. Same colour represent different volume fraction of SiC in different figures. This is why every picture has a volume fraction of SiC scale bar included in the left side of it.

Settling of SiC particulate in water is shown in figure B.4 (a), (c) and (e). After 2 s settling begins in water. After 12 s significant settling is observed. After 60 s practically fully settled SiC was found. Settling of SiC particulate in glycerol/water is shown in figure B.4 (b), (d) and (f). After 1 minute no settling was observed in glycerol/water. After 60 minutes settling begins. After 70 minutes, significant settling of SiC was observed.

(a) (b)

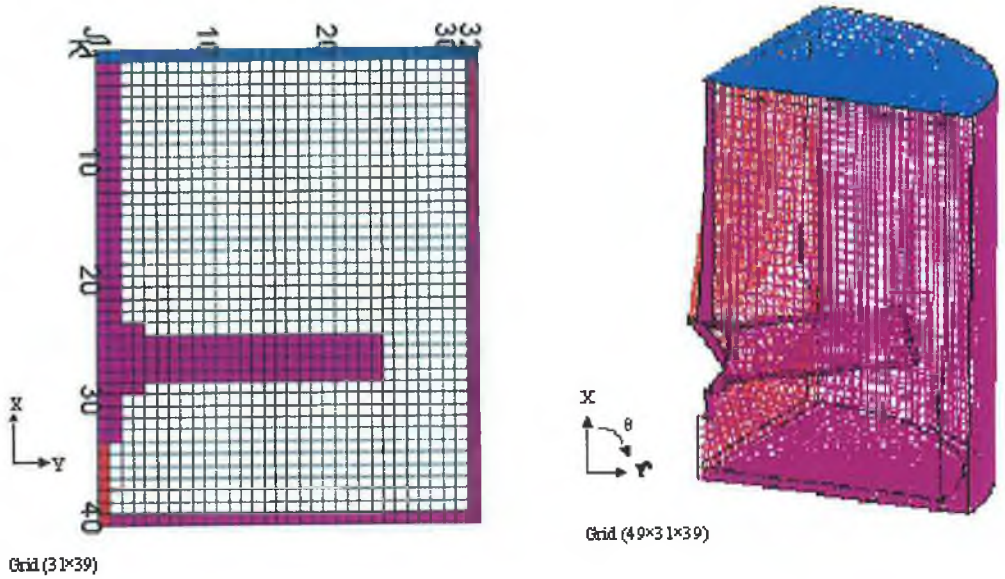

Figure B.1: (a) Grid generated in FLUENT for 2D simulation (b) Grid generated in FLUENT for 3D simulation.

(a) (b)

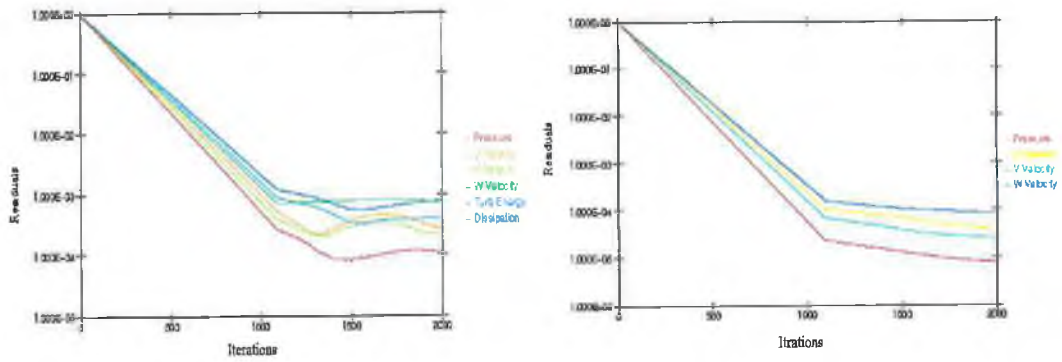

Figure B.2: Iteration-residual diagram for (a) water and (b) glycerol/water in Fluent solution process for 3D problems.

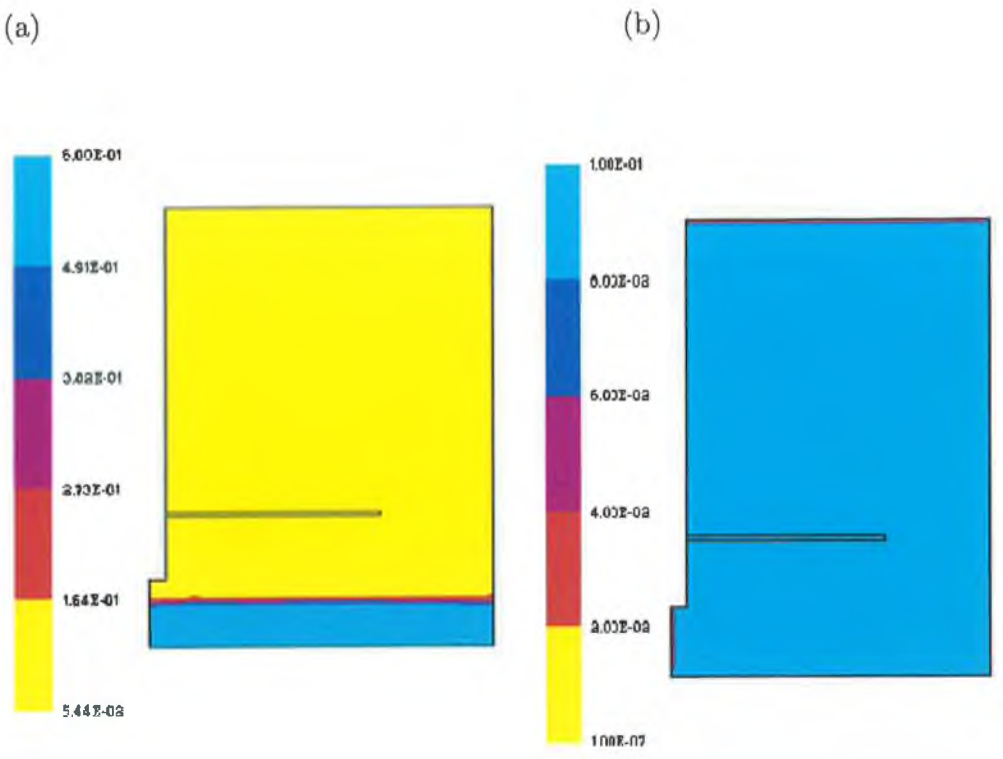

Figure B.3: Model set-up (a) for dispersion (b) for settling.

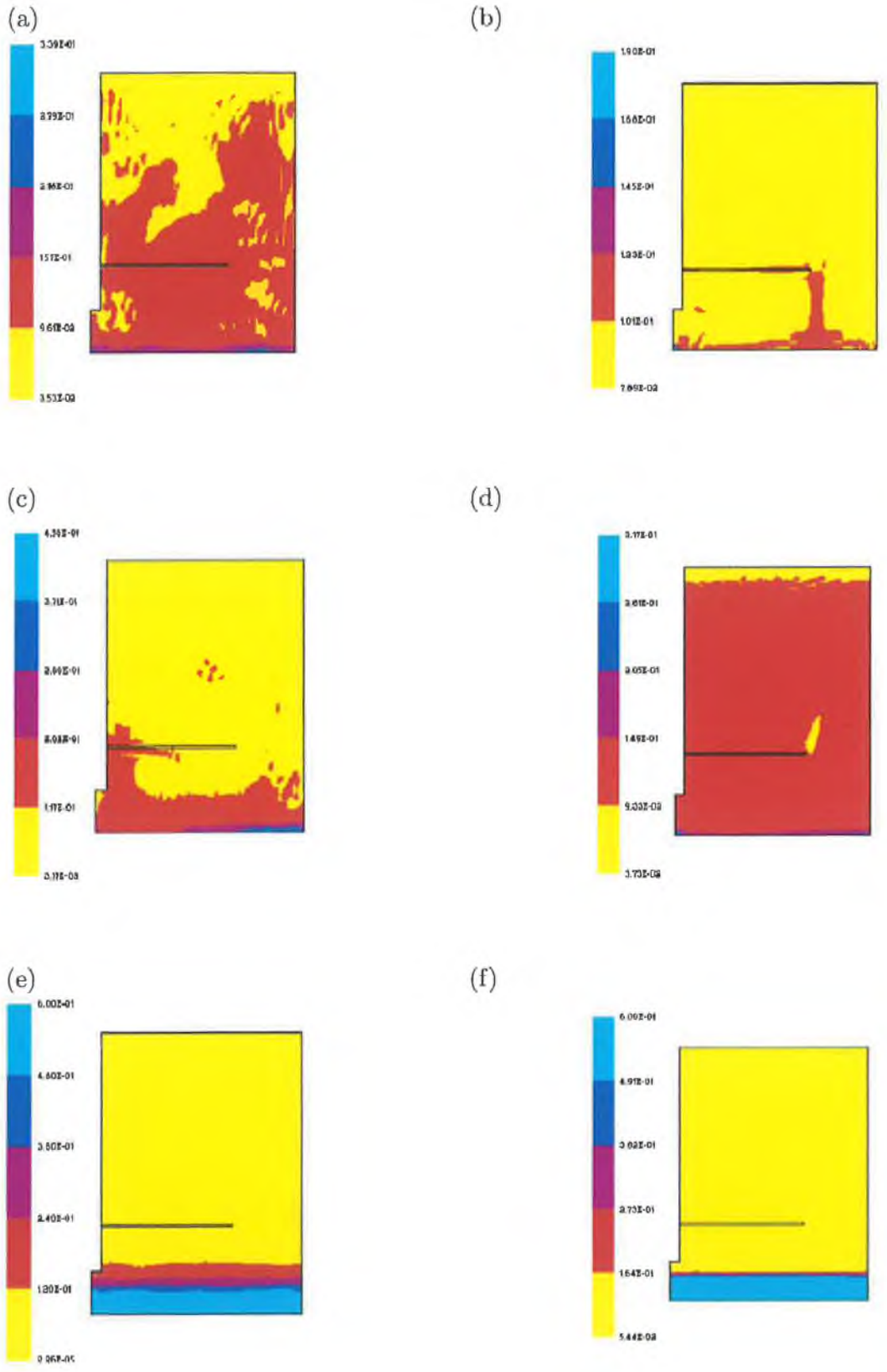

Figure B.4: Settling figures (a) in water after 2 seconds (b) in glycerol/water after 1 minute (c) in water after 12 seconds (d) in glycerol/water after 60 minutes (e) in water after 60 seconds (f) in glycerol/water after 70 minutes.

Appendix C

Engineering drawing

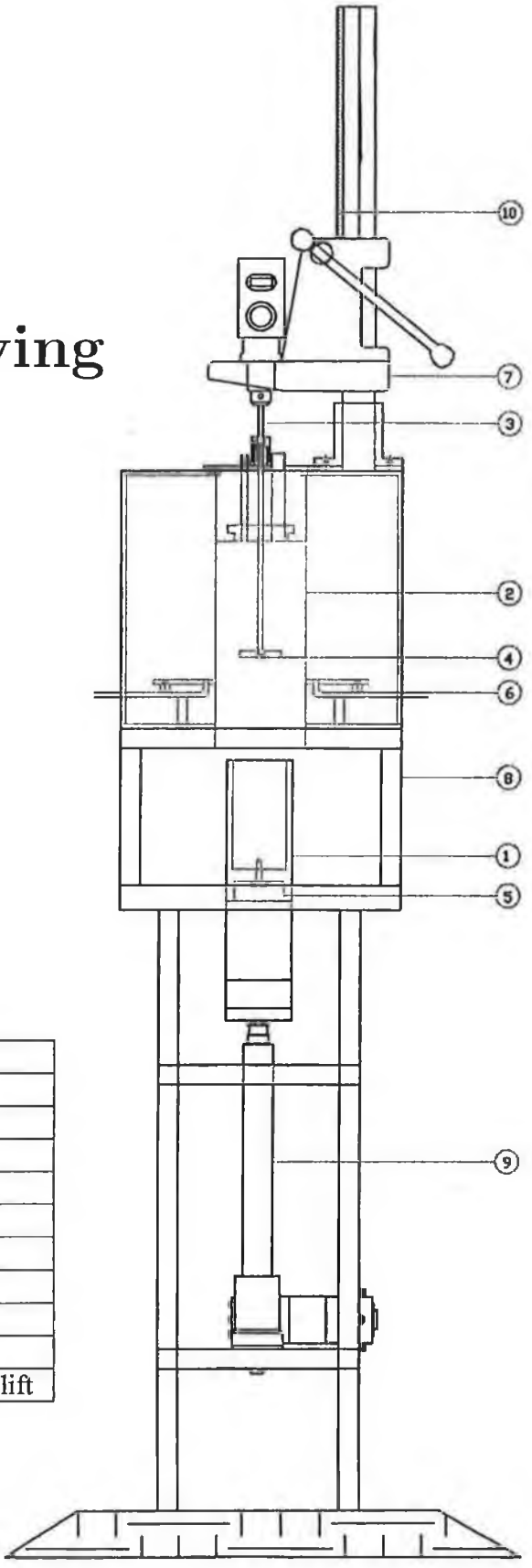

Part No.	Description
1	Crucible
2	Heater band
3	Stirring rod
4	Stirrer impeller
5	Crucible base
6	N_2 delivery tube
7	Stirring Motor holder
8	Furnace stands
9	Crucible Actuator
10	Rack and pinion screw driven lift

Figure C.1: Engineering drawing of the stir-caster. All the dimensions are relative and following a scale of 100 mm.

Appendix D

Temperature profiling experiments

D.1 Procedure

Temperature profiling was carried out to know the exact temperature distribution along the height of a compocaster graphite crucible. Control over the temperature (1 °C) profile is required for fraction solid control. The semi-solid range of the alloy is about 50 °C (figure 1.8). The solidus, eutectic and liquidus temperature of the alloy has been recorded at 538, 572 and 614 °C respectively [4].

Two K-type thermocouples were used in these experiments. One, the control thermocouple, was fixed at a constant height of 170 mm from the top of the furnace. This thermocouple was marked as control thermocouple. The other, thermocouple used for profiling was placed in contact with the bottom, inside surface of the crucible. Four different controlling temperatures settings were used, 550, 600, 650 and 700 °C. When temperatures stabilized at each set temperature, the profile thermocouple was moved up in 10 mm steps and left to record the temperature at that location for 8 minutes by which time the temperature had stabilized. The temperatures of every sub-step were recorded by a Pico data logger.

This experimental procedure was performed once with an empty crucible and once with a charge of A356.

D.2 Results

Figure D.1 represents the variation of some of the recorded temperatures with time for both the control and profile thermocouples. The results for both the empty and charged crucible set-up is shown. The furnace chamber top tempera-

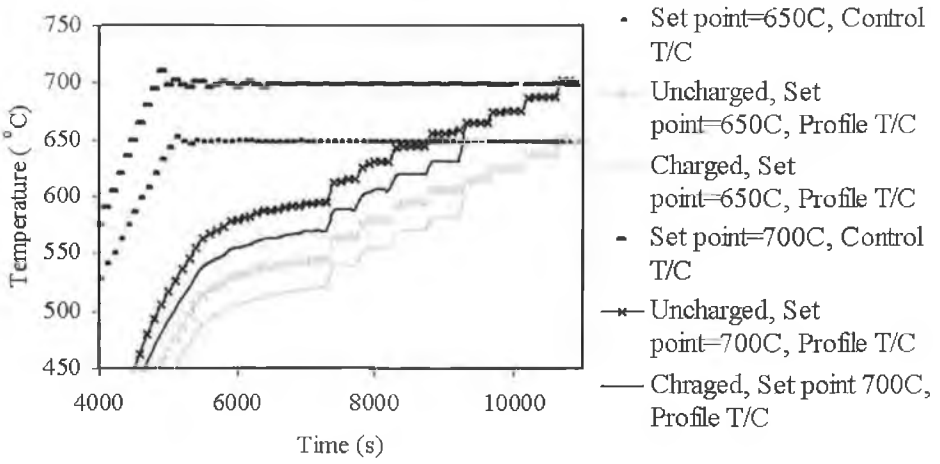

Figure D.1: Variation of temperatures with time for control and profile thermocouples both in charged and uncharged condition.

ture is higher than the bottom due to convection. As the control thermocouple was at the top, the control (set) temperature was same as the profile thermocouple temperature when it reached this position.

Figure D.2 represents the variation of the temperature along the length of the crucible with different temperatures set-points for the uncharged crucible. It is evident from this figure that the temperature increased almost linearly with the height of crucible from the bottom surface to the top. The variations are distinct with a temperature gradient (dt/dh) of 1.25 °C/mm up to 80 mm off base.

Figure D.3 shows the variation of the temperature along the length of the crucible for A356 charge and two different set-points. In this case, the variation of temperature with the length of the crucible was found to be different compared with the charged crucible. The temperature increased with increasing height off the crucible base until a height of 40 mm was reached. Then it increased abruptly near to the profile thermocouple. This is because of the change of environment from charged to uncharged region inside the crucible.

The charged area can be seen as a conduction zone and the uncharged area as an insulation zone.

It is clear from the figure D.2 and figure D.3 that the maximum temperatures at the bottom surface of the crucible for 650 °C and 700 °C temperature were found around 550 °C and 600 °C respectively for the uncharged condition. In the case of the charged condition, these temperatures at the base dropped to 500 °C and 575 °C respectively. It is clear that temperature in the charged region of the crucible decrease the surface temperature because of their conductivity of metal.

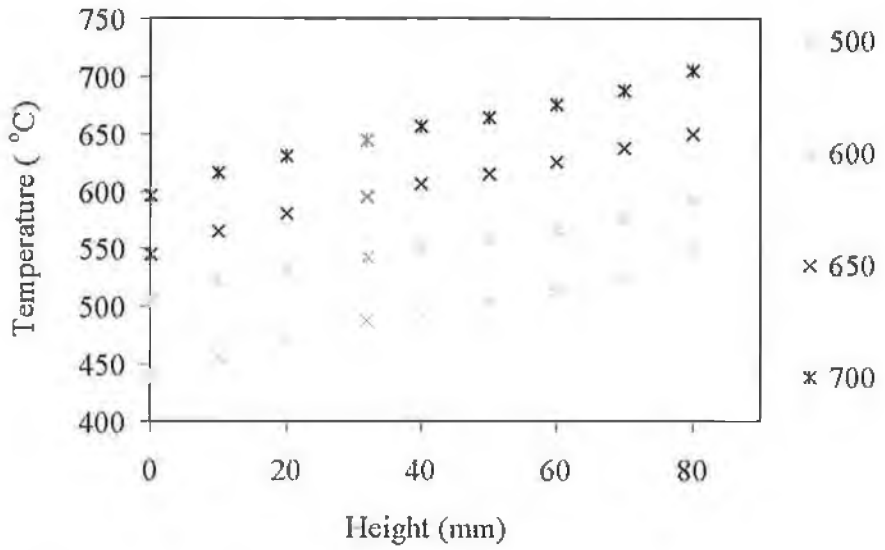

Figure D.2: Variation of temperature along the length from bottom to top of the crucible in uncharged condition.

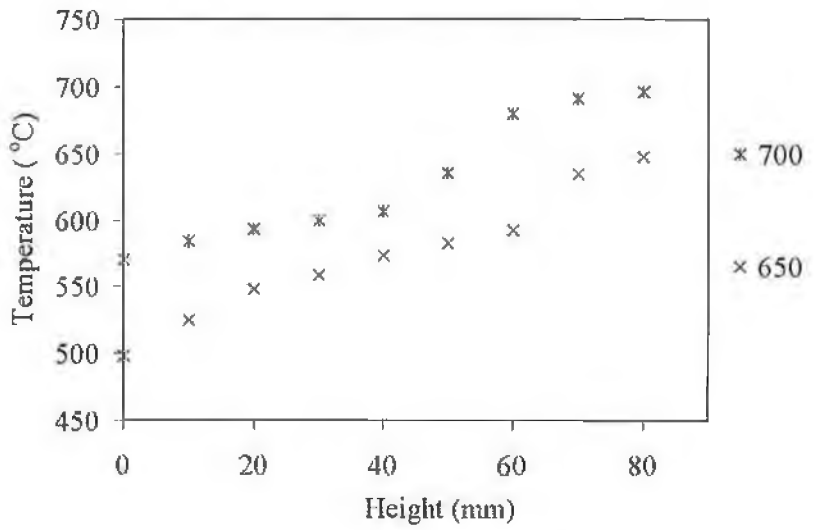

Figure D.3: Variation of temperature along the length from bottom to top of the crucible with charged A356.